

2-P. (mix)

R-747

**SIRU UTILIZATION  
VOLUME I**

**THEORY, DEVELOPMENT AND  
TEST EVALUATION**

by

**Howard Musoff**

March 1974

N74-28098

(NASA-CR-138574) SIRU UTILIZATION.  
 VOLUME 1: THEORY, DEVELOPMENT AND TEST  
 EVALUATION (Draper (Charles Stark) Lab.,  
 Inc.) 289 p HC \$17.25 CSCL 17G

Unclas  
63/21 16950

271



**The Charles Stark Draper Laboratory, Inc.**  
 Cambridge, Massachusetts 02139

R-747

SIRU UTILIZATION  
VOLUME I

THEORY, DEVELOPMENT AND  
TEST EVALUATION

by

Howard Musoff

March 1974

CHARLES STARK DRAPER LABORATORY, INC.  
CAMBRIDGE, MASSACHUSETTS  
02139

Approved: David J. Hoag

D.G. Hoag

Date: 27 Mar 74

## ACKNOWLEDGEMENT

This report was prepared by the Charles Stark Draper Laboratory under Contract NAS9-8242 with the Lyndon B. Johnson Space Center of the National Aeronautics and Space Administration.

The successful completion of the Utilization phase of the SIRU program and the publication of this Final Report culminates a long period of dedicated effort by both the C. S. Draper Laboratory and the sponsoring organization.

Malcolm Jones, the NASA project engineer at the Johnson Space Center, provided suggestions, creative criticism and continued support throughout the course of the contract. Appreciation is also extended to William Swingle, NASA Chief of the Technology Development Branch, Guidance and Control Division for program support of the SIRU Utilization task.

Individuals responsible for the engineering of individual portions of the task are identified here and their significant contributions acknowledged.

Jerold Gilmore, Division Director, provided technical supervision and in addition, substantial inputs to the Final Report.

Richard McKern, Project Engineer, managed the engineering and supervisory aspects of the project.

T. T. Chien developed the basic analysis applying to the statistical failure detection, isolation, and classification concept.

Eugene Salamin contributed the analysis of Quaternions presented in Appendix A of chapter 1.

Kenneth Vincent designed and reduced to routine practice the navigation function required to confirm the SIRU overall performance.

Robert Booth was responsible for the development of the single position calibration concept utilized in SIRU and contributed technical advice and counsel over a broad spectrum of engineering tasks.

John Oehrle and Roy Whittredge developed programming vital to the successful incorporation of the extended SIRU functions into the existing software.

David Swanson was responsible for SIRU testing and test data analysis.

Martin Landey, was responsible for much of the Reliability presentation.

David Brown was responsible for the integration, operation and maintenance of the DDP 516 computation facility associated with the SIRU system.

David Dove performed the Space Shuttle trajectory simulations presented in appendix A, Chapter 6.

John Sinkiewicz, Jr. was responsible for Gyro Module testing and maintenance support and George Bukow provided equivalent services for the Accelerometer Modules.

William Trosky, system test technician, is selected for special commendation for patient and painstaking effort.

Martin Landey and Stephen Helfant deserve special mention for data handling and storage services prepared under the direction of Julius Feldman.

In the preparation of the Final Report, the contributions of both Ross Cooper and Stephen Helfant to the composition, editing and preparation of the document for publication were invaluable. Also, the efforts of Linda Willy in preparation of technical illustrations and of the Technical Publications Group, with special mention to Therese Anciello, are acknowledged and appreciated.

The publication of this report does not constitute approval by the National Aeronautics and Space Administration of the findings or the conclusions contained herein. It is published for the exchange and stimulation of ideas.

R-747

## SIRU UTILIZATION REPORT

### ABSTRACT

This report presents a complete description of the additional analysis, development and evaluation provided for the SIRU system as identified in the requirements for the SIRU Utilization program set forth in Amendment 7S of NASA/Johnson Space Center Contract NAS 9-8242.

The SIRU configuration is a modular inertial subsystem with hardware and software features that achieve fault tolerant operational capabilities. The SIRU redundant hardware design is formulated about a six gyro and six accelerometer instrument module package. The modules are mounted in this package so that their measurement input axes form a unique symmetrical pattern that corresponds to the array of perpendiculars to the faces of a regular dodecahedron. This six axes array provides redundant independent sensing and the symmetry enables the formulation of an optimal software redundant data processing structure with self-contained fault detection and isolation (FDI) capabilities.

The SIRU Utilization program consisted of additional analytical and developmental effort in these four specific areas:

1. Failure Detection, Isolation, Classification and Recompensation (FDICR).
2. Error Source Propagation Characteristics.
3. Single Position Self Calibration.
4. Self Alignment System (Gyro Compassing).
5. Local Level Navigation Performance Demonstrations.

The theory, analysis, development description, software integration and performance evaluation of each of these advanced adjuncts comprised the SIRU Utilization program.

This report consists of three volumes.

Volume I, Theory, Development and Test Evaluations contains a complete description of the theory, analysis, implementation and test results for each of the tasks.

Volume I also contains a review of the reliability performance statistics, possible future applications for the developed techniques and conclusions and recommendations.

Volume II, **Software Documentation**, provides documentation of the additional software and software modifications required to implement the Utilization capabilities including assembly listings and flowcharts.

Volume III, contains the system-log of significant events from the beginning of the system testing program until it was completed in December, 1972.

A companion to this report, SIRU Development Final Report R-746, has been issued documenting the design, development and evaluation of the basic SIRU system.

## TABLE OF CONTENTS

	Page
1. Introduction	1
1.0 Scope	1
1.1 SIRU Utilization Scope	10
1.2 FDICR	11
1.3 Single Position Self Calibration	12
1.4 Attitude Algorithm Small Angle Error Equations	12
1.5 SIRU Self-Alignment	13
1.6 Local Level Navigator and Error Propagation	13
1.7 End-to-End Navigation Demonstrations	14
1.8 Software Memory and Timing Requirements	14
Appendix	15
A1 Quaternions	15
A1.0 Introduction	15
A1.1 Notation	15
A1.2 Relation Between the Quaternion and the Corresponding Direction Cosine Matrix	16
2. Failure Detection, Isolation, Classification and Recompensation (FDICR)	19
2.0 Introduction	19
2.1 Statistical FDICR	21
2.2 Statistical FDICR Detection System	26
2.3 Isolation of a Degraded Instrument - Statistical FDICR	33
2.4 Statistical FDICR Classification System	35
2.5 Recalibration - FDICR	36
2.6 FDICR Test Results	40
2.6.1 Inclusion of a Spike Degradation at a Gyro Output	45
2.7 Software Memory and Timing Requirements	46
Appendix	
A2 SIRU Equations	47

## TABLE OF CONTENTS (cont)

	Page
A2.0 Statistical FDICR Parity Equations	47
A2.1 Parity Equations Used to Detect a First Failure	47
A2.2 Parity Equations Used to Detect a Second Failure	47
A2.3 TSE Parity Equations	49
3. Single Position Self-Calibration	51
3.0 Introduction	51
3.1 Required SIRU Level Tolerance	51
3.2 Parity Equations	52
3.3 SIRU Body Axis Drifts	53
3.4 Single Position Calibration Equations Selected for the Calibration Position 2	53
3.5 Deviation of Direction Cosine Matrix, $C_B^C$	57
3.6 Single Position Calibration Error Equations	59
3.7 Additional Equations Useful in Analyzing Single Position Calibration Test Data	61
3.8 Single Position Calibration Data Taken with No Base Motion	62
3.9 Calculated East Axis Drifts Before and After Using Single Position	68
3.10 Data Taken with Oscillations About the Vertical Axis	68
3.10.1 Oscillatory Test, +0.15°/hr Miscompensation, Gyros A and B	69
3.10.2 Dynamically Induced Gyro Drifts	70
3.10.3 Analysis of SPC Oscillatory Tests	70
3.11 Software Memory and Timing Requirements	73
Appendix	
A3 Proposed New Vertical Drift Estimation Procedure	75
A3.0 Introduction	75
A3.1 Proposed Method	75
A3.2 Estimates to be Used if New Filtering Method is Implemented	76
B3 X-Body Axis Drift Filter	79
4. Attitude Algorithm Small Angle Error Equations	83

TABLE OF CONTENTS (cont)

	Page
5. SIRU Self-Alignment	89
5.0 Introduction	90
5.1 Coarse Alignment - Introduction	89
5.2 Coarse Alignment Leveling Procedure	90
5.3 Azimuth Coarse Alignment Procedure	93
5.4 SIRU Coarse Alignment Data	96
5.5 Selection of Fine Alignment Algorithm	99
5.6 Special Considerations When Using Quaternions	99
5.7 Conventional Alignment vs. Alignment Using the East Gyro as a Sensor	99
5.8 Alignment Methods	101
5.8.1 Least Squares Method	101
5.8.2 Luenberger Observer	101
5.8.3 Alignment to an Inertial Frame	101
5.8.4 Final Selection of a Method	102
5.9 Fine Alignment Introduction	102
5.10 Alignment System Analog Models	102
5.11 Leveling Loop Design	103
5.12 Azimuth Loop Design	107
5.13 Final Values of Parameters Chosen	110
5.14 Alignment Loop Algorithm	110
5.15 SIRU Fine Alignment Data	113
5.16 Software Memory and Timing Requirements	119
Appendix	
A5 Least Squares Filter	121
6. Local Level Navigator System	125
6.0 Introduction	125
6.1 Local Level Navigator System	125
6.2 Local Level Attitude Damping	125
6.3 Local Level Navigator Error Sensitivities	130
6.4 Error Propagation in a Dynamic Environment	138
6.4.1 Anisoinertia and Float Offset Drifts	139
6.4.2 Pseudo-Coning Drifts $W_{pc}$	144
6.4.3 Examination of SIRU Test Data for Dynamic Inputs	146

TABLE OF CONTENTS (cont)

	Page
6.4.4 Examination of SIRU Test Data for Errors Propagated when FDICR is Implemented	150
6.5 Software Memory and Timing Requirements	153
Appendix	
A6 SIRU Software Simulation Results	155
7. End-to-End Navigation Demonstrations	165
7.0 Introduction	165
7.1 Static Test Results	166
7.1.1 Test Sequence #1	166
7.1.2 Test Sequence #2	168
7.1.3 Test Sequence #3	170
7.2 Dynamic Test Results	171
7.2.1 Test Sequence #4	172
7.2.2 Test Sequence #5	173
7.2.3 Test Sequence #6	176
7.2.4 Test Sequence #7	178
7.2.5 Test Sequence #8	180
7.3 Conclusions	180
Appendix	
A7 Computation Axis Drifts as a Function of Gyro Drifts in SIRU Offset Position of $\Delta RA32 = 45^\circ$ , $\Delta RA16 = +5^\circ$	183
8. SIRU System Reliability Experience and Prediction	185
8.0 Introduction	185
8.1 Assumptions Made in this Analysis	185
8.2 Assessment of SIRU Hardware Failure Rates	185
8.3 Triad Reliability Calculations	192
8.4 SIRU Reliability Calculations	193
8.4.1 EA Reliability	194
8.4.2 Inertial Component Module Axis Reliability	195
8.4.3 Consideration of Axis Electronics	196
8.4.4 Summary	197
8.5 SIRU Reliability Summary	197
8.6 FDI Reliability	198

TABLE OF CONTENTS (cont)

	Page
8.6.1 Introduction	198
8.6.2 FDI Reliability	198
8.6.3 First Failure	202
8.6.4 Second Failure	209
8.6.5 Simulation Accuracies	215
8.6.6 Limitations of Preceding Analysis	222
8.7 Statistical FDICR Reliability	222
8.7.1 Basic Equations	222
8.7.2 False and Missed Detection and Isolation	223
8.8 Mission Abort and Loss Probabilities	225
8.8.1 TSE Abort and Vehicle Loss Probabilities	227
8.8.2 Statistical FDICR Abort and Vehicle Loss Probabilities	231
8.9 SIRU Reliability Conclusions	235
9. Applications of SIRU Utilization Results	237
9.0 Introduction	237
9.1 Multiple Gimbal Systems	237
9.2 Aircraft Redundant Guidance System	244
9.3 Precision Attitude Pointing System	248
9.4 Computation, Software, and Hardware Reorganization After a Failure	250
9.5 Threshold and Filtering Criteria for Reliable Fault Detection and Non-Ambiguous Isolation	251
9.6 Requalification of Soft Failures	252
10. Conclusions and Recommendations	253
10.0 Conclusion	253
10.1 Capabilities and Limitations of the Redundant Strap- down Approach	254
10.2 Recommendations	255

## LIST OF ILLUSTRATIONS

Figure No.		Page
1.1	Instrument Input Axes Orientation Relative to the Instrument Frame Triad and the Dodecahedron	2
1.2	SIRU Instrument Package	3
1.3	SIRU Data Processing	9
2.0	Overall View of SIRU Utilization FDICR	20
2.1	Block Diagram of a Statistical FDICR System	25
2.2	Block Diagram of the Detection System	27
2.3a	Noise Probability Densities	29
2.3b	Detection Function of SPRT	29
2.4	Illustration of Extra Delay for Detection in SPRT	29
2.5	Suboptimal Detection System - Block Diagram	30
2.6	Illustration of Variance Degradation	33
2.7	Isolation Table for Degraded Gyros	34
2.8	Recompensation Management Procedure - Constant Bias Degradation	37
2.9	Block Diagram of Identification System	38
2.10	Recompensation Management Procedure - Ramp Bias Degradation	39
2.11	Detection of Ramp Bias Degradation	40
2.12	Statistical FDICR Average Detection Time - Static Case - SIRU - Bias Degradation of Gyro	41
2.13	Statistical FDICR Average Classification Time - Static Case - SIRU - Bias Degradation	42

PRECEDING PAGE BLANK NOT FILMED

LIST OF ILLUSTRATIONS (cont)

Figure No.		Page
2.14	Estimation of Constant Gyro Bias Degradation Magnitude - Static Case - SIRU FDICR Tests	43
2.15	Detection, Isolation and Classification of Gyro Ramp Bias Degradation Cal Pos. 2 - Static Case - SIRU - FDICR Tests	43
2.16	Detection, Isolation, and Classification of Gyro Constant Bias Degradations - Dynamic Environment - SIRU FDICR	44
2.17	Detection, Isolation, and Classification of Accelerometer Constant Bias Degradations - Static Environment - SIRU FDICR	46
2.18	Estimation of Constant Accelerometer Bias Degradation Magnitudes - Static Case - SIRU FDICR	46
3.1	Error in E or F Single Position Calibration Reference Gyro as a Function of SIRU X Axis Tilt from the Vertical	52
3.2	Definition of True Azimuth Angle $\phi_D$	58
B3.1	Residual Vertical Noise Amplitude vs. Frequency (System Tilt = 5°) for Eq. B3.2 Filter	80
B3.2	Residual Vertical Noise Amplitude vs. Frequency (System Tilt = 5°) for Eq. B3.2 Filter Output Averaged $\frac{1}{2}$ Hour where Eq. B3.2 Filter has $\frac{1}{2}$ Hour Settling Time	81
4.0	Block Diagram	83
5.1	Coarse Leveling Vectors	91
5.2	Rotation of Level from Navigational Frame	93
5.3a	North Leveling Loop	104
5.3b	East Leveling Loop	105
5.3c	Azimuth Loop	105
5.4	Modified Leveling Loop	106

LIST OF ILLUSTRATIONS (cont)

Figure No.		Page
5.5a	Fig. 5.3a Bode Plot	106
5.5b	Fig. 5.4 Bode Plot	106
5.6a	Fig. 5.3a Root Loci	107
5.6b	Fig. 5.4 Root Loci	107
5.7	Modified Azimuth Loop	109
5.8a	Fine Alignment Azimuth Gain $K_Z$	111
5.8b	Fine Alignment Azimuth Gain $K_F$	111
5.8c	Fine Alignment Leveling Gain $K_B$	112
5.8d	Fine Alignment Leveling Gain $K_L$	112
5.8e	Fine Alignment Leveling Gain $K_V$	112
5.9	North Leveling Loop (Fig 5.3a) Equivalent Signal Flow Diagram	113
5.10	SIRU Fine Alignment Algorithm (Static) - 12 Hour Test	113
5.11	SIRU Fine Alignment Algorithm (Static) - 12 Hour Test	114
5.12	SIRU Fine Alignment Algorithm (Static)	115
5.13	SIRU Fine Alignment Algorithm (Static)	115
5.14	SIRU Fine Alignment Algorithm (Static)	116
5.15	SIRU Fine Alignment Algorithm (Static)	116
5.16	SIRU Fine Alignment Algorithm (Static)	117
5.17	SIRU Fine Alignment Algorithm - Oscillatory 1° P-P at 0.5 Hz	117
5.18	SIRU Fine Alignment Algorithm - Oscillatory 1° P-P at 0.25 Hz	118
5.19	SIRU Fine Alignment Algorithm - Oscillatory 1° P-P at 0.25 Hz	119

LIST OF ILLUSTRATIONS (cont)

Figure No.		Page
6.0	Conceptual Block Diagram - Local Navigator	126
6.1	Local Level Region of Stability	131
6.2	Attitude Error for Compensated Local Navigational Axis Drift - Cal. Position 2	132
6.3	Radial Velocity Error for Compensated Local Navigational Axis Drift - Cal. Position 2	132
6.4	Latitude Error for A .060 deg/hour Drift Introduced into the East Axis - Cal. Position 2	133
6.5	Longitude Error for A .060 deg/hour Drift Introduced into the North Axis - Cal. Position 2	133
6.6	Longitude Error for a 1 cm/sec <sup>2</sup> Bias Error Introduced into the East Axis - Cal. Position 2	135
6.7	Latitude Error for a 1 cm/sec <sup>2</sup> Bias Error Introduced into the North Axis - Cal. Position 2	135
6.8	Latitude Error for a 4 milliradians Offset About the Vertical Axis in Cal. Position 2	136
6.9	Longitude Error for a 4 milliradians Offset About the Vertical Axis in Cal. Position 2	136
6.10	Longitude Error for a .060 deg/hour Drift Introduced into the East Axis-Cal. Position 2	137
6.11	Latitude Error for a .060 deg/hour Drift Introduced into the North Axis - Cal. Position 2	137
6.12	SIRU Navigation Performance Longitude Error 5°/second (for 6 hours) About the Vertical Axis	149
6.13	SIRU Navigation Performance Latitude Error 5°/second (for 6 hours) About the Vertical Axis	149
A6.1(a)	Simulated Body Rate vs. Time - Pitch	150
A6.1(b)	Simulated Body Rate vs. Time - Roll	156
A6.1(c)	Simulated Body Rate vs. Time - Yaw	157
A6.2(a)	Simulated Body Specific Force vs. Time - Pitch	157
A6.2(b)	Simulated Body specific Force vs. Time - Roll	158

LIST OF ILLUSTRATIONS (cont)

Figure No.		Page
A6.2(c)	Simulated Body Specific Force vs. Time - Yaw	158
7.1	SIRU Mounted on Test Table System - Showing Orientation of 16 and 32 inch Table Axes	165
7.2	Test #1 - Latitude Error	168
7.3	Test #2 - Latitude and Longitude Errors	169
7.4	Test #3 - Latitude and Longitude Errors	171
7.5	Test #4 - Latitude and Longitude Errors	173
7.6	Test #5 - Latitude and Longitude Errors	175
7.7	Test #6 - Latitude and Longitude Errors	177
7.8	Test #7 - Latitude and Longitude Errors	177
7.9	Navigation Errors Incurred During Low Frequency, Zero-Mean Oscillation of SIRU System	180
A7.1	Approximate Orientation of SIRU During Test Sequence	183
8.1	SIRU System Reliability: System Configured to Isolate Two Failures (Experienced Failure Rates)	186
8.2	SIRU System Reliability: System Configured to Isolate Three Failures (Experienced Failure Rates)	186
8.3	SIRU System Reliability: System Configured to Isolate Two Failures (90% Confidence Failure Rates)	187
8.4	SIRU System Reliability: System Configured to Isolate Three Failures (90% Confidence Failure Rate)	187
8.5	SIRU Reliability Schematic	193
8.6	Redundancy Block Diagram	194
8.7	Accumulated Angle (No Quantization) for a Bias Shift in Drift	199
8.8	Total Squared Error (No Noise) for a Bias Shift in Drift (No Quantization)	199

LIST OF ILLUSTRATIONS (cont)

Figure No.		Page
8.9	Total Squared Error for High Drift Degradation (No Quantization)	201
8.10	Total Squared Error for Low Drift Degradation (No Quantization)	201
8.11	Probability of Detection vs. Drift Rate Degradation	202
8.12	Probability of Not Detecting a Failure - First Failure (A-Gyro)	206
8.13	Probability of Not Isolating a Failure - First Failure	208
8.14	Probability of Not Isolating a Failure - First Failure (A-Gyro)	210
8.15	Probability of Not Isolating a Failure - First Failure (A-Gyro)	211
8.16	Probability of Not Detecting a Failure - 2nd Failure (A then B Failed)	214
8.17	Probability of Not Isolating Second Failure (B-Gyro)	216
8.18	Probability of Not Isolating Second Failure (B-Gyro)	217
8.19	Probability of Falsely Isolating E-Gyro as 2nd Failure (B-Gyro is 2nd Failure)	218
8.20	Probability of Falsely Isolating F-Gyro as 2nd Failure (B-Gyro is 2nd Failure)	219
8.21	Probability of Falsely Isolating E-Gyro as 2nd Failure (B-Gyro is 2nd Failure)	220
8.22	Standard Deviation of Estimated Probability	221
8.23	EDICR Simplified Block Diagram	224
8.24	Probability of Not Detecting and Isolating A Degradation - Statistical FDICR	226

LIST OF ILLUSTRATIONS (cont)

Figure No.		Page
9.1	Triple Redundant Force Actuator Block Diagram	245
9.2	Analog Likelihood Ratio Detection Filter	248
9.3	Precision Attitude Pointing System	248
9.4	Attitude Sensor Noise Characteristics	249

LIST OF TABLES

Table No.		Page
1.1	SIRU Parity Equations	5
2.0	Parity Equation Set (for Mechanized System)	24
3.9.1	SPC Estimation Errors with 0.15°/hr Constant Bias Degradation on Gyros A, B, C and D	65
3.9.2	SPC Estimation Errors with a Miscompensation of 0.15°/hr on Gyros A and C	65
3.9.3	SPC Estimation Errors with a Miscompensation of +0.15°/hr on Gyro A and a Miscompensation of -0.15°/hr on Gyro B	66
3.9.4	SPC Estimation Errors with a Miscompensation of -0.15°/hr on Gyro A and a Miscompensation of +0.15°/hr on Gyros B and C	66
3.9.5	SPC Estimation Errors with a Miscompensation of +0.15°/hr on Gyro C and a Miscompensation of -0.15°/hr on Gyro D	66
3.9.6	SPC Estimation Errors with a Miscompensation of +0.030°/hr on Gyro E	67
3.9.7	SPC Estimation Errors with a Miscompensation of +0.030°/hr on Gyro F	67
3.9.8	SPC Estimation Errors with a Miscompensation of +0.030°/hr on Gyros E and F	67
3.10	Calculated East Axis Drifts, Cal. 2 Position. Before and After a Single Position Calibration	68
3.11	Oscillatory Test, +0.15°/hr Miscompensation, Gyros A and B	69
3.12	Dynamically Induced Gyro Drifts	70
3.13	Single Position Calibration Estimation Errors	71

PRECEDING PAGE BLANK NOT FILMED

LIST OF TABLES (cont)

Table No.		Page
5.0	Coarse Alignment Errors Static Environment (Azimuth About X)	97
5.1	Coarse Alignment Errors Dynamic Environment (1 P-P Oscillation About Vertical Axis)	98
5.2	Alignment Errors for Oscillations about the Vertical	118
5.3	Software Memory and Timing Requirements for Fine and Coarse Alignment Programs	119
6.0	Error Sensitivites Computed from SIRU Test Data for the First Two Hours and Draper Lab Latitude	138
6.1	Theoretical Average Anisoinertia and SRA Cross Coupling Drift, $W_{DA}$ , for Oscillatory Input to The Test Table	142
6.2	Theoretical Anisoinertia and SRA Cross Coupling Drift for Slew Inputs to the Test Table	142
6.3	Theoretical Pseudo-Coning Drifts for Oscillatory Inputs to the Test Table and no OA Coupling Compensation	144
6.4	Attitude Drift with and without OA Coupling Com- pensation	146
6.5	SIRU Navigation Tests for Dynamic Environments	147
6.6	Land Navigation Errors Due to Delay in Detecting and Isolating Gyro Constant Bias Degradations	151
6.7	Land Navigation Errors Due to Delay in Detecting and Isolating Accelerometer Constant Bias Degradations Cal. 2 Pos.	152
6.8	Land Navigation Errors Due to Delay in Detecting and Isolating Gyro and Accelerometer Constant Bias	152
A6.1	SIRU Software Simulation Sensor Performance Parameters	155
A6.2	Sensor Performance Parameter Error Coefficients	157
A6.3	Performance Summary	161
A6.4	Down Range and Cross Range Error Ratio Simulation Results	162

LIST OF TABLES (cont)

Table No.		Page
A6.4	Typical Monte Carlo Run	163
A6.6	Monte Carlo Run with "1 $\sigma$ RSS Performance"	163
7.1	Gyro and Accelerometer Failure Detection, Classification, and Recompensation Parameters During the Test Sequence	
8.1	SIRU System Hardware Failure History	189
8.2	SIRU System Hardware Failure Rate Estimation	190
8.3	Derivation of Triad Failure Rate	192
8.4	Reliability Analysis Summary (Mission Time = 730 Hours)	197

## DICTIONARY OF TERMS

SIRU	Strapdown Inertial Reference Unit
NASA	National Aeronautics and Space Administration
MSC	Manned Spacecraft Center (now L.B. Johnson Space Center)
FDI	Failure Detection and Isolation
EA	Electronics Assembly
CRT	Cathode Ray Tube
FDICR	Failure Detection, Isolation, Classification and Recompensation
TSE	Total Squared Error
NBD	Normal Bias Drift
OA	Output Axis
IMU	Inertial Measurement Unit
SF	Scale Factor
SPRT	Sequential Probability Ratio Test
ADIA	Acceleration-Dependent Gyro Drift Due to Acceleration Along the Input Axis
BD	Bias Drift
IRIG	Inertial Reference Integrating Gyro
ADSRA	Acceleration-Dependent Gyro Drift Due to Acceleration Along the Spin Reference Axis
SPC	Single Position Calibration
WRT	With Respect To
IA	Input Axis
NM (nm)	Nautical Miles
PPM	Parts Per Million
SA	Spin Axis
RSS	Root Sum Squared
A/D	Analog to Digital
D/A	Digital to Analog
SPOT	Strapdown System Performance Optimization Test Evaluations
BITE	Built-In Test Equipment
PTE	Pulse Torque Electronics
IC	Inertial Component

## Chapter 1

### Introduction

#### 1.0 Scope

This technical report covers the development, test activities and evaluation of the Strapdown Inertial Reference Unit (SIRU), NASA/MSC Contract NAS 9-8242 over the period from August, 1971 to December, 1972. Report R-746, SIRU Development Final Report<sup>1</sup>, issued separately, covers the fundamental features of the SIRU system hardware and basic software complement as developed over the period from June, 1968 to November, 1971.

This report is issued in three volumes. Volume I covers the theory, analysis, implementation and test results of the statistical failure detection and isolation (FDI), single position calibration and self alignment techniques that were implemented during the above period.

Volume II documents the software developed in this period and Volume III is a system log summary that identifies various meaningful laboratory events over the entire SIRU program.

The following system introductory summary is provided for continuity and to furnish a basic understanding of the SIRU concept as described in detail in R-746.

SIRU is a redundant modular instrument package employing six gyroscopes and six accelerometers and developed to achieve and investigate high reliability Guidance and Navigation system concepts. A symmetrical instrument array is used in which gyro and accelerometer input axes are aligned to correspond with the normals of dodecahedron faces (Fig. 1.1).

The dodecahedron geometry yields a unique symmetry in which all instrument input axes (IA) are at a spherical angle  $2\alpha(63.4^\circ)$  from each other. In the particular orientation used, pairs of gyro or accelerometer axes lie in the orthogonal planes of a reference triad and are displaced by an angle  $\alpha$  from principal triad axes. This symmetry enables optimal redundant reorganization data processing with minimum error propagation. Further, by means of instrument output comparisons, self-contained failure isolation of up to two out of six of both instrument types is achieved and a third failure may be detected. With the aid of additional diagnostics,

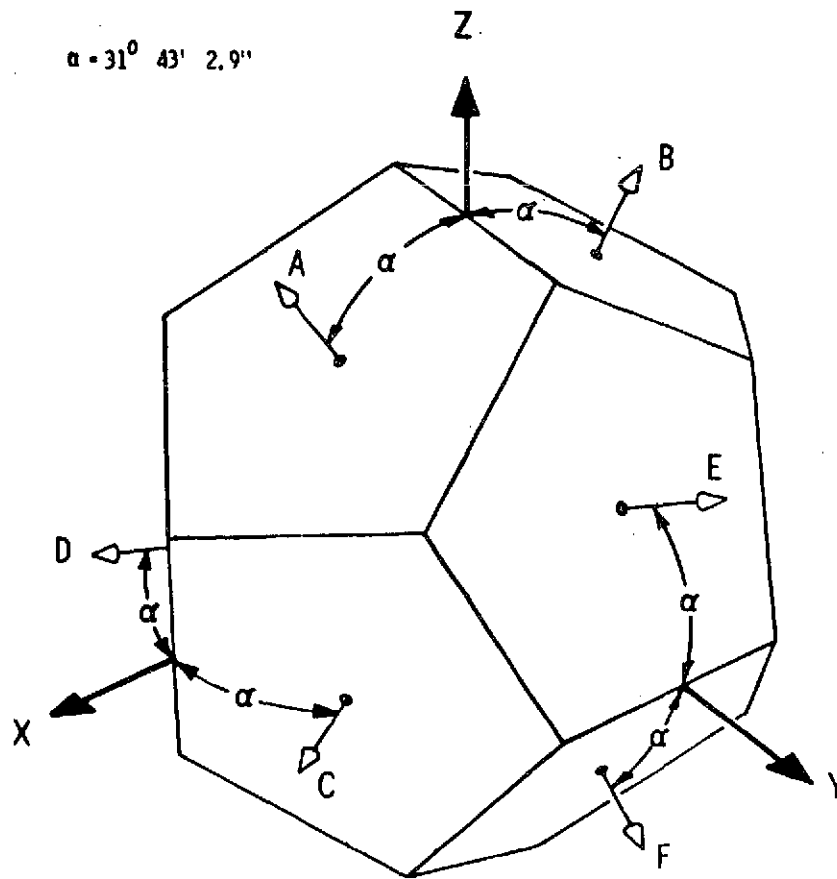


Fig. 1.1 Instrument Input Axes Orientation Relative to The Instrument Frame Triad and the Dodecahedron

the processing structure also allows continued operation with three out of six failures. The Redundant Instrument Package is an assembly of gyro and accelerometer modules in which each instrument module is a prealigned normalized assembly that contains its own torque-to-balance electronics, temperature controller, etc. (Fig. 1.2).

These modular features provide enhanced system maintainability. The redundant hardware concepts are also applied in the electronics (dual power supplies, triple redundant clocks, etc.) The degree of redundancy used in the Electronics Assembly (EA) is based upon the relative reliability of the individual circuits and circuit isolation concepts. The EA is mechanized so that it is free from the possibility of a system failure resulting from a single-point failure mechanism. In summary, the system is tolerant of electronic and instrument degradation and catastrophic failures and yields the predicted performance with multiple failures.

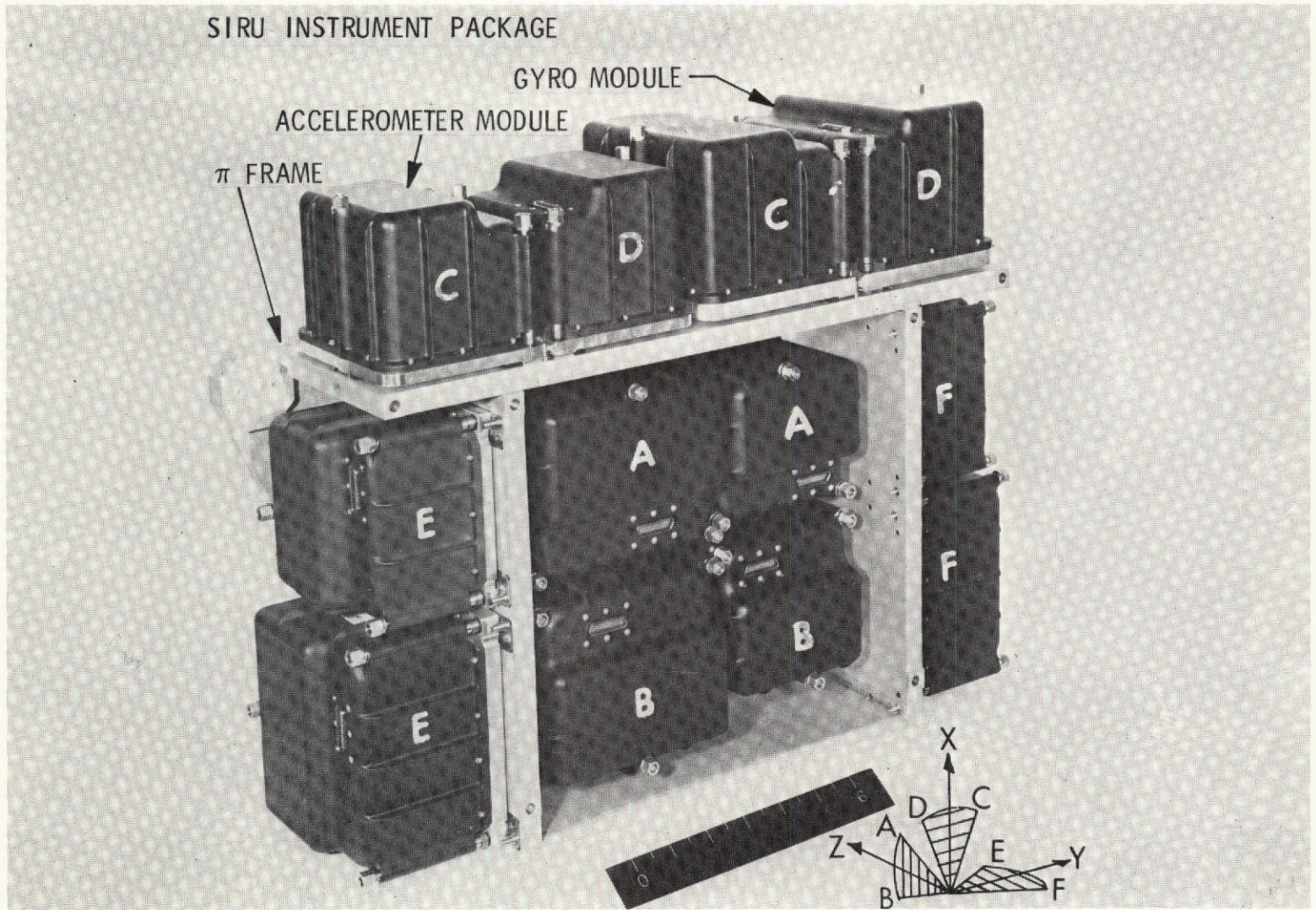


Fig. 1.2 SIRU Instrument Package

The SIRU basic processing redundancy concepts may be placed in perspective by considering the redundant nature of the measurement data. Visualize gyro and accelerometer input axes aligned to be colinear with the normals A through F of the dodecahedron, and oriented with respect to an orthogonal triad (Fig. 1.1) so that input axis pairs lie in orthogonal planes and are equally displaced by an angle ( $\alpha$ ) about each positive triad axis. For a gyro set, this orientation yields a relationship between angular rate inputs ( $W$ ) about triad axes and the gyro measurements ( $m$ ) that may be expressed in matrix form in terms of the orientation geometry as;

$$\begin{aligned} \underline{m} &= \underline{H} \underline{b} \\ \underline{b}^T &= [W_X \ W_Y \ W_Z] \\ \underline{m}^T &= [m_a \ m_b \ m_c \ m_d \ m_e \ m_f] \\ \underline{H}^T &= \begin{bmatrix} s & -s & c & c & 0 & 0 \\ 0 & 0 & s & -s & c & c \\ c & c & 0 & 0 & s & -s \end{bmatrix} \end{aligned} \quad (1.1)$$

where:

$$\begin{aligned} c &= \cos \alpha = \left( \frac{5 + \sqrt{5}}{10} \right)^{1/2} \approx 0.851 \\ s &= \sin \alpha = \left( \frac{5 - \sqrt{5}}{10} \right)^{1/2} \approx 0.526 \end{aligned}$$

As seen from the equation, each instrument provides a measure of redundant data, i.e., instruments A, B, C, and D all sense a component of input along the X triad-axis. By algebraic solution of the equations, equivalent triad-axis rate or acceleration solutions can be obtained from any three gyros or accelerometers.

The processing structure used to obtain equivalent triad solutions from the dodecahedron array corresponds to a least squares solution form:

$$\hat{\underline{b}} = (\underline{H}^T \underline{\lambda} \underline{H})^{-1} \underline{H}^T \underline{\lambda} \underline{m} \quad (1.2)$$

where  $\underline{b}$  is defined as the "best" triad solution estimate and  $\underline{\lambda}^{-1}$  corresponds to a diagonal 6x6 matrix whose terms represent the individual instrument's failure status.

This solution provides a "best" estimate for the geometry corresponding to the instruments that are considered usable ( $\lambda = 1$ ). Thus the  $\lambda$ , 6x6 matrix is unity

if all instruments are performing satisfactorily, and the appropriate elements are set to zero when a failure is detected. A triad solution can be determined for any combination of instruments (i.e., 5-, 4-, and 3-gyro or accelerometer combinations) by manipulation of  $\lambda$ . This structure is completely regenerative in that, if instrument "healing" is observed in the failure isolation process, the instrument may be recertified.

A self-contained FDI algorithm that has been used to establish the  $\lambda$  status is based upon a simple comparison of measurement outputs. The unique symmetrical properties of the array allow one to generate a series of 15 equations (parity equations) based on comparison of four measurements, all of which result in  $\epsilon$ , the residual output that ideally would be zero if all instruments are operating perfectly, Table 1.1.

TABLE 1.1 SIRU Parity Equations

No.	Instruments	Equations
1	ABCD	$(m_a - m_b) c + (m_c + m_d) s =  \epsilon $
2	ABCE	$(m_b - m_c) c - (m_a + m_e) s =  \epsilon $
3	ABCF	$-(m_a + m_c) c + (m_b + m_f) s =  \epsilon $
4	ABDE	$-(m_a + m_d) c + (m_b + m_e) s =  \epsilon $
5	ABDF	$(m_b - m_d) c - (m_a + m_f) s =  \epsilon $
6	ABEF	$(m_e + m_f) c - (m_a + m_b) s =  \epsilon $
7	ACDE	$(m_d - m_e) c + (m_a - m_c) s =  \epsilon $
8	ACDF	$(m_c - m_f) c + (m_a - m_d) s =  \epsilon $
9	ACEF	$(m_a - m_f) c + (m_c - m_e) s =  \epsilon $
10	ADEF	$(m_a - m_e) c + (m_d - m_f) s =  \epsilon $
11	BCDE	$(m_c + m_e) c - (m_b + m_d) s =  \epsilon $
12	BCDF	$-(m_d + m_f) c + (m_b + m_c) s =  \epsilon $
13	BCEF	$(m_b - m_c) c - (m_c + m_f) s =  \epsilon $
14	BDEF	$(m_b - m_f) c - (m_d + m_e) s =  \epsilon $
15	CDEF	$(m_c - m_d) c + (m_e - m_f) s =  \epsilon $

Note:  $m_a$  = measurement of axis A accelerometer or gyro       $s = \sin(\alpha)$   
 $c = \cos(\alpha)$        $\epsilon = \text{Threshold Level}$

In the case of the gyros, each term in the equation corresponds to an accumulated  $\Delta\theta$  count over a comparison period.

When all system measurements are operating satisfactorily, the residuals from these equations using the  $\Delta\theta$  count in the comparison period will be below the failure threshold. If, however, the gyro along A has malfunctioned, the series of equations 1 through 10 indicate incorrectly, while 11 through 15 agree, thereby isolating the failure. If a second instrument failure occurs, inspection of the remaining equations (11 through 15) allows another level of failure isolation. If a third failure occurs, none of the equations are satisfied and the failure is detected.

If one compares the relative magnitudes and polarities of the residuals, dependent upon the nature of the third failure, isolation may also be possible.

Another technique which has been synthesized in the computational software is based on the use of best-estimate solution,  $\hat{\underline{b}}$ , (Eq. 1.2). For example, the best-estimate of what the instrument measurements should be is:

$$\hat{\underline{m}} = \underline{H} \hat{\underline{b}} \quad (1.3)$$

A comparison of the actual measurement,  $\underline{m}$ , with the estimated measurement yields an estimate of the measurement error for all six instruments ( $\underline{E}_O$ ).

$$\hat{\underline{E}}_O = \underline{m} - \hat{\underline{m}} = \underline{m} - \underline{H} \hat{\underline{b}} \quad (1.4)$$

where:

$$\hat{\underline{E}}_O^T = \left[ \hat{E}_a \hat{E}_b \hat{E}_c \hat{E}_d \hat{E}_e \hat{E}_f \right]$$

For example, the estimated error in the measurement of the A-axis instrument is:

$$E_a = \left[ m_a - \sqrt{0.2} (m_b - m_c - m_d + m_e + m_f) \right] \quad (1.5)$$

The corresponding measurement error variance ( $TSE_O$ ) of the six instruments is:

$$TSE_O = \underline{E}_O \cdot \underline{E}_O = E_a^2 + E_b^2 + E_c^2 + E_d^2 + E_e^2 + E_f^2 \quad (1.6)$$

If no instrument errors exist, both equations reduce to zero. If an instrument failure occurs, the error propagates through both equations 1.5 and 1.6, but is dominant in the faulty instrument's error estimate. However, the error is also reflected at reduced magnitude in each of the other instrument-error estimates. If one knew which instrument were at fault and adapted the processing structure, a corresponding five-instrument variance ( $TSE_j$ ) could be generated with the faulty instrument omitted and it would also reduce to zero. In general, it can be shown that the relationship between  $TSE_j$ , the faulty instrument error  $E_j$ , and the  $TSE_0$  is:

$$TSE_j = TSE_0 - 2 (\hat{E}_j)^2 \quad (1.7)$$

Thus (from Eq. 1.7), if a failure exists, the estimate of the failed instrument's error is equal to 50% of the total six-instrument variance ( $TSE_0$ ).

Detection of a second failure (k) is achieved in a similar manner. Its error estimate,  $E_{jk}$ , may be derived on the basis of a corrected processing, i.e., instrument (j) previously failed is not used, and the general derivation form corresponds to:

$$TSE_{jk} = TSE_j - 2.5 (\hat{E}_{jk})^2 \quad (1.8)$$

where  $TSE_{JK}$  corresponds to the four-instrument variance that would be computed if the initial faulty instrument (j) and the new but unknown failed instrument (k) were omitted in the processing.

The failure isolation algorithm implements these concepts in the following manner. First, all six individual errors are computed using Eq. 1.6 to calculate  $TSE_0$ . The total squared error is compared to an allowable limit. If the system is operating within the acceptable bounds of the  $TSE_0$  criteria, no further activity would be required until the next failure isolation iteration. If the  $TSE_0$  criterion is violated, the ratio of each individual instrument squared error is taken with respect to the  $TSE_0$ . If, for example,  $E_a^2$  is a significant percentage of  $TSE_0$ , failure of instrument A is indicated. Practically, the 50% criterion previously noted would represent an upper limit. Both strapdown system data quantization and the relative quality of the instruments represent additional computational error noise that influences all the  $E_j$  terms and the  $TSE_0$ . Thus, if the 50% criterion is used, a failure could go undetected. Similarly, the use of a very low percentage would result in false alarms. During the test and evaluation effort, a ratio of 0.44 has been used and has resulted in sensitive reliable failure isolation performance. The second failure-isolation technique is similar in that another failure is indicated if the  $TSE_j$  criterion is

exceeded. This failure is isolated by taking the ratio of  $E_{jk}^2$  to  $TSE_J$  and in this case, Eq. 1.8 shows that the theoretical limit is 40%.

The failure isolation algorithm operates on measurement data that are iteratively accumulated. The accumulator period is selected to be consistent with the acceptable error resolutions and to minimize the noise effects resulting from the use of quantized data.

Finally, after isolation of two failures, detection of a third is achieved by monitoring the single remaining parity equation (Table 1.1) that corresponds to the operational state of the system.

The FDI capability repeatability achieved in test using these basic techniques corresponds to a performance FDI threshold resolution of  $0.375^{\circ}/\text{hr}$  gyro drift (or equivalent error sources) using a 6 minute accumulator time and a  $0.1 \text{ cm}/\text{sec}^2$  accelerometer bias change (or equivalent error sources) using a 4 min. accumulator. Higher fault levels are detected much more rapidly. Dependent upon the environment of the test conditions, finer resolution has been achieved. The statistical FDI techniques developed in the SIRU Utilization program and described in this report were specifically designed to enable FDI resolution at thresholds that are comparable to the basic noise and performance statistics of the system's nominal measurement capability (i.e. approximately 1.5 times the one sigma performance status in a static environment; for example, detection of a gyro mean drift shift of  $0.068^{\circ}/\text{hr}$  has been demonstrated).

These FDI techniques, as well as the basic system processing to correct the instrument calibration parameters and to effect the strapdown algorithms, are implemented in a general-purpose DDP-516 computer. It is a 16-bit machine with a memory cycle time of 0.96 microsecond, high-speed arithmetic package, and 16,384 words of core memory. Peripherals include: two disc drives, an ASR-35 teletype unit, a Sanders #720 character CRT display, and a high-speed paper tape reader. The DDP-516 interface allows on-line processing of timing signals and the test table encoder angle, as well as the SIRU instrument module output data and thereby enables real-time system testing and evaluation.

The overall basic SIRU software mechanization is shown in Fig. 1.3. In this mechanization, the torque-to-balance instrument loop delivers incremental information at a 4800-pps rate. The basic matrix processors and the attitude and velocity algorithms have been operated at 100 and also at 50 iterations per second. The velocity and attitude processing is done sequentially in each iteration interval

and uses velocity and attitude data accumulations that are staggered by 1/2 the iteration period. This permits the incremental acceleration accumulation to be processed into the inertial frame using the average attitude over the accumulation interval.

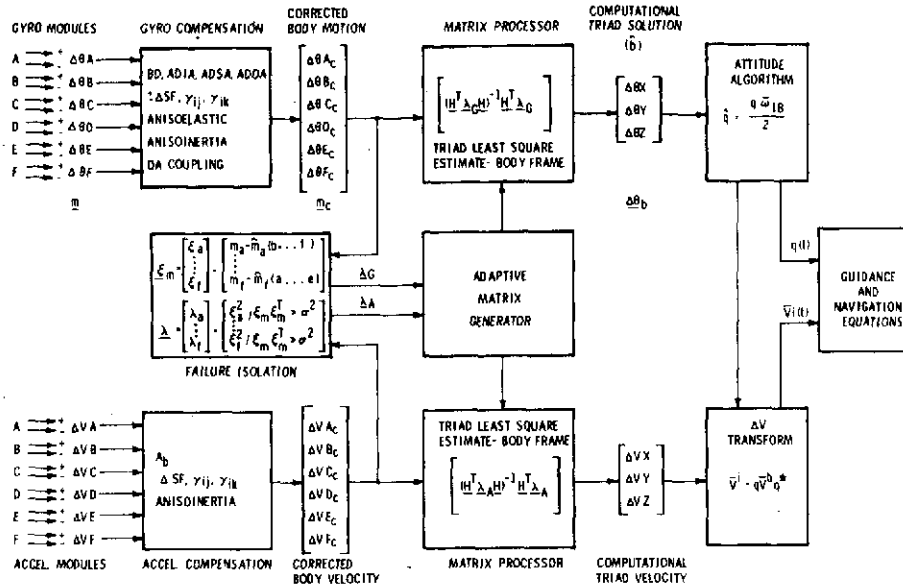


Fig. 1.3 SIRU Data Processing

The raw gyro and accelerometer data accumulation is compensated to account for the instrument errors. The compensating software routines generate corrections by modeling the error sources and estimating the static and dynamic environment inputs to each instrument. The coefficients of the error model are determined from a series of static and dynamic calibration tests. The error terms that are modeled, the modeling techniques, and the calibration methods are described in R-746. Compensation terms include correction for: bias drift, acceleration sensitive drift, positive and negative scale factors, misalignment, output axis coupling and accelerometer bias, scale factor, misalignment, etc.

The corrected body data is then processed by the appropriate least square matrix, and the failure isolation equations. The output of the least square processing is the reference triad body solution equation, Eq. 1.2. The FDI operates prior to every iteration cycle using all the measurement data in the accumulators. In the basic development program it effected the TSE algorithms (Eqs. 1.5 through 1.8) and the parity equations, Table 1.1. In the period of performance covered by the

SIRU Utilization program it was extended to include the statistical FDI techniques operating from the parity equation residuals as described later in this report. Provisions for on-line recalibration of stable performance changes that exceeded the failure detection thresholds were incorporated in this software.

If a failure is detected and isolated, the failure state is entered to adapt the processing structure to accommodate for the fault status  $\lambda$ .

The output of the matrix processors is used by the attitude and velocity algorithms. The attitude algorithm is a third-order quaternion of rotation (see Appendix A1). A third-order Taylor series expansion is used to achieve high performance at low iteration rates. The  $\Delta V$  transformation derived from the quaternion attitude output is processed into a conventional three-by-three direction cosine transformation. A significant advantage in using a quaternion for this transformation is that perfect  $\Delta V$  orthogonalization is assured by simply normalizing the quaternion single-length constraint.

### 1.1 SIRU Utilization Scope

Specific areas covered in the further development of SIRU under the designation "SIRU Utilization program" are as follows:

1. Implementation of statistical failure detection, isolation, classification and recompensation (FDICR) algorithms.
2. Implementation and evaluation of a single position self-calibration method for the gyros.
3. Development and implementation of a sequence of coarse and fine self-alignment programs.
4. Development of a land navigation program to permit a normalized investigation of error propagation due to dynamic inputs, to delays in detecting and isolating a failure, and to the geometric changes associated with different failure combinations.
5. Investigation of error propagation resulting from area 4 above.

The following chapters cover the specific areas mentioned above. In addition, Chapter 8 presents SIRU reliability calculations from the most recent reliability data (through December 28, 1972) and a study of statistical and deterministic failure

detection and isolation reliability. Chapter 9 presents a discussion of SIRU Utilization results that are applicable to other systems. An index of chapter headings is shown below.

- Chapter 2 - Failure Detection, Isolation, Classification and Compensation (FDICR)
- Chapter 3 - Single Position Self-Calibration
- Chapter 4 - Attitude Algorithm Small Angle Error Equations
- Chapter 5 - SIRU Self-Alignment
- Chapter 6 - Local Level Navigator and Error Propagation
- Chapter 7 - End to End Navigation Demonstrations
- Chapter 8 - SIRU Reliability Appraisal
- Chapter 9 - SIRU Utilization Applications
- Chapter 10 - Conclusions and Recommendations

A brief description of the contents of Chapters 2-7 is provided in the following sections. Complete software and computational requirements are documented in Volume II, Software, of this report. Operating records and SIRU system experience, including a listing of hardware failures, are provided in Volume III, System Log, of this report. Appendix A1 to this chapter presents the quaternion notation and a discussion of the reasons for the use of quaternions in the SIRU system. The results shown hold for any quaternion or direction cosine algorithms independent of the algorithm order.

## 1.2 FDICR

A statistical on-line technique was developed to provide SIRU with a capability to utilize an additional potential in reliability and performance. The technique is structured as a multistage process of detection of a failure, classification of the failure (constant bias jump, ramp, variance increase or normal) and recompensation of the failed instrument if the degradation mode is either a constant bias jump or a ramp.

The suboptimal detection system operates to identify the SIRU parity equation residuals that have exceeded a pre-determined value and immediately isolates the instrument responsible. The detection threshold is specified on the basis of the acceptable performance degradation mean and noise and the desired FDI reliability (missed alarm and false alarm probabilities). The detection system is based on a modification of Wald's sequential analysis and its performance is remarkably close to an optimal non-linear detection system. An invariant transformation is utilized

such that classification can be reduced to a set of disjoint simple hypotheses tests using Wald's analysis. Recompensation values are determined by simple averaging since the parity equation residual noise is dominated by quantization noise that has the characteristics of white noise.

The above described statistical detection is applied only to the gyros because the TSE detection system (see R-746) can adequately detect and isolate those accelerometer degradations that cause appreciable navigation errors. The TSE method is also used with the gyros to detect and isolate "hard" failures whose magnitudes exceed  $0.75^{\circ}/\text{hr}$  (The statistical FDICR isolates errors below this value down to approximately the standard deviation of the parity equation residual noise ).

### 1.3 Single Position Self-Calibration

A single position self-calibration method was developed in which the plane containing the SIRU Z and Y body axes is kept approximately level (to within  $10^{\circ}$ ) so that only the stable Null Bias Drift (NBD) term contributes significantly to the total lumped drifts of the two reference gyros (whose output axes (OA) are approximately vertical). The lumped drifts of the other four gyros are obtained by solving three independent parity equations and an equation involving vertical axis drift and assuming zero drift changes for the two reference gyros.

The single position self-calibration method used for the gyros is not applicable to the accelerometers because there are no preferred accelerometer orientations where bias shifts will statistically be at a minimum. Instead, the single position calibration of accelerometers is performed by detection of shifts and recompensation of the accelerometers using only the parity equations. This approach recognizes that significant bias shifts occurring in more than two accelerometers simultaneously would not be properly compensated. However, it has been shown (Reference 2) that the probability of more than two shifts occurring simultaneously is extremely small (on the order of  $10^{-5}$ ).

### 1.4 Attitude Algorithm Small Angle Error Equations

In Chapter 4 it is demonstrated that small angle error equations from the quaternion differential equation are the same as those for the direction cosine differential equation or for gimballed IMU errors.

This small angle error equation is fundamental in the design and analysis of alignment and navigation algorithms and for earth rate compensation.

### 1.5 SIRU Self-Alignment

Both coarse and fine alignment algorithms were developed. The coarse alignment algorithm is valid for very large initial offset angles (from the desired local level navigation frame) for which the small angle error equation is not valid. Hence, use of coarse alignment eliminates any concern over stability or very high gains (needed to slew from the large offset position) where noise becomes a significant factor.

The use of the attitude quaternion as an analytic platform (used for the fine alignment algorithm) is investigated compared to other methods such as Kalman filtering.

The fine alignment loop (operating with an initial offset angle on the order of 1 degree) was developed to deal with the problem of a noisy environment. The design is simple and easy to implement and can be easily modified (by simple gain changes) to take into account a wide range of noisy environments.

### 1.6 Local Level Navigator and Error Propagation

A local level navigation algorithm was designed with necessary altitude damping and Coriolis compensation. This navigator design was chosen over an inertially stabilized navigator algorithm because it is easier to integrate with external navigation aids whose outputs are in local navigational frame coordinates (i.e., latitude and longitude). Also the local level navigator can be evaluated using latitude and longitude as a measure of the error without need for further transformations that would be needed for the inertially stabilized navigator.

The navigator was used to study error propagation arising from the dynamic environment and the delay in detecting and isolating an instrument failure.

It is shown that the dominant dynamic error (if not compensated) is pseudo-coning drift due to gyro OA coupling. It is also demonstrated (by measuring attitude and navigation errors) that this pseudo-coning drift is virtually eliminated when OA coupling compensation is used. Another important result is implied by the successful use of OA coupling compensation in SIRU; that is, the compensation is stable regardless of the number of gyros and the magnitude of the compensation used.

Investigation of errors due to delay in detecting and isolating a failure demonstrates that these errors are indeed small and are due to the attitude error introduced by the failure.

### 1.7 End-to-End Navigation Demonstrations

The complete software package (Single Position Calibration, FDICR, Alignment, and Navigation) was tested as a whole. It is shown that FDICR correctly detected, isolated, identified, and recompensated every instrument degradation introduced. The effect caused by delay in detecting and isolating the error is shown in appropriate graphs along with the effects of a dynamic environment on error propagation. It is also noted that single position calibration, alignment, and navigation worked well under the various environments.

### 1.8 Software Memory and Timing Requirements

Software memory and timing requirements for the FDICR, single position calibration, self-alignment and navigation programs are presented at the end of the pertinent chapters.

## Appendix A1

### Quaternions

#### A1.0 Introduction

Quaternions, used to represent attitude in SIRU, are a convenient four parameter representation of rotations. The quaternion has a single length constraint to normalize rather than the complete reorthonormalization required of the direction cosine matrix. (Note that normalizing a quaternion takes only 4 multiplications and 2 additions whereas matrix reorthonormalization takes 54 multiplications and 42 additions.) Also, multiplication of two quaternions requires only 16 multiplications and 9 additions, whereas multiplication of two direction cosine matrices requires 27 multiplications and 18 additions. However, to actually rotate a vector requires 22 multiplications and 11 additions using quaternions but only 9 multiplications and 6 additions using matrices. If the same rotation is to be applied to more than one vector (which is the case for alignment, calibration and local level navigation), time is saved by first computing the matrix from the quaternion, which takes 13 multiplications and 12 additions. Below is a new presentation of this transformation (from quaternion to matrix) in a compact notation. Equations for the inverse transformation (from matrix to quaternion) are also presented.

#### A1.1 Notation

The following notation is useful in writing the quaternion formulas compactly.

Summation is implied for any pair of repeated subscripts. For example:

$$A_{ik} B_{kj} = \sum_{k=1}^3 A_{ik} B_{kj} \quad \text{A1.0}$$

The Kronecker delta symbol is given by:

$$\delta_{ij} = \begin{cases} 1, & i=j \\ 0, & i \neq j \end{cases} \quad \text{A1.1}$$

The epsilon symbol is defined as:

$$\epsilon_{i,j,k} = \begin{cases} 0 & \text{if any 2 indices are equal} \\ +1 & \text{if } i, j, k \text{ is an even permutation of } 1, 2, 3 \\ -1 & \text{if } i, j, k \text{ is an odd permutation of } 1, 2, 3 \end{cases}$$

The epsilon symbol can be used to express vector cross products as follows:

$$(\underline{a} \times \underline{b})_i = \epsilon_{ijk} a_j b_k \quad (\text{A1.2})$$

where:

$$\underline{a} = \begin{bmatrix} a_1 \\ a_2 \\ a_3 \end{bmatrix} \quad (\text{A1.3})$$

The anti-symmetric matrix corresponding to this vector is given by:

$$\underline{A} = \begin{bmatrix} 0 & a_3 & -a_2 \\ -a_3 & 0 & a_1 \\ a_2 & -a_1 & 0 \end{bmatrix} \quad (\text{A1.4})$$

or, more compactly:

$$\begin{aligned} A_{ij} &= \epsilon_{ijk} a_k \\ a_i &= \frac{1}{2} \epsilon_{ijk} A_{jk} \end{aligned} \quad (\text{A1.5})$$

### A1.2 Relation Between the Quaternion and the Corresponding Direction Cosine Matrix

The quaternion is defined as follows:

$$q = \cos \frac{\theta}{2} + \underline{n} \sin \frac{\theta}{2}$$

where:

$$q = q_0 + \begin{bmatrix} q_1 \\ q_2 \\ q_3 \end{bmatrix} \quad (\text{A1.6})$$

where  $\theta$  is the rotation angle about an axis represented by the unit vector  $\underline{n}$ .

By comparing the elements of a vector rotated by using a quaternion to the corresponding elements of the same vector rotated by using a direction cosine matrix, the following relationship is found for transforming the quaternion to the equivalent direction cosine matrix.

$$C_{ij} = (q_0^2 - q_k q_k) \delta_{ij} + 2q_i q_j + 2\epsilon_{ijk} q_0 q_k \quad (\text{A1.7})$$

Here,  $C_{ij}$  is a direction cosine element.

Using Eq. A1.7, it can be shown that the quaternion elements are given by Eq. A1.8 when the angle of rotation  $\theta$  is not near  $\pi$ .

$$\begin{aligned}q_0 &= \cos \frac{\theta}{2} = \frac{\sqrt{1 + \text{tr}C}}{2} \\q_k &= \frac{\epsilon_{ijk} (C_{ij} - C_{ji})}{8q_0} \\ \text{tr}C &\triangleq C_{ii}\end{aligned}\tag{A1.8}$$

For  $\theta$  near  $\pi$ ,  $q_0$  and  $q_i$  can be obtained using a more complex procedure.

Chapter 2  
Failure Detection, Isolation, Classification  
and Recompensation (FDICR)

2.0 Introduction

The Fig. 2.0 block diagram is an overall view of the FDICR system as developed for SIRU Utilization.<sup>2</sup> It is assumed that the reader is already familiar with the SIRU parity equations (See Appendix A2) and the deterministic total squared error (TSE) method of failure detection (See SIRU Development Report R-746)<sup>1</sup>.

Note that in the FDICR system only TSE failure detection is used for the accelerometers. TSE failure detection is adequate for this purpose since a reliable detection TSE level of  $0.1 \text{ cm/sec}^2$  of accelerometer bias can be readily achieved. Such a bias causes no more than 0.7 nautical mile error in 10 hours (deduced from SIRU land navigation tests at a fixed laboratory position).

This decision not to use statistical FDICR for the accelerometers is specific for the SIRU System hardware. As noted before, there is relatively high resolution available from the TSE as it relates to the navigation test demonstrations in this program. It is reasonable to expect that for some other instrument population or for some specific test demonstration, statistical failure detection for accelerometers would be of value. The use of statistical FDICR for accelerometers would not be required for applications, such as the space shuttle and normal airborne navigation, that use instruments whose performance is equivalent to the SIRU accelerometers.

The TSE gyro failure detection level is presently set at about a  $.75^\circ/\text{hr}$  level in order to avoid false recertification after a failure has been detected. A  $.75^\circ/\text{hr}$  shift would yield large navigation errors. Therefore, as shown in Fig. 2.0, a statistical FDICR is run in parallel with the deterministic FDI method. The deterministic TSE algorithm samples the parity equation residuals at a frequency of 50 hz and has a minimum detection threshold of  $132 \overline{\text{sec}}$  for the residual. Full details on the derivation of the TSE criteria and how it relates to drift rate resolution and attitude errors is described in Chapter 2 of the SIRU Development report R-746. It should be noted that, in general, the system attitude error for the first failure corresponds to approximately 0.425 of the instrument single error at detection and isolation. This effect is due to the least squares processing which effectively minimizes the total error propagation. The statistical FDICR monitors the parity equation residuals every 2 minutes and allows an average error no greater than  $80 \overline{\text{sec}}$ . In this case, also, the system attitude error for a first failure is 0.425 of the gyro error. Use of the statistical FDICR thus leads to at least a 40% reduction in attitude

error as well as providing the means for classification of the type of gyro failure (constant bias jump, ramp bias, variance increase), estimation of the constant and ramp bias shift magnitudes and recompensation of the gyros if these shifts are stable. The gyro deterministic failure detection system (TSE), run at the 50 Hz rate, detects large performance failures ( $.75^{\circ}/\text{hr}$  or higher) before they are detected by the statistical algorithm which samples the parity equation residuals at a much slower frequency. The failure status philosophy used in the event that the statistical and TSE failure decisions disagree (i.e., the statistical detector has detected a soft failure below the threshold of the TSE detector or the hard failure has not yet been detected by the statistical detector due to its low sampling frequency) is as follows:

- a) TSE failure status dominates
- b) No TSE failure, use statistical
- c) If 2 TSE failures, ignore statistical
- d) If 1 TSE and 1 statistical, not the same unit, take in that order
- e) If 1 TSE and 1 statistical, same unit, take statistical
- f) If 1 TSE and 2 statistical, one common, take common as 1st failure, other statistical as second failure
- g) If 1 TSE and 2 statistical, all different, take TSE as 1st failure and 1st statistical as 2nd failure

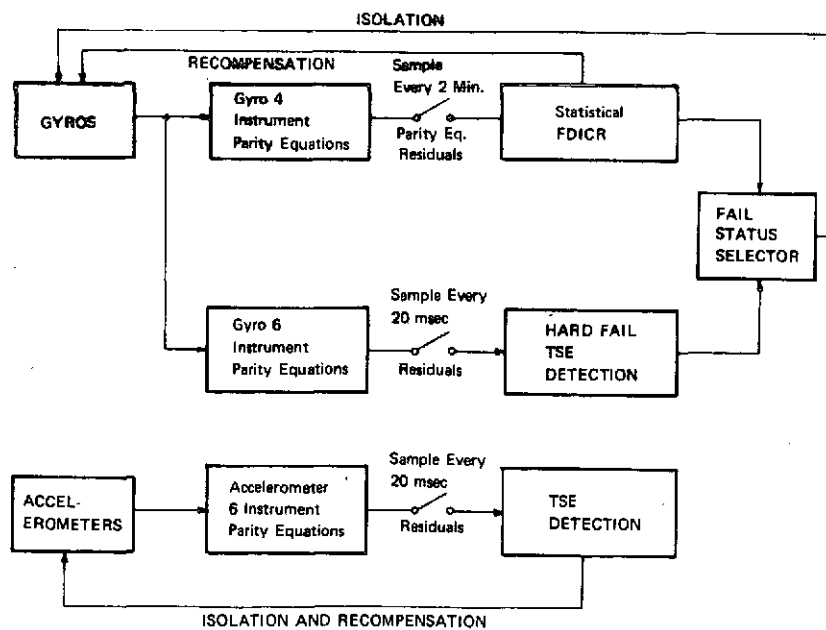


Fig. 2.0 Overall View of SIRU Utilization FDICR

It is the purpose of the failure status selector box in Fig. 2.0 to implement the above philosophy.

During the writing of this report, development of a method for isolating a third worst failure was initiated. This scheme works as follows in the TSE algorithm. Assume there are two failures. The TSE equation sets for isolating the first failure and second failure respectively are examined. If a third failure occurs, the parity equation set detects its presence. The existing 2nd failure is remembered and is used in the second failure search (TSE equations), but is not used in the matrix processor equations (i.e., least squares solution). The second failure FDI cycle is now operating using five instrument measurement axis outputs. One of these measurements is the unknown 3rd failure and the known 2nd failure. If the 3rd failure is now of a larger magnitude (about 10 times) than that of the existing 2nd failure the FDI algorithm isolates it and all three failures are isolated (the original 2nd failure was memorized). The matrix processing equations (reference 1, Appendix A) are then changed to discontinue use of the 3rd failure axis as well as the two prior failures. This procedure can also be extended to the statistical FDICR algorithm.

The SIRU system may also be computationally implemented so that the propagation of attitude or velocity errors resulting from instrument failures can be prevented if three redundant computers are used to process the data as well as to implement FDICR. Computer #1 would compute attitude and velocity using, for example, instruments A, B, C, and D. Computer #2 would utilize instruments C, D, E, and F and computer #3 would utilize instruments E, F, A, and B. If any one instrument fails, one of the three computers would provide an errorless attitude and velocity computed from a set of non-failed instruments. For example, if instrument F had failed, the attitude given by computer #1 would be used to yield errorless results.

Each computer would also process complete FDICR using all six instruments.

A similar scheme for the second failure could also be implemented with the computer utilizing different sets of instruments for triad processing but all instruments for FDICR.

## 2.1 Statistical FDICR

In long-term operations the uncompensated gyro drift rate is considered to be the most important source of system performance error. The mathematical modeling of gyro drift rate on the basis of the technique for stationary and nonstationary time series analysis has been applied to actual gyro data. Gyro noise in SIRU is found to be due to quantization and closely resembles Gauss-Markov

white noise. The gyro is defined to be operating in the normal mode if the values of the parameters associated with driving noise of the model are of zero mean and normal variance. The degradation modes are characterized by either the presence of a systematic mean value or an increase in the variance of the driving noise of the model. However, the dominant modes resulting in navigation performance degradation are shown to be a constant bias jump and a ramp bias of the gyro drift rate. In this section the discussion will be at first restricted to the case of degradation modes characterized by the presence of a mean drift rate but with normal variance. A discussion of the extension of the technique to cover treatment of the degradation mode arising from an increase in variance will be presented later.

The mathematical model of the gyro drift rate process will now be defined. With the gyros operated in a pulse torque-to-balance mode, the signal outputs correspond to an accumulated angle counted over some interval. Since the gyro error is modeled on drift rate rather than angle, the state variable is derived by averaging measurements over a sampling period. The sampling period of 2 minutes is chosen to provide a reasonable measurement rate noise due to quantization. The state equations of the stochastic drift rate processes in continuous time are presented as follows:

Gyro in normal operating mode (denoted as  $H_0$ ): The state equation is defined as:

$$\dot{D}_G(t) = 0 \quad (2.0)$$

where  $D_G(t)$  is the gyro state variable.

The measurement equation is represented by:

$$D(t) = D_G + v_G(t) \quad (2.1)$$

where notations are defined as:

$v_G(t)$  = white quantization noise with given statistics

$$E [v_G(t)] = 0, \quad E [v_G(t) v_G(\tau)] = v_G \cdot \delta(t-\tau) \quad (2.2)$$

Gyro in degradation mode in the form of a constant mean bias jump (denoted as  $H_1$ ): The state equation remains unchanged, while the measurement equation is represented by,

$$D(t) = D_G + m + v_G(t) \quad (2.3)$$

where  $m$  is the constant bias.

The degradation state may be caused by a jump of: bias drift rate, acceleration sensitive drift rate in thrusting phase, scale factor (SF) or alignment change in the presence of vehicle rate, etc.

Gyro in degradation mode in the form of a ramp rate (denoted as  $H_2$ ): The measurement equation can be represented as:

$$D(t) = D_G + nt + v_G(t) \quad (2.4)$$

where  $n$  is the constant ramp rate. The degradation state,  $n$ , for the ramp case may be caused by a ramp bias mean drift rate or a ramp change of SF in the case of continuous maneuver with a constant vehicle rate, etc.

In addition, a degradation mode corresponding to operation with an unacceptable noise level variance increase (denoted as  $H_3$ ) is also of concern.

The corresponding state equation of the drift rate in the discrete time case can be similarly defined. To define the degradation modes of the mean drift rate in these two simple forms permits the solution to be analytically tractable and the degradation to be practically compensatable yet preserves the dominant nature of the real degradation characteristic.

In order to isolate the gyro errors from the desired vehicle rate information, a set of parity equations is implemented using the direct comparison of instrument outputs. Each parity equation is generated by a linear combination of gyro outputs such that the vehicle rate, if it is present, will be canceled out. In general, there are 15 combinations of parity equations that can be generated, but a set of 6 parity equations is sufficient for unique isolation of a single failed instrument. A discussion of the case of two failed instruments will also be presented. The set of parity equations to be actually implemented is shown in Table 2.0.

Table 2.0 Parity Equation Set (for Mechanized System)

No.	Instrument	Equation
1	ABCD	$(m_a - m_b) c + (m_c + m_d) s = y_1$
2	ABCF	$(m_a + m_c) c + (m_b + m_f) s = y_2$
3	ABEF	$(m_e + m_f) c - (m_a + m_b) s = y_3$
4	ADEF	$(m_a - m_e) c + (m_d - m_f) s = y_4$
5	BCDE	$(m_c + m_e) c - (m_b + m_d) s = y_5$
6	CDEF	$(m_c - m_d) c + (m_e - m_f) s = y_6$

$$c = \cos \phi = 0.851, \quad s = \sin \phi = 0.526, \quad \phi = 31^{\circ} 43' 2.9''$$

$m_a$  = measurement of A-axis gyro

$y_j$  = residual gyro error

The residuals,  $y_j$  ( $j=1,..6$ ), which reflect the gyro errors, are the inputs to be processed by the adaptive system. It is easily shown that each residual can be modeled by a scalar equation. For example, the first parity equation,  $y_1$ , with gyro A degraded and a mean of  $m_G$  in form of mode  $H_1$  can be represented as:

$$\dot{x}(t) = 0 \quad (2.5)$$

$$y_1(t) = x(t) + m + v(t) \quad (2.6)$$

where the aggregated scalar state  $x$  is defined as:

$$x(t) = \cos \phi D_{GA} - \cos \phi D_{GB} + \sin \phi D_{GC} + \sin \phi D_{GD}$$

$$\text{and} \quad m = m_G \cdot \cos \phi$$

It is noted that the parity equation residuals in Table 2.0 will reflect an instrument signal output attenuated by either a factor  $\sin \phi$  or  $\cos \phi$ .

The statistical system is structured as a multistage stochastic process:

1. A detection system is designed to detect a degradation of parity equation residuals in a minimum time delay under the constraint of a tolerable false alarm error criterion. The degraded gyro is isolated by monitoring the detected degraded parity equation residuals and making a logical isolation decision by considering which gyros affect these degraded parity equations.
2. The classification system is designed to make one of four decisions with regard to the type of degradation with small error probability: 1) a verification of normal mode,  $H_0$ , due to a possible false detection or a possible requalification of the instrument, 2) a classification of degradation mode,  $H_1$ , a change in the mean, or 3) classification of degradation mode  $H_2$ , a ramping bias mean, or 4) classification of degradation mode,  $H_3$ , variance increase.
3. A compensation system is designed to estimate the unknown parameter associated with the classified degradation mode and to recover the degraded sensor performance by recompensation.

This multistage structure is motivated to solve the dilemma of measurement time versus compensation accuracy in the statistical system design. Because of the availability of redundant sensors, the "degraded" gyro can be detected quickly and switched off for navigation information (the instruments will continue to be used in both statistical and TSE FDI algorithms). More time is required to make a reliable classification and an accurate estimation of the necessary recompensation (when possible). A block diagram of the statistical FDICR system is shown in Fig. 2.1.

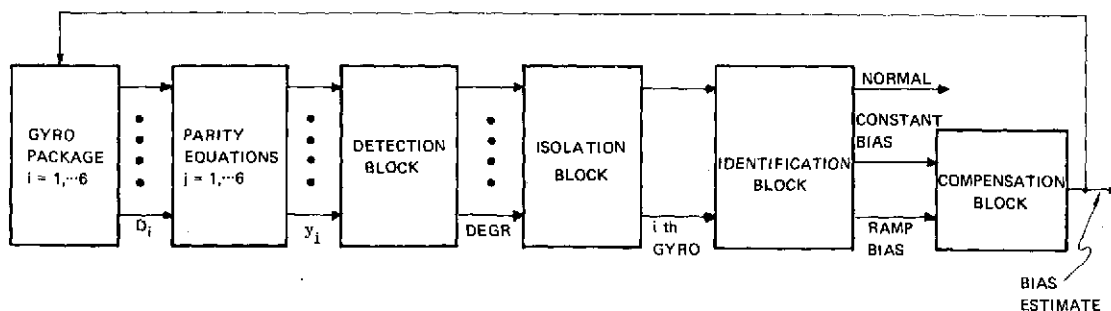


Fig. 2.1 Block Diagram of a Statistical FDICR System

## 2.2 Statistical FDICR Detection System

During a mission, a system may degrade at a random instant,  $\theta$ , to one of the degradation modes. If gyro A degrades, the measurement equation, Eq. 2.6, will then reflect a transition from the normal mode,  $H_0$ , to the mode  $H_1$  (or to the mode  $H_2$  or  $H_3$ ) at an instant  $\theta$  determined by the unobservable (i.e. inaccessible to direct measurements) component process,  $\theta(t)$ . In the formulation it is assumed that the parameter,  $\theta$ , the instant at which the process,  $\theta(t)$ , makes a transition (i.e., the instrument is degraded) is defined by an a priori exponential distribution with a constant failure rate,  $q$ . The solution of the detection problem is approached by deriving an expression for the posterior probability of the degradation state condition on the a priori information and the measurement history.

The posterior probability,  $\pi(t)$ , and the equivalent likelihood ratio function,  $\lambda(t)$ , where:

$$\lambda(t) = \ln \left( \frac{\pi(t)}{1-\pi(t)} \right) \quad (2.7)$$

are given respectively by the following equations, 2.8 and 2.9. These probabilities are for the optimal detection of a degradation (to states  $H_1$ ,  $H_2$  or  $H_3$ ) in minimum time:

$$d\pi(t) = \frac{\pi(t)(1-\pi(t))}{\sigma_p^2} a_1 (d_y(t) - a_1(\pi(t) dt) + q(1-\pi(t))dt \quad (2.8)$$

- $a_1$  = bias degradation used in system design
- $\sigma_p$  = parity equation noise standard deviation
- $q$  = gyro constant failure rate

$$d\lambda(t) = \frac{a_1}{\sigma_p^2} (dy(t) - \frac{1}{2} a_1 dt) + q(e^{-\lambda(t)} + 1) dt \quad (2.9)$$

The optimal detection rule is simple. The solution consists of observing the evolution of the posterior probability (or equivalently the likelihood ratio function) until the first moment when the posterior probability crosses the preset stopping detection boundary. Thus, for mechanization of the optimal detection system only two pieces of information are required. The optimal stopping boundary is determined

by the mission specification and can be precomputed. The mechanization can, therefore, be reduced to the on-line generation of the evolution of the posterior probability. This operation is performed by the first two blocks in the block diagram as shown in Fig. 2.2.

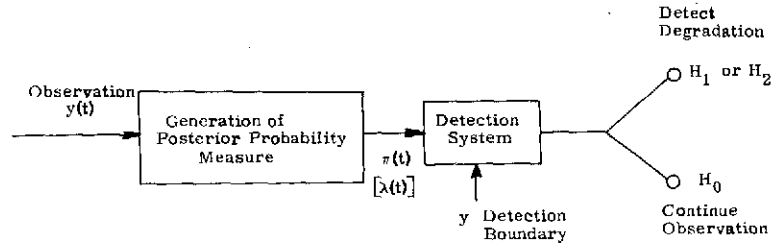


Fig. 2.2 Block Diagram of the Detection System

Notice, however, that both posterior probability equations, 2.8 and 2.9, are non-linear.

A suboptimal detection system can be formulated so that the likelihood ratio function equation is linear. The time to detect a degradation with the suboptimal system is very close to the minimum times obtained with 2.8 or 2.9. This suboptimal system uses a modification of the likelihood function used in the classic Wald sequential probability ratio test (SPRT). Wald's SPRT was originally formulated in the discrete form and consists of choosing one mode,  $H_1$ , or alternate mode,  $H_0$ . The optimal decision rule for Wald's SPRT is defined as follows. Observe the joint likelihood ratio function,  $\lambda_n$ , defined by:

$$\lambda_n = \lambda_{n-1} + \frac{a_1}{\sigma_p^2} \left( y_n - \frac{a_1}{2} \right) \quad (2.10)$$

with respect to an upper boundary, B, and a lower boundary, A, where:

$\sigma_p$  = parity equation noise standard deviation

$\frac{a_1}{2}$  = degradation threshold

$$B = \ln \left( \frac{1-\beta}{\alpha} \right) \quad (2.11)$$

$$A = \ln \left( \frac{\beta}{1-\alpha} \right)$$

(2.12)

$\alpha$  = specified false alarm probability

$\beta$  = specified missed alarm probability

The boundary conditions are therefore a specification of the confidence one wishes to have in the decision. The upper boundary, B, corresponds to a specified confidence (reliability) that a failure ( $H_1$  mode) exists (i.e., the probability that the failure exists and that it is not a false failure). Similarly, the lower boundary, A, corresponds to a confidence specification that the data is normal and is not an undetected (missed) failure. The observation is terminated and mode  $H_1$  accepted if  $\lambda_n$  reaches boundary B. The mode  $H_0$  is accepted if boundary A is reached. Otherwise the observation is continued.

An intuitive explanation of the detection function trajectory generated by Eq. 2.10 is given in Fig. 2.3a. Curve 1 corresponds to a normal data distribution while Curve 2 corresponds to measurement data with a bias jump change. It can be seen that each observation,  $y$ , can be divided into two regions by the value  $1/2 a_1$  (recall that  $a$  was selected as the allowable limit of bias degradation). Data in the right half region represents the case when the instrument is more likely operating in the degradation mode,  $H_1$ , than in the nominal mode,  $H_0$ . Thus, if a jump bias failure has occurred ( $H_1$  mode), each observation will contribute a positive increment of  $\lambda_n$ . However, from the  $p(y|H_1)$  curve we note that the parity equation may yield some data falling into the left half region. The initial trajectory of curve 2, Fig. 2.3b, which depicts an  $H_1$  mode degradation, illustrates this possibility. However, if the instrument is indeed operating in the degraded mode, as more data are accumulated, the function  $\lambda_n$  will eventually cross the boundary B, and the conclusion that an  $H_1$  mode exists is made. Curve 1 illustrates the case where the sequential test confirms that the data corresponds to the normal mode,  $p(y|H_0)$ . There is a balance between the number of samples (observations) required and the risk of making erroneous decisions, i.e., if B and A were set with a smaller separation. If A and B are spaced farther apart (to provide an even higher confidence (reliability) in one's decision), one has to pay the the cost (i.e., observation time) to generate the necessary information. It can be seen from Eq. 2.10 that the trajectory of the  $\lambda(t)$  process will show, on the average, a negative drift rate for the system defined in the normal mode,  $H_0$ , and will show, on the average, a positive drift rate when the system is defined in the degradation mode,  $H_1$ . If a degradation occurs at  $t = \theta$  as shown in Fig. 2.4, the likelihood ratio function  $\lambda(t)$  will require extra time to cancel the negative magnitude of the likelihood ratio function that accumulated before the occurrence of the degradation. Thus, Wald's test suffers an extra detection time delay in comparison with the optimal system.

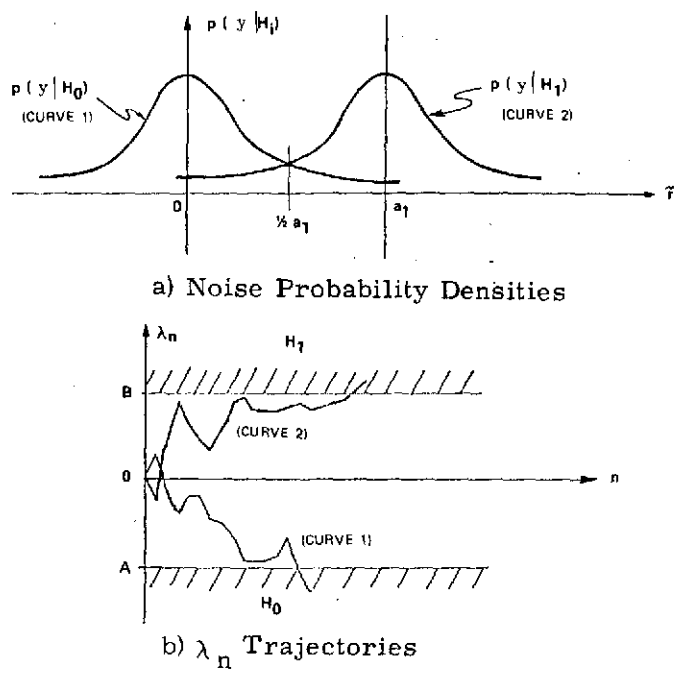


Fig. 2.3 Detection Function of SPRT

The decisions are made on both alternative hypotheses in Wald's system, but in the optimal or suboptimal detection system one is interested in detecting a degradation but not in verifying if the mode, ( $H_0$ ), is present. Therefore, in the implementation used in SIRU, if the normal mode is present and  $\lambda(t)$  begins to drift toward the normal threshold, A,  $\lambda(t)$  is reset to zero. The extra time delay, T, shown in Fig. 2.4 is eliminated.

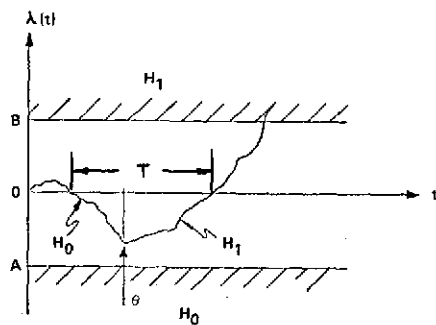


Fig. 2.4 Illustration of Extra Delay for Detection in SPRT.

A block diagram of this suboptimal detection system is illustrated in Fig. 2.5. In this system the likelihood function,  $\lambda_n$ , is generated by the linear equation Eq. 2.10 of Wald's SPRT. At each sample,  $n$ , a control of size,  $\zeta_n$ , is applied. The detection rule consists of observing this modified likelihood function until the moment it crosses the detection boundary,  $B$ . If the function,  $\lambda_n$ , is negative,  $\zeta_n$  is set to  $-\lambda_n$  so, in effect, the likelihood function,  $\lambda_n$ , is set to zero. It will only be non-zero (i.e., not set to zero) if  $\lambda_n$  is drifting toward  $B$ . In this case  $\zeta_n = 0$ . That is the feedback control law defined as:

$$\zeta(\lambda_n) = \begin{cases} -\lambda_n & \lambda_n < 0 \\ 0 & \lambda_n \geq 0 \end{cases} \quad (2.13)$$

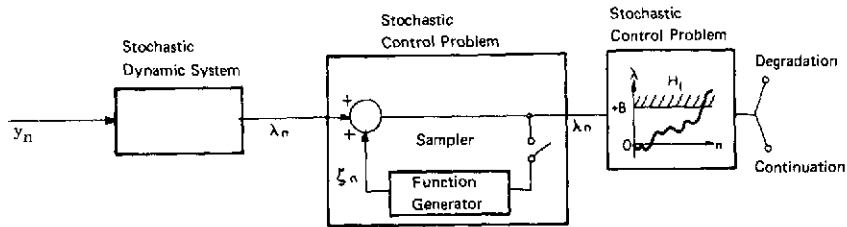


Fig. 2.5 Suboptimal Detection System - Block Diagram

The control,  $\zeta(\lambda_n)$ , corrects the current state,  $\lambda_n$ , to the boundary,  $\lambda = 0$ , whenever the state,  $\lambda_n$ , is negative, and no control is applied if  $\lambda_n > 0$ .

The suboptimal system can be simply modified to detect and classify, for example, the bias degradation which has occurred and also to simultaneously identify its unknown polarity. This modification is necessary for efficient isolation of the degraded instrument and uniquely determines the degradation polarity in the failure classification system. The modified detection rule is a suboptimal detection system defined on both polarities. A simple disjoint decision rule can be defined as follows. Observe the joint likelihood ratio functions:

$$\lambda_n = \lambda_{n-1} + \frac{a_1}{\sigma^2} (\tilde{y}_n - \frac{1}{2}a_1) \quad (2.14)$$

$$M_n = M_{n-1} + \frac{a_1}{\sigma^2} (\tilde{y}_n + \frac{1}{2}a_1) \quad (2.15)$$

where the parameter  $a_1$  is now defined as the absolute magnitude of the "design" value.

If  $\lambda_n$  is used as the decision function,  $a_1$  is specified as an absolute magnitude and the trajectory,  $\lambda_n > 0$ , crosses the upper positive boundary, one detects the degradation mode and identifies the bias to be of positive polarity. As noted previously, the reset control operates so that if  $\lambda_n$  goes negative, confirming normal operation, the function is set to zero, Eq. 2.13.

Similarly, from Eq. 2.15,  $M_n$  is used as the decision function for the detection system and if  $M_n$  crosses a lower negative boundary, the degradation mode is detected and the bias is identified to be of negative polarity. If  $\lambda_n < 0$  or  $M_n > 0$ , reset  $\lambda_n$  or  $M_n$  to zero and continue the observation.

The choice of performance criteria for the detection system will now be discussed. For a sequential system with a one-sided boundary for degradation detection, the meaningful performance criteria are the mean delay time for detection and the false alarm error specification.

The miss alarm error probability is not a criterion in the detection for a one-sided sequential system, for if the instrument is operating in the degradation mode and the mean bias magnitude of the actual outputs is greater than half of the "design" value,  $a_1$ , the miss alarm error probability is zero. A convenient false alarm criterion for the detection system is the mean time between two false alarms. It has been shown that there exists a deterministic relationship between this mean time and the false alarm error probability, and thus the two criteria are mathematically equivalent in the formulation of the detection system.

For a mean time,  $T$ , between two false alarms, the boundary,  $B$ , for indicating a degradation is given implicitly by the following equation:

$$T = \frac{2\sigma^2}{a_1^2} \Delta (e^B - B - 1) \quad (2.16)$$

where  $\Delta$  is the observation sampling period, 2 minutes in the SIRU implementation.

For the case of a large specified mean time, the boundary,  $B$ , is given approximately by:

$$B \approx \ln \left( \frac{a_1^2}{2\sigma^2} \right) \frac{T}{\Delta} \quad (2.17)$$

The mean time delay,  $T_{(t)}$ , in detecting a degradation of magnitude  $a_1$  with parity residual noise standard deviation,  $\sigma_p$ , and a given mean time between two false alarms is as follows:

$$T_{(t)} \approx \left( \frac{2\sigma_p^2}{a_1^2} \right) (\Delta) \left( B - \frac{3}{2} \right) \quad (2.18)$$

$$T_{(t)} \approx \left( \frac{2\sigma_p^2}{a_1^2} \right) (\Delta) \left( \ln \left( \frac{a_1^2}{2\sigma_p^2} \frac{T}{\Delta} \right) - \frac{3}{2} \right)$$

The suboptimal detection system's average time delay in detection, with a given mean time between two false alarms, is remarkably close to that of the nonlinear optimal detection system. This conclusion was confirmed by computer simulation results in report T-560<sup>2</sup>.

The above techniques have been extended to detect the degradation mode in the form of an increase of variance with or without the presence of a mean bias.

In order to classify the degradation mode due to an increase in variance from the presence of a mean bias, some transformation is required to eliminate the effect of the mean bias. This can be done by the following transformation.

$$\tilde{z}_{n-1} = \frac{1}{\sqrt{2}} (\tilde{y}_n - \tilde{y}_{n-1}) \quad (2.19)$$

This transformation will eliminate the effect of a constant bias and will essentially remove the effect of a ramp bias if the ramp rate has a small magnitude. Based on the transformed data,  $z_n$ , the detection of an increase in variance can be treated by Wald's SPRT to test the mode,  $H_0$ , of the normal variance against the mode,  $H_3$ , of a specified "degraded" variance. The procedure consists of observing the likelihood function of the joint conditional probability density against two boundaries set by error criteria. If the lower boundary is reached first (indicating that the system is operating with the normal variance), the test procedure starts anew. The detection procedure continues until the likelihood ratio function crosses the upper boundary and the degradation is detected.

The likelihood ratio function,  $\beta$ , used in this variance detection procedure is given by:

$$\beta_n = \beta_{n-1} + z_n^2 - \frac{K \ln K}{K-1} \sigma^2 \quad (2.20)$$

with:

$$K > 1$$

where

$$\begin{aligned}
 K &= \text{variance degradation coefficient} = \sigma_d^2 / \sigma^2 \\
 \sigma_d^2 &= \text{degraded variance} \\
 \sigma^2 &= \text{normal variance}
 \end{aligned}
 \tag{2.21}$$

Figure 2.6 shows the noise distribution with the mean value of  $z$  equal to zero.

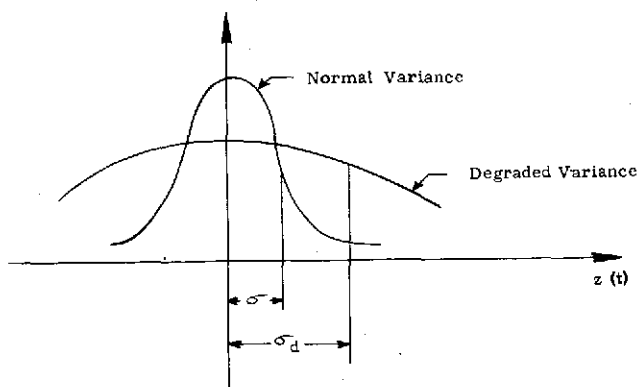


Fig. 2.6 Illustration of Variance Degradation

This variance detection was implemented during the SIRU Utilization program. One of the problems of on-line estimation of the "degraded" noise variance is the large amount of estimation time needed to make an estimate of the variance from the measurement residuals with high confidence. An instrument with performance degraded due to an increase in variance cannot be requalified, but the updated variance may provide information for optimal weighting of the measurement data among different instruments in the navigation system.

### 2.3 Isolation of a Degraded Instrument-Statistical FDICR

It was mentioned in Section 2.1 that the parity equation residuals in Table 2.0 reflect an attenuation of instrument signal outputs by a factor  $\sin \phi$  (0.52573) or  $\cos \phi$  (0.85065) where  $\phi$  is the appropriate SIRU geometrical angle.

With the additional information of polarity, a degraded instrument can be reliably isolated by ignoring those parity equation residuals whose magnitudes are attenuated by the factor  $\sin \phi$ . These residuals are located in the "don't care" status in the isolation table illustrated in Fig. 2.7.

		PARITY EQUATIONS					
		$y_1$	$y_2$	$y_3$	$y_4$	$y_5$	$y_6$
GYROS	A	(+1)	-1	X	(+1)	o	o
	B	(-1)	X	X	o	X	o
	C	X	(-1)	o	o	+1	(+1)
	D	X	o	o	X	X	(-1)
	E	o	o	(+1)	+1	(+1)	X
	F	o	X	(+1)	X	o	X

**LEGEND:**

- 1 "degraded" state (signal attenuated by  $\cos \phi$ )
- X "don't care" (signal attenuated by  $\sin \phi$ )
- o "normal" state
- +,- identified polarity information

Fig. 2.7 Isolation Table for Degraded Gyros.

The isolation logic is initialized whenever any one of the residuals,  $y_1$  through  $y_6$  is detected as degraded. In case two residuals are detected at the same sample instant, the residual with the larger magnitude of detection function would be used for isolation. To illustrate the use of the isolation table:-if the residual,  $y_1$ , was degraded, and the residual,  $y_6$ , was normal, the candidate for the degraded gyro is either A or B. If  $y_1$  was identified with a positive polarity, one examines the detection function of  $y_4$  for positive polarity. It can be seen (from the parity equations Table 2.0) that if the instrument A was indeed degraded, the detection function of  $y_4$  for positive polarity must be positive at and after the instant when  $y_1$  was detected. However, if the  $y_4$  detection function was negative at the current sample and hence reset to zero, one can reliably decide that the instrument, B, is degraded. Thus, if the detection function of  $y_4$  has crossed the detection boundary, one isolates the instrument, A. If neither of the above cases is true, one has to wait for another sample. One need not wait long before the residual,  $y_4$ , is detected if the instrument, A, has indeed degraded. Likewise, if the instrument, B, was failed, the residual,  $y_4$ , would be operated in the normal mode and therefore the detection function of  $y_4$  (for positive polarity test) will show a negative value at some time.

At this point the case of double failed instruments will be discussed. Statistically, the probability of two failures in a mission period for systems using long life high reliability components is very small. Furthermore, the probability of two failures in the same FDI cycle in a truly redundantly designed system is even more remote. For the SIRU system with the software self-repairing

(recompensation) capability, the case of double failures implies that a second instrument will fail before the first failed instrument can be recovered. The actual system implementation is based on the assumption that no double failed instruments will appear during the detection stage, but the system is provided with the capability of isolating a second failed instrument if this occurs during the classification and/or recompensation stage of the first failure. Second failure detection is based on a set of five parity equations that does not include the measurement axis corresponding to the first failure. Similarly, an isolation table can be constructed for these five parity equations that would take the form of Fig. 2.7 less one equation residual. To account for all combinations of failures, single and double, all sixty different combinations were considered. The corresponding isolation logic with these different combinations was then verified in simulations using actual instrument normal performance data and simulated failures. In all cases the correct degraded instruments were uniquely and properly isolated.

#### 2.4 Statistical FDICR Classification System

The classification system is characterized by the following features. First, the "degraded" instrument is and remains operating in one of the unknown modes; no transition of modes is assumed to occur. This is a reasonable assumption because the mean lifetime of a gyro is so much longer than the duration of the classification mode. Secondly, no a priori information about the instrument operating condition can be assumed. Having already determined that a degradation exists and that it is not from a noise variance, it is now necessary to classify the degradation either as a bias shift or as a ramping bias. The classification system must test for these possibilities using the two sided decision process. Classification is achieved whenever the process, using the degradation specifications, yields a cumulative indication that the specified boundaries have been exceeded. Third, the reliability of the decision is of main concern in the classification system. The false alarm and miss alarm error probabilities are chosen as the boundary criteria. Since in the classification system the boundaries of alternate modes must be specified, both error probabilities are well-defined in contrast to the detection system used for bias and ramp degradations.

The classification system proceeds as follows. We first verify whether an instrument that has been detected as failed is indeed a failure. This verification is accomplished by operating on the failed instrument parity equation residual with Wald's SPRT. In this case the decision is definitely two sided since we are to determine whether the instrument can be classified as normal or degraded.

Having reconfirmed the presence of a degradation, one next effects a transformation that discriminates between a bias ramp and a bias shift degradation. The following transformation is made on the failed parity equation residual:

$$\tilde{z}_{n-1} = \frac{1}{\sqrt{n(n-1)}} \left( \sum_{i=1}^{n-1} \right) - \frac{(n-1)}{\sqrt{n(n-1)}} y_n \quad (2.22)$$

This transformation will eliminate the effect of a constant bias but will not remove the effect of a ramp rate. The effect of a variance increase is also not removed, but the likelihood function given below is not sensitive to variance increase. Based on the transformed data (Eq. 2.22), the detection of a ramp is treated by Wald's SPRT to test the mode of no ramp rate against the mode of a ramp degradation. The procedure again consists of observing a likelihood function against two boundaries set by error criteria. If the lower boundary is reached, this indicates that a ramp degradation has not occurred; if the upper boundary is reached, a ramp degradation has occurred.

The likelihood ratio function,  $\lambda_n$ , in this ramp detection procedure is given by:

$$\lambda_n = \frac{\delta \sigma_p}{\sigma_p} \frac{1}{2} \left( \sum_{i=1}^n \tilde{z} + n\phi \cdot \frac{\delta \sigma_p}{2} \right) \cdot (-\phi) \quad (2.23)$$

In the above equation,  $\delta$  is a preassigned positive parameter and  $\sigma_p$  is the given standard deviation.  $\phi$  is assigned to be +1 or -1 for positive or negative polarity respectively to enable classification of the ramping polarity.

If both equations (Eqs 2.20 and 2.23) indicate that a ramp or variance degradation is not present, the degradation is classified as a constant bias.

It is also noted that very large ramps may be falsely classified as variance degradations. This is not a drawback since the instrument will not be recompensated. The appearance of such a large ramp bias leads to catastrophic failure and in this case it is an advantage not to attempt recompensation.

## 2.5 Recalibration-FDICR

Figure 2.8 is a block diagram of the recompensation process for a constant bias degradation. Since the parity equation residual consists of the fixed bias

degradation with additive white noise (i.e., quantization noise), the estimation algorithm is given by:

$$\hat{a}_{p_n} = \frac{1}{n} \sum_{i=1}^n \epsilon_i \quad (2.24)$$

where the standard deviation of  $\hat{a}_{p_n}$  is given by:

$$\sigma_{\hat{a}_{p_n}} = \frac{\sigma_p}{\sqrt{n}} \quad (2.25)$$

Here  $\hat{a}_{p_n}$  is the constant bias estimate at the nth iteration and  $\epsilon_i$  is the parity equation residual at the ith iteration.  $\hat{a}_{I_n}$  is the compensation change estimate for the degraded instrument at the nth iteration. Note that in Fig. 2.8,  $\hat{a}_{I_n}$  must be divided by  $\cos \phi$  in order to compensate for the parity equation attenuation of  $\cos \phi$ .

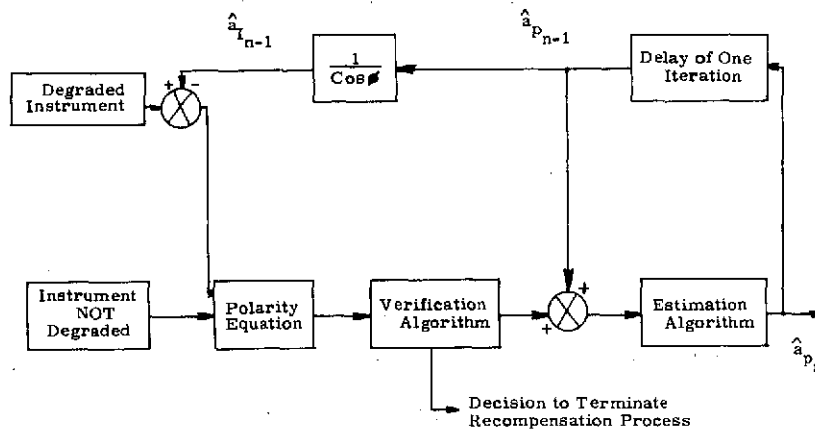


Fig. 2.8 Recompensation Management Procedure-Constant Bias Degradation

This recompensation estimation is logically initiated when the detection and classification system, Fig. 2.9, identifies a bias degradation mode. In the actual software implementation, the estimator is operated for 20 minutes before it feeds back a change to the original compensation calibration correction parameter for the degraded instrument. This period is used to guard against the possibility of an undetected 2nd failure affecting the recompensation value of the first failure. Such a condition would prevail if the 2nd failed gyro were represented in the parity equation used for recompensation of the 1st failed gyro. The delay allows a reasonable time for detection of the 2nd failure, the idea being that any 2nd failure not detected

in these 20 minutes would be small enough not to adversely affect the 1st gyro's recompensation value. Of course, once the 2nd failure is detected, recompensation of the 1st gyro is restarted using a new parity equation. After the delay, the  $\hat{a}_{I_n}$  bias estimate is fed back to the gyro compensation block (Fig. 1.3) and the compensation is then changed by this estimate.

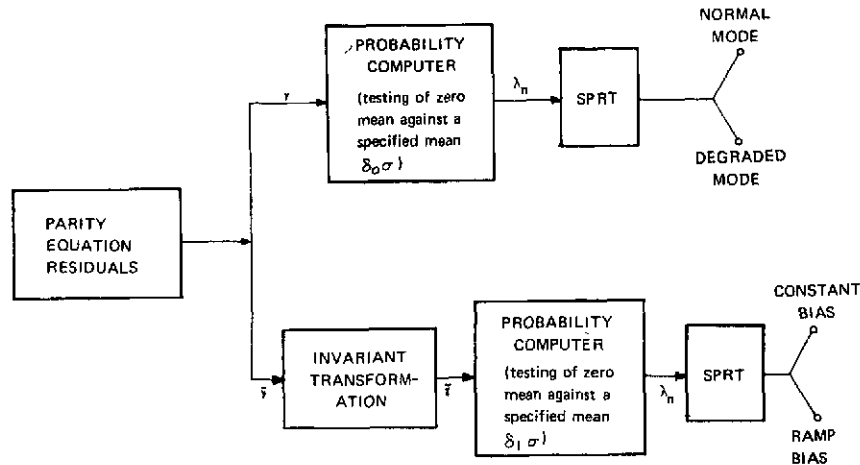


Fig. 2.9 Block Diagram of Identification System

This action effectively changes the total bias compensation used for the degraded instrument. Thereafter, the compensation load is reestimated and updated at each iteration. In the software used, the estimator improves until such time as the verification algorithm (Fig. 2.9) confirms that the parity equation residual is operating in a normal mode. The verification algorithm is initiated when the  $\hat{a}_{I_n}$  estimate is fed back. It is the Wald SPRT operating on the applicable parity equation and using the likelihood ratio test, Eq. 2.10. In this case, however, we do not implement the zero reset function described in Section 2.2. Recall from the prior discussion that if the reset control is omitted and normal mode operation exists (no bias degradation), the SPRT trajectory, Fig. 2.3b, curve 1, will go negative and cross the confirming normal operation boundary condition, A. Thus, when the correct change in compensation has been made, it is confirmed by the verification algorithm and the estimation process is terminated.

The estimated degradation,  $\hat{a}_{p_{n-1}}$ , is fed back positively at the input to the estimation algorithm in order to cancel the influence of the  $a_{I_n}$  calibration that has

been fed back to the gyro compensation block. This positive feedback is necessary in order to allow the estimation algorithm (Eq. 2.24) to use all of the parity equation residual data starting from the first iteration after classification. The result is that the standard deviation of the error in the estimate (Eq. 2.24) decreases with each iteration. The final estimate,  $\hat{a}_{I_n}$ , at termination is, therefore, an average estimate of the degradation over the entire estimating period.

Figure 2.10 is a block diagram of the recompensation process for a ramp bias degradation. The verification algorithm and all of the block diagram to the left of dotted line AB is identical to the corresponding portion of Fig. 2.8. The slope estimation algorithm transforms the parity equation residuals ( $\epsilon_i$ , Fig. 2.11) according to the transformation, (Eq. 2.26), before estimating the slope in order to eliminate the constant (and unknown) residual error in the parity equation output that had been accumulated at detection. Although the classification system has identified the degradation as a ramping bias change, we must use a transformation in the ramp estimation procedure that removes any bias accumulations. This estimated slope,  $\hat{b}_{p_n}$ , is given by (Eq. 2.27).

$$y_{j-1} = \frac{1}{j-\frac{1}{2}} \left[ \sum_{i=1}^{j-1} \epsilon_i - (j-1) \epsilon_j \right], \quad j \geq 2 \quad (2.26)$$

$$\hat{b}_{p_n} = \frac{-4}{(n+1)(n-1)} \left[ \sum_{j=2}^n y_{j-1} \right], \quad n \geq 2 \quad (2.27)$$

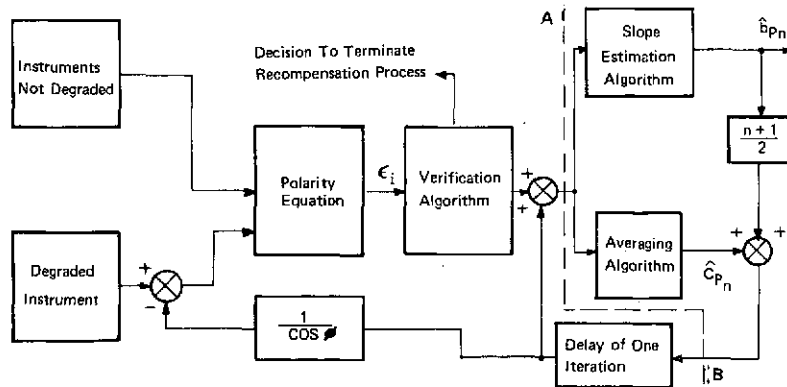


Fig. 2.10 Recompensation Management Procedure-Ramp Bias Degradation

In addition to estimating the slope, recompensation also requires an estimate of the bias at detection. The estimating is done by the averaging algorithm (Fig. 2.10, block diagram). The output of this algorithm,  $\hat{c}_{p_n}$ , is given by:

$$\hat{c}_{p_n} = \frac{1}{n} \sum_{i=1}^n \epsilon_i \quad (2.28)$$

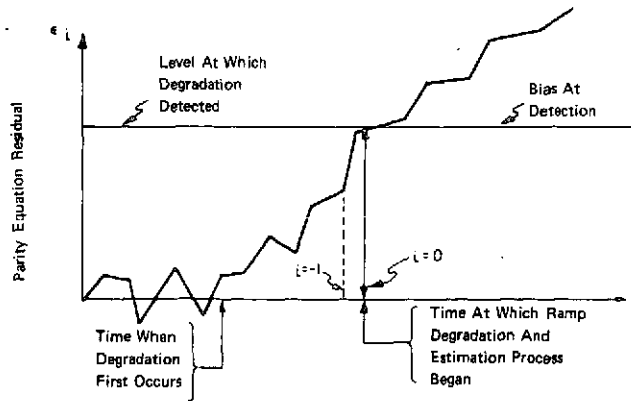


Fig. 2.11 Detection of Ramp Bias Degradation

In order to feed back the proper bias plus ramp at degradation,  $\hat{C}_{P_n}$  and  $\hat{b}_{P_n}$  are combined as shown in the block diagram.

The standard deviations of  $\hat{b}_{P_n}$  and  $\hat{C}_{P_n}$  are given respectively by:

$$\sigma_{\hat{b}_{P_n}} \approx \frac{4\sqrt{n+1}}{(n+1)(n-1)} \sigma_p \quad (2.29)$$

$$\sigma_{\hat{C}_{P_n}} = \frac{\sigma}{\sqrt{n}} \quad (2.30)$$

Here  $\sigma_p$  is the standard deviation of the parity equation noise.

## 2.6 FDICR Test Results

Figure 2.12 is a plot of the statistical FDICR average detection time as a function of gyro constant bias degradation for a static environment (in all of the test runs presented in this section, degradations of instruments were simulated by changing the software constant bias compensation values of the appropriate instrument). This figure was derived from the results of 49 test runs with bias degradations of  $.0675^\circ/\text{hr}$  to  $0.3^\circ/\text{hr}$  inserted in each of the six instrument axes. The system reference body triad was in the X axis vertical orientation for most runs and several tests were conducted with the Z axis vertical. Note that the shape of this curve is that of a hyperbola. This curve type implies that the attitude error buildup before detection is a constant, independent of the degradation, for degradation values ranging from 0 to  $0.3^\circ/\text{hr}$  (for the static calibration position#2, see Fig. 7.1, Chapt. 7). This constant, calculated from the values shown in Fig. 2.12, is about 30 sec where for the first failure maximum attitude error is  $\approx .425$  (instrument error). For all static tests, the parity equation mean residuals were nulled

to within  $0.015^\circ/\text{hr}$  to eliminate the effect of the normal table calibration procedure uncertainties on the test results. Calibration uncertainties, dependent on the long term instrument characteristics and the frequency of calibration, could necessitate the use of a higher degradation level specification for the FDI (Eqs. 2.10 and 2.20).

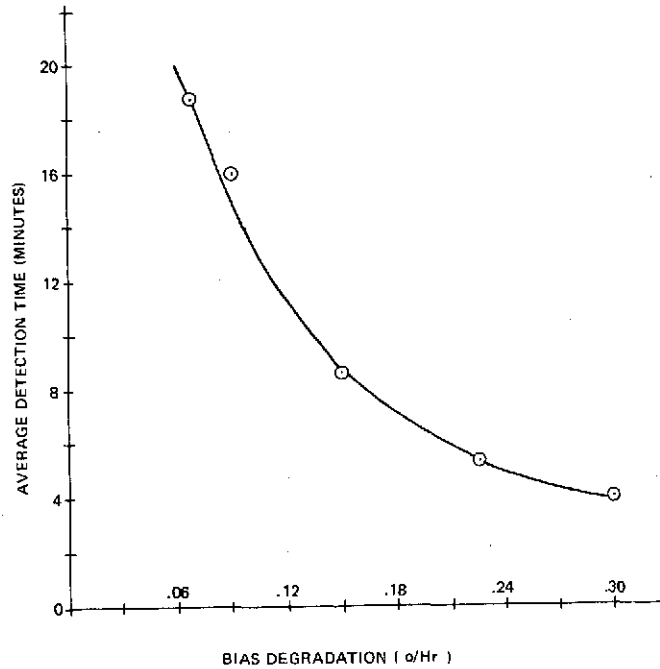


Fig. 2.12 Statistical FDICR Average Detection Time-Static Case-SIRU-Bias Degradation of Gyro

The leftmost point of the curve in Fig. 2.12 can be used to experimentally verify Eq. 2.18, presented earlier. This equation gives average detection time as a function of the FDICR algorithm parameters when the bias degradation detected is about equal to the design degradation value,  $a_1$ . The average detection time at this point is a maximum and decreases for larger bias degradation values. The parameter values are:

$$\begin{aligned} \sigma_p &= .055 \text{ }^\circ/\text{hr} & B &= 6.12 \\ a_1 &= .051 \text{ }^\circ/\text{hr} & \Delta &= 2 \text{ minutes} \end{aligned} \quad (2.31)$$

Substituting Eq. 2.31 into Eq. 2.16 yields a mean time,  $T$ , between two false alarms of:

$$T \approx 34 \text{ hours} \quad (2.32)$$

For such a large value of T, the detection time  $\tau(T)$  can be calculated using the approximate relation given by Eq. 2.18. Thus:

$$\tau(T) = \frac{2\sigma^2}{a_1} (\Delta) (B - 3/2) = 21 \text{ minutes} \quad (2.33)$$

This value of 21 minutes (for a .05°/hr degradation) is quite close to the leftmost point of 20 minutes shown in Fig. 2.12.

Figure 2.13 is a plot of the average classification time observed during the 49 test runs vs. the constant bias degradation magnitude for a static environment. The curve is approximately a horizontal line for a degradation greater than .09°/hr. The results hold true for the false and missed alarm probabilities of 1% used for these tests.

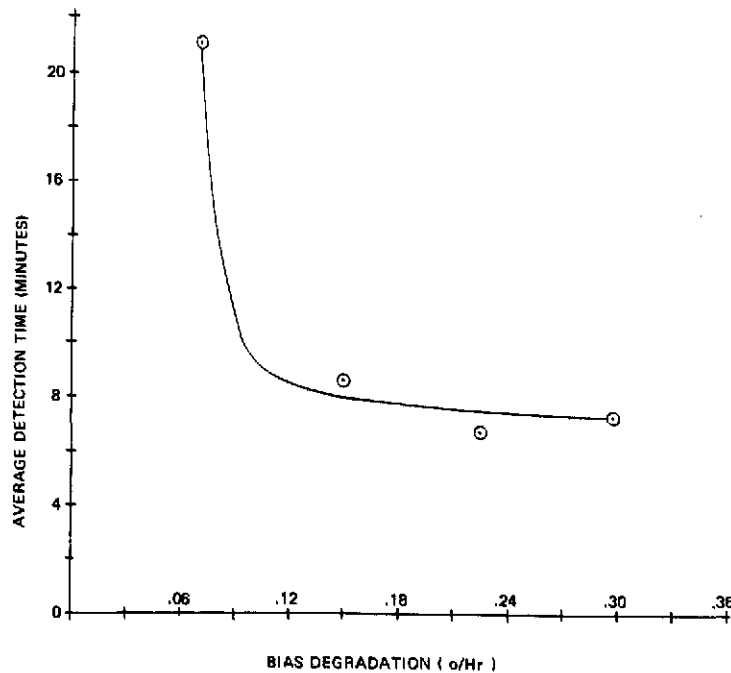


Fig. 2.13 Statistical FDICR Average Classification Time-Static Case-SIRU-Bias Degradation

Figure 2.14 is a tabulated listing of the results of a subset of 18 test runs in which an evaluation of the bias estimation software was effected. The data shows that in a static environment the average error in estimating a degradation change is 0.0075°/hr or less, the worst standard deviation of the error is 0.0126°/hr and

the average estimation time is about 30 minutes. The standard deviations closely reflect the variability of each individual estimate and show that an individual estimate will be accurate with a one sigma value of less than  $.015^{\circ}/\text{hr}$  and, since the variation tends to be both positive and negative, the average estimation error is quite small.

Constant Bias Degradation Magnitude to be Estimated $^{\circ}/\text{hr}$	No. of Samples Used	Average Estimation Error $^{\circ}/\text{hr}$	Estimation Error Standard Deviation $^{\circ}/\text{hr}$	Average Estimation Time (min)	Theoretical Standard Deviation $^{\circ}/\text{hr}$
0.068	2	0.075	0.013	39	0.012
0.090	11	0.002	0.012	27.2	0.015
0.150	5	0.001	0.009	31.2	0.014

Fig. 2.14 Estimation of Constant Gyro Bias Degradation Magnitudes-Static Case-SIRU FDICR Tests

If there is a second failure during estimation of a first failure bias, the estimation of the bias is automatically recomputed from a parity equation that does not use the output of the second failed instrument. Also, the second failure bias is always estimated using a parity equation that does not use the output of the first failed instrument. The average estimation times given in Fig. 2.14 do not include the extra time needed for any recomputation due to the effect of a 2nd failure and hence properly reflect the typical time needed for estimation.

Figure 2.15 lists the data for tests of detection, isolation, and classification of gyro ramp bias degradations for a static environment. Note that for each case (.007, .003 or  $.015^{\circ}/\text{hr}/\text{minute}$ ) the difference between the detection time and the time at which the ramp reached  $.07^{\circ}/\text{hr}$  is less than the 18.7 minutes that was required to detect a  $.07^{\circ}/\text{hr}$  bias in Fig. 2.12. This result is a consequence of the comparison theorem given in reference 2. This theorem states in effect that the constant bias detection performance is an upper bound on the ramp bias detection performance in the manner described above for the data in Fig. 2.15. Also note that the classification time for the ramp bias degradation is generally higher than that for the constant bias degradation, Fig. 2.12, because it takes a longer time for the ramp to build up to the necessary value for classification by the algorithm.

Gyro	Ramp Slope ( $^{\circ}/\text{hr}/\text{min}$ )	Time at which ramp = $.0675^{\circ}/\text{hr}$ (minutes)	Ramp Value at Detection $^{\circ}/\text{hr}$	Detection Time (minutes)	Classification Time (minutes)	Estimated Slope ( $^{\circ}/\text{hr}/\text{minute}$ )	Estimation Time (minutes)
C	0.075	9	0.21	28	20	-	-
E	0.003	22.5	0.108	36	48	-	-
F	0.015	4.5	0.180	12	16	0.015	54

Fig. 2.15 Detection, Isolation and Classification of Gyro Ramp Bias Degradation Cal Pos. 2-Static Case-SIRU FDICR Tests

Figure 2.16 shows data for detection, isolation, and classification of gyro constant bias degradations in dynamic environments. A bias degradation was inserted in the system software model in selected axes, A, B, C and F. The system environment included a continuous rotational input of  $5^{\circ}/\text{sec}$  and several  $1/2$  Hz oscillatory inputs about the X axis. The degradation thresholds for these tests were increased over the static tests because the parity equation residuals are higher with a dynamic environment. The standard deviation values for the residuals are also higher in the dynamic tests. The FDICR algorithm parameters used in these tests were:

Static Tests

$$a_1 = .05^{\circ}/\text{hr}$$

$$\sigma_p = .053^{\circ}/\text{hr}$$

Oscillatory Tests

$$a_1 = .15^{\circ}/\text{hr}$$

$$\sigma_p = .1^{\circ}/\text{hr}$$

Slew Tests

$$a_1 = .27^{\circ}/\text{hr}$$

$$\sigma_p = .24^{\circ}/\text{hr}$$

these  $\sigma_p$  parameters are somewhat higher than the actual system performance in these environments.

Table Rotation About Vertical Axis	No. Of Tests	Constant Bias Degradation Magnitude (o/hr)	Average Detection Time (minutes)	Average Classification Time (minutes)
slew $5^{\circ}/\text{sec}$	1	0.375	12	4
osc. $.5^{\circ}$ P-P 1/2 Hz	3	0.225	8.7	4.7

Fig. 2.16 Detection, Isolation, and Classification of Gyro Constant Bias Degradations-Dynamic Environment-SIRU FDICR

Changing these specifications correspondingly changes the minimum detectable degradation from  $.05^{\circ}/\text{hr}$  to  $.15^{\circ}/\text{hr}$  in the oscillatory tests and to  $.27^{\circ}/\text{hr}$  in the slew tests. For the test conducted with degradations somewhat higher than these specified levels (Fig. 2.16), reasonably short detection and classification times were observed. Also note that these thresholds are still significantly below the  $.7^{\circ}/\text{hr}$  hard fail TSE threshold. In general, the FDICR specifications should be altered to reflect the influence of dynamic conditions in an adaptive manner consistent with the mission phase requirements.

In the TSE method, the detection level for gyros is adjusted to account for changes in the dynamic environment. This adjustment is accomplished by raising

the detection threshold by a small fraction of the expression  $\sum(\Delta\theta_x + \Delta\theta_y + \Delta\theta_z)$ , where  $\Delta\theta_x, \Delta\theta_y, \Delta\theta_z$  are the gyro counts for the X, Y, and Z body axes respectively.

The statistical FDICR algorithm could be modified so that the values of  $\sigma_p$  and  $a_1$  are adjusted according to the estimated value of  $\sigma_p$  for the particular dynamic environment that the system senses. However, to effect a direct estimation of the correct  $\sigma_p$  is impractical as it takes a considerable amount of time. This is seen as follows: Assume a Gaussian distribution for the parity equation residual. The standard deviation,  $\sigma_v$ , of the estimated standard deviation is related to the actual standard deviation,  $\sigma_T$ , by the following equation.

$$\sigma_v^2 = \frac{2}{n-1} \sigma_T^2 \quad (2.34)$$

If  $\sigma_v$  is to be  $0.015^\circ/\text{hr}$  and  $\sigma_T$  is  $0.15^\circ/\text{hr}$ , approximately 200 sample points would be required. Two hundred data points is equivalent to about seven hours for two minute data points. During the estimation process, the environment could change and there would be an intolerable lag between the estimated standard deviation and the required standard deviation. It is therefore recommended that  $\sigma_p$  be adjusted for the particular dynamic environment according to mission phase. The dynamic test results presented in this chapter show that the statistical FDICR adaptations for the different environments performed effectively.

In addition to the tabulated tests above, evaluation of the detection, isolation, and classification of variance increase software was conducted.

Random noise with zero average and a standard deviation of  $.18^\circ/\text{hr}$  was added to the output of the F-gyro. The increased variance was detected in 20 minutes. The F-gyro was also isolated at the same time (i.e., 20 minutes).

### 2.6.1 Inclusion of a Spike Degradation at a Gyro Output

A constant bias of  $.6^\circ/\text{hr}$  was inserted at the output of the C-gyro. This degradation was detected and the C-gyro was isolated. Two minutes later the  $.6^\circ/\text{hr}$  degradation was removed. The C-gyro was recertified and put back on line 8 minutes after removal of the degradation.

Accelerometer FDICR tests (see Fig. 2.0) were run in addition to the gyro FDICR tests described above.

Figure 2.17 is a data listing for detection, isolation and classification of accelerometer constant bias degradations in a static environment. All six instrument

axes were exercised with bias degradation changes between 0.1 and 0.2 cm/sec<sup>2</sup>. The accelerometer detection algorithm has a degradation threshold of 24 cm/sec accumulated over a four minute interval (240 sec). It is thus seen that the minimum threshold of 0.1 cm/sec<sup>2</sup> would be detected in 4 minutes as confirmed by the data in Fig.2.17 (also 0.2 cm/sec<sup>2</sup> was detected in 2 minutes). The software algorithm accelerometer classification time is a constant of 10 minutes.

No. of Tests	Constant Bias Degradation Magnitude(cm/sec <sup>2</sup> )	Average Detection Time (minutes)	Average Classification Time (minutes)	Theoretical Classification Time (minutes)
6	0.1	4	10	10
2	0.2	2	10	10

Fig. 2.17 Detection, Isolation, and Classification of Accelerometer Constant Bias Degradations-Static Environment-SIRU FDICR

Figure 2.18 is a data compilation for performance of the estimation of constant accelerometer bias degradation magnitudes in a static environment. It is seen that the average error in the estimation of the bias change and the standard deviation of the estimate are 0.02 cm/sec<sup>2</sup> or less. Average estimation time is 10 minutes.

Constant Bias Degradation Magnitude (cm/sec <sup>2</sup> )	No. of Tests	Average Estimation Error (cm/sec <sup>2</sup> )	Estimation Error Standard Deviations (cm/sec <sup>2</sup> )	Average Estimation Time (min)
0.1	6	.002	.009	10.3
0.2	2	.02	.02	10

Fig. 2.18 Estimation of Constant Accelerometer Bias Degradation Magnitudes-Static Case-SIRU FDICR

Accelerometer ramp bias degradation detection, isolation, and classification were also evaluated.

A ramp bias degradation of 0.02 cm/sec<sup>2</sup> was added to the output of the D-accelerometer. This degradation was detected 10 minutes after initiation of the degradation. The instrument was also isolated at the same time. Classification of the degradation as being a ramp was completed 20 minutes after the start of the test.

## 2.7 Software Memory and Timing Requirements

The following are the memory and timing requirements for statistical FDICR on the Honeywell DDP516 computer:

Memory: 2126 words

Time per Update: 4563.8msec

Update Rate: once every 2 minutes

%Machine Time for 50 Attitude Update per sec is 0.004%

Appendix A2  
SIRU Equations

A2.0 Statistical FDICR Parity Equations

A2.1 Parity Equations Used To Detect a First Failure

The following are the parity equations used to detect a first failure. Here  $\epsilon_i$  denotes the residual of the  $i$ th parity equations, and  $m_a$  through  $m_f$  denote the outputs (in angular rate) of the A through F-gyros respectively. Also,  $c = \cos\alpha$ ,  $s = \sin\alpha$ , where  $\alpha$  is the appropriate SIRU geometrical angle.

$$\epsilon_1 = c(m_a - m_b) + s(m_c + m_d) \quad (A2.1)$$

$$\epsilon_2 = -c(m_a + m_c) + s(m_b + m_f) \quad (A2.2)$$

$$\epsilon_3 = c(m_e + m_f) - s(m_a + m_b) \quad (A2.3)$$

$$\epsilon_4 = c(m_a - m_e) + s(m_d - m_f) \quad (A2.4)$$

$$\epsilon_5 = c(m_c + m_e) - s(m_b + m_d) \quad (A2.5)$$

$$\epsilon_6 = c(m_c - m_d) + s(m_e - m_f) \quad (A2.6)$$

A2.2 Parity Equations Used to Detect a Second Failure

The following sets of parity equations are used to detect a second failure.

A2.2.1 A is First Failure

In addition to parity equations A 2.5 and A 2.6 above, we have:

$$\epsilon_7 = c(m_b - m_e) - s(m_c + m_f) \quad (A2.7)$$

$$\epsilon_8 = c(m_b - m_f) - s(m_d + m_e) \quad (\text{A2.8})$$

$$\epsilon_9 = -c(m_d - m_f) + s(m_b + m_c) \quad (\text{A2.9})$$

#### A2.2.2 B is First Failure

In addition to equations A2.4 and A2.6 we have:

$$\epsilon_{10} = c(m_d - m_e) + s(m_a - m_c) \quad (\text{A2.10})$$

$$\epsilon_{11} = c(m_c - m_f) + s(m_a - m_d) \quad (\text{A2.11})$$

$$\epsilon_{12} = c(m_a - m_f) + s(m_c - m_e) \quad (\text{A2.12})$$

#### A2.2.3 C is First Failure

In addition to Eqs. A2.3, A2.4 and A2.8 we have:

$$\epsilon_{13} = -c(m_a + m_d) + s(m_b + m_e) \quad (\text{A2.13})$$

$$\epsilon_{14} = c(m_b - m_d) - s(m_a + m_f) \quad (\text{A2.14})$$

#### A2.2.4 D is First Failure

In addition to Eqs. A2.2, A2.3, A2.7 and A2.12 we have :

$$\epsilon_{15} = c(m_b - m_c) - s(m_a + m_e) \quad (\text{A2.15})$$

#### A2.2.5 E is First Failure

Equations A2.1, A2.2, A2.9, A2.11 and A2.14 apply.

#### A.2.2.6 F is First Failure

Equations A2.1, A2.5, A2.10, A2.13 and A2.15 apply.

### A2.3 TSE Parity Equations

#### A2.3.1 Parity Equations Used to Detect First Failure

The following are the parity equations used to detect a first failure (TSE method).  
(The notation is the same as in paragraph A2.1.)

$$\epsilon_1 = m_a - A_a \quad (\text{A2.16})$$

$$\epsilon_2 = m_b - A_b \quad (\text{A2.17})$$

$$\epsilon_3 = m_c - A_c \quad (\text{A2.18})$$

$$\epsilon_4 = m_d - A_d \quad (\text{A2.19})$$

$$\epsilon_5 = m_e - A_e \quad (\text{A2.20})$$

$$\epsilon_6 = m_f - A_f \quad (\text{A2.21})$$

where:

$$A_a = \sqrt{2}(m_b - m_c - m_d + m_e + m_f) \quad (\text{A2.22})$$

$$A_b = \sqrt{2}(m_a + m_c + m_d + m_e + m_f) \quad (\text{A2.23})$$

$$A_c = \sqrt{2}(-m_a + m_b + m_d - m_e + m_f) \quad (\text{A2.24})$$

$$A_d = \sqrt{2}(-m_a + m_b + m_c + m_e - m_f) \quad (\text{A2.25})$$

$$A_e = \sqrt{2}(m_a + m_b - m_c + m_d - m_f) \quad (\text{A2.26})$$

$$A_f = \sqrt{2}(m_a + m_b + m_c - m_d - m_e) \quad (\text{A2.27})$$

#### A.2.3.2 Parity Equations Used to Detect a Second Failure

If A is failed, replace  $m_a$  in Eqs. A2.16-A2.21 by  $A_a$ .

If B is failed, replace  $m_b$  in Eqs. A2.16-A2.21 by  $A_b$ . Similar changes apply to C-F.

Chapter 3  
Single-Position Self-Calibration

3.0 Introduction

A single-position self-calibration method has been developed. In this method, the plane containing the SIRU Y and Z body axes is kept approximately level (to within 10 degrees) so that only the stable null bias drift (NBD) term dominates the total lumped drifts of the two reference gyros since their output axes (OA) are approximately vertical. (Note that the instrument drifts discussed in this chapter refer to the gyro residual drift remaining after proper ADIA, NBD, etc., compensations have been applied to each unit to cancel out the laboratory-calibrated drift terms.) In this calibration method, these two reference gyros are assumed to have zero drift changes from a prior component level or laboratory level BD calibration. The lumped drifts of the other four gyros are then obtained by solving three independent parity equations and an equation involving the vertical axis drift. Note that the lumped drifts of the four non-reference gyros include the acceleration dependent drift terms which are more unstable across power downs, etc., than the NBD terms which comprise most of the reference gyro drift (for example the observed highest ADIA shifts for the 18 IRIG Mod B's used in this test program were statistically 5 times greater than the lowest BD shifts).<sup>1</sup> Hence the drift of these four gyros is corrected by reference to the much more stable drift of the reference gyros in the application of this calibration procedure.

3.1 Required SIRU Level Tolerance

Vertical axis drift refers to the combination of gyro residual drifts appearing at the vertical axis of the system. These residual drifts are due to the instruments and should not be confused with the actual input rate appearing at the system axes due to motion of the system.

With SIRU perfectly level, the assumption of zero drift for the reference gyros depends only on the stability of NBD. The one sigma value of NBD for these two gyros is 0.017<sup>o</sup>/hr. The drift contributed simultaneously by the ADIA and acceleration dependent drift-spin reference axis (ADSRA) terms for these two gyros for a non-level SIRU has a one sigma value that is bounded by 0.12<sup>o</sup>/hr/g. An upper bound on the error in assuming the reference gyros to have zero drift for a non-level SIRU is given by the following standard deviation:

$$\begin{aligned} \sigma(\text{one reference gyro}) &= \sqrt{(.017)^2 + \left(\frac{.12}{57.3} \theta\right)^2} \\ &\cong \sqrt{.000289 + .000004 \theta^2} \end{aligned} \tag{3.1}$$

where  $\theta$  is the deviation of the SIRU X axis from the vertical in degrees. Figure 3.1 is a plot of Eq. 3.1 for  $\theta$  ranging from 0 to  $10^\circ$ . From this figure it can be seen that the error standard deviation for the single position calibration reference will be well within a standard deviation of  $0.03^\circ/\text{hr}$  for SIRU level to within  $10^\circ$ .

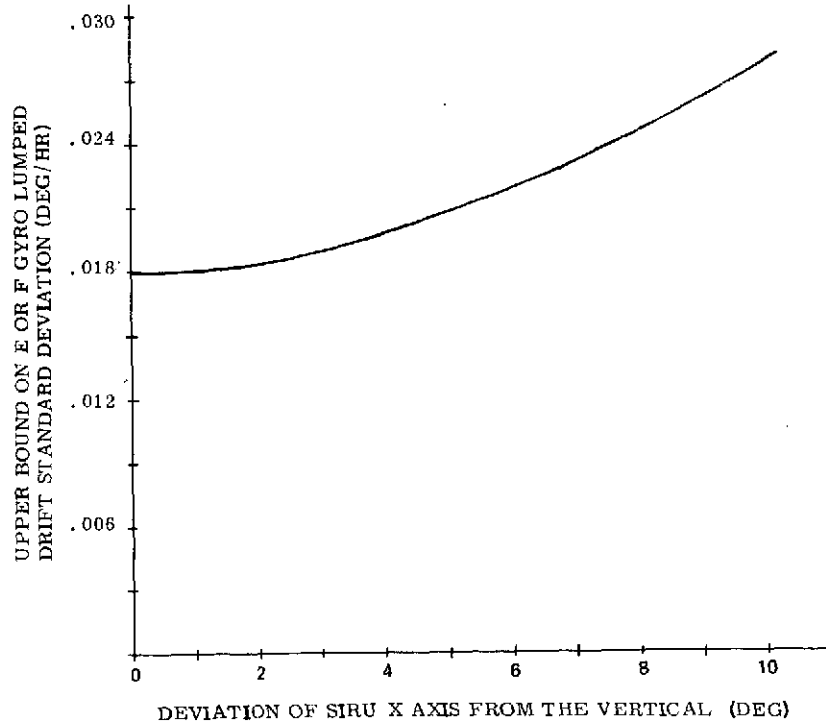


Fig. 3.1 Error in E or F Single Position Calibration Reference Gyro as a Function of SIRU X axis Tilt from the Vertical

### 3.2 Parity Equations

For no failures (considering all 6 gyros to be operational), there are three independent parity equations. They are:

$$\begin{aligned}
 c\epsilon_a - c\epsilon_b + s\epsilon_c + s\epsilon_d &= c(m_a - m_b) + s(m_c + m_d) \\
 s\epsilon_a + s\epsilon_b - c\epsilon_e - c\epsilon_f &= s(m_a + m_b) - c(m_e + m_f) \\
 c\epsilon_c - c\epsilon_d + s\epsilon_e - s\epsilon_f &= c(m_c - m_d) + s(m_e - m_f)
 \end{aligned} \tag{3.2}$$

$c = \cos \alpha \approx .85$   
 $s = \sin \alpha \approx .525$   
 $\alpha =$  SIRU geometrical configuration angle  
 $\epsilon_a$  through  $\epsilon_f$  represent the lumped gyro drifts  
 $m_a$  through  $m_f$  represent the gyro outputs

The above equations, Eqs. 3.2, can be rewritten as :

$$\begin{aligned}
 c\epsilon_a - c\epsilon_b + s\epsilon_c + s\epsilon_d &= V_1 \\
 s\epsilon_a + s\epsilon_b - c\epsilon_e - c\epsilon_f &= V_2 \\
 c\epsilon_c - c\epsilon_d + s\epsilon_e - s\epsilon_f &= V_3
 \end{aligned} \tag{3.3}$$

where  $V_1$  through  $V_3$  represent the appropriate right hand sides of Eqs. 3.2 after being filtered.

### 3.3 SIRU Body Axis Drifts

The body axis drifts of SIRU are related to the gyro drifts by the least squares estimate of the body axis inputs as a function of the gyro outputs. For all six gyros operating we have:

$$\hat{\underline{x}} = \left(\frac{1}{2}\right) \begin{bmatrix} s & -s & -c & -c & 0 & 0 \\ 0 & 0 & -s & s & c & -c \\ c & c & 0 & 0 & s & s \end{bmatrix} \begin{bmatrix} m_a \\ m_b \\ m_c \\ m_d \\ m_e \\ m_f \end{bmatrix} \quad (3.4)$$

where  $\hat{\underline{x}}$  is the vector whose terms are the least squares estimate of the SIRU X, Y, and Z computational (i.e. body) axes.

Thus the body axis drifts  $d_{X_B}$ ,  $d_{Y_B}$ ,  $d_{Z_B}$  at the SIRU X, Y, and Z axes, respectively, are related to the individual instrument lumped drift terms in Eq. 3.4 by substituting  $(\epsilon_a \dots \epsilon_f)$  in Eq. 3.4.

$$s\epsilon_a - s\epsilon_b - c\epsilon_c - c\epsilon_d = 2d_{X_B} \quad (3.5)$$

$$-s\epsilon_c + s\epsilon_d + c\epsilon_e - c\epsilon_f = 2d_{Y_B} \quad (3.6)$$

$$c\epsilon_a + c\epsilon_b + s\epsilon_e + s\epsilon_f = 2d_{Z_B} \quad (3.7)$$

### 3.4 Single-Position Calibration Equations Selected for the Calibration Position 2

If it is desired to solve for the four non-reference gyro drifts  $\epsilon_a$ ,  $\epsilon_b$ ,  $\epsilon_c$ ,  $\epsilon_d$ , using the E and F gyros as references, then Eqs. 3.3 can be solved in conjunction with Eq. 3.5 where  $X_B$  is the body axis that is almost vertical (i.e., deviates from the vertical no more than  $10^0$ ). The processing, in terms of verticality,

automatically takes care of compensation for the known acceleration sensitive drift of the reference gyros (OA's near vertical) so that if they are tipped (within the  $10^0$  region) changes in these terms will have negligible effect. This choice of equations is one of many possibilities. It is assumed that since the calibration is effected while the vehicle is stationary, no net body motion occurs about the vertical axis; thus instantaneous body motions about the X axis  $X_B$  can be filtered to allow measurement of  $dX_B$  and its subsequent use in Eq. 3.5. An alternative is to use an equation involving the vertical drift  $dX_N$ . This approach is discussed in Appendix A3.0 of this chapter. It is not practical to use any equations involving the north axis drift,  $dZ_N$ , because the solution for  $\epsilon_a$  through  $\epsilon_d$  is indeterminate when the three parity equations, the vertical (or  $X_B$  body axis) drift equation and the north drift equation are solved simultaneously for particular azimuth values. The solution is always indeterminate when the vertical drift (or  $dX_B$ ) equation is omitted. Also note that the east axis drift is never measurable in a self-contained system having no optical alignment.

Solving Eq. 3.2 and 3.5 simultaneously with the assumption of zero drift for the reference gyros E and F yields.

$$\hat{\epsilon}_a = \frac{cV_1}{2} + \frac{V_2}{2s} + sd\hat{X}_B \quad (3.8)$$

$$\hat{\epsilon}_b = \frac{V_2}{s} - \hat{\epsilon}_a \quad (3.9)$$

$$\hat{\epsilon}_c = \frac{sV_1}{2} + \frac{V_3}{2c} - cd\hat{X}_B \quad (3.10)$$

$$\hat{\epsilon}_d = \hat{\epsilon}_c - \frac{V_3}{c} \quad (3.11)$$

$$\hat{\epsilon}_e = 0 \quad (3.12)$$

$$\hat{\epsilon}_f = 0 \quad (3.13)$$

Where  $\hat{\epsilon}_a$  through  $\hat{\epsilon}_f$  are the single position calibration estimates of drifts  $\epsilon_a$  through  $\epsilon_f$ .

In the above estimates (Eqs. 3.8 - 3.13) the values  $V_1$ ,  $V_2$ , and  $V_3$  are obtained as follows:

Let :

$\Delta\theta_{a_i}$  = angular bit from gyro A at time i

$\Delta\theta_{f_i}$  = angular bit from gyro F at time i

Compute :

$$\begin{aligned} m_a &= \frac{H_i}{T} \sum_{i=0}^T \Delta\theta_{a_i} \\ &\vdots \\ m_f &= \frac{H_i}{T} \sum_{i=0}^T \Delta\theta_{f_i} \end{aligned} \quad (3.14)$$

where :

$H_i$  = Scaling coefficient

$T$  = time interval over which the pulses are averaged (1800 seconds).

The following is then calculated using Eq. 3.14:

$$V_1 = c(m_a - m_b) + s(m_c + m_d) \quad (3.15)$$

$$V_2 = s(m_a + m_b) - c(m_e + m_f) \quad (3.16)$$

$$V_3 = c(m_c - m_d) + s(m_e - m_f) \quad (3.17)$$

The X body axis drift  $d_{X_B}$  is obtained as follows:

The vertical body axis angular rate output  $W_{X_B}$  is given by:

$$\underline{W}_{X_B} = d_{X_B} + \begin{bmatrix} W_{nb}^b \end{bmatrix} X_B + \begin{bmatrix} W_{in}^b \end{bmatrix} X_B \quad (3.18)$$

Where :

$\begin{bmatrix} W_{nb}^b \end{bmatrix}_{X_B}$  = angular base motion about the  $X_B$  axis

$\begin{bmatrix} W_{in}^b \end{bmatrix}_{X_B}$  = earth rate component about  $X_B$  axis

The earth rate component about the  $X_B$  axis can be estimated as follows:

$$\begin{bmatrix} W_{in}^b \end{bmatrix}_{X_B} = C_{31} W_h + C_{33} W_v \quad (3.19)$$

Where  $W_h$  and  $W_v$  are the horizontal and vertical components of earth rate respectively and  $C_{31}$  and  $C_{33}$  are the appropriate elements of the direction cosine matrix,  $C_B^C$ , obtained from gyrocompassing, that relate the X reference axis of the SIRU package to the earth frame.

Substituting Eq. 3.19 into Eq. 3.18 and rearranging the resulting equation yields:

$$d_{X_B} = W_{X_B} - C_{31} W_h - C_{33} W_v - \begin{bmatrix} W_{nb}^b \end{bmatrix}_{X_B} \quad (3.20)$$

$\underline{W}_{in}^b$  may be estimated from the launch site earth rate components and the gyrocompassing direction cosine terms; however,  $\underline{W}_{nb}^b$  is unknown. Thus, an instantaneous estimate of  $d_{X_B}$  would reflect an error due to any vehicle base motion and must be filtered to eliminate  $\underline{W}_{nb}^b$ .

However, we can assume that  $\begin{bmatrix} W_{nb}^b \end{bmatrix}_{X_B}$  has a zero mean (which seems appropriate for a vehicle on the launch pad) and a filter may be devised that minimizes the effect of base motion. The estimate of drift,  $\hat{d}_{X_B}$  then corresponds to:

$$\begin{aligned} \hat{d}_{X_B} &= \overline{\left[ W_{X_B} - C_{31} W_h - C_{33} W_v \right]} \\ &\cong d_{X_B} + \begin{bmatrix} W_{nb}^b \end{bmatrix}_{X_B} \end{aligned} \quad (3.21)$$

where the bar denotes the time averaged and filtered value.

For further details about the method used to filter  $W_{X_B}$  so that the base motion effects,  $\begin{bmatrix} W_{nb}^b \end{bmatrix}_{X_B}$ , are attenuated, see Appendix B3.0 of this chapter.

In addition to base motion errors in estimating  $d\mathbf{x}_B$ , there will be a term that is due to the gyrocompassing azimuth error,  $A_z$ , appearing in the element,  $C_{31}$ . Errors resulting from any errors in  $C_{33}$  are negligible since the error is a small angle which reflects as a second order effect. This is discussed in the next section.

### 3.5 Derivation of Direction Cosine Matrix, $\underline{C}_B^C$

Let  $\underline{C}_B^C$  denote the direction cosine matrix transforming the body frame to the computed frame. The direction cosine matrix  $\underline{C}_B^N$  transforming the body frame to the local navigational frame is related to  $\underline{C}_B^C$  through the unknown error in azimuth,  $A_z$ , as follows:

$$\underline{C}_B^C = \underline{C}_N^C \underline{C}_B^N \quad (3.22)$$

where  $\underline{C}_N^C$  reflects the azimuth error,  $A_z$ :

$$\underline{C}_N^C = \begin{bmatrix} 1 & A_z & 0 \\ -A_z & 1 & 0 \\ 0 & 0 & 1 \end{bmatrix} \quad (3.23)$$

An expression for  $\underline{C}_B^C$  in terms of the true but unknown azimuth and leveling angles of a referenced body that is pointing north is derived as follows:

$$\underline{C}_N^B \begin{bmatrix} \cos \phi_D & \sin \phi_D & 0 \\ -\sin \phi_D & \cos \phi_D & 0 \\ 0 & 0 & 1 \end{bmatrix} \begin{bmatrix} 1 & 0 & -\phi_E \\ 0 & 1 & \phi_N \\ \phi_E & -\phi_N & 1 \end{bmatrix} \quad (3.24)$$

$$\underline{C}_B^C = \begin{bmatrix} \cos \phi_D + A_z \sin \phi_D & -\sin \phi_D & \phi_E - A_z \phi_N \\ & +A_z \cos \phi_D & \\ -A_z \cos \phi_D & A_z \sin \phi_D & -A_z \phi_E \\ +\sin \phi_D & +\cos \phi_D & -\phi_N \\ -\phi_E \cos \phi_D & \phi_E \sin \phi_D & 1 \\ +\phi_N \sin \phi_D & +\phi_N \cos \phi_D & \end{bmatrix} \quad (3.25)$$

where:

- $A_z$  = Gyrocompassing azimuth error
- $\phi_E$  = True east leveling angle
- $\phi_N$  = True north leveling angle
- $\phi_D$  = True azimuth angle

$\phi_E$  and  $\phi_N$  are considered to be small angles (less than  $10^\circ$ ), and  $\phi_D$  corresponds to the azimuth angle of the body frame. These angles have been arbitrarily defined for convenience of analysis and are not the gyrocompassing error angles. The angles correspond to a Euler angle derivation that assumes that the SIRU X, Y, Z axes were aligned with the Down, East, and South axes respectively and then rotated. Thus,  $\phi_N$  represents a rotation about the East axis,  $\phi_E$  represents a rotation of the North axis and then the entire frame is rotated about the X axis by  $\phi_D$ . Since  $\phi_N$  and  $\phi_E$  are small,  $\phi_D$  is essentially the azimuth angle. The gyrocompassing error angle,  $A_z$ , is the deviation from this azimuth angle,  $\phi_D$ . See Fig. 3.2.

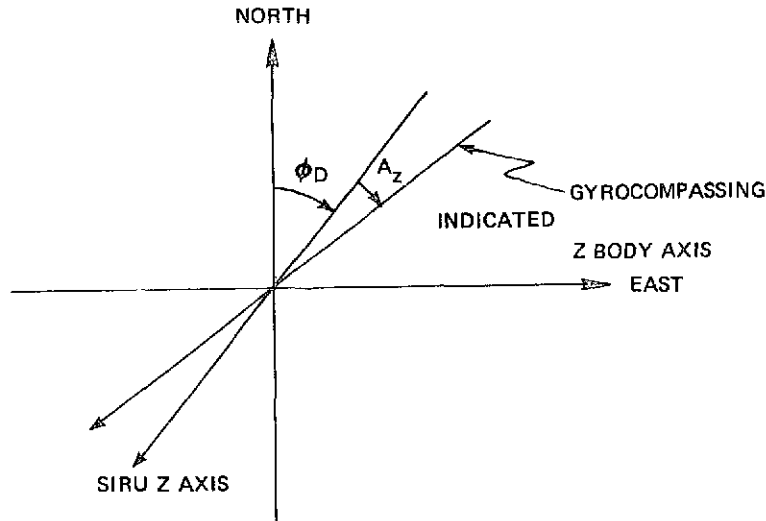


Fig. 3.2 Definition of True Azimuth Angle  $\phi_D$ .

Similar results may be obtained by assuming rotation about the vertical axis first. The derived equation, Eq. 3.25, also corresponds to the direction cosine matrix that would be obtained from gyrocompassing.

The direction cosine matrix,  $\underline{C}_C^B$ , can be represented in general by:

$$\underline{C}_C^B = \left[ \underline{C}_C^B \right]^T = \begin{bmatrix} C_{11} & C_{12} & C_{13} \\ C_{21} & C_{22} & C_{23} \\ C_{31} & C_{32} & C_{33} \end{bmatrix} \quad (3.26)$$

where  $C_{11}$  through  $C_{33}$  are the time varying elements actually obtained from gyrocompassing.

The element  $C_{31}$  in Eq. 3.20 is, therefore, given by:

$$C_{31} = \phi_E - A_z \phi_N \quad (3.27)$$

As previously noted, the second order effects associated with gyrocompassing leveling errors have been neglected. Therefore,  $C_{33}$  in Eq. 3.20 is:

$$C_{33} = 1 \quad (3.28)$$

The error in  $d_{X_B}$  (Eq. 3.20) due to the gyrocompassing azimuth error is given by  $A_z \phi_N$ , the product of two small numbers (since the SIRU plane containing the YZ axes is approximately level). Furthermore, a second single position calibration iteration will remove  $A_z$  because the east axis drift error after a single position calibration is virtually independent of any error in vertical ( $d_{X_B}$ ) drift estimation. This condition will be explained in the next section.

### 3.6 Single Position Calibration Error Equations

We denote the errors in the single position calibration estimates,  $\hat{\epsilon}_a$  through  $\hat{\epsilon}_f$ , by  $\tilde{\epsilon}_a$ ,  $\tilde{\epsilon}_b$ ,  $\tilde{\epsilon}_c$ ,  $\tilde{\epsilon}_d$ ,  $\tilde{\epsilon}_e$ , and  $\tilde{\epsilon}_f$  and obtain:

$$\begin{aligned} \tilde{\epsilon}_a &\triangleq \hat{\epsilon}_a - \epsilon_a \\ &\vdots \\ \tilde{\epsilon}_f &\triangleq \hat{\epsilon}_f - \epsilon_f \end{aligned} \quad (3.29)$$

where  $\epsilon$  is the true drift,  $\hat{\epsilon}$  is the drift estimate, Eqs. 3.8-3.13.

Also denote the vertical drift estimation error,  $\tilde{\epsilon}_{X_B}$ , by:

$$\tilde{\epsilon}_{X_B} = \hat{d}_{X_B} - d_{X_B} \quad (3.30)$$

where  $\hat{d}_{X_B}$  is the vertical drift estimate, Eq. 3.21.

Substituting Eqs. 3.8 through 3.13, 3.30 and 3.5 into Eq. 3.29 yields the following equations for the errors in the estimates:

$$\tilde{\epsilon}_a \stackrel{\Delta}{=} \hat{\epsilon}_a - \epsilon_a = -0.81(\epsilon_e + \epsilon_f) + 0.525 \tilde{\epsilon}_{X_B} \quad (3.31)$$

$$\tilde{\epsilon}_b \stackrel{\Delta}{=} \hat{\epsilon}_b - \epsilon_b = -0.81(\epsilon_e + \epsilon_f) - 0.525 \tilde{\epsilon}_{X_B} \quad (3.32)$$

$$\tilde{\epsilon}_c \stackrel{\Delta}{=} \hat{\epsilon}_c - \epsilon_c = 0.31(\epsilon_e - \epsilon_f) - 0.850 \tilde{\epsilon}_{X_B} \quad (3.33)$$

$$\tilde{\epsilon}_d \stackrel{\Delta}{=} \hat{\epsilon}_d - \epsilon_d = -0.31(\epsilon_e - \epsilon_f) - 0.850 \tilde{\epsilon}_{X_B} \quad (3.34)$$

Also:

$$\tilde{\epsilon}_e = -\epsilon_e \quad \tilde{\epsilon}_f = -\epsilon_f \quad (3.35)$$

It is of interest to have an analytic derivation of how the estimation errors in the single position calibration influence subsequent gyrocompassing performance. The gyrocompassing performance will be essentially defined by the inertial E-W axis drift resulting from the estimation errors defined in Eqs. 3.31-3.35. To derive an equivalent E-W drift, one must first obtain the Y body axis drift,  $\epsilon_{Y_B}$ , and the Z body axis drift,  $\epsilon_{Z_B}$ , that result after compensation by the values given by Eqs. 3.8-3.13. These drifts are obtained by substituting Eqs. 3.31-3.35 into the equation form, Eq. 3.4.

$$\tilde{\epsilon}_{Y_B} = 0.588(\epsilon_e - \epsilon_f) \quad (3.36)$$

$$\tilde{\epsilon}_{Z_B} = 0.95(\epsilon_e + \epsilon_f) \quad (3.37)$$

In calibration position #2, Eq. 3.36 yields the east axis drift. Note that both  $\tilde{\epsilon}_{Y_B}$  and  $\tilde{\epsilon}_{Z_B}$  are independent of the vertical drift estimation error,  $\tilde{\epsilon}_{X_B}$ .

For an arbitrary azimuth angle,  $\phi_D$ , the east axis drift after calibration is given approximately by:

$$\tilde{\epsilon}_{Y_N} \cong (\cos \phi_D) \tilde{\epsilon}_{Y_B} - (\sin \phi_D) \tilde{\epsilon}_{Z_B} \quad (3.38)$$

Substituting Eqs. 3.36 and 3.37 into Eq. 3.38 yields:

$$\tilde{\epsilon}_{Y_N} = - \left[ \epsilon_e \sin (\phi_D - \psi) + \epsilon_f \sin (\phi_D + \psi) \right] \quad (3.39)$$

where  $\psi = \arctan 0.62$ .

From Eq. 3.39 we can derive an upper bound for the standard deviation,  $\sigma_{\tilde{\epsilon}_{Y_N}}$ , of  $\tilde{\epsilon}_{Y_N}$  in terms of the standard deviation of the E and F-gyro drifts (see Eq. 3.1) that is given by:

$$\sigma_{\tilde{\epsilon}_{Y_N}} < (1.2) \sigma_{E \text{ or } F} = (1.2) \sqrt{.000289 + .000004 \theta^2} \quad (3.40)$$

The upper bound on the standard deviation of the east axis drift after calibration can therefore be obtained from Fig. 3.1 by multiplying the ordinate of that graph by 1.2.

### 3.7 Additional Equations Useful in Analyzing Single Position Calibration Test Data

$$\epsilon_e = 0.81 \tilde{D}_{CD} - 0.31 \tilde{S}_{AB} \quad (3.41)$$

$$\epsilon_f = -0.81 \tilde{D}_{CD} - 0.31 \tilde{S}_{AB} \quad (3.42)$$

$$\tilde{\epsilon}_{X_B} \cong \tilde{D}_{AB} \text{ and} \quad (3.43)$$

$$\tilde{\epsilon}_{X_B} = -0.588 (\tilde{S}_{CD}) \quad (3.44)$$

$$\tilde{\epsilon}_{Y_B} = 0.95 \tilde{D}_{CD} \quad (3.45)$$

$$\tilde{\epsilon}_{Z_B} = -0.59 \tilde{S}_{AB} \quad (3.46)$$

where:

$$\tilde{S}_{AB} \triangleq \tilde{\epsilon}_A + \tilde{\epsilon}_B \quad (3.47)$$

$$\tilde{S}_{CD} \triangleq \tilde{\epsilon}_C + \tilde{\epsilon}_D \quad (3.48)$$

$$\tilde{D}_{AB} \triangleq \tilde{\epsilon}_A - \tilde{\epsilon}_B \quad (3.49)$$

$$\tilde{D}_{CD} \triangleq \tilde{\epsilon}_C - \tilde{\epsilon}_D \quad (3.50)$$

The following equation (obtained from Eqs. 3.6, 3.48, 3.41, and 3.42) yields the estimated east axis drift,  $\hat{\epsilon}_{YB}$ , (for the calibration position #2) before recompensation using the estimated gyro drifts. This estimated drift can be used as a close approximation to the actual east axis drift.

$$\hat{\epsilon}_{YB} = -.263 \hat{D}_{CD} + 0.684 \tilde{D}_{CD} \quad (3.51)$$

$$\hat{D}_{CD} = \hat{\epsilon}_C - \hat{\epsilon}_D \quad (3.52)$$

### 3.8 Single Position Calibration Data Taken with No Base Motion

The data presented in this section were taken from tests where no base motion was present. Therefore, the full base motion isolation algorithm was not run and the algorithm used was run for only 1/2 hour. Also, gyrocompassing (in order to determine the vertical drift) was done only once at the beginning of the level tests and at the beginning of the 5° offset tests and these initial values were then subsequently used for the remaining tests.

Table 3.9.1 yields the estimation errors of the single position calibration method for a constant bias degradation of  $0.15^\circ/\text{hr}$  introduced into gyros A, B, C, and D. The first half of the table (designated "System Level") presents data for the SIRU X-axis vertical (calibration position # 2). The lower portion of the table (designated "System Not Level") presents data for the system X body axis tilted  $5^\circ$  as described later (See Eq. 3.53). This  $5^\circ$  tilt leads to a second order error.

The column labeled "Baseline Drift" presents the residual drift of the A, B, C, and D gyros as estimated by the single-position calibration before the  $0.15^\circ/\text{hr}$  degradations were introduced. The column labeled "Drift After Miscompensation" presents the total drift as estimated by the single-position calibration method after the  $0.15^\circ/\text{hr}$  miscompensations were introduced. The third column labeled "Estimation Error" is the difference between the degradation introduced plus the base line drift and the drift after miscompensation. For example, the baseline drift for the B gyro and "System Not Level" in the Table 3.9.1 is  $-0.063^\circ/\text{hr}$ . After the introduction of  $+0.15^\circ/\text{hr}$  miscompensation in the B gyro, the resulting B gyro drift should be given by  $0.150$  minus  $0.063^\circ/\text{hr}$  or  $+0.087^\circ/\text{hr}$ . However, the resulting drift measured (by the single position calibration) is  $+0.108^\circ/\text{hr}$ . The difference between these two values is given by  $0.108$  minus  $0.087^\circ/\text{hr}$  or  $0.021^\circ/\text{hr}$  and is listed under "Estimation Error". Note that this estimation error of  $0.021^\circ/\text{hr}$  not only includes the error in measuring the baseline and miscompensation drifts but also any changes in residual drift which occurred between the time the baseline drifts were estimated and the time the miscompensations were introduced.

Table 3.9.2 presents data for a miscompensation of  $+0.150^\circ/\text{hr}$  introduced into gyros A and C. The "Estimation Error" column values are obtained as described above. Taking the "System Level" portion of Table 3.9.2 as another example, we see that the A gyro, after miscompensation by  $+0.150^\circ/\text{hr}$  should have a residual drift of  $0.15$  minus  $0.006^\circ/\text{hr}$  or  $0.144^\circ/\text{hr}$ ; instead the drift after miscompensation was estimated to be  $+0.158^\circ/\text{hr}$ . The difference between  $0.144^\circ/\text{hr}$  and  $0.158^\circ/\text{hr}$  is  $0.014^\circ/\text{hr}$  and is listed under "Estimation Error" for gyro A. The baseline drift for gyro B (System Level) was estimated as  $-0.040^\circ/\text{hr}$ . Since no miscompensation was applied to gyro B the estimation error is given by the difference between  $-0.040^\circ/\text{hr}$  and the drift of gyro B that was estimated as  $-0.031^\circ/\text{hr}$  after gyros A and C were miscompensated. This error is  $-0.031$  minus  $-0.040^\circ/\text{hr}$  or  $0.009^\circ/\text{hr}$ .

Table 3.9.3 presents the results for a  $+0.150^\circ/\text{hr}$  miscompensation applied to gyro A and a  $-0.150^\circ/\text{hr}$  miscompensation applied to gyro B. The results are interpreted in the same way as for the previous tables.

Table 3.9.4 applies to the case of a  $-0.150^{\circ}/\text{hr}$  miscompensation to gyro A and a  $+0.150^{\circ}/\text{hr}$  miscompensation to gyros B and C.

Table 3.9.5 presents the data for  $+0.150^{\circ}/\text{hr}$  miscompensation to gyro C and  $-0.150^{\circ}/\text{hr}$  miscompensation to gyro D.

Tables 3.9.1 - 3.9.5 show that single position calibration is accurate to about  $0.015^{\circ}/\text{hr}$  in the present SIRU system provided that the two reference gyros (E and F) are properly compensated and stable.

Tables 3.9.6 through 3.9.8 present data for those cases where no miscompensations are introduced into gyros A, B, C, D, but the reference gyros E and F are miscompensated.

Table 3.9.6 shows the results of a  $+0.030^{\circ}/\text{hr}$  miscompensation to gyro E. Taking gyro A "System Not Level" as an example, we see from the table that the gyro A baseline residual drift, before the introduction of the miscompensation to reference gyro E, was estimated (by single position calibration) to be  $-0.013^{\circ}/\text{hr}$ . The estimation after miscompensation of gyro E was  $-0.040^{\circ}/\text{hr}$ . The estimation error is the difference between the two and is given by  $-0.040$  minus  $-0.013$  or  $-0.027^{\circ}/\text{hr}$ .

Table 3.9.7 presents data for the case of a  $+0.030^{\circ}/\text{hr}$  miscompensation to gyro F.

Table 3.9.8 shows the results of a  $+0.030^{\circ}/\text{hr}$  miscompensation applied to both reference gyros E and F. Note that the single position calibration estimation errors resulting from E and F reference gyro miscompensations are on the order of the miscompensations themselves and are therefore bounded.

For the  $5^{\circ}$  offset tests, ("System Not Level") the rotary axis of the 16 inch table (RA 16) and the trunnion axis of the 32 inch table (TA 32) were set as follows:

$$\begin{aligned} \text{RA16} &= 154^{\circ} 37' 10'' \\ \text{TA32} &= 5^{\circ} 27' 50'' \end{aligned} \tag{3.53}$$

All other settings were for the calibration position # 2.

When the  $5^{\circ}$  offset tests were made, it was discovered that the C-gyro drift was erratic. Tipping SIRU by  $5^{\circ}$  from its calibration position #2 (per Eq. 3.53) resulted in a shift of  $0.3^{\circ}/\text{hr}$  as shown below. It is also inferred (by comparing the

results of Eqs. 3.43 and 3.44) that the baseline value for the C gyro drift shifted by approximately  $-0.055^{\circ}/\text{hr}$  after the first  $5^{\circ}$  offset test was run. This approximate correction has been included in the data presented below (designated by \*) along with the uncorrected data. Calculated equivalent Y axis drifts before and after single position calibration are given in Section 3.9 .

Table 3.9.1 SPC Estimation Errors with  $0.15^{\circ}/\text{hr}$  Constant Bias Degradation on Gyros A, B, C and D.

	Gyro	Baseline Drift ( $^{\circ}/\text{hr}$ )	Drift After Miscompensation ( $^{\circ}/\text{hr}$ )	Estimation Error ( $^{\circ}/\text{hr}$ )
System Level	A	-.006	+.140	-.003
	B	-.039	+.104	-.006
	C	-.036	+.112	-.002
	D	+.001	+.155	+.005
System Not Level	A	-.013	.140	.003
	B	.063	.108	.021
	C	-.336	-.151	.025
	D	.008	.157	.009

Table 3.9.2 SPC Estimation Errors with a Miscompensation of  $0.15^{\circ}/\text{hr}$  on Gyros A and C.

	Gyro	Baseline Drift ( $^{\circ}/\text{hr}$ )	Drift After Miscompensation ( $^{\circ}/\text{hr}$ )	Estimation Error ( $^{\circ}/\text{hr}$ )
System Level	A	-.006	.158	.015
	B	-.039	-.031	.009
	C	-.036	.115	.001
	D	.001	.000	-.001
System Not Level	A	-.013	.132	-.005
	B	-.063	-.058	.005
	C	-.336	-.200	.014/.041*
	D	.008	.018	.010

Table 3.9.3 SPC Estimation Errors with a Miscompensation of +0.15°/hr on Gyro A and a Miscompensation of -0.15°/hr on Gyro B.

	Gyro	Baseline Drift (°/hr)	Drift After Miscompensation (°/hr)	Estimation Error (°/hr)
System Level	A	-.006	.155	.011
	B	-.039	-.174	.015
	C	-.036	-.039	-.002
	D	.001	.000	-.001
System Not Level	A	-.013	.138	.002
	B	-.063	-.182	.031
	C	-.336	-.369	.033/.022*
	D	.008	.021	.013

Table 3.9.4 SPC Estimation Errors with a Miscompensation of -0.15°/hr on Gyro A and a Miscompensation of +0.15°/hr on Gyros B and C.

	Gyro	Baseline Drift (°/hr)	Drift After Miscompensation (°/hr)	Estimation Error (°/hr)
System Level	A	-.006	-.147	.009
	B	-.039	.125	.015
	C	-.036	.118	.003
	D	.001	-.003	-.003
System Not Level	A	-.013	-.173	-.039
	B	-.063	.097	.010
	C	-.336	-.231	-.045/.010*
	D	.008	.023	.015

Table 3.9.5 SPC Estimation Errors with a Miscompensation of +0.15°/hr on Gyro C and a Miscompensation of -0.15°/hr on Gyro D.

	Gyro	Baseline Drift (°/hr)	Drift After Miscompensation (°/hr)	Estimation Error (°/hr)
System Level	A	-.006	.008	.015
	B	-.039	-.028	.011
	C	-.036	.114	-.001
	D	.001	-.151	-.002
System Not Level	A	-.013	-.014	-.000
	B	-.063	-.035	.028
	C	-.336	-.217	-.031/.024*
	D	.008	-.130	.012

Table 3.9.6 SPC Estimation Errors with a Miscompensation of +0.030°/hr on Gyro E.

	Gyro	Baseline Drift (°/hr)	Drift After Miscompensation (°/hr)	Estimation Error (°/hr)
System Level	A	-.006	-.015	-.009
	B	-.039	-.054	-.015
	C	-.038	-.046	-.010
	D	.001	-.013	-.014
System Not Level	A	-.013	.040	-.027
	B	-.063	.053	.011
	C	-.336	.358	.022/.033*
	D	.008	.014	.006

Table 3.9.7 SPC Estimation Errors with a Miscompensation of +0.030°/hr on Gyro F.

	Gyro	Baseline Drift (°/hr)	Drift After Miscompensation (°/hr)	Estimation Error (°/hr)
System Level	A	-.006	-.035	-.028
	B	-.039	-.052	-.013
	C	-.036	-.092	-.056
	D	.001	.017	.017
System Not Level	A	-.013	-.053	-.050
	B	-.063	-.073	-.010
	C	-.336	-.405	-.069/.015*
	D	.008	.034	.026

Table 3.9.8 SPC Estimation Errors with a Miscompensation of +0.030°/hr on Gyros E and F.

	Gyro	Baseline Drift (°/hr)	Drift After Miscompensation (°/hr)	Estimation Error (°/hr)
System Level	A	.006	-.043	-.037
	B	.039	-.073	-.033
	C	.036	-.106	-.070
	D	.001	-.000	-.001
System Not Level	A	.013	-.068	-.055
	B	.063	-.077	-.014
	C	.336	-.378	-.042/.013*
	D	.008	.023	.015

3.9 Calculated East Axis Drifts Before  
and After Using Single Position Calibration Estimates

Using the above test results (where the C gyro estimation error has been corrected as shown) and Eqs. 3.45 and 3.51, the estimated east axis drift (for the calibration position #2) can be compared to the east axis drift expected after the single position calibration drift estimates are used to recompensate the drifts. Table 3.10 presents these calculated drifts for each test above (Tables 3.9.1 - 3.9.8).

Table 3.10 Calculated East Axis Drifts Cal. 2 Position  
 Before and After a Single Position Calibration

Test (section)	SYSTEM LEVEL		SYSTEM NOT LEVEL	
	Initial $\epsilon_{Y_B}$ ( $^{\circ}$ /hr)	After SPC $\epsilon_{Y_B}$ ( $^{\circ}$ /hr)	Initial $\epsilon_{Y_B}$ ( $^{\circ}$ /hr)	After SPC $\epsilon_{Y_B}$ ( $^{\circ}$ /hr)
(3.9.1)	.011	.006	.098	-.015
(3.9.2)	-.030	-.001	.078	-.015
(3.9.3)	.010	.002	.101	-.008
(3.9.4)	-.030	-.006	.063	.005
(3.9.5)	-.069	-.001	.029	-.011
(3.9.6)	.011	-.003	.116	-.026
*(3.9.7)	-.018	.069	.089	.039
(3.9.8)	-.019	.057	.105	-.002

\*Errors introduced into reference gyros E & F .

Note that in every case, except Tables 3.9.7 and 3.9.8 (system level), where errors are introduced into the E and F reference gyros, there is an improvement in east axis drift after calibration.

3.10 Data Taken with Oscillations About the Vertical Axis

To test the full single position calibration algorithm including the base-motion isolation characteristics, two tests were run (each with a duration of 80 minutes) with a 10 minute, 1/2 hz oscillation about the vertical table axis. In the first test, SIRU was kept level in the calibration position #2 and gyros A and B were each miscompensated by  $+0.150^{\circ}$ /hr. In the second test, SIRU was offset from the level calibration position #2 in exactly the same manner (described in Section 3.9) as was done for the tests with no base motion.

The test table on which SIRU is mounted has a steady-state bias drift superimposed on the sinusoidal oscillation when driven by a sinusoidal signal applied to the table servo. In order to eliminate this effect (which does not represent a realistic environment for prelaunch) the table was oscillated manually between two precise stops placed 20 minutes apart (in equivalent table rotation). This manual operation was performed by a continuous succession of different personnel during each 80 minute test. Thus the base motion in each test is somewhat random (having an approximate frequency of 1/2 Hz) and is never repeated exactly.

After the two tests described above were run, two additional 1/2 hour oscillatory runs were made (with SIRU level and then offset from level) in order to measure about each body axis, any drift that might be induced by the oscillations (due, for example, to imperfect dynamic compensation).

### 3.10.1 Oscillatory Test, +0.15°/hr Miscompensation, Gyros A & B

The base line drifts presented below were obtained in the absence of base motion (i.e. no oscillations about the vertical table axis). The drifts after miscompensation were estimated in the presence of the 10 minute oscillation described above (Section 3.10) and therefore, include dynamically induced drifts. These additional drifts add to the actual single position calibration errors. These total values are listed in Table 3.11 under the heading "Estimation Error".

Table 3.11 Oscillatory Test, +0.15 °/hr Miscompensation, Gyros A & B

Gyro	Baseline Drift No Base Motion (°/hr)	Drift With Miscompensation & Base Motion (°/hr)	Estimation Error (°/hr)	
System Level	A	.004	.092	-.062
	B	-.012	.015	-.019
	C*	.006	.780	.001
	D	.005	.016	.010
System Not Level	A	.006	.168	.012
	B	.000	.210	.060
	C*	.005	.011	.005
	D	.006	.048	.042

\*Erratic C gyro used in section 3.8 tests replaced.

### 3. 10. 2 Dynamically Induced Gyro Drifts

The drifts about each SIRU body axis induced by the 10 minute, 1/2 hz, vertical table oscillations in two separate 1/2 hour tests are presented in Table 3.12. These drifts were obtained by comparing the components of the attitude quaternion before and after the oscillation. The quaternion components were observed not to change in the absence of oscillations.

Table 3.12 Dynamically Induced Gyro Drifts

SIRU Body Axis	Dynamically Induced Drift (°/hr)	
	System Level	System Not Level
X	-.012	-.015
Y	-.002	-.036
Z	-.039	-.080

### 3. 10. 3 Analysis of SPC Oscillatory Tests

Equations 3.5-3.7 yield the following equations for body axis drifts in terms of the gyro drifts.

$$\epsilon_{X_B} = 0.263 (\epsilon_a - \epsilon_b) - 0.425 (\epsilon_c + \epsilon_d) \quad (3.54)$$

$$\epsilon_{Y_B} = 0.263 (\epsilon_d - \epsilon_c) + 0.425 (\epsilon_e - \epsilon_f) \quad (3.55)$$

$$\epsilon_{Z_B} = 0.425 (\epsilon_a + \epsilon_b) + 0.263 (\epsilon_e + \epsilon_f) \quad (3.56)$$

Examination of the data in Section 3.10.1 with SIRU positioned level indicates that the dynamically induced drift occurs mostly in the A and B gyros and that the C and D gyros have small dynamically induced drifts. Furthermore, let us assume that the drifts induced in gyros E and F are small when SIRU is level because the E and F gyros input axes are perpendicular to the axis of oscillation. With these assumptions we have for the oscillatory and level case:

$$\epsilon_c \approx \epsilon_d \approx \epsilon_f \approx \epsilon_e \approx 0 \quad (3.57)$$

We will then solve Eqs. 3.54-3.56 using the Table 3.12 data and see how well it compares with the single position calibration estimates for the level system presented

in Section 3.1. Substituting the appropriate data into Eqs. 3.54-3.56 along with Equation 3.57 yields:

$$-0.012 = 0.263 (\epsilon_a - \epsilon_b) \quad (3.58)$$

$$-0.039 = 0.425 (\epsilon_a + \epsilon_b) \quad (3.59)$$

Solving Eqs. 3.58 and 3.59 yields:

$$\epsilon_a = -0.069^\circ/\text{hr} \quad (3.60)$$

$$\epsilon_b = -0.021^\circ/\text{hr}$$

These values, Eqs. 3.60, compare very closely with the single position calibration values (system level) given in Table 3.11 ( $\tilde{\epsilon}_a = -0.062^\circ/\text{hr}$ ,  $\tilde{\epsilon}_b = -0.019^\circ/\text{hr}$ ) justifying the assumption that most of the single position calibration error (system level) in Table 3.11 is due to the dynamically induced drifts in the A and B gyros.

When the system is not level, there are dynamically induced drifts in the reference gyros E and F as well as in gyros A and B. This condition can be shown by comparing the results of calculations using Table 3.11 and Table 3.12 data for the system not level.

Assume that the dynamically induced drifts in A, B, C and D gyros for the system not level are given by the calculations performed in the level case (this is a reasonable assumption because a tilt of less than  $10^\circ$  will not appreciably affect the four gyros whose output axes are skewed from the vertical when the system is level). Subtracting these values from the estimation errors presented in Table 3.11, system not level, yields the "true" single position calibration estimation errors (due to the dynamically induced drifts in the E and F gyros). Table 3.13 presents these results.

Table 3.13 Single Position Calibration Estimation Errors

Gyro (System Not Level)	SPC Estimation Error ( $^\circ/\text{hr}$ ) (Section (3.1))	Dynamically Induced Drift ( $^\circ/\text{hr}$ )	"True" SPC Estimation Error ( $^\circ/\text{hr}$ )
A	.012	.069	.081
B	.060	.021	.080
C	.005	.000	.005
D	.042	.000	.042

Using Eqs. 3.41 and 3.42 and the true estimation errors given above yields the following values for the dynamically induced drifts in gyros E and F.

$$\epsilon_e = -0.080^\circ/\text{hr} \quad (3.61)$$

$$\epsilon_f = -0.020^\circ/\text{hr}$$

These values can be compared to corresponding values calculated using Table 3.12 data for the system not level. Examination of Eqs. 3.54-3.56 shows that the dynamically induced drift in gyros E and F as calculated above (Equation 3.61) can adequately account for the differences in the corresponding body axis drifts when the system is level and not level. The differences,  $\Delta\epsilon_{X_B}$ ,  $\Delta\epsilon_{Y_B}$  and  $\Delta\epsilon_{Z_B}$ , are calculated using Eqs. 3.54-3.56 and the computed dynamically induced drifts of gyros E and F (Eq. 3.61), as follows:

$$\begin{aligned} \Delta\epsilon_{X_B} &\approx 0 \\ \Delta\epsilon_{Y_B} &= 0.425 (\epsilon_e - \epsilon_f) = -0.026^\circ/\text{hr} \\ \Delta\epsilon_{Z_B} &= 0.263 (\epsilon_e + \epsilon_f) = -0.026^\circ/\text{hr} \end{aligned} \quad (3.62)$$

The corresponding differences calculated from Table 3.12 are as follows:

$$\begin{aligned} \Delta\epsilon_{X_B} &= -0.002^\circ/\text{hr} \\ \Delta\epsilon_{Y_B} &= -0.033^\circ/\text{hr} \\ \Delta\epsilon_{Z_B} &= -0.041^\circ/\text{hr} \end{aligned} \quad (3.63)$$

The values given by Eqs. 3.61 and 3.62 compare reasonably well (especially considering that the dynamic table input is somewhat random) and support the conclusion that when the system is not level the single position calibration results are affected considerably by the dynamically induced drifts in the E and F gyros (Eq. 3.61) as well as by the dynamically induced drifts in the A and B gyros (Eq. 3.60) that are present even when the system is level. It is believed that these dynamically induced drifts or sensitivity to oscillations are due to a characteristic of the H switch in the pulse torque-to-balance loop, especially in certain of the gyro modules. It has been determined that there is a difference in the transistor leakage current dependent on the residual polarity of the switch at the conclusion of a torquing pulse. The effect is to produce a bias shift when torquing continuously with the residual polarity opposite to that which was present during calibration. For oscillatory inputs a bias shift would always exist equivalent to the average difference. The effect of the phenomenon is being reduced (1) by selection of H switches to eliminate switches showing a difference greater than a  $0.075^\circ/\text{hr}$  equivalent leakage unbalance, and (2) by modifying the system compensation program and computer interface so that a separate accumulation of plus and minus  $\Delta\theta$  pulses in

each input/output iteration is maintained to enable tracking of the individual polarity state of each switch. This knowledge will permit implementation of a precise software compensation routine for the dual bias drift magnitudes.

### 3.11 Software Memory and Timing Requirements

The single position calibration program software requirements on the Honeywell DDP516 computer are as follows:

Memory:	3731 words
Timing Requirements:	7.032 ms used per update
Update Rate:	once per second
Machine Time for Attitude Update:	35% (50 updates per sec)

Note: no attempt was made to minimize the number of words in memory and the timing when programming.

Appendix A3  
Proposed New Vertical Drift Estimation Procedure

A3.0 Introduction

This appendix presents a theoretical alternative to the vertical drift estimation procedure presently used in the SIRU single position calibration algorithm. This alternative procedure makes the vertical drift estimation completely independent of base motion of any frequency having a non-zero mean. The present method works well with zero mean base motion having frequencies greater than  $10^{-3}$  Hz. However, the present method yields the "vertical" body axis drift (Z body axis) whereas the method proposed here estimates the vertical drift in the navigational frame. Hence the single position calibration equations presently in use would have to be modified to those presented in Section A3.2.

A3.1 Proposed Method

Two identical attitude algorithms are to be maintained in the full leveling and gyrocompassing modes. At the initiation of the vertical drift estimation, one of the algorithms is changed to a free azimuth mode with leveling still maintained. The azimuth equation for this mode is given by<sup>2</sup>.

$$\dot{\phi}_{D_2} \cong -d_D, \quad \phi_E \cong \phi_N \cong 0 \quad (A3.0)$$

Here  $\phi_N$ ,  $\phi_E$ ,  $\phi_{D_2}$  are the north, east, and down misalignment angles respectively,  $d_D$  is the vertical drift.  $\phi_E$  and  $\phi_N$  are close to zero because the leveling mode is still present. The other attitude algorithm has a fixed azimuth error which we denote by  $\phi_{D_1}$ . The solution to Eq. A3.0 is given by:

$$\phi_{D_2} = \phi_{D_1} - d_D t \quad (A3.1)$$

Equation A 3.1 shows that if we can measure the difference,  $\phi_{D_2} - \phi_{D_1}$ , we can derive an estimate of the vertical drift that is completely independent of base motion. That is:

$$d_D = \frac{-(\phi_{D_2} - \phi_{D_1})}{t} \quad (A3.2)$$

This difference is obtained as follows. Denote  $q_b^c1$  as the quaternion obtained from the algorithm with full gyrocompassing and  $q_b^c2$  as the quaternion obtained from the free azimuth algorithm.

Then:

$$q_b^{c_1} = q_n^{c_1} q_b^n \quad (A3.3)$$

$$q_b^{c_2} = q_n^{c_2} q_b^n \quad (A3.4)$$

$$\begin{aligned} q_b^{c_1} q_b^{c_2} &= q_n^{c_1} q_b^n q_n^{c_2} q_b^n = q_n^{c_1} q_n^{c_2} q_b^{2n} \\ &= \left[ 1 - \frac{\phi D_1}{2} \right] \left[ 1 + \frac{\phi D_2}{2} \right] \\ &\approx 1 + \frac{\phi D_2 - \phi D_1}{2} = 1 + \frac{-d_D t}{2} \end{aligned} \quad (A3.5)$$

Here  $c_1, c_2$  denote the respective computational frames of the two algorithms. The body and local navigational frames are denoted by  $b$  and  $n$  respectively.

The error in estimating  $d_D$  is caused by the "noise" in the gyrocompassing algorithm. Reference 3 data indicates a maximum gyrocompassing standard deviation of 0.2 mr. If  $t$  in Eq. A3.5 is set to 1.5 hour the error in estimating  $d_D$  will be given by:

$$\frac{0.2 \text{ mr}}{1.5 \text{ hr}} \times \frac{1}{17.4 \text{ mr/deg}} = .008 \text{ deg/hr}$$

without any filtering. Filtering, if used, can be done in conjunction with the above algorithm.

### A3.2 Estimates to be Used if New Filtering Method is Implemented

If the filtering method presented in this appendix were implemented, the following single position calibration estimates would yield more accurate results.

$C_{31}, C_{32}, C_{33}$  are the elements of the direction cosine matrix  $C_B^C$ :

$$\alpha_2 \stackrel{\Delta}{=} -sC_{33} + cC_{31} \quad (\text{A3.6})$$

$$\alpha_3 \stackrel{\Delta}{=} -cC_{33} - sC_{32} \quad (\text{A3.7})$$

$$M = \frac{V_1}{2c} + \frac{V_2}{2s} - \frac{sV_3}{2c^2} \quad (\text{A3.8})$$

$$\hat{\epsilon}_D = c s M + \frac{c}{C_{33}} \left[ \frac{\alpha_2 V_2}{2s} + \frac{\alpha_3 V_3}{2c} - d_{Z_N} \right] \quad (\text{A3.9})$$

$$\hat{\epsilon}_A = M - \frac{s}{c} \hat{\epsilon}_D \quad (\text{A3.10})$$

$$\hat{\epsilon}_B = \frac{V_2}{s} - \hat{\epsilon}_A \quad (\text{A3.11})$$

$$\hat{\epsilon}_C = \frac{V_3}{c} + \hat{\epsilon}_D \quad (\text{A3.12})$$

$$\hat{\epsilon}_E = 0 \quad (\text{A3.13})$$

$$\hat{\epsilon}_F = 0 \quad (\text{A3.14})$$

Appendix B3  
X-Body Axis Drift Filter

In order to determine the proper filtering we assume a sinusoidal vehicle sway (with zero mean) having a  $0.5^\circ$  amplitude. The sway is about the horizontal axes. The maximum sway that will be seen about the vertical computational axis is given by:

$$\left[ \frac{W_{nb}^b}{X_B} \right] = (2\pi) \sqrt{2} (0.5) \frac{\theta}{57.3} \sin 2\pi ft \quad (B3.0)$$

where  $\theta$  is the tilt (in degrees) of the  $X_B$  axis from the vertical axis  $X_N$  and  $\left[ \frac{W_{nb}^b}{X_B} \right]$  is in deg/sec.

For a tilt of  $5^\circ$ , the base motion about  $X_B$  to be filtered is given by:

$$\left[ \frac{W_{nb}^b}{X_B} \right] = (8.7 \times 10^4) f \sin 2\pi ft \quad (B3.1)$$

where  $\left[ \frac{W_{nb}^b}{X_B} \right]$  is expressed in  $^\circ/\text{hr}$  and the frequency,  $f$ , is in Hz.

A convenient filter to use for relatively high frequencies is given by the following La Place transform.

$$\frac{\text{Output}}{\text{Input}} = \frac{f_0^2}{\left(\frac{s}{2\pi} + f_0\right)^2} \quad (B3.2)$$

where the frequency,  $f_0$ , is a filter parameter.

The approximate settling time for the above filter is given by the following:

$$\text{Settling Time} = T_s = \frac{6}{2\pi f_0} \approx \frac{0.96}{f_0} \text{ seconds} \quad (B3.3)$$

The amplitude of the noise that is attenuated by the filter is given by:

$$\text{Residual Noise Amplitude for Filter} = \frac{(.13 \times 10^4) f f_0^2}{f^2 + f_0^2} \text{ }^\circ/\text{hr} \quad (B3.4)$$

Figure B3.1 is a plot of the residual noise amplitude vs. frequency for two different values of  $f_0$  corresponding to settling times of 1/2 hour and 1.5 hours (i.e.  $2\pi f_0 = .003$  and  $.001$ , respectively).

PRECEDING PAGE BLANK NOT FILMED

C-2

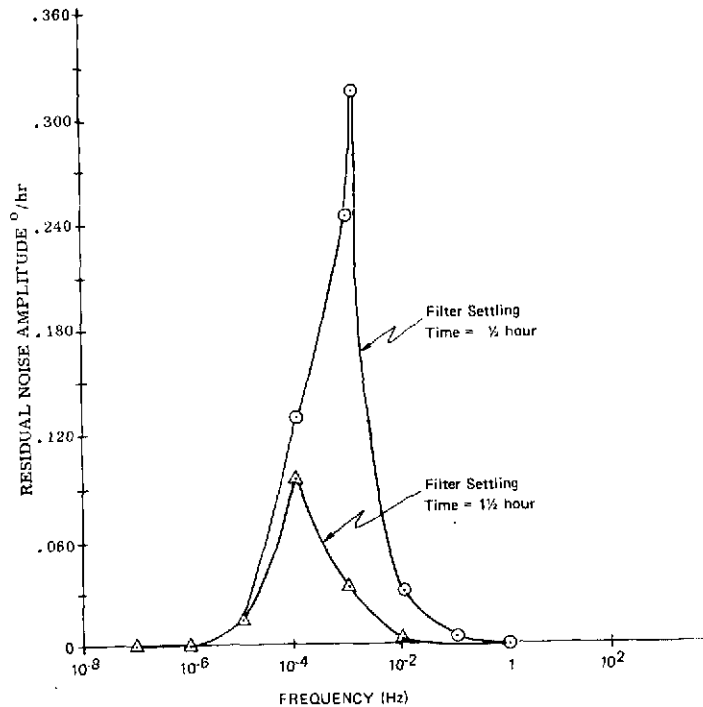


Fig. B3.1 Residual Vertical Noise Amplitude vs. Frequency (System Tilt =  $5^{\circ}$ ) for Eq. B3.2 Filter

It is seen that for the 1/2 hour filter, most of the noise above 0.1 Hz and below  $10^{-5}$  Hz is removed. This filter response can be modified so that the noise residual between  $10^{-1}$  and  $10^{-5}$  Hz is further reduced by averaging the output of the filter, Eq. B3.2 (after it has settled out). Equation B3.5 yields the residual noise amplitude obtained by averaging over a time period of 1/2 hour.

$$\begin{array}{l}
 \text{Residual Noise} \\
 \text{Amplitude Obtained} \\
 \text{by Time} \\
 \text{Averaging} \\
 \text{Filter Output} \\
 \text{for 1/2 Hour}
 \end{array}
 = \frac{.12 f_0^2}{f^2 + f_0^2} \text{ o/hr} \quad (\text{B3.5})$$

Figure B3.2 is a plot of the residual noise amplitude vs. frequency where  $2 f_0 = .003$  (i.e., Eq. B3.1 filter settling time is 1/2 hour). The averaging starts when the filter has settled out (this takes 1/2 hour). Hence, the total filtering time is 1 hour. Comparison of Fig. B3.2 with Fig. B3.1 shows that for frequencies above  $10^{-3}$  Hz, averaging the output of a 1/2 hour filter over a period of 1/2 hour yields lower residual noise amplitudes than the filter having a 1-1/2 hour settling time with no averaging. Since most of the base motion is concentrated at frequencies above  $10^{-2}$  hz, the filtering arrangement represented by the Fig. B3.2 plot was chosen. The following is, therefore, the algorithm that will be used in estimating the drift,  $d_{XB}$  (expressed as a computer program).

$$KF = 0.003$$

$$\text{DRIFT1} = W_{X_B} - C_{31}W_h - C_{33}W_v$$

$$\text{DRIFT2} = (1-KF) \text{DRIFT2} + (KF) \text{DRIFT1}$$

$$\text{DRIFT3} = (1-KF) \text{DRIFT3} + (KF) \text{DRIFT2}$$

After 1/2 hour operation of the above we begin to average DRIFT3 for 1/2 hour so that :

$$d_{X_B} = \frac{1}{T} \sum_0^T \text{DRIFT3}$$

where:

$$T = 1800 \text{ sec.}$$

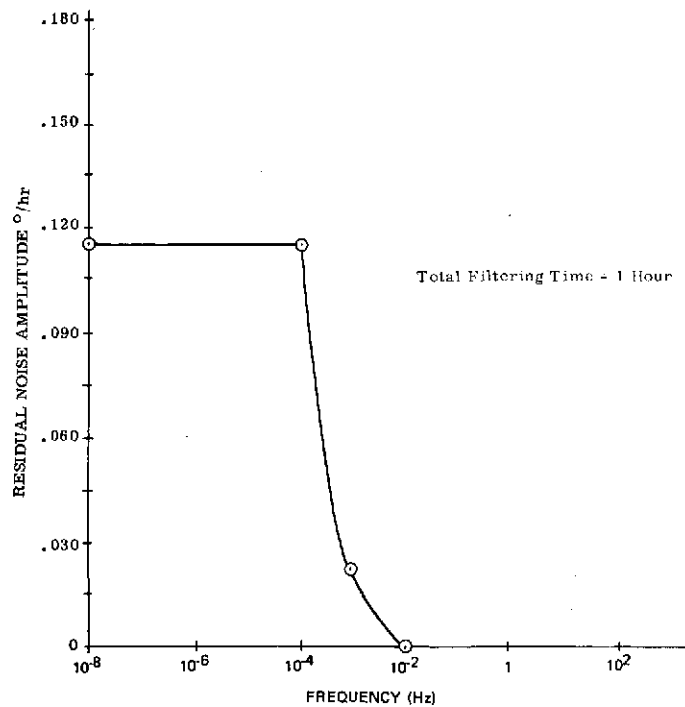


Fig. B3.2 Residual Vertical Noise Amplitude vs. Frequency (System Tilt = 5°) for Eq. B3.2 Filter Output Averaged 1/2 Hour Where Eq. B3.2 Filter has 1/2 hour Settling Time

Attitude Algorithm Small Angle Error Equations<sup>4</sup>

This chapter derives the quaternion algorithm misalignment angle differential equations. These differential equations will be needed in the presentation of SIRU utilization alignment and land navigation algorithm developments in the next two chapters.

The equations for the small angle deviations of the computed frame from the navigation frame for an earth fixed system base are derived from the quaternion differential equation. These equations turn out to be the same as those derived from either the direction cosine matrix differential equation for strapdown systems or the platform misalignment angle equations for gimballed systems.

Figure 4.0 is a block diagram showing the quaternion differential equation, with earth-rate compensation (since we wish to align with the local north, east and down coordinate system) and the algorithm command signal.

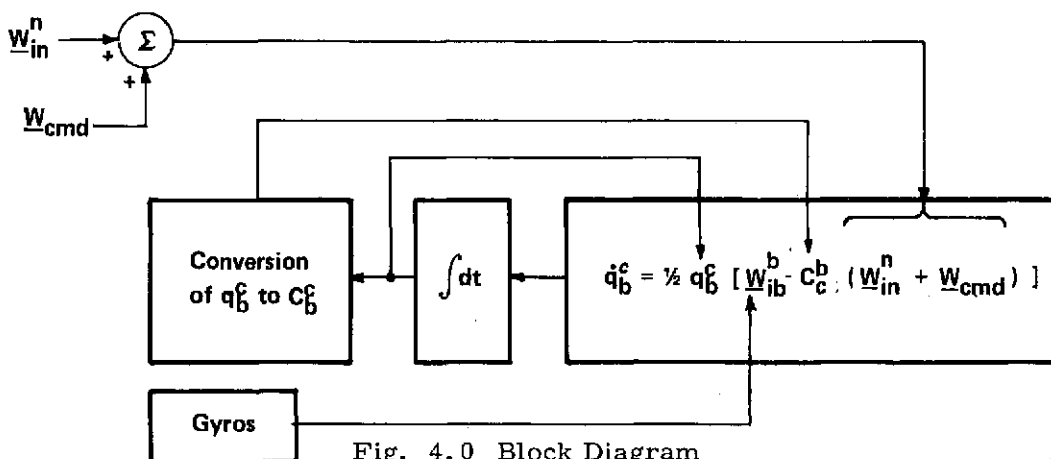


Fig. 4.0 Block Diagram

- $C_c^b$  = Direction cosine matrix going from the computed frame to the body frame.
- $W_{ib}^b$  = Angular rate vector of body with respect to inertial space in body frame coordinates including gyro drift.
- $W_{cmd}$  = command signal used to drive computed frame,  $C_c^b$ , into alignment with navigational frame,  $n$ .
- $q_b^c$  = quaternion giving attitude of computed frame with respect to the body frame.

PRECEDING PAGE BLANK NOT FILMED

$$\underline{W}_{in}^n = \begin{bmatrix} W_{ie} \cos L \\ 0 \\ -W_{ie} \sin L \end{bmatrix} = \begin{bmatrix} W_h \\ 0 \\ W_v \end{bmatrix} = \text{angular rate of navigational frame (north, east, down) with respect to inertial space in navigational frame coordinates}$$

$W_{ie}$  = earth rate,  $L$  = latitude

The derivation of the differential equations for the misalignment angles is as follows:

$$\dot{q}_b^c = \frac{1}{2} q_b^c (\underline{W}_{ib'}^b - C_c^b (\underline{W}_{in}^n + \underline{W}_{cmd}^n)) \quad (4.1)$$

$$\underline{W}_{ib'}^b = \underline{W}_{in}^b + \underline{W}_{nb}^b + \underline{d}^b \quad (4.2)$$

$\underline{W}_{nb}^b$  = angular rate of body with respect to navigation frame in body coordinates.

$\underline{d}^b$  = gyro drift for the equivalent north, east, and down gyros.

For  $C_b^c$  close to  $C_b^n$  we have:

$$C_n^c = \underline{I} + \underline{\Phi} \quad (4.3)$$

where:

$$\underline{\Phi} = \begin{bmatrix} 0 & \phi_D & -\phi_E \\ -\phi_D & 0 & \phi_N \\ \phi_E & -\phi_N & 0 \end{bmatrix} \quad (4.4)$$

where  $\underline{\Phi}$  is the anti-symmetric matrix composed of the small misalignment error angles  $\phi_N, \phi_E, \phi_D$  about the north, east, and down axes respectively.

The inverse of  $C_n^c$  is given approximately by:

$$C_c^n = \underline{I} - \underline{\Phi} \quad (4.5)$$

Substituting Eq. 4.5 into the following yields Eq. 4.7.

$$\underline{W}_{in}^c = C_n^c \underline{W}_{in}^n \quad (4.6)$$

$$\underline{W}_{in}^n = \underline{W}_{in}^c - \underline{\Phi} \underline{W}_{in}^c \quad (4.7)$$

Therefore:

$$\begin{aligned} C_c^b \underline{W}_{in}^n &= C_c^b \underline{W}_{in}^c - C_c^b \underline{\Phi} C_b^c C_c^b \underline{W}_{in}^c \\ &= \underline{W}_{in}^b - \underline{B} \underline{W}_{in}^b \end{aligned} \quad (4.8)$$

where:

$$\underline{B} = C_c^b \underline{\Phi} C_b^c \quad (4.9)$$

Substituting Eq. 4.2 and Eq. 4.8 into Eq. 4.1 yields:

$$\dot{q}_b^c = \frac{1}{2} q_b^c (\underline{W}_{nb}^b + \underline{d}^b + \underline{B} \underline{W}_{in}^b - C_c^b \underline{W}_{cmd}^b) \quad (4.10)$$

Since quaternion multiplication is associative we have:

$$q_b^c = q_n^c q_b^n \quad (4.11)$$

$$\dot{q}_b^c = \dot{q}_n^c q_b^n + q_n^c \dot{q}_b^n \quad (4.12)$$

But:

$$\dot{q}_b^n = \frac{1}{2} q_b^n \underline{W}_{nb}^b \quad (4.13)$$

Substituting Eq. 4.13 in Eq. 4.12 and using Eq. 4.10 in the resulting equation yields:

$$\begin{aligned} \dot{q}_n^c q_b^n &= \frac{1}{2} q_b^c \left[ \underline{d}^b + \underline{B} \underline{W}_{in}^b - C_c^b \underline{W}_{cmd}^b \right] \\ \dot{q}_n^c &= \frac{1}{2} q_b^c \left[ \underline{d}^b + \underline{B} \underline{W}_{in}^b - C_c^b \underline{W}_{cmd}^b \right] q_n^b \\ &= \frac{1}{2} q_n^c q_b^n \left[ \underline{d}^b + \underline{B} \underline{W}_{in}^b - C_c^b \underline{W}_{cmd}^b \right] q_n^b \end{aligned} \quad (4.14)$$

The second term in the bracket of Eq. 4.14 when fully expanded corresponds to:

$$q_b^n \underline{B} W_{in}^b q_n^b = \left[ q_b^n \underline{B} q_n^b \right] \left[ q_b^n \underline{W}_{in}^b q_n^b \right] \quad (4.15)$$

from Eq. 4.9 one notes that:

$$\underline{\Phi} = q_b^c \underline{B} q_c^b = q_n^c q_b^n \underline{B} q_n^b q_c^n \quad (4.16)$$

$q_c^n$  is approximately a unit quaternion, because there are only small angle errors between the navigational and computational frame. Therefore:

$$\underline{\Phi} = q_n^b \underline{B} q_b^n \quad (4.17)$$

The second half of Eq. 4.15 is simply a coordinate transformation, ie:

$$q_b^n \underline{W}_{in}^b q_n^b = \underline{W}_{in}^n \quad (4.18)$$

Equation 4.14, therefore, reduces to:

$$\begin{aligned} \dot{q}_n^c &\cong \frac{1}{2} q_n^c \left[ \underline{d}^n + \underline{\Phi} \underline{W}_{in}^n - q_b^n C_c^b \underline{W}_{cmd} q_n^b \right] \\ &\cong \frac{1}{2} q_n^c \left[ \underline{d}^n + \underline{\Phi} \underline{W}_{in}^n - C_b^n C_c^b \underline{W}_{cmd} \right] \\ &\cong \frac{1}{2} q_n^c \left[ \underline{d}^n + \underline{\Phi} \underline{W}_{in}^n - C_c^n \underline{W}_{cmd} \right] \end{aligned} \quad (4.19)$$

Equation 4.19 can be further reduced by noting that the quaternion coordinate transformation,  $q_b^n$ -Vector- $q_n^b$ , is equivalent to the direction cosine transformation:

$$C_b^n \left[ C_c^b \underline{W}_{cmd} \right] = C_c^n \underline{W}_{cmd} \quad (4.20)$$

Thus, using Eq. 4.5 and the assumption that  $\underline{W}_{cmd}$  will be directly proportional to small angles, we have:

$$\begin{aligned} C_c^n \underline{W}_{cmd} &\cong \underline{W}_{cmd} - \underline{\Phi} \underline{W}_{cmd} \\ &\cong \underline{W}_{cmd} \end{aligned} \quad (4.21)$$

since all products of small angles are neglected.

Substituting this approximation into Eq. 4.19 yields:

$$\dot{q}_n^c = \frac{1}{2} q_n^c \left[ \underline{d}^n + \underline{\Phi} \underline{W}_{in}^n - \underline{W}_{cmd} \right] \quad (4.22)$$

It can be verified by direct calculations that, if all products of small angles are ignored, the quaternion transformation  $q_n^c$  corresponding to  $C_n^c$  (Eqs. 4.3 and 4.4) is:

$$q_n^c = 1 - \begin{bmatrix} \frac{\phi_N}{2} \\ \frac{\phi_E}{2} \\ \frac{\phi_D}{2} \end{bmatrix} = 1 - [\phi] \quad (4.23)$$

Then:

$$\dot{q}_n^c = - \begin{bmatrix} \dot{\phi}_N \\ \dot{\phi}_E \\ \dot{\phi}_D \end{bmatrix} \quad (4.24)$$

Substituting Eq. 4.24 and Eq. 4.23 into Eq. 4.22 and again neglecting the products of small angles yields:

$$- \begin{bmatrix} \dot{\phi}_N \\ \dot{\phi}_E \\ \dot{\phi}_D \end{bmatrix} \cong \underline{d}^n + \underline{\Phi} \underline{W}_{in}^n - \underline{W}_{cmd} \quad (4.25)$$

or:

$$\dot{\underline{\phi}} = \underline{\Omega} \underline{\phi} + \underline{W}_{cmd} - \underline{d}^n \quad (4.26)$$

where:

$$\underline{\dot{\phi}} = \begin{bmatrix} \dot{\phi}_N \\ \dot{\phi}_E \\ \dot{\phi}_D \end{bmatrix}, \underline{\Omega} = \begin{bmatrix} 0 & W_v & 0 \\ -W_v & 0 & W_h \\ 0 & -W_h & 0 \end{bmatrix} \quad (4.27)$$

Equation 4.26 can be rewritten as follows:

$$\begin{bmatrix} \dot{\phi}_N \\ \dot{\phi}_E \\ \dot{\phi}_D \end{bmatrix} = \begin{bmatrix} W_v \phi_E - d_N \\ -W_v \phi_N + W_h \phi_D - d_E \\ -W_h \phi_E - d_D \end{bmatrix} + \underline{W}_{cmd} \quad (4.28)$$

These derivation results, Eqs. 4.26 through 4.28, are significant in that the expression is a general purpose differential equation that represents the error propagation,  $\phi$ , of the computational local vertical navigational coordinate frame with respect to the true reference navigational frame. From Eq. 4.26, one notes that the error rate of the computational frame corresponds to the errors associated with the gyro drift as projected in the navigational frame, ( $\underline{d}^n$ ), the alignment errors as they reflect in the miscompensation of the earth rate terms,  $\underline{\Omega}\phi$ , and lastly the command rates,  $\underline{W}_{cmd}$ , are applied computationally to maintain alignment between the computational and the navigational frame. In the gyrocompassing mode,  $\underline{W}_{cmd}$  is derived computationally from the leveling and equivalent N-S processed accelerometer data. In the local vertical mode, the equivalent level accelerometer data, integrated and scaled, provides the command rate. This differential equation is used as the base for the error equation derivation developed for the alignment function described in Chapter 5, Section 5.10.

## Chapter 5

### SIRU Self-Alignment

#### 5.0 Introduction

SIRU self-alignment (to the local navigational frame) occurs in two stages, coarse alignment followed by fine alignment. Alignment in the strapdown mechanization is a computational function wherein the body frame orientation with respect to the local vertical frame, level and azimuth is established and maintained in the computer. The instrumentation data,  $\Delta\theta$  &  $\Delta V$  s, that indicate the earth rate and gravity vector in the body frame are computationally manipulated to establish the local vertical reference frame. In the coarse alignment phase, the level orientation reference is established using the indicated accelerometer data, and the direction of the horizontal component of earth rate is roughly determined by computing the rate of change of the gravity vector in an inertial coordinate frame. In the fine alignment phase that follows, the direction of the earth rate vector is precisely determined by computational implementation of conventional gyrocompassing concepts. The coarse alignment settling time, immunity to noise, and algorithm gain settings are independent of the initial offset angles (for angles ranging over  $\pm 90^\circ$ ). In actual system tests, coarse alignment maximum errors were less than  $5^\circ$ , and in every orientation representative of actual system operation, accuracy was better than  $1^\circ$  (Data is presented in Section 5.4 and 5.5. of this chapter). Fine alignment accuracies (starting from initial angles of  $2^\circ$ ) are better than 1 milliradian. Settling time for fine alignment is approximately 15 minutes, and for coarse alignment is 260 seconds (4.3 minutes). The details of coarse and fine alignment design, operation and performance are provided in the following sections. Note that in this chapter, the X, Y, Z body axes in the theoretical discussion are expected to coincide with the north, east, down axes when the SIRU test table is aligned to the local navigation frame. In Chapter 3 and in obtaining the data in this chapter, calibration position #2 (where the X body axis coincides with the down axis, the Z body axis coincides with the south axis and the SIRU test table is aligned to the local navigation frame) was used.

#### 5.1 Coarse Alignment-Introduction

The coarse alignment method presented here derives a base to calculated frame direction cosine matrix,  $C_b^c$ , that is within a few degrees of the true base to navigation frame matrix,  $C_b^n$ . The method consists of a leveling stage followed by an azimuth alignment of the leveled frame. Leveling uses the outputs of the accelerometers. Azimuth alignment makes use of the rate of change of gravity

(i.e. the accelerometer outputs) in an inertial frame. This method of azimuth alignment is much less sensitive to the effects of launch vehicle sway than any method using the earth rate vector derived directly from the gyros.

## 5.2 Coarse Alignment Leveling Procedure<sup>5</sup>

The gravity vector in the navigation frame is given by:

$$\underline{g}^n = \begin{bmatrix} 0 \\ 0 \\ g \end{bmatrix}, \quad g = 32.2 \text{ ft/sec}^2 \quad (5.1)$$

The base to navigational frame direction cosine matrix is given by:

$$C_n^b = \begin{bmatrix} C_{11} & C_{12} & C_{13} \\ C_{21} & C_{22} & C_{23} \\ C_{31} & C_{32} & C_{33} \end{bmatrix} \quad (5.2)$$

The gravity vector in the body frame is, therefore, given by:

$$\underline{g}^b = C_n^b \underline{g}^n = \begin{bmatrix} C_{11} & C_{12} & C_{13} \\ C_{21} & C_{22} & C_{23} \\ C_{31} & C_{32} & C_{33} \end{bmatrix} \begin{bmatrix} 0 \\ 0 \\ g \end{bmatrix} = \begin{bmatrix} C_{13} g \\ C_{23} g \\ C_{33} g \end{bmatrix} \quad (5.3)$$

Note that  $C_n^b$  is orthonormal. The direction of the local vertical in the body frame is:

$$\frac{\underline{g}^b}{\|\underline{g}^b\|} = \frac{1}{g} \begin{bmatrix} C_{13} \\ C_{23} \\ C_{33} \end{bmatrix} = \begin{bmatrix} a_X \\ a_Y \\ a_Z \end{bmatrix} \frac{1}{g} \quad (5.4)$$

where  $a_X, a_Y, a_Z$  are the filtered accelerometer readings.

The rotational axis about which the body frame is to be rotated into coincidence with the level frame is obtained from the cross product of the body unit vector in the  $Z_b$  direction with the gravity vector in body coordinates (See Fig. 5.1). Thus:

$$\mathbf{i}_{lev}^b \sin \zeta = \mathbf{i}_{Z_b} \times \mathbf{i}_g^b = \begin{bmatrix} 0 \\ 0 \\ 1 \end{bmatrix} \times \begin{bmatrix} C_{13} \\ C_{23} \\ C_{33} \end{bmatrix} = \begin{bmatrix} -C_{23} \\ C_{13} \\ 0 \end{bmatrix} \quad (5.5)$$

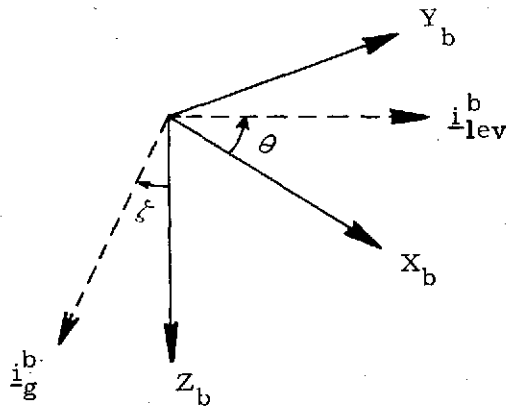


Fig. 5.1 Coarse Leveling Vectors

$\sin \zeta$  is the magnitude of the resultant cross product vector and is given by:

$$\sin \zeta = \sqrt{C_{23}^2 + C_{13}^2} = \sqrt{\left(\frac{a_Y}{g}\right)^2 + \left(\frac{a_X}{g}\right)^2} \quad (5.6)$$

Also,

$$\cos \zeta = C_{33} = \frac{a_Z}{g} \quad (5.7)$$

Since:

$$C_{13}^2 + C_{23}^2 + C_{33}^2 = 1 \quad (5.8)$$

Since  $i_{lev}^b$  is perpendicular to  $\hat{z}_b$ , it lies in the  $X_b, Y_b$  plane as shown in Fig. 5.1. Therefore:

$$i_{lev}^b = \begin{bmatrix} \cos \theta \\ \sin \theta \\ 0 \end{bmatrix} = \frac{1}{\sin \zeta} \begin{bmatrix} -C_{23} \\ C_{13} \\ 0 \end{bmatrix} \quad (5.9)$$

The body frame is transformed into the leveled frame by rotating it about the  $i_{lev}^b$  axis through an angle of  $\zeta$ . The quaternion corresponding to this rotation is given by:

$$q_B^{lev} = \cos \left( \frac{\zeta}{2} \right) - \sin \left( \frac{\zeta}{2} \right) \begin{bmatrix} \sin \theta \\ \cos \theta \\ 0 \end{bmatrix} \quad (5.10)$$

or, equivalently:

$$q_B^{lev} = \left( \frac{1 + \frac{a_Z}{g}}{2} \right)^{1/2} - \left( \frac{1 - \frac{a_Z}{g}}{2} \right)^{1/2} \begin{bmatrix} -\frac{a_Y}{(a_X^2 + a_Y^2)^{1/2}} \\ \frac{a_X}{(a_X^2 + a_Y^2)^{1/2}} \\ 0 \end{bmatrix} \quad (5.11)$$

using Eqs. 5.6 through 5.10 and the following identities:

$$\cos \left( \frac{\zeta}{2} \right) = \sqrt{\frac{1 + \frac{a_Z}{g}}{2}} \quad (5.12)$$

$$\sin \left( \frac{\zeta}{2} \right) = \sqrt{\frac{1 - \frac{a_Z}{g}}{2}} \quad (5.13)$$

The acceleration values  $a_X, a_Y, a_Z$  are obtained by averaging the velocity output of the accelerometers over a one minute period. Thus:

$$a_X = \frac{1}{60} \sum_{t=1}^{60} \Delta V_X(t) \quad (5.14)$$

and similarly for  $a_Y$  and  $a_Z$ .

The standard routines used with the quaternion algorithm converts  $q_B^{lev}$  to the equivalent direction cosine matrix,  $C_B^{lev}$ .

### 5.3 Azimuth Coarse Alignment Procedure

The quaternion,  $q_B^{lev}$ , obtained from the leveling procedure is inertially stabilized by inserting  $q_B^{lev}$  as the initial value in the proper quaternion attitude algorithm. This algorithm can be represented by the following differential equation.

$$\begin{aligned} \dot{q}_b^i(t) &= \frac{1}{2} q_b^i(t) \underline{W}_{ib} \\ q_b^i(0) &= q_B^{lev} \end{aligned} \quad (5.15)$$

where  $\underline{W}_{ib}$  is the base to inertial velocity obtained from the gyros.

Acceleration is measured in an inertial frame that is initially roughly level. Figure 5.2 shows the derivative of acceleration along each axis of an inertial frame that is perfectly level and rotated from the local navigational frame by an azimuth angle,  $A_Z$ .

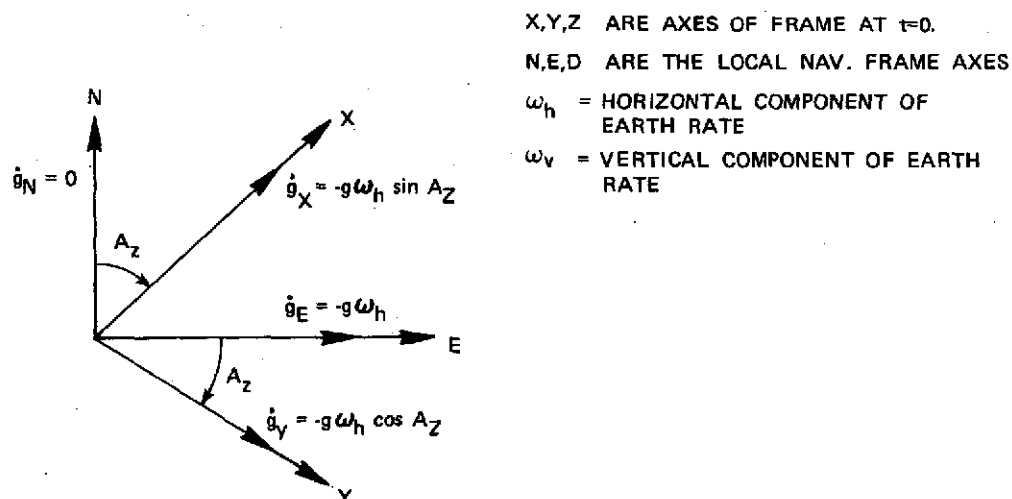


Fig. 5.2 Rotation of Level from Navigational Frame.

However, the inertial frame is initially not perfectly level due to the leveling errors from the leveling stage. Also, the frame would obviously not remain level, even if it was so initially, due to the rotation of the local navigation frame in inertial space.

The small angles (on the order of a degree),  $\phi_X, \phi_Y, \phi_Z$ , designate the rotations of the true inertial frame with respect to the level frame illustrated in Fig. 5.2.

Thus:

$$\begin{bmatrix} \dot{\phi}_X \\ \dot{\phi}_Y \\ \dot{\phi}_Z \end{bmatrix} = - \begin{bmatrix} 1 & \phi_Z & -\phi_Y \\ -\phi_Z & 1 & \phi_X \\ \phi_Y & -\phi_X & 1 \end{bmatrix} \begin{bmatrix} W_h \cos A_Z \\ -W_h \sin A_Z \\ W_v \end{bmatrix} \quad (5.16)$$

$$\begin{bmatrix} \dot{\phi}_X \\ \dot{\phi}_Y \\ \dot{\phi}_Z \end{bmatrix} = \begin{bmatrix} -W_h \cos A_Z + \phi_Z W_h \sin A_Z + \phi_Y W_v \\ \phi_Z W_h \cos A_Z + W_h \sin A_Z - \phi_X W_v \\ -\phi_Y W_h - \phi_X W_h \sin A_Z - W_v \end{bmatrix} \quad (5.17)$$

Since  $\phi_X, \phi_Y, \phi_Z$  are small angles (Fig. 5.2), we note that:

$$-W_h \cos A_Z + \phi_Z W_h \sin A_Z + \phi_Y W_v \cong -W_h \cos A_Z \quad (5.18)$$

$$-W_v - \phi_X W_h \sin A_Z - \phi_Y W_h \cong -W_v \quad (5.19)$$

Thus, substituting these approximations Eq. 5.18 and Eq. 5.19 in Eq. 5.17 we obtain:

$$\begin{aligned} \dot{\phi}_X &\cong -W_h \cos A_Z \\ \dot{\phi}_Y &\cong W_h \sin A_Z + \phi_Z W_h \cos A_Z - \phi_X W_v \\ \dot{\phi}_Z &\cong -W_v \end{aligned} \quad (5.20)$$

From Eq. 5.20 we obtain:

$$\begin{aligned} \phi_X(t) &= \phi_X^{\check{}}(0) - W_h (\cos A_Z)t \\ \phi_Y(t) &= (W_h \sin A_Z - \phi_X(0)W_v)t + \phi_Y(0) \\ \phi_Z(t) &= -W_v t, \\ (\phi_Z(0) \text{ is absorbed by } A_Z) \end{aligned} \quad (5.21)$$

The accelerations along the X and Y axes are given by:

$$\begin{aligned} f_X &= -\phi_Y(t)g \\ f_Y &= \phi_X(t)g \end{aligned} \quad (5.22)$$

Thus:

$$\begin{aligned} f_X &= (-W_h g \sin A_Z + \phi_X(0)gW_v)t - \phi_Y(0)g \\ f_Y &= (-W_h g \cos A_Z)t + \phi_X(0)g \end{aligned} \quad (5.23)$$

The velocities are given by:

$$\begin{aligned} V_X &= -\phi_Y(0)gt + (-W_h g \sin A_Z + \phi_X(0)gW_v)\frac{t^2}{2} \\ V_Y &= \phi_X(0)gt + (-W_h g \cos A_Z)\frac{t^2}{2} \end{aligned} \quad (5.24)$$

$V_X(0) = V_Y(0) = 0$ , where noise is neglected for the moment.

A least squares filter<sup>6</sup> is used to extract the coefficients of the parabolic terms in Eq. 5.24 in order to obtain the desired azimuth information.

Letting  $a_X$  and  $a_Y$  and  $b_X$  and  $b_Y$  correspond to the linear and parabolic coefficients of Eq. 5.24 and adding noise, the equation is rewritten as:

$$V_X = a_X t + b_X t^2 + \text{noise}_X \quad (5.25)$$

$$V_Y = a_Y t + b_Y t^2 + \text{noise}_Y \quad (5.26)$$

The quaternion,  $q_{lev}^c$ , corresponding to the transformation from the level reference frame to the computed navigational frame based on the instrument measurements,  $V_X$  and  $V_Y$ , are:

$$q_{lev}^c = \sqrt{\frac{1 - b_Y}{2}} \pm \sqrt{\frac{1 + b_Y}{2}} \begin{bmatrix} 0 \\ 0 \\ 1 \end{bmatrix} \quad (5.27)$$

and

$$B = \sqrt{b_X^2 + b_Y^2}$$

The plus sign in Eq. 5.27 is used when  $b_X < 0$  and the minus sign is used when  $b_X > 0$  (See Fig. 5.2).

The final quaternion,  $q_b^c$ , is given by:

$$q_b^c = q_{lev}^c q_b^{lev} \quad (5.28)$$

Note that the errors due to the accelerometer bias and gyro drift are neglected. These error sources do not add more than  $1/2^\circ$  to the total error (assuming a maximum gyro drift of  $0.15^\circ/\text{hr}$  and an accelerometer bias of  $100\mu\text{g}$ ).

The error due to the term  $\phi_X(0)gW_v$  in  $b_X$

where:

$$b_X = (-W_h g \sin A_Z + \phi_X(0) g W_v) \quad (5.29)$$

will be  $1^\circ$ , for a  $1^\circ$  leveling error in  $\phi_X(0)$ .

#### 5.4 SIRU Coarse Alignment Data

The following tables present coarse alignment errors for various table positions with static and dynamic environments (the dynamic environment consists of oscillations about the table vertical axis). The reference table position used was calibration position #2 shown in Fig. 7.1, Chapter 7. The table axis angular increments with respect to calibration position #2 listed in Table 5.0 refer to the rotations of the table (on which the SIRU system is mounted) about the rotary and trunnion table axes designated in Fig. 7.1.

Table 5.0 Coarse Alignment Errors  
Static Environment (Azimuth About X)

Table Axis Angular Increments WRT Cal. #2 Settings (Degrees)			Coarse Alignment Errors (Degrees) (Nearest 0.100)		
X (RA 32)	Y (TA 16)	Z (RA 16)	$\Delta X$	$\Delta Y$	$\Delta Z$
45	0	0	-.2	-	-
50	0	0	-.1	-	-
5	0	0	0	-	-
-1	0	0	-.8	-	-
-60	0	0	-0.3	-	-
90	0	0	-0.4	-	-
-80	0	0	+0.2	-	-
70	0	0	-0.3	-	-
-25	0	0	-0.3	-	-
0	-30	0	-	0	-
0	-5	0	-	0	-
0	2	0	-	0	-
0	-10	0	-	0	-
0	0	-10	-	-	-0.6
0	0	-5	-	-	-0.6
0	0	5	-	-	-0.6
0	0	30	-	-	-0.6
80	30	30	5.7	0.3	2.8
30	30	-10	0.1	0.4	0.6
60	10	10	0.6	0.1	0.6

Table 5.1 lists the results of oscillatory tests. Here the table positions designated are also with respect to calibration position #2 as in Table 5.0 as explained above. In addition, oscillations are impressed about the table vertical axis (i. e. rotary axis 32 in Fig. 7.1, Chapter 7).

Table 5.1 Coarse Alignment Errors  
 Dynamic Environment (1° P-P  
 Oscillation About Vertical Axis)

Oscillation Frequency (hz)	Table Axis Angular Increments WRT Cal. #2 Settings (Degrees)			Coarse Alignment Errors (Degrees)		
	X (RA 32)	Y (TA 16)	Z (RA 16)	ΔX	ΔY	ΔZ
1	90	0	0	.3	-	-
0.5	90	0	0	-.6	-	-
0.5	60	0	0	-.6	-	-
1	60	0	0	-.4	-	-
1	25	0	0	-.2	-	-
0.5	25	0	0	-.8	-	-
0.5	-45	0	0	-.1	-	-
0.5	-45	0	0	.5	-	-
1	-45	10	-10	-1.5	0.04	0.7
0.5	-45	10	-10	-0.8	0.04	0.7
1	30	10	-10	-0.2	0.05	0.6
0.5	30	10	-10	-.3	0.05	0.6
0.5	60	10	10	-0.4	0.03	0.5
1	60	10	10	-4.3	0.5	0.4

Examination of Tables 5.0 and 5.1 reveals that in all but three cases the errors are less than 1°. The maximum error among the three cases is 5.7°. This initial angle can be adequately handled by the fine align algorithm without excessive delay.

## 5.5 Selection of Fine Alignment Algorithm

A fixed base, self-contained, fine alignment scheme is one in which no optics or other external aids are used and initial misalignment angles are small. The following sections present a number of such schemes and compare them with respect to the sensitivity of the azimuth misalignment angle to accelerometer noise induced by vehicle sway motion.

Chapter 4 derived the small misalignment angle differential equations when using the quaternion attitude algorithm for fine alignment.

## 5.6 Special Considerations When Using Quaternions

For a system using quaternions, all fine alignment schemes should calculate the attitude quaternion directly rather than obtaining the direction cosine matrix first and then converting the matrix to a quaternion. This requirement is imposed because of the complexity in transforming a direction cosine matrix to a quaternion (which involves taking square roots as shown in appendix A1 of chapter 1). The reverse operation (from a quaternion to a direction cosine matrix) is relatively simple.

## 5.7 Conventional Alignment vs. Alignment Using the East Gyro as a Sensor

Unlike a gimballed system, the strapdown system can use the gyros as angular rate sensors. It has been suggested in some papers<sup>4</sup> that the east gyro in a strapdown system can therefore be used for azimuth indication. However, in the presence of vehicle sway motion, it is shown below that the postulated east gyro technique is impractical.

The azimuth misalignment angle as a function of unfiltered accelerometer noise for the conventional alignment technique is given by:

$$\phi_D \approx \frac{(\tan L)n_E}{g} \quad (5.30)$$

where:

L = latitude

$n_E$  = unfiltered east accelerometer noise

g = gravity

$\phi_D$  = azimuth misalignment

The azimuth misalignment angle as a function of unfiltered accelerometer noise and gyro noise for the east gyro technique is given by:

$$\phi_D = \frac{(\tan L)n_E}{g} + \frac{\epsilon_E}{W_h} \quad (5.31)$$

where:

$\epsilon_E$  = unfiltered east gyro noise

$W_h = W_{ie} \cos L$  = horizontal component of earth rate.

Since:

$$\frac{\epsilon_E}{W_h} \gg \frac{(\tan L)n_E}{g}$$

Eq. 5.31 is approximately:

$$\phi_D \approx \frac{\epsilon_E}{W_h} \quad (5.32)$$

Considered independently with a 1 mrad azimuth error at  $L = 45^\circ$ , Eqs. 5.30 and 5.32 correspond to accelerometer and gyro noise levels of:

$$n_E = .001 \text{ g}, \epsilon_E = 0.011^\circ/\text{hr}$$

Note that a 0.001 g accelerometer uncertainty is considerably higher than that which would be expected from any inertial grade accelerometer in a static environment. Now we assume a sinusoidal missile sway having a  $1/2^\circ$  amplitude and a 10 second period. The height of the system above the ground is 200 ft.

The gyro noise (i.e., amplitude of the sinusoidal sway rate) is given by:

$$|\epsilon_E| = (1/2) (.2\pi) (3600) = 1130.4^\circ/\text{hr}$$

The gyro filter attenuation would have to be:

$$\frac{0.011}{1130.4} = .97 \times 10^{-5}$$

The accelerometer noise (i.e., amplitude of the sinusoidal acceleration) is given by:

$$|n_E| = \frac{200 \times (.2\pi)^2}{2 \times 57.4 \times 32} = .022 \text{ g}$$

The acceleration filter attenuation need be only:

$$\frac{.001}{.022} = .046$$

Hence the conventional alignment method is far superior to the east gyro technique and the east gyro technique was therefore discarded.

## 5.8 Alignment Methods

In addition to the conventional alignment method<sup>7</sup>, there are other methods which utilize only the outputs of the accelerometers. These methods are reviewed as follows.

### 5.8.1 Least Squares Method<sup>6</sup>

The least squares method utilizes a polynomial function (in powers of time, t) fitted to the accelerometer outputs in order to obtain estimates of  $\phi_N$ ,  $\phi_E$  and  $\phi_D$ . Analysis of the azimuth error due to vehicle sway shows that data gathering periods of ten to twenty minutes must be used for errors in the range of 1 mrad. Acceptable leveling errors are obtained in several hundred seconds.

### 5.8.2 Luenberger Observer<sup>8</sup>

Since the accelerometer outputs measure only  $\phi_E$  and  $\phi_N$ , it has been suggested that  $\phi_D$  be estimated using a Luenberger Observer. This method allows estimation of  $\phi_D$  by construction of an observer; which is a compromise between differentiating the system output a number of times and combining the result to form the estimated output, and constructing a model of the system and exciting it with the same inputs and initial conditions as the real system. Once  $\phi_D$  is estimated, a "bang-bang" control scheme can be used to obtain rapid alignment. However, the Luenberger Observer is useful only in a low noise environment.

### 5.8.3 Alignment to an Inertial Frame<sup>9</sup>

A method that employs Kalman filtering to align to an inertial frame instead of to the north, east, down frame used in the previous sections of this chapter has been proposed. This method uses three identical, uncoupled, Kalman filters. Calculations show that the method has a large sensitivity to vehicle sway motion.

#### 5.8.4 Final Selection of a Method

Satisfactory fine alignment in the presence of vehicle sway has been achieved with conventional alignment (i.e. leveling and gyrocompassing using only accelerometers as sensors). Use of Kalman filtering in a modification of the conventional alignment is also a possibility.<sup>10</sup> However, a conventional method of fine alignment using a low pass filter was used instead of the Kalman filter. This solution was chosen because of the far simpler implementation and algorithm complexity of the modified conventional method. Also, the Kalman filter is very sensitive to changes in the vehicle sway parameters whereas the low pass filter can be easily adjusted to accommodate any noise parameter changes. We also note that SIRU fine alignment settling times and accuracy are comparable to the reported results obtained with Kalman filtering.

#### 5.9 Fine Alignment Introduction

A fine alignment scheme is presented<sup>7</sup> which has been modified for application in a more severe environment. This environment is assumed to induce a sinusoidal sway of  $1/2^\circ$  amplitude in the frequency range of 0.1 to 1 Hz. A lever arm of 200 ft from the ground to the system is assumed. The modified scheme was also evaluated using the random sway postulated for Apollo<sup>11</sup>.

#### 5.10 Alignment System Analog Models

The following differential equations for the small angle deviations of the computed frame from the navigation frame for an earth-fixed system base were derived in Chapter 4:

$$\dot{\phi}_N = W_v \phi_E + W_N - d_N \quad (5.33)$$

$$\dot{\phi}_E = -W_v \phi_N + W_h \phi_D + W_E - d_E \quad (5.34)$$

$$\dot{\phi}_D = -W_h \phi_E + W_D - d_D \quad (5.35)$$

$\phi_N$ ,  $\phi_E$  and  $\phi_D$  are the small misalignment error angles about the north, east, and down axes respectively.  $W_N$ ,  $W_E$  and  $W_D$  are the appropriate command signals.  $d_N$ ,  $d_E$  and  $d_D$  are the gyro drifts for the respective north, east, and down axes.  $W_v$  and  $W_h$  are the respective vertical and horizontal components of earth rate.

Fine alignment occurs in two stages. With the azimuth angle,  $\phi_D$ , remaining "untorqued" by a command signal, the system is first leveled (i.e.,  $\phi_E$  and  $\phi_N$  are driven toward zero), and then azimuth alignment (driving  $\phi_D$  toward zero) is allowed to take place.

The following simplifications are made to the above equations. When leveling, we can uncouple Eqs. 5.33 and 5.34 by ignoring the  $W_v$  terms. That this is allowable can be seen by noting that the magnitude of  $W_v \phi_E$  or  $W_v \phi_N$  when  $\phi_E = \phi_N = 1^\circ$  is  $0.00018^\circ/\text{hr}$ . This magnitude is obviously much lower than the initial (at  $1^\circ$  offset) command signal required for leveling. The terms  $W_v \phi_E$  and  $W_v \phi_N$  will, of course, approach zero faster than the  $W_N$  or  $W_E$  command signals. Note that in Eq. 5.34 the  $W_h \phi_E$  term cannot be neglected relative to  $W_E$  because  $\phi_D$  does not approach zero during leveling and the term  $W_h \phi_D$  becomes significant. For azimuth alignment,  $W_h \phi_E$  can be neglected relative to  $W_D$  in Eq. 5.35 using the same arguments for neglecting the  $W_v$  terms in Eq. 5.33 and 5.34. Using these simplifications Eqs. 5.33, 5.34 and 5.35 can be reduced as follows:

$$\dot{\phi}_N = W_N - d_N \quad (5.36)$$

$$\dot{\phi}_E = W_h \phi_D + W_E - d_E \quad (5.37)$$

$$\dot{\phi}_D = W_D - d_D \quad (5.38)$$

The following signal flow diagrams represent the appropriate analog models. The choice of these particular schemes for generating  $W_N$ ,  $W_E$  and  $W_D$ , out of many alternatives, was based on their successful use in a real strapdown system.

### 5.11 Leveling Loop Design

The characteristic second order equation of the loops in Fig. 5.3A and 5.3B is given by:

$$s^2 + 2\zeta_L W_{nL} s + W_{nL}^2 = s^2 + K_B s + gK_V = 0 \quad (5.39)$$

Where  $\zeta_L$  = damping ratio and  $W_{nL}$  = loop natural frequency,  $s$  is the LaPlace Transform variable and  $K_B$ ,  $K_V$  and  $K_Z$  are design constants as shown in Fig. 5.3C. Hence the following design parameters are formulated.

$$D_L = \frac{\phi_{SS}}{d} = K_B / gK_V$$

$$\phi_{SS} = \text{steady state angle } (\phi_{N_{SS}} \text{ or } \phi_{E_{SS}}) \quad (5.40)$$

$d$  = gyro drift

$D_L$  = ratio of steady-state loop offset to gyro drift

$$\text{Settling time} = \tau_L = \frac{3}{\zeta_L W_{nL}} = \frac{6}{K_B} \quad (5.41)$$

$$\text{Damping ratio} = \zeta_L = \frac{K_B}{2\sqrt{gK_V}} \quad (5.42)$$

$$\text{Natural frequency} = W_{nL} = \sqrt{gK_V} \quad (5.43)$$

$$\text{Noise (rms)} = N_L = \frac{K_V(200) \left(\frac{1}{2}\right) (3600) W_S^2}{W_S (\sqrt{W_S^2 + K_B^2})} \text{ sec} \quad (5.44)$$

$$\cong 3.6 \times 10^5 K_V \text{ for } W_S \gg K_B$$

where  $W_S$  is the sinusoidal sway frequency, the lever arm is 200 ft and the amplitude is  $1/2^\circ$ .

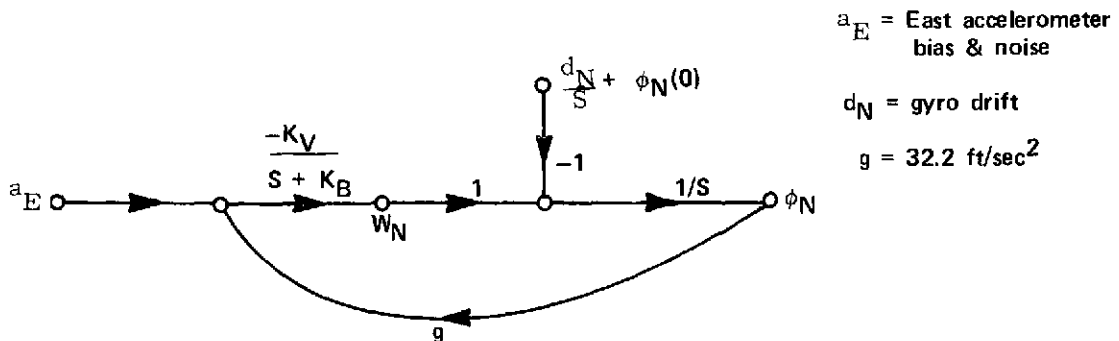


Fig. 5.3A North Leveling Loop

$a_N$  = North accelerometer bias & noise

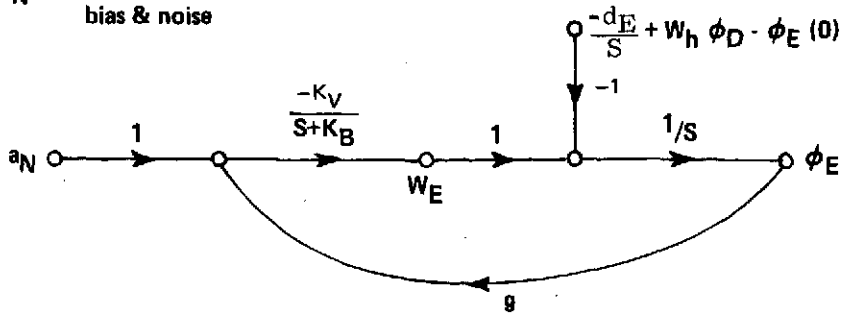


Fig. 5.3B East Leveling Loop

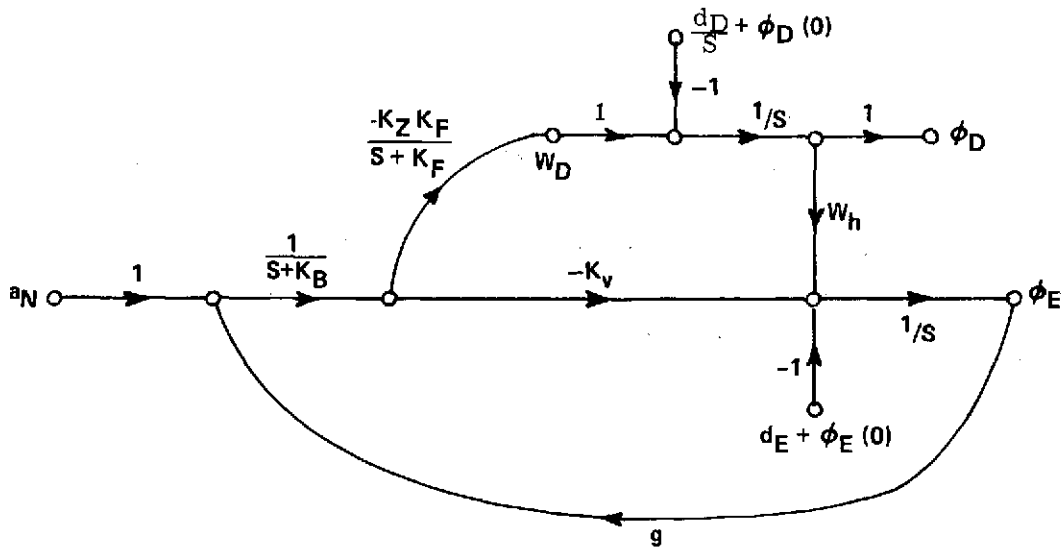


Fig. 5.3C Azimuth Loop

There are four desired quantities ( $D_L$ ,  $\tau_L$ ,  $\zeta_L$  and  $N_L$ ) but only two variables ( $K_B$  and  $K_V$ ) that can be chosen. Hence the design procedure is to choose  $K_B$  and  $K_V$  primarily for a satisfactory transient response. This response, however, is not ideal because we still require  $N_L$  and  $D_L$  to be as low as possible. Once the transient response is chosen, such changes are made to either the Bode plot or root locus diagram to further reduce  $D_L$  and/or  $N_L$  but only affect minimally the dominant pole pair that determines  $\tau_L$  and  $\zeta_L$ .

Also, an additional filter was chosen having a break frequency half a decade above  $K_B$  in order to further attenuate vehicle sway. Fig. 5.4 is the signal flow diagram for the modified north leveling loop (compare this diagram with Figs. 5.3.A and 5.3.B). The east loop is modified in the same way.

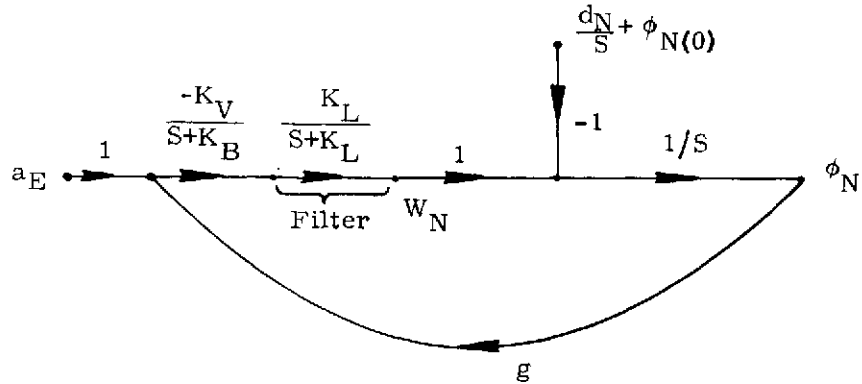


Fig. 5.4 Modified Leveling Loop

Figure 5.5 compares the Bode plots for Figs. 5.3A and 5.4. Fig. 5.6 compares the corresponding root loci. It can be seen from both figures that the transient response will remain about the same with or without the filter if  $K_L$  is sufficiently higher than  $K_B$ .

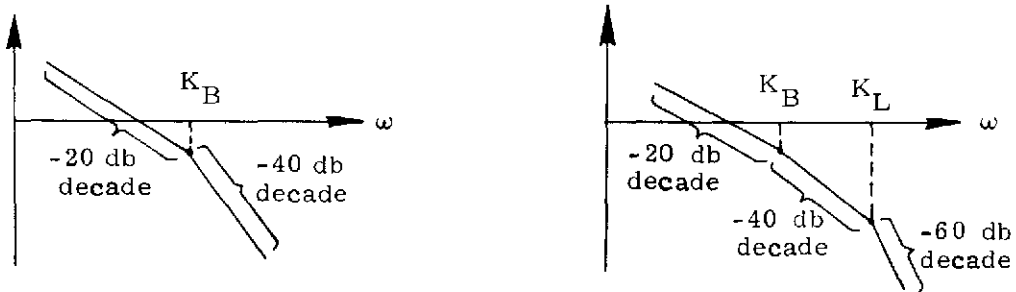


Fig. 5.5A , Fig. 5.3A Bode Plot      Fig. 5.5B , Fig. 5.4 Bode Plot

Fig. 5.5 Leveling Loop Bode Plots

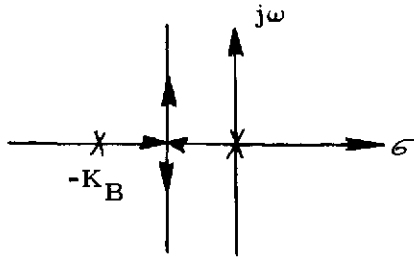


Fig. 5.6A, Fig. 5.3A Root Loci

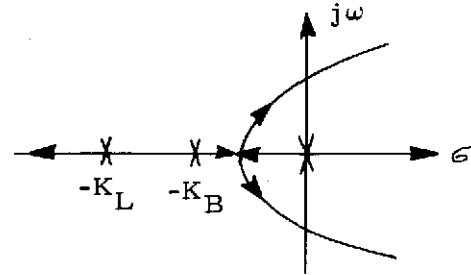


Fig. 5.6B, Fig. 5.4 Root Loci

Fig. 5.6 Leveling Loop Root Loci

### 5.12 Azimuth Loop Design

The characteristic fourth order equation of the azimuth loop in Fig. 5.3C is given by:

$$s^4 + (K_B + K_F) s^3 + (gK_V + K_B K_F) s^2 + gK_V K_F s + gK_Z K_F W_h = 0 \quad (5.45)$$

We define the following second order characteristic equation:

$$s^2 + 2\zeta_A W_{nA} s + W_{nA}^2 = s^2 + K_F s + K_F K_Z \frac{W_h}{K_V} = 0 \quad (5.46)$$

and multiply it by the leveling loop characteristic, Eq. 5.39, to obtain:

$$\begin{aligned} (s^2 + K_B s + gK_V) (s^2 + K_F s + K_F K_Z \frac{W_h}{K_V}) = \\ s^4 + (K_F + K_B) s^3 + (gK_V + K_B K_F + K_F K_Z \frac{W_h}{K_V}) s^2 \\ + (gK_V K_F + \frac{K_B K_F K_Z W_h}{K_V}) s + gK_F K_Z W_h = 0 \end{aligned} \quad (5.47)$$

Equation 5.45 and Eq. 5.46 are equivalent if the terms  $K_F \frac{K_Z W_h}{K_V}$  and  $K_B K_F \frac{K_Z W_h}{K_V}$  can be deleted from Eq. 5.47. This deletion is valid if the following is true:

$$K_B \gg \frac{K_Z W_h}{K_V} \quad (5.48)$$

$$\frac{gK_V}{K_B} \gg \frac{K_Z W_h}{K_V}$$

The following parameters can be defined for Eq. 5.46:

$$\text{Settling Time} = \tau_A = \frac{3}{\zeta_A \omega_{n_A}} = \frac{6}{K_F} \quad (5.49)$$

$$\text{Damping ratio} = \zeta_A = \frac{1}{2} \sqrt{\frac{K_V K_F}{K_Z W_h}} \quad (5.50)$$

$$\text{Natural frequency} = \omega_{n_A} = \sqrt{\frac{K_F K_Z W_h}{K_V}} \quad (5.51)$$

$$\left. \begin{array}{l} \text{Ratio of steady-state} \\ \text{azimuth loop offset to} \\ \text{down gyro drift} \end{array} \right\} = D_{AD} = \frac{K_V}{K_Z W_h} \quad (5.52)$$

$$\left. \begin{array}{l} \text{Ratio of steady-state loop} \\ \text{offset to east gyro drift} \end{array} \right\} = D_{AE} = \frac{1}{W_h}$$

Then with the appropriate substitutions:

$$\frac{K_Z W_h}{K_V} = (3/2) (1/\zeta_A^2 \tau_A) \quad (5.53)$$

Also using Eqs. 5.41 through 5.43 we obtain:

$$\frac{gK_V}{K_B} = \left(\frac{3}{2}\right) \left(\frac{1}{\zeta_L^2 \tau_L}\right) \quad (5.54)$$

$$K_B = \frac{6}{\tau_L} \quad (5.55)$$

Substituting Eqs. 5.53, 5.54 and 5.55 into 5.48 yields:

$$\frac{6}{\tau_L} \gg \frac{3}{2} (1/\zeta_A^2 \tau_A) \quad (5.56)$$

$$\zeta_A^2 \tau_A \gg \frac{\tau_L}{4} \quad (5.57)$$

$$\left(\frac{3}{2}\right) (1/\zeta_L^2 \tau_L) \gg \left(\frac{3}{2}\right) (1/\zeta_A^2 \tau_A) \quad (5.58)$$

$$\zeta_A^2 \tau_A \gg \zeta_L^2 \tau_L \quad (5.59)$$

If  $\zeta_A \approx \zeta_L$ , Eq. 5.47 can be used in place of Eq. 5.45 if  $\tau_A \gg \tau_L$  and  $\zeta_A > 0.5$ , but if  $\tau_A \gg \tau_L$  and  $\zeta_A \approx \zeta_L$ , the poles of  $s^2 + K_F s + K_Z K_F W_h / K_V$  dominate and the azimuth loop can be treated as a second order loop having the characteristic equation given by Eq. 5.46. The addition of the filter designed for the leveling loop affects the azimuth loop transient response even less than it affects the leveling loop. Figure 5.7 is the signal flow diagram of the modified azimuth loop containing the leveling loop filter. In order to minimize the effect of noise on the azimuth loop,  $K_F$  is chosen 1/2 decade below the leveling loop natural frequency. Thus we choose:

$$K_F = \frac{W_{nL}}{\sqrt{10}} \quad (5.60)$$

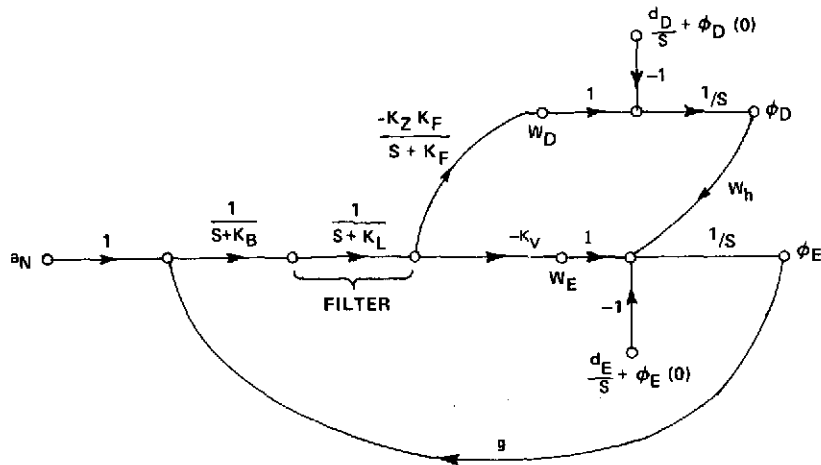


Fig. 5.7 Modified Azimuth Loop

### 5.13 Final Values of Parameters Chosen

Figure 5.8 shows the gain profiles for  $K_Z$ ,  $K_F$ ,  $K_B$ ,  $K_L$ , and  $K_V$  that were experimentally chosen with the aid of the preceding design equations.

### 5.14 Alignment Loop Algorithm

Figure 5.9 is equivalent to the north leveling loop diagram, Fig. 5.3A, but is redrawn to enable the derivation of a north leveling loop algorithm.

From the diagram in Fig. 5.9:

$$\int_{(n-1)T}^{nT} (a - K_B x) dt = x(nT) - x[(n-1)T] \quad (5.61)$$

$$x(nT) - x[(n-1)T] \cong -K_B T x[(n-1)T] + v(nT) - v[(n-1)T] \quad (5.62)$$

$$x(nT) = (1 - K_B T) x[(n-1)T] + v(nT) - v[(n-1)T] \quad (5.63)$$

Here:

$$v = \int a dt$$

where:

$v$  is the velocity output of the accelerometer.

$T$  (sampling time) = 1 sec

The command signal at  $nT$  is given by:

$$W_N(nT) = -K_V x(nT) \quad (5.64)$$

The command increment of angle  $\Delta\phi_N(nT)$  is, therefore, given by:

$$\Delta\phi_N(nT) = \phi_N(nT) - \phi_N[(n-1)T] = -K_V x(nT)T \quad (5.65)$$

The digital algorithms for the other loops (east and azimuth) are derived in a similar manner.

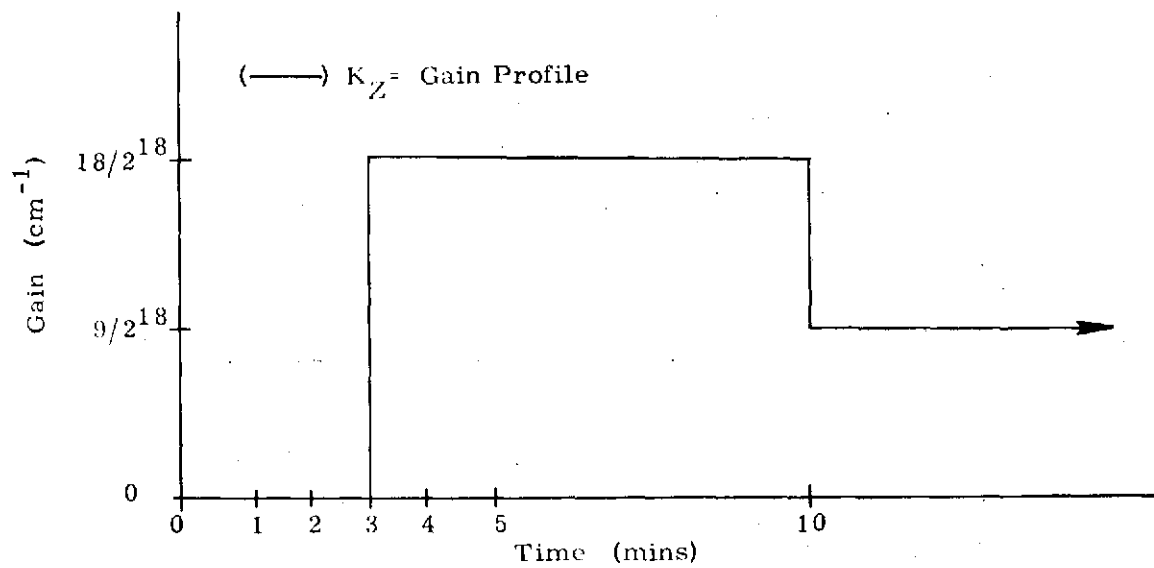


Fig. 5.8A Fine Alignment Azimuth Gain  $K_Z$

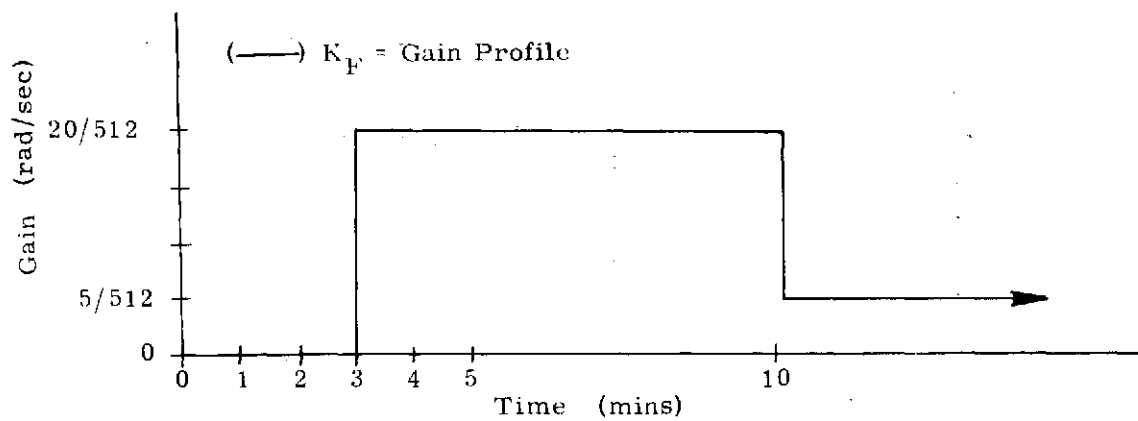


Fig. 5.8B Fine Alignment Azimuth Gain  $K_F$

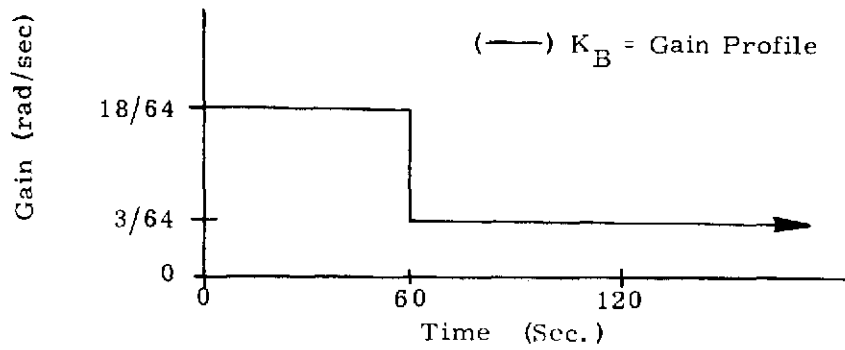


Fig. 5.8C Fine Alignment Leveling Gain  $K_B$

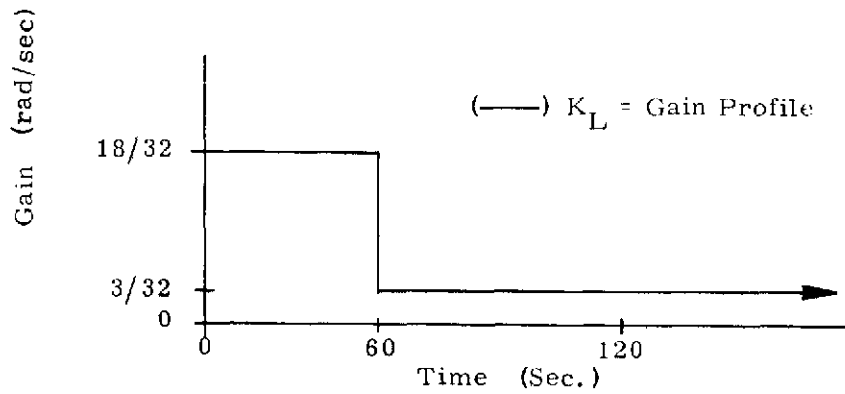


Fig. 5.8D Fine Alignment Leveling Gain  $K_L$

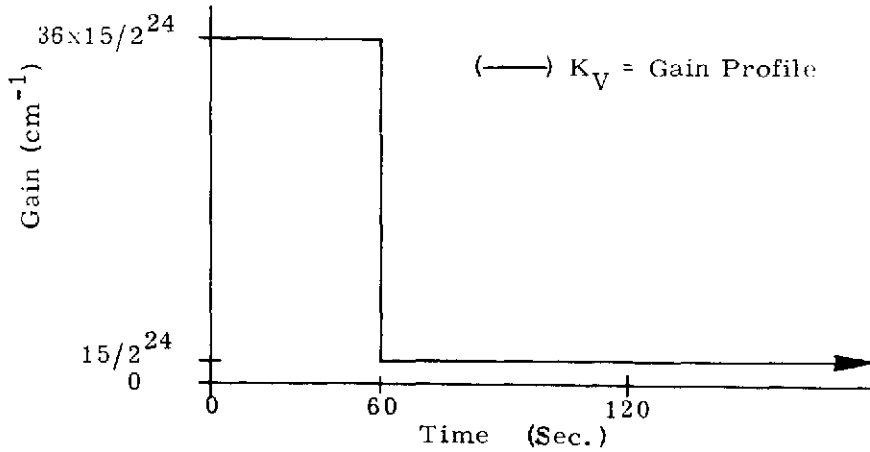


Fig. 5.8E Fine Alignment Leveling Gain  $K_V$

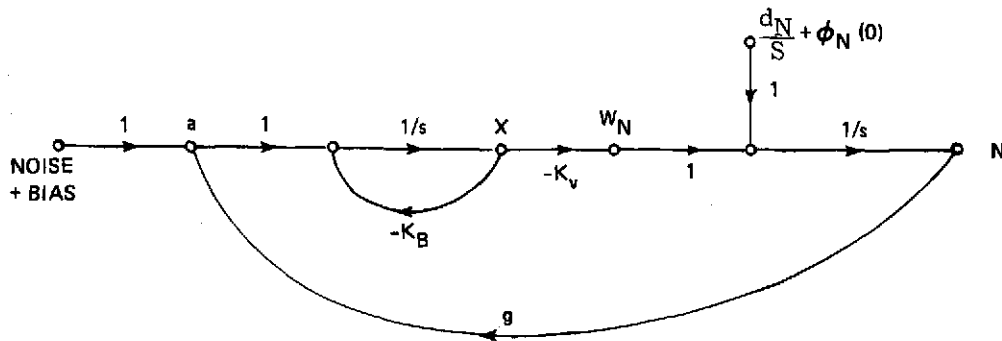


Fig. 5.9 North Leveling Loop (Fig. 5.3A) Equivalent Signal Flow Diagram

### 5.15 SIRU Fine Alignment Data

Figure 5.10 shows the azimuth error profile for a 12 hour SIRU test run with the gyrocompassing algorithm. The mean, which is a direct function of the east axis gyro drift (since  $D_{AE} = 1/W_h$ , Eq. 5.52), is  $-0.19$  mr and merely reflects how well the system was calibrated at the start of the run. Of more significance is the standard deviation for the run which was  $0.07$  mr. This low figure is indicative of both the short term stability of the system gyros and the performance of the loop.

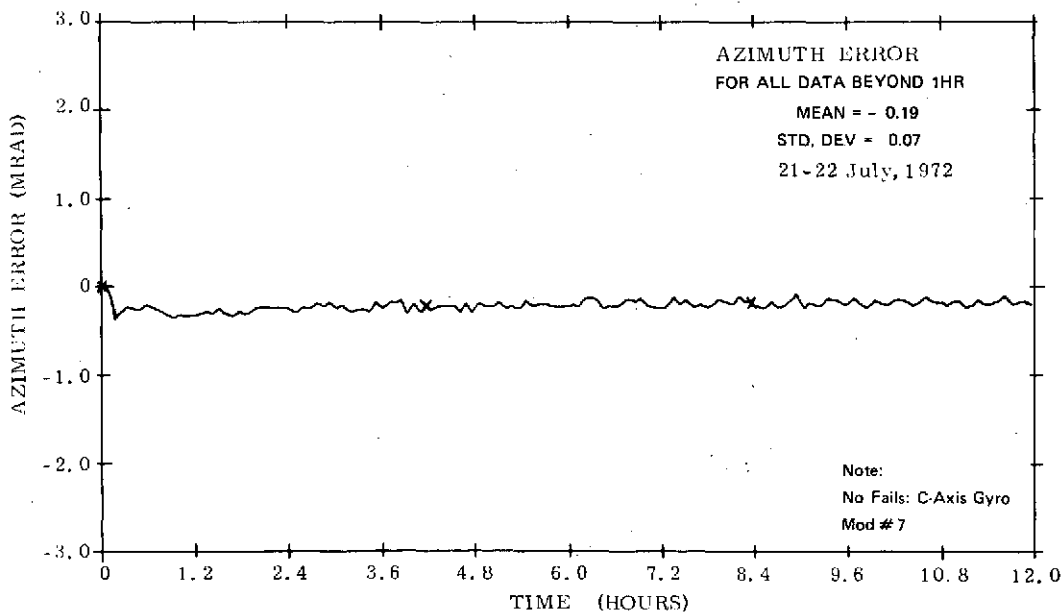


Fig. 5.10 SIRU Fine Alignment Algorithm (Static) - 12 Hour Test

Figure 5.11 shows the leveling errors for the same run depicted in Fig. 5.10. Here the means were  $14.23 \text{ sec}$  and  $0.93 \text{ sec}$  for the east and south axes respectively. These mean values are indicative of how well the accelerometers were calibrated at the start of the run. The respective standard deviations (east and south axes) were  $5.84 \text{ sec}$  and  $2.93 \text{ sec}$  and reflect short term accelerometer stability as well as the performance of the leveling loops.

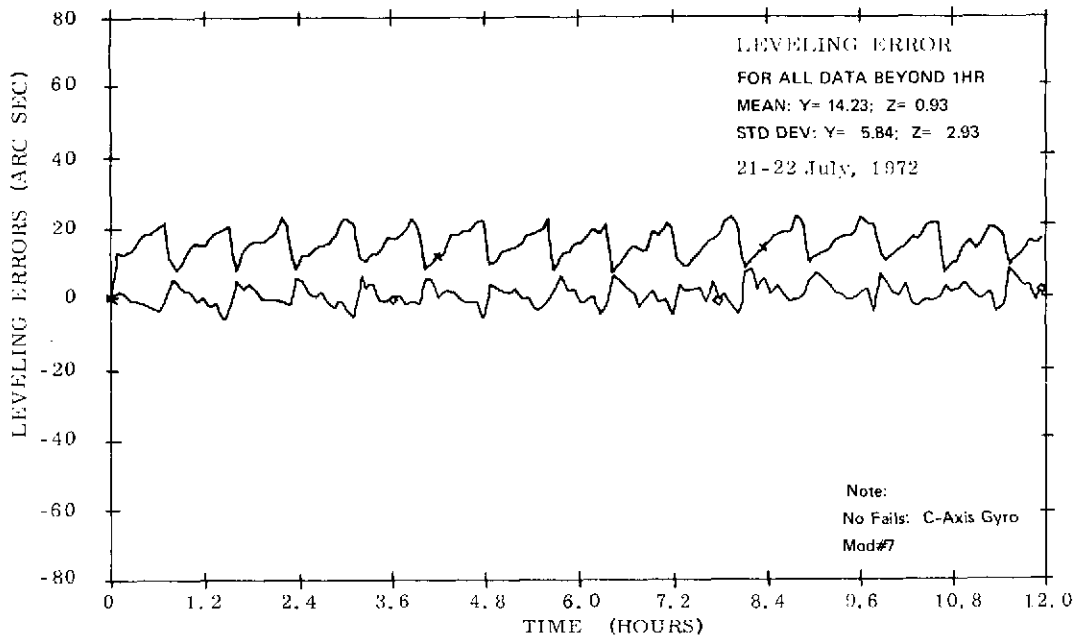


Fig. 5.11 Fine Alignment Algorithm (Static) - 12 Hour Test

Figure 5.12 shows the azimuth error over a 14 hour run for the C axis gyro which was erratic (the Fig. 5.10 run had a different C-gyro). This erratic behavior is reflected in a higher standard deviation ( $0.19 \text{ mr}$ ) than for Fig. 5.10. Note that both standard deviation values ( $0.07 \text{ mr}$  and  $0.19 \text{ mr}$ ) are well below  $1 \text{ mr}$  which was the initial design goal.

Figures 5.13 and 5.14 depict the transient response of the azimuth loop for a two degree initial offset. The error is well within  $1 \text{ mr}$  in less than 15 minutes and has completely settled out after 20 minutes. This transient behavior is typical for a wide range of initial offset magnitudes (below  $2^\circ$ ) and for various combinations of azimuth and leveling offsets.

Figures 5.15 and 5.16 show the transient responses of the leveling loops for  $1^\circ$  initial offsets. The east leveling loop settles to within  $10 \text{ sec}$  in one minute. The south leveling loop settles to within  $20 \text{ sec}$  in the same time. The higher  $20 \text{ sec}$  value for the south loop merely reflects a difference in accelerometer calibration accuracy before the run was started.

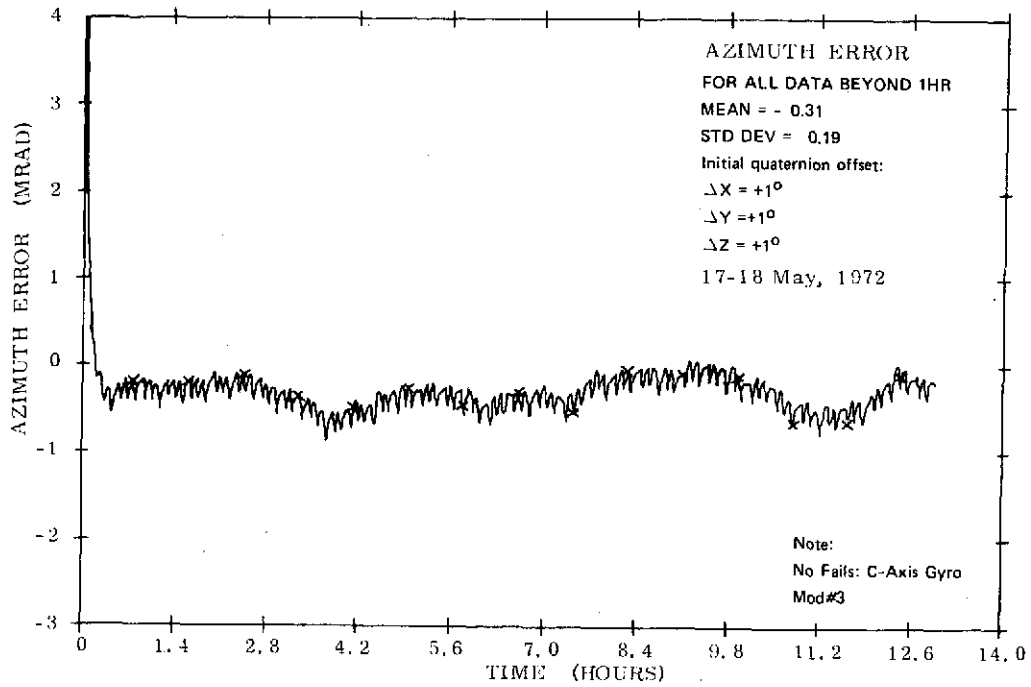


Fig. 5.12 SIRU Fine Alignment Algorithm (Static)

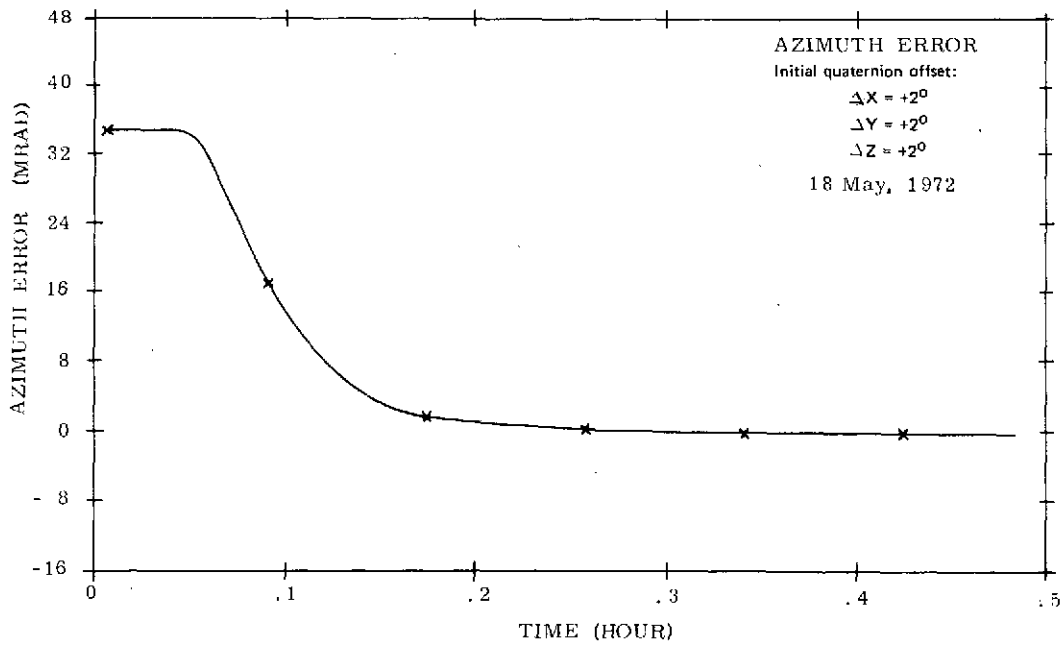


Fig. 5.13 SIRU Fine Alignment Algorithm (Static)

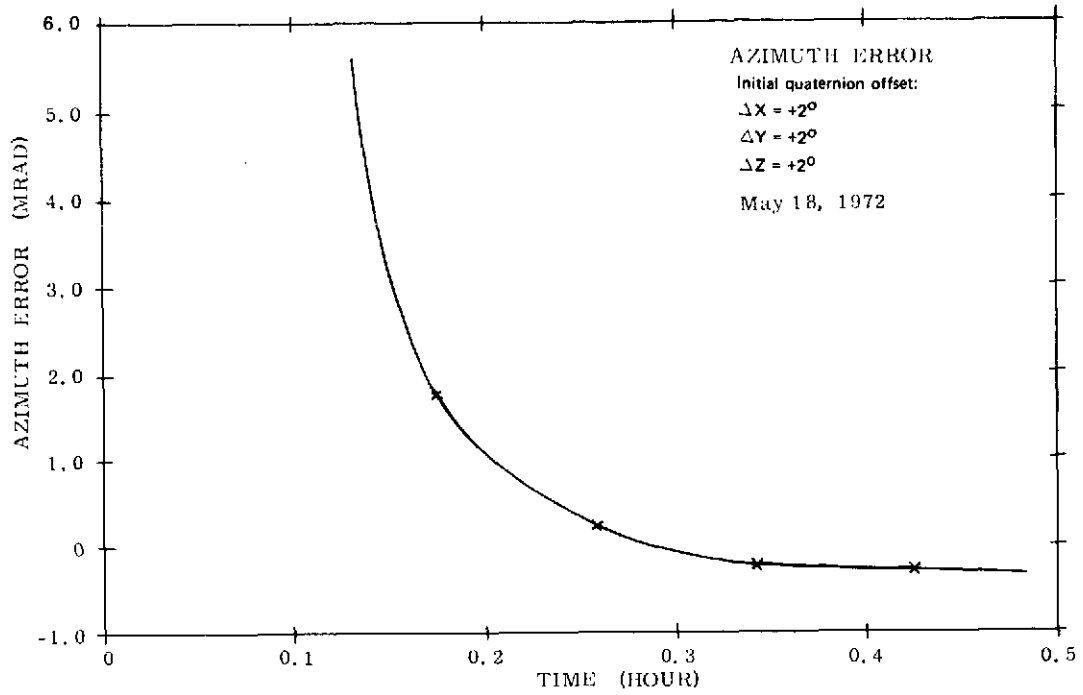


Fig. 5.14 SIRU Fine Alignment Algorithm (Static)

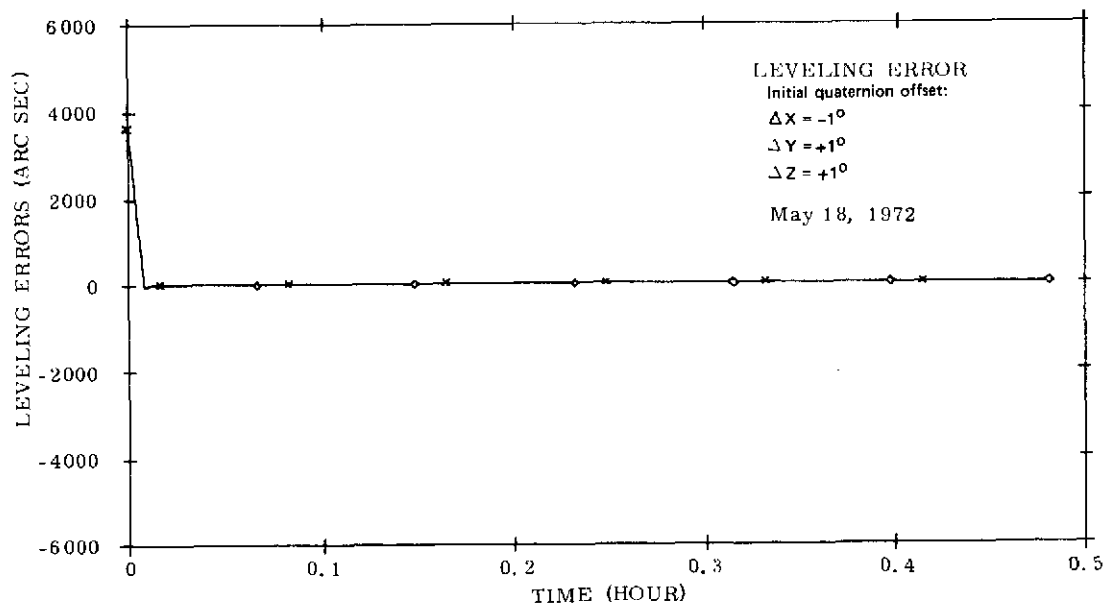


Fig. 5.15 SIRU Fine Alignment Algorithm (Static)

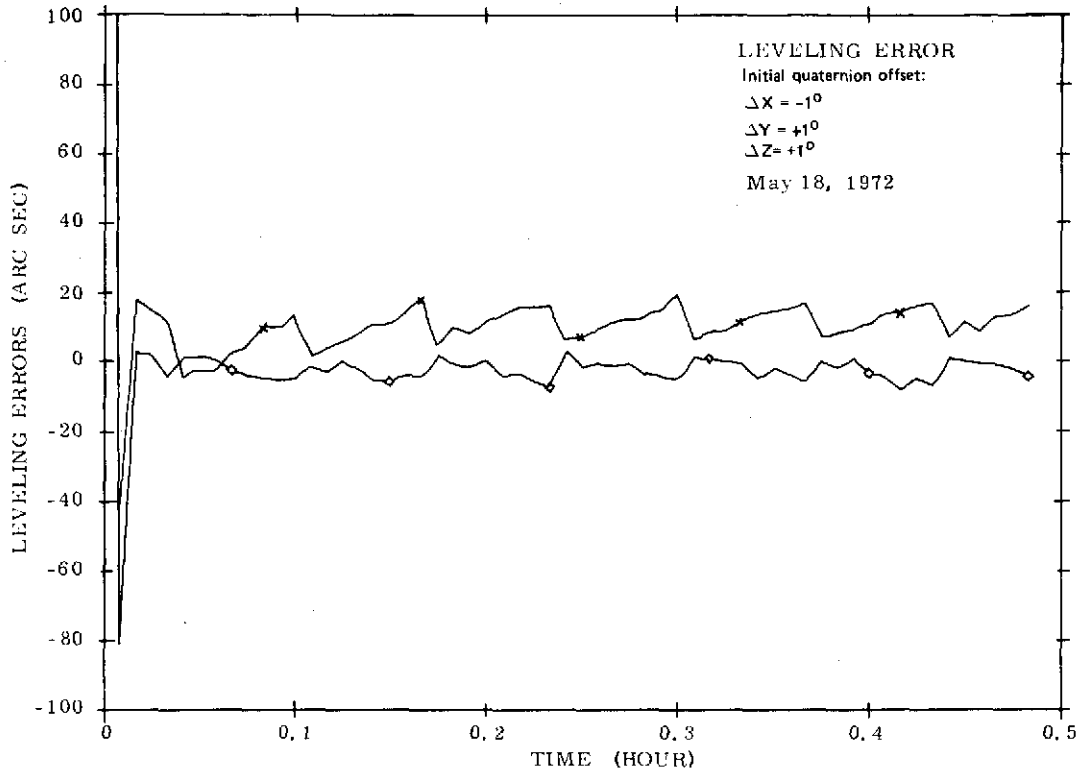


Fig. 5.16 SIRU Fine Alignment Algorithm (Static)

Figure 5.17 shows the actual displacement of SIRU in azimuth for a  $1^\circ$  peak-to-peak, 0.5 hz oscillation about the system vertical axis.

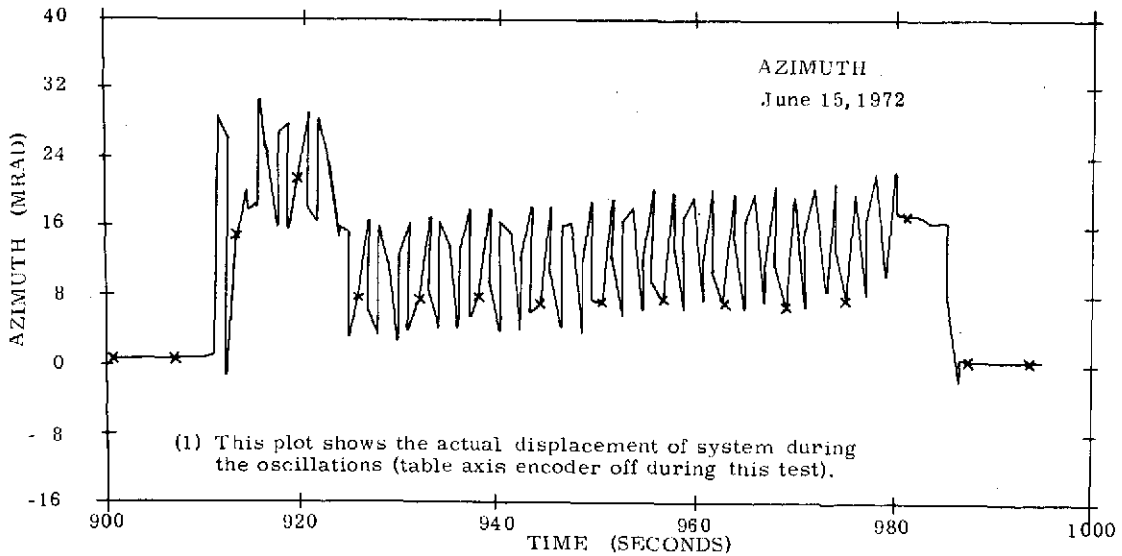


Fig. 5.17 SIRU Fine Alignment Algorithm - Oscillatory  $\approx 1^\circ$  P-P at 0.5 Hz

Table 5.2 lists the gyrocompassing and leveling errors for several oscillatory tests during which the system was oscillated about the vertical axis at different amplitudes and frequencies.

Table 5.2 Alignment Errors For Oscillations About The Vertical

Frequency And Peak- Peak Amplitude	Azimuth Error (mr)		Leveling Error (sec)			
			East(Y)		West(Z)	
	MAX	MIN	MAX	MIN	MAX	MIN
0.1 hz, 1° P-P	-.2	-.24	10.1	1.9	1.44	-3.9
0.5 hz, 1° P-P	-.13	-.21	12.6	-1.24	3.3	-4.74

In addition to Table 5.2, Figs. 5.18 and 5.19 depict the alignment errors for a 1° pk-pk, 0.25 Hz oscillation about the vertical.

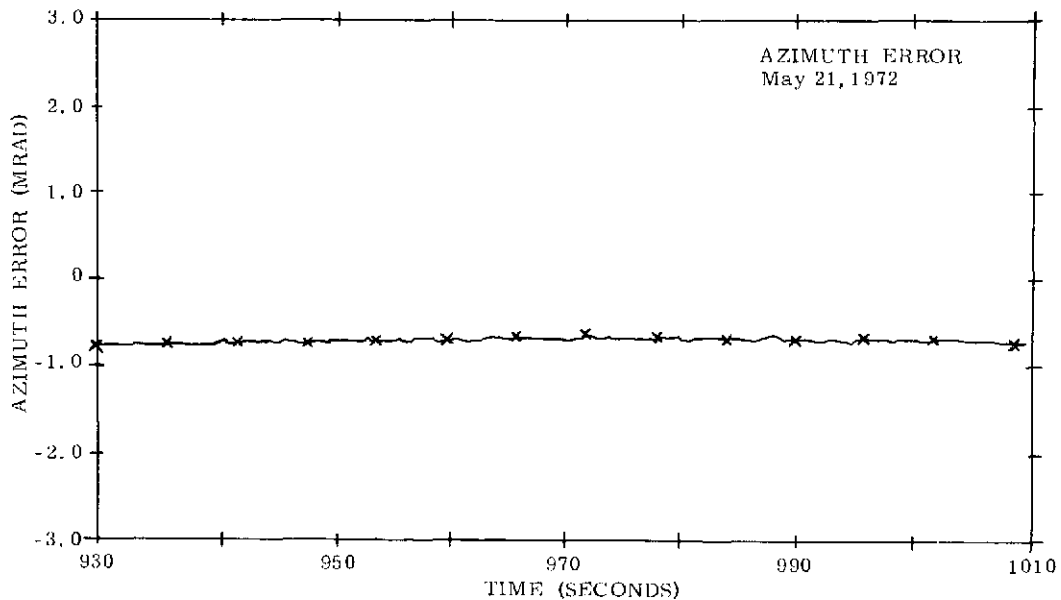


Fig. 5.18 SIRU Fine Alignment Algorithm - Oscillatory  $\approx 1^\circ$  P-P at 0.25 Hz

It can be seen from both Table 5.2 and Figs. 5.18 and 5.19 that leveling and gyrocompassing performance is not affected by the oscillations.

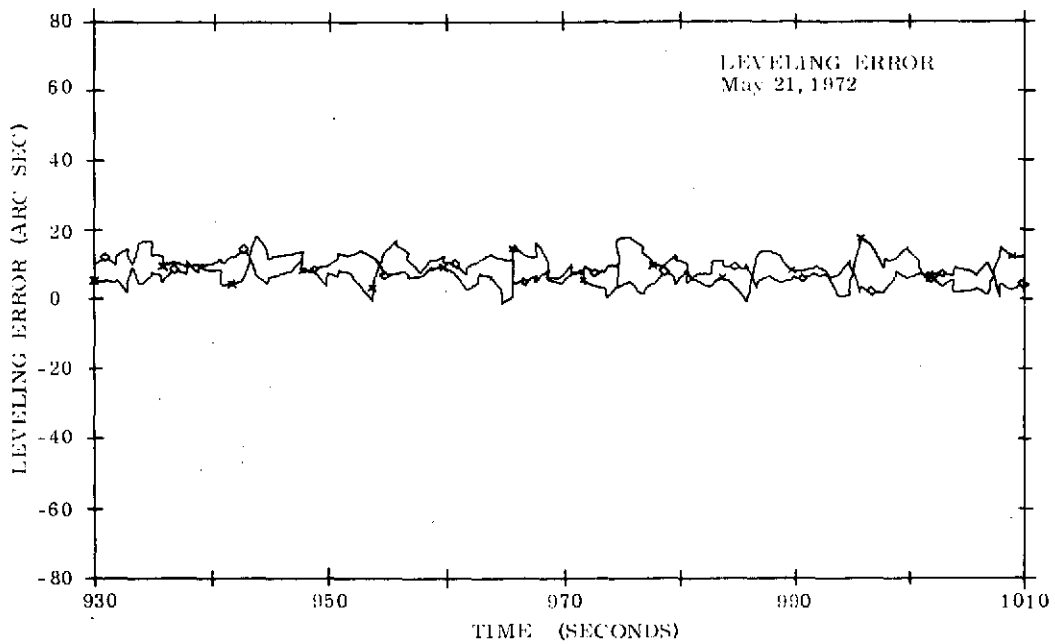


Fig. 5.19 SIRU Fine Alignment Algorithm - Oscillatory  $\approx 1^\circ$  P-P at 0.25 Hz

#### 5.16 Software Memory and Timing Requirements

Table 5.3 shows the software memory and timing requirements for implementation of the fine and coarse alignment programs on the Honeywell DDP-516 computer :

Program	Memory	Machine Cycles	Machine Time $\mu$ sec	Update Rate	% Machine Time for 50 updates per second of attitude algorithm
<u>I. COARSE ALIGNMENT</u>					
a) Level Accumulation	103	330	316.8	(1 Time)	-
b) $\Delta$ Filter	105	350	336.0	20 msec	1.7
c) Azimuth Calculation	277	772	741.1	(1 Time)	-
<u>II. FINE ALIGNMENT</u>	175	325	312.0	1 sec	.03

Table 5.3 Software Memory and Timing Requirements for Fine and Coarse Alignment Programs

Appendix A5

Least Squares Filter<sup>6</sup>

The general form of a least squares filter for estimating the coefficients of the polynomial:

$$v = a_0 + a_1 t + a_2 t^2 + \dots + a_n t^n + \text{noise} \quad (\text{A5.0})$$

is given by the following equation:

$$\begin{bmatrix} \hat{a}_0 \\ \hat{a}_1 \\ \hat{a}_2 \\ \vdots \\ \hat{a}_n \end{bmatrix} = \begin{bmatrix} \sum_{i=1}^K 1 & \sum_{i=1}^K t_i & \sum_{i=1}^K t_i^2 & \dots & \sum_{i=1}^K t_i^n \\ \sum_{i=1}^K t_i & \sum_{i=1}^K t_i^2 & \dots & \vdots & \\ \sum_{i=1}^K t_i^n & \dots & \vdots & & \end{bmatrix}^{-1} \begin{bmatrix} \sum_{i=1}^K v_i \\ \sum_{i=1}^K t_i v_i \\ \vdots \\ \sum_{i=1}^K t_i^n v_i \end{bmatrix} \quad (\text{A5.1})$$

the hat "A" denotes estimated value.

With the Eq. 5.20 polynomial rewritten as Eq. A5.2, the filter equation reduces to Eq. A5.3:

$$v = a_1 t + a_2 t^2 + \text{noise} \quad (\text{A5.2})$$

$$\begin{bmatrix} \hat{a}_1 \\ \hat{a}_2 \end{bmatrix} = \begin{bmatrix} \sum_{i=1}^K t_i^2 & \sum_{i=1}^K t_i^3 \\ \sum_{i=1}^K t_i^3 & \sum_{i=1}^K t_i^4 \end{bmatrix}^{-1} \begin{bmatrix} \sum_{i=1}^K t_i v_i \\ \sum_{i=1}^K t_i^2 v_i \end{bmatrix} \quad (\text{A5.3})$$

PRECEDING PAGE BLANK NOT FILMED

Let:

$$T = K \delta t = (.01)K \quad (A5.4)$$

where  $\delta t$  is the step time for each iteration.

Then:

$$\sum_{i=1}^K t_i^2 \approx \frac{1}{\delta t} \int_0^T t^2 dt = \frac{1}{\delta t} \frac{T^3}{3} \quad (A5.5)$$

Likewise:

$$\sum_{i=1}^K t_i^3 \approx \frac{1}{\delta t} \frac{T^4}{4} \quad (A5.6)$$

$$\sum_{i=1}^K t_i^4 \approx \frac{1}{\delta t} \frac{T^5}{5} \quad (A5.7)$$

The matrix,  $[ \quad ]^{-1}$ , in Eq. A5.3 can be well approximated by:

$$\begin{bmatrix} K & K \\ \sum_{i=1} t_i^2 & \sum_{i=1} t_i^3 \\ K & K \\ \sum_{i=1} t_i^3 & \sum_{i=1} t_i^4 \end{bmatrix}^{-1} \approx \frac{240\delta t}{T^5} \begin{bmatrix} \frac{T^2}{5} & -\frac{T}{4} \\ -\frac{T}{4} & \frac{1}{3} \end{bmatrix} \quad (A5.8)$$

So that:

$$\begin{bmatrix} \hat{a}_1 \\ \hat{a}_2 \end{bmatrix} = \frac{(240)\delta t}{T^5} \begin{bmatrix} \frac{T^2}{5} & -\frac{T}{4} \\ -\frac{T}{4} & \frac{1}{3} \end{bmatrix} \begin{bmatrix} \sum t_i v_i \\ \sum t_i^2 v_i \end{bmatrix} \quad (A5.9)$$

We are only concerned with the parabolic coefficient  $a_2$ . Thus from Eq. A5.9:

$$\hat{a}_2 = \frac{20\delta t}{T^5} \left[ 4 \sum t_i^2 v_i - 3T \sum t_i v_i \right] \quad (\text{A5.10})$$

Since Eq. 5.27 deals only with ratios of the  $a_2$ 's (i.e.,  $b_Y/B$ ), any common factors cancel and the scaling of  $a_2$  can be changed. If  $T=200$  seconds, a scale factor of  $20 t/T^5$  is impractical. Instead we choose a scale factor of  $1/T^3$  so that:

$$\hat{a}'_2 = \frac{4 \sum t_i^2 v_i}{T^3} - \frac{3}{T^2} \sum t_i v_i \quad (\text{A5.11})$$

with  $T=200$  seconds.

$$\hat{a}'_2 = \frac{4 \sum t_i^2 v_i}{8 \times 10^6} - \frac{3 \sum t_i v_i}{4 \times 10^4} \quad (\text{A5.12})$$

or in terms of the  $b$  coefficients used in Eq. 5.27:

$$N \hat{b}_X = \frac{4 \sum t_i^2 v_{X_i}}{8 \times 10^6} - \frac{3 \sum t_i v_{X_i}}{4 \times 10^4} \quad (\text{A5.13})$$

$$N \hat{b}_Y = \frac{4 \sum t_i^2 v_{Y_i}}{8 \times 10^6} - \frac{3 \sum t_i v_{Y_i}}{4 \times 10^4} \quad (\text{A5.14})$$

Here  $N$  is the common term given by:

$$1/N = \frac{20\delta t}{T^2} \quad (\text{A5.15})$$

or:

$$N = \frac{T^2}{20\delta t} = 2 \times 10^5 \quad (\text{A5.16})$$

## Chapter 6

### Local Level Navigator and Error Propagation

#### 6.0 Introduction

As part of the SIRU Utilization requirements, land navigation demonstrations were used to evaluate the error propagation arising from a failed instrument when FDICR is used and in a dynamic environment when dynamic compensation is present.

A local level navigator<sup>12,13</sup> (with the necessary altitude damping and Coriolis compensation) was used. The local level navigator implementation was selected because it is in common usage and integration with external navigation aids could be readily implemented if ever required. Since the error propagation is expressed in latitude and longitude, the local level navigator already has the proper output for data presentation without the need for further transformation as would be required if an inertially stabilized navigation mechanization had been used.

#### 6.1 Local Level Navigator System

The coordinate system for the local level navigator is a simplified local level coordinate system where one component is directed from the center of the earth to the navigated vehicle, one component is tangent to the circular meridian and directed north, and the final component is tangent to a circle of constant latitude and directed east.

The quantities computed by the navigator are: Radial, North, and East velocity; coordinate system rotation about Radial, North, and East directed vectors; and latitude, longitude, and altitude.

The inherent altitude divergence is controlled by feeding back into the radial velocity difference equation the altitude error and altitude error rate derived from an external source (e.g. an altimeter). The stability of this scheme is discussed later in this chapter.

Figure 6.0 is a conceptual block diagram of the local level navigator (in the actual algorithm the accelerometer outputs are increments of velocity rather than acceleration as shown in the diagram and the gyro outputs are in increments of angle rather than angular velocity as indicated in the diagram). The algorithm actually implemented is given in Volume II, SIRU Utilization Software Documentation.

PRECEDING PAGE BLANK NOT FILMED

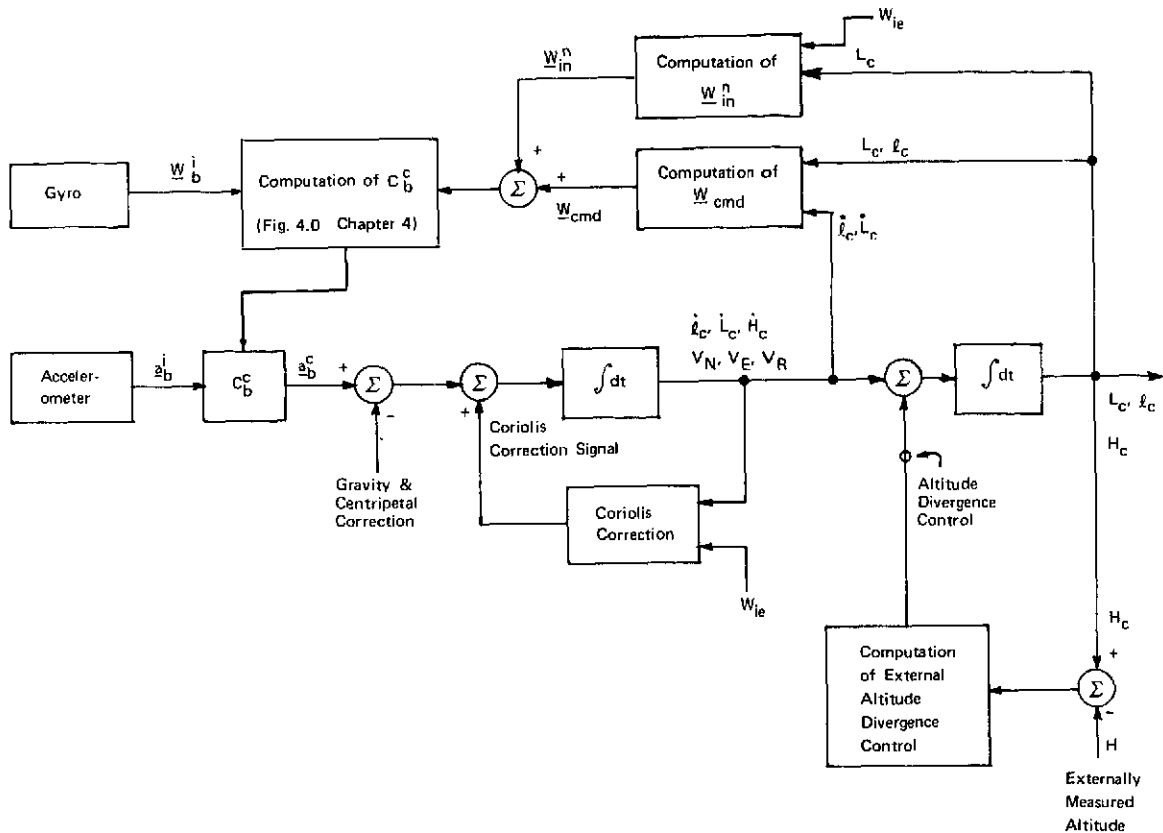


Fig. 6.0 Conceptual Block Diagram-Local Navigator

Referring to Fig. 6.0, when the local coordinate frame is described by UP (X), EAST (Y), NORTH (Z) axes, we have the following:

- $W_{ie}$  = earth rate
- $L_c$  = computed latitude
- $l_c$  = computed longitude
- $H_c$  = computed altitude
- $H$  = altitude measured by an external sensor (such as a barometer)
- $V_N$  = computed north velocity
- $V_E$  = computed east velocity
- $V_R$  = computed radial velocity
- $R_c = 6378163 (1 - (1/279)\sin^2 L_c) + H_c$   
= computed radial coordinate
- $W_N$  = angular velocity about north directed vector
- $W_E$  = angular velocity about east directed vector
- $W_R$  = angular velocity about radially directed vector

$$\dot{L}_c \triangleq \frac{V_N}{R_c} = -W_E \quad (6.1)$$

$$i_c \triangleq \frac{V_E}{R_c \cos L_c} = \frac{W_N}{\cos L_c} \quad (6.2)$$

$$\underline{W}_{in}^n + \underline{W}_{cmd} \triangleq \begin{bmatrix} (\dot{i}_c + W_{ie}) \sin L_c \\ -\dot{L}_c \\ (\dot{i}_c + W_{ie}) \cos L_c \end{bmatrix} \quad (6.3)$$

$$\text{Coriolis Correction} = \begin{bmatrix} V_E(W_N + 2W_{ie} \cos L_c) - V_N W_E \\ V_N(W_R + 2W_{ie} \sin L_c) - V_R(W_N - 2W_{ie} \cos L_c) \\ V_R W_E - V_E(W_R + 2W_{ie} \sin L_c) \end{bmatrix} \quad (6.4)$$

$$\text{Gravity \& centripetal correction} = \begin{bmatrix} -9.80402 \left(1 - \frac{2H_c}{R_c - H_c}\right) + W_{ie}^2 R_c \cos^2(L_c) \\ 0 \\ -W_{ie}^2 R_c \sin L_c \cos L_c \end{bmatrix} \quad (6.5)$$

$$\begin{aligned} \text{Altitude} \\ \text{divergence} \\ \text{control} \end{aligned} = K_1 E + K_2 \dot{E} \quad (6.6)$$

where  $E = H_c - H$

Equations 6.3 - 6.5 are standard equations for the simplified local level navigator described here.

Calculation of the divergence control parameters,  $K_1$  and  $K_2$  is of further interest and is presented in the following section.

## 6.2 Local Level Altitude Damping

The stability of a local level altitude damping mechanism is discussed. This discussion is based on a vehicle with small local velocity, such as the SIRU test stand. The following are the vertical difference equations:

$$\begin{aligned}
 H_K &= H_{K-1} + \Delta t V_{R_{K-1}} \\
 E_K &= H_K - H_{EXT} \\
 \Delta E_K &= E_K - E_{K-1} \\
 V_{R_K} &= V_{R_{K-1}} + \Delta V_{R_K} + \Delta t \left( -G_R + \frac{V_{E_{K-1}}^2}{R_{K-1}} + 2 V_{E_{K-1}} W_{ie} \cos \lambda_{K-1} \right. \\
 &\quad \left. + \frac{V_{N_{K-1}}^2}{R_{K-1}} \right) + K_1 E_K + K_2 \Delta E_K
 \end{aligned} \tag{6.7}$$

where:

- $H_K$  is the altitude at the Kth step
- $H_{EXT}$  is the altitude from any external source: it is assumed to be exact
- $V_{R_K}$  is the vertical velocity at the Kth step
- $\Delta V_{R_K}$  is the accelerometer output at the Kth step
- $G_R$  is the radial component of Gravitation
- $K_1, K_2$  Are parameters whose values are to be determined
- $\lambda_{K-1}$  = latitude at the (K-1)<sup>th</sup> step

The problem is to determine how an error in one step is propagated into successive steps. To do this, the deviations (considered as the difference between true and computed values) of Eq. 6.7 are sought.

They are:

$$\delta H_K = \delta H_{K-1} + \Delta t \delta V_{R_{K-1}} \tag{6.8}$$

$$\delta E_K = \delta H_K \tag{6.9}$$

$$\delta\Delta E_K = \delta H_K - \delta H_{K-1} \quad (6.10)$$

$$\delta V_{R_K} = \delta V_{R_{K-1}} + \delta\Delta V_{R_K} - \Delta t\delta G_R + K_1\delta E_K + K_2\delta\Delta E_K \quad (6.11)$$

All other terms of Eq. 6.11 are of order  $\frac{\delta V}{R}$  or  $\delta V \cdot W_E$  where  $\frac{1}{R} \approx 10^{-7}$  and  $W_E \approx 10^{-4}$  and may be neglected.

Subtracting Eq. 6.8 from the same equation for a previous time step yields:

$$\delta H_K - 2\delta H_{K-1} + \delta H_{K-2} = \Delta t(\delta V_{R_{K-1}} - \delta V_{R_{K-2}}) \quad (6.12)$$

Equation 6.11 for (K-1) cycle with Eq. 6.9 and Eq. 6.10 substituted can be arranged as follows:

$$\begin{aligned} \delta V_{R_{K-1}} - \delta V_{R_{K-2}} &= \delta\Delta V_{R_{K-1}} - \Delta t\delta G_R + K_1\delta H_{K-1} \\ &+ K_2(\delta H_{R-1} - \delta H_{K-2}) \end{aligned} \quad (6.13)$$

Substituting Eq. 6.13 into Eq. 6.12 and rearranging terms yields:

$$\begin{aligned} \delta H_K - (2 + \Delta tK_1 + \Delta tK_2)\delta H_{K-1} + (1 + \Delta tK_2)\delta H_{K-2} \\ = \Delta t(\delta\Delta V_{R_{K-1}} - \Delta t\delta G_R) \end{aligned} \quad (6.14)$$

Now let:

$$\begin{aligned} u &= \Delta t K_1 \\ v &= \Delta t K_2 \\ \epsilon_{K-1} &= \Delta t (\delta\Delta V_{R_{K-1}} - \Delta t\delta G_R) \end{aligned} \quad (6.15)$$

Substituting these terms in Eq. 6.14 yields:

$$\delta H_K - (2 + u + v)\delta H_{K-1} + (1 + v)\delta H_{K-2} = \epsilon_{K-1} \quad (6.16)$$

This is a second order difference equation with driving term  $\epsilon_{K-1}$  (error in accelerometer measured and computed gravity).

The solution to the homogenous equation is:

$$\delta H_K = A h_1^K + B h_2^K$$

where  $h_1, h_2$  are given by:

$$\begin{aligned} h_1 &= 1 + \frac{u+v}{2} - \frac{1}{2} \sqrt{(u+v)^2 + 4u} \\ h_2 &= 1 + \frac{u+v}{2} + \frac{1}{2} \sqrt{(u+v)^2 + 4u} \end{aligned} \tag{6.17}$$

A and B are determined by initial values. It is the solution of the homogenous equation that is of interest; we would like to be assured that initial errors do not cause the homogenous solution to become unbounded.

Thus, we would like to insure that  $h_1$  and  $h_2$  are less than 1.

A MAC program was written to evaluate  $h_1, h_2$  and their modulus and argument. This program has been run for  $-1 \leq u \leq 1$  and  $-1 \leq v \leq 1$  in steps of 0.1 and the results are plotted in Fig. 6.1. This chart gives the locus of acceptable points in this region, i.e. the dots in the chart represent those values of  $u$  and  $v$  that are unacceptable because they lead to sinusoidal solutions for  $h_1$  and  $h_2$  and the crosses in the chart represent values of  $u$  and  $v$  that yield those solutions for  $h_1$  and  $h_2$  that are acceptable because they are damped exponentials. The values of:

$$\begin{aligned} u &= -0.6 \\ v &= -0.3 \end{aligned}$$

have been used in simulations, and provide good altitude damping. The performance using these values is illustrated in Figs. 6.2 and 6.3 for the altitude and radial velocities respectively. These results are typical for all the navigation runs made on SIRU.

### 6.3 Local Level Navigator Error Sensitivities

Because SIRU geometry is well defined in a normal navigation mode static test, the best way to define the sensitivity of the navigation errors to instrument errors (drifts and biases) is to introduce these errors into the triad body axes (note that in a static field, scale factor errors show up as biases). Thus we do not have to spend the entire time testing each instrument individually. Individual errors

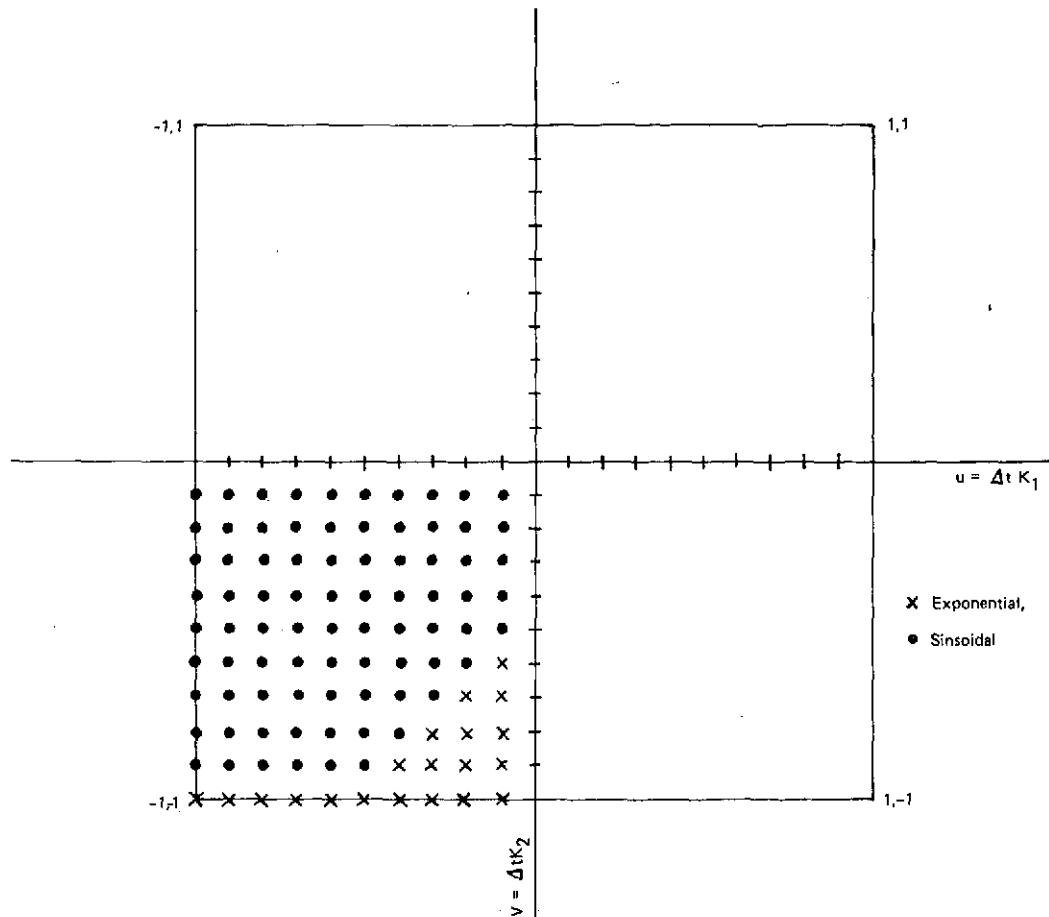


Fig. 6.1 Local Level Region of Stability

of instruments and combinations of instruments can be easily related to the triad errors through the geometrically fixed least squares matrices. This relationship is explored in Section 6.4.3 and in Chapter 7.

A number of error sensitivity runs (over 12 hours) were made with the SIRU local level navigator implemented. In each run a different computational axis gyro drift or accelerometer bias or alignment error was introduced and the errors were plotted. The general shape and magnitude of the resulting error waveforms proved to be typical for a local level navigator.

Gyro drifts cause the latitude errors to have a predominant 24 hour period sinusoid with a much smaller magnitude Schuler period sinusoid superimposed on it. Figure 6.4 is an example of such a waveform generated in SIRU using a 0.06 deg/hr drift about the north axis.

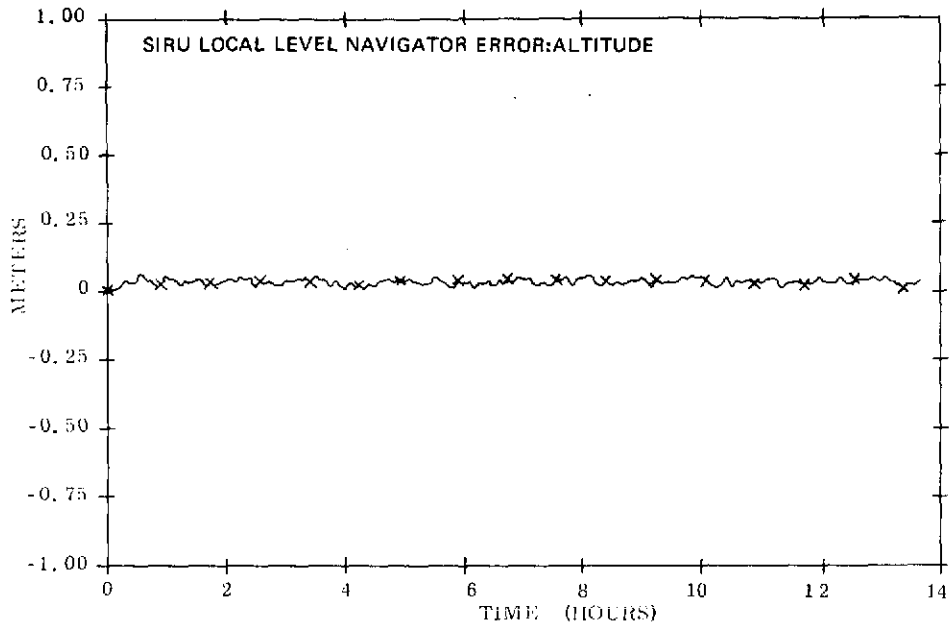


Fig. 6.2 Altitude Error for Compensated Local Navigational Axis Drift - Cal. Position 2

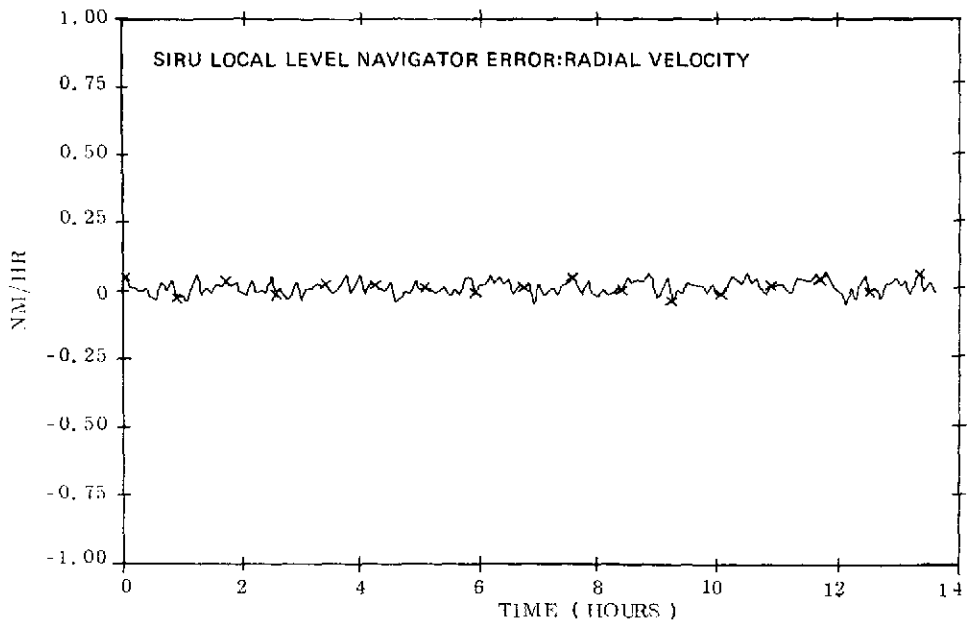


Fig. 6.3 Radial Velocity Error for Compensated Local Navigational Axis Drift - Cal. 2 Position

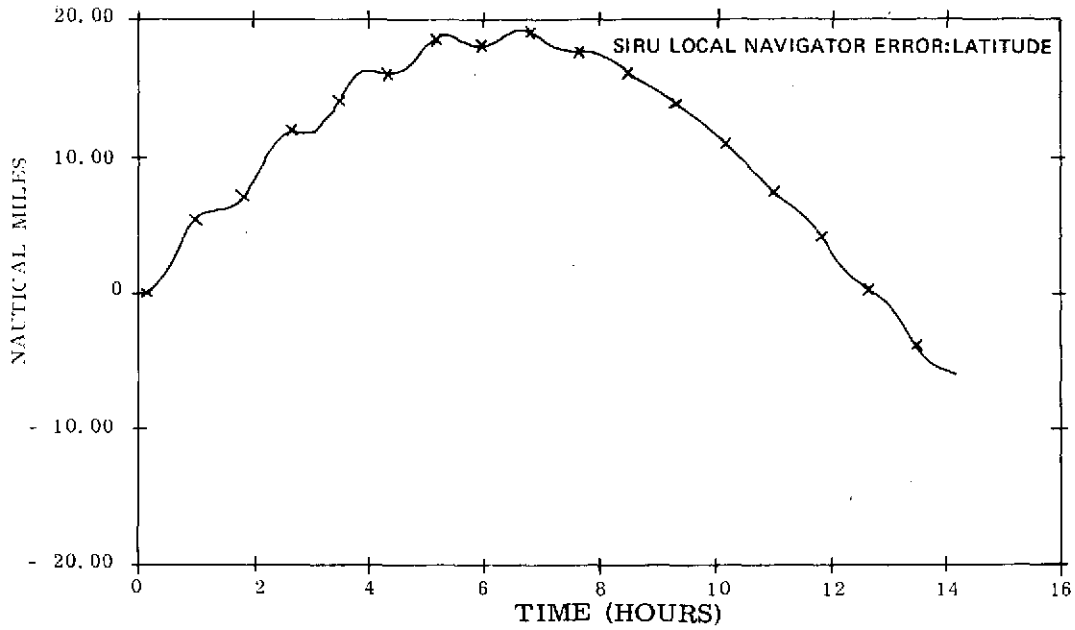


Fig. 6.4 Latitude Error for a .060 Deg/hour Drift Introduced into the East Axis - Cal. Position 2

The longitude errors due to gyro drifts are unstable, i.e. have a ramp as well as the 24 hour and Schuler period sinusoids. The ramp dominates. Figure 6.5 is an example of such a waveform generated in SIRU using a 0.06 deg/hr drift about the north axis.

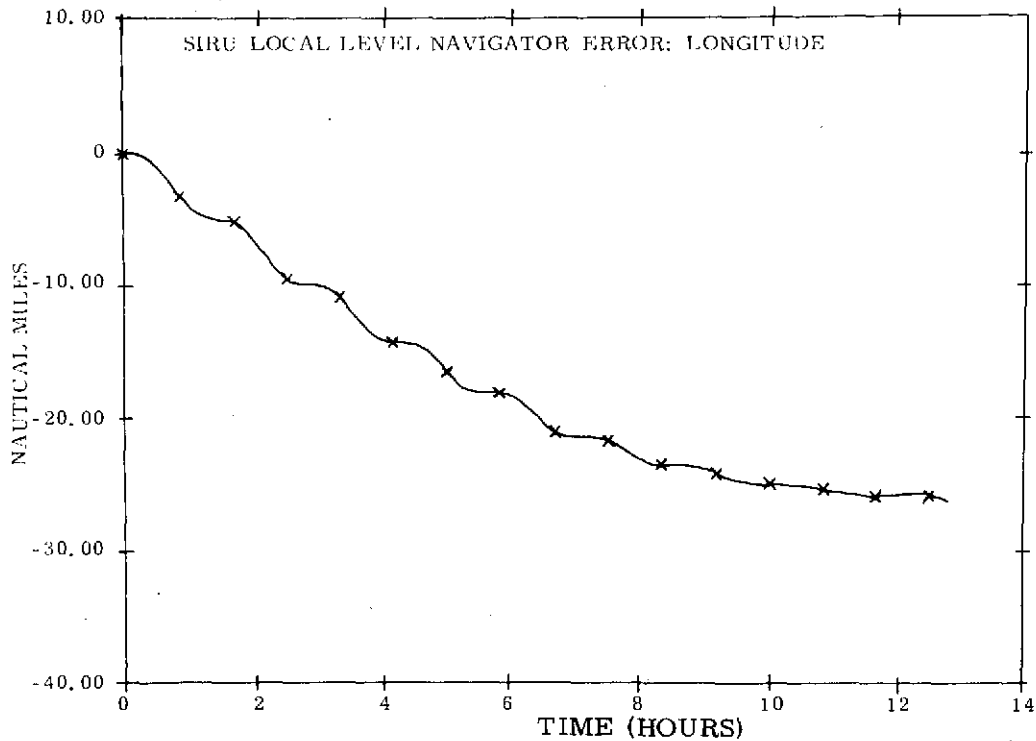


Fig. 6.5 Longitude Error for a .060 Deg/hour Drift Introduced into the North Axis - Cal. Position 2

Both latitude and longitude errors due to accelerometer bias or leveling misalignments have a predominant Schuler period sinusoid amplitude modulated by a Foucault period sinusoid. Figures 6.6 and 6.7 are examples of this type of error response.

A misalignment in azimuth produces an error with a predominant 24 hour period sinusoid. Figure 6.8 is an example of this type of error response.

Figure 6.9 depicts the longitudinal error for a misalignment in azimuth. This error also has a 24 hour period sinusoid, but the amplitude is close to zero during the first few hours.

For many applications it is necessary only to know the error responses during the first few hours. For these cases, the 24 hour period response looks like a ramp and the average slope characterizes the waveform. However, Schuler period sinusoids go through the complete period in less than 3 hours and should therefore be characterized by the peak error during the first few hours. Initially, for the first few hours, the errors in latitude are zero for an accelerometer bias in the east axis, gyro drift about the north and vertical axes, and misalignment about the north axis. Similarly, the longitude error is zero (for several hours) for an accelerometer bias in the north axis, gyro drift about the east and vertical axes, and misalignment about the east and vertical axes (see Fig. 6.9). These errors remain zero (or close to it) until cross coupling becomes large enough to initiate the general responses described in the preceding paragraphs.

Here cross coupling refers to the projection of an earth rate error component on an axis that has zero nominal earth rate initial error when the computational frame is perfectly aligned to the local navigational frame. The earth rate error component causes the frame to rotate out of alignment to such a degree that the accelerometer that was initially "level" now receives an input such that the accelerometer output is integrated to yield a noticeable latitude or longitude error. This effect of zero initial error response (due to initially small cross coupling) is illustrated for both longitude and latitude in Fig. 6.10 and 6.11 (Initial acceleration bias error and misalignment magnitudes were of course close to zero for these examples).

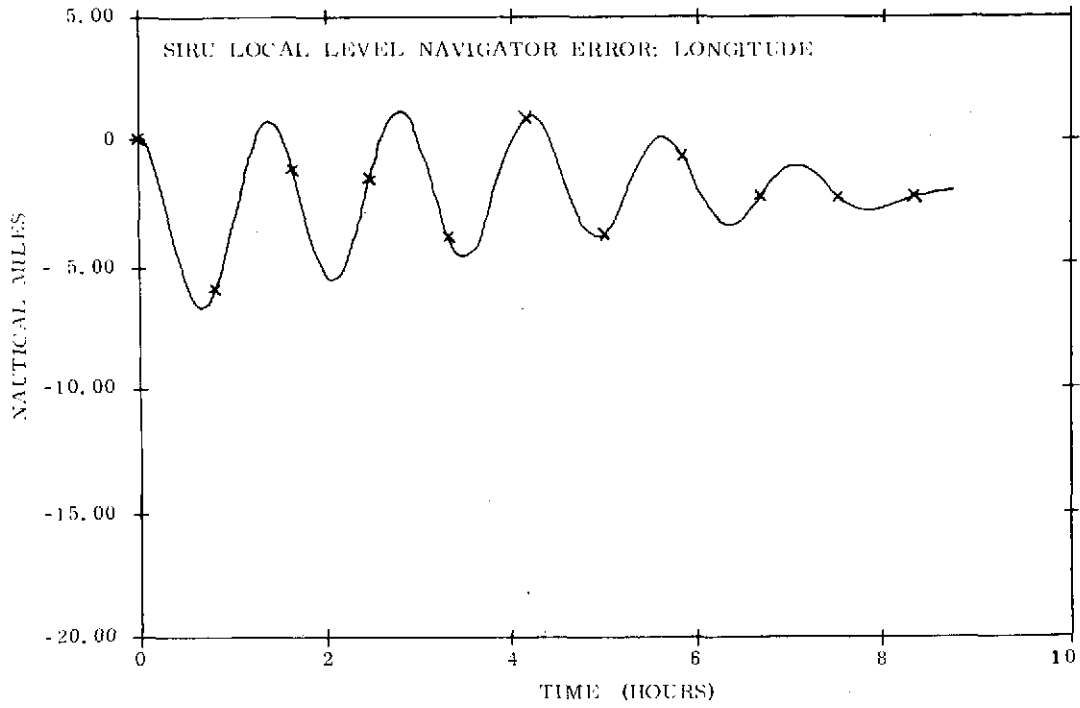


Fig. 6.6 Longitude Error for a  $1\text{cm}/\text{sec}^2$  Bias Error Introduced into the East Axis - Cal. Position 2

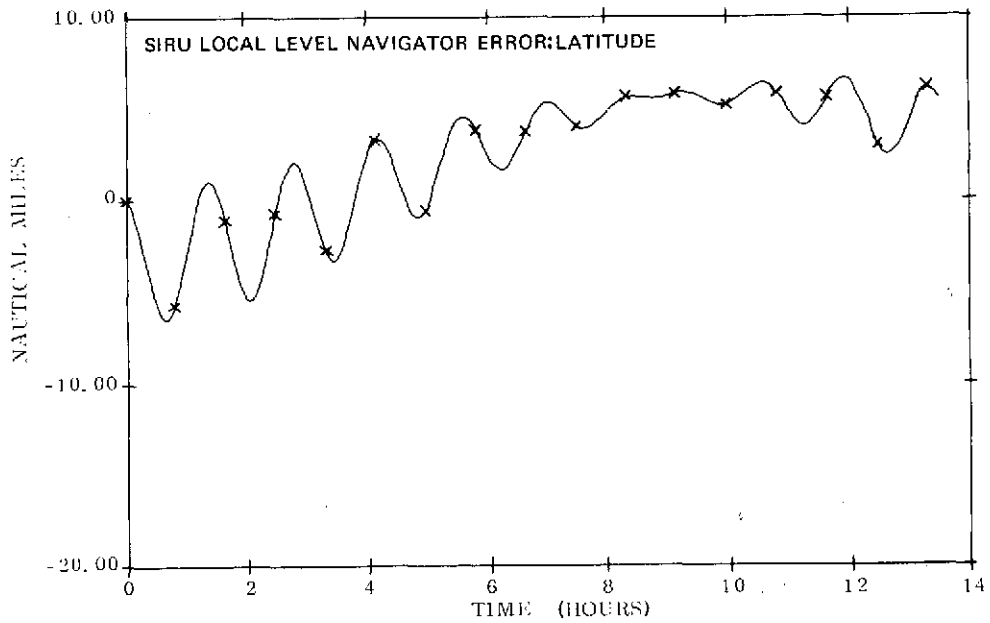


Fig. 6.7 Latitude Error for a  $1\text{cm}/\text{sec}^2$  Bias Error Introduced into the North Axis - Cal. Position 2

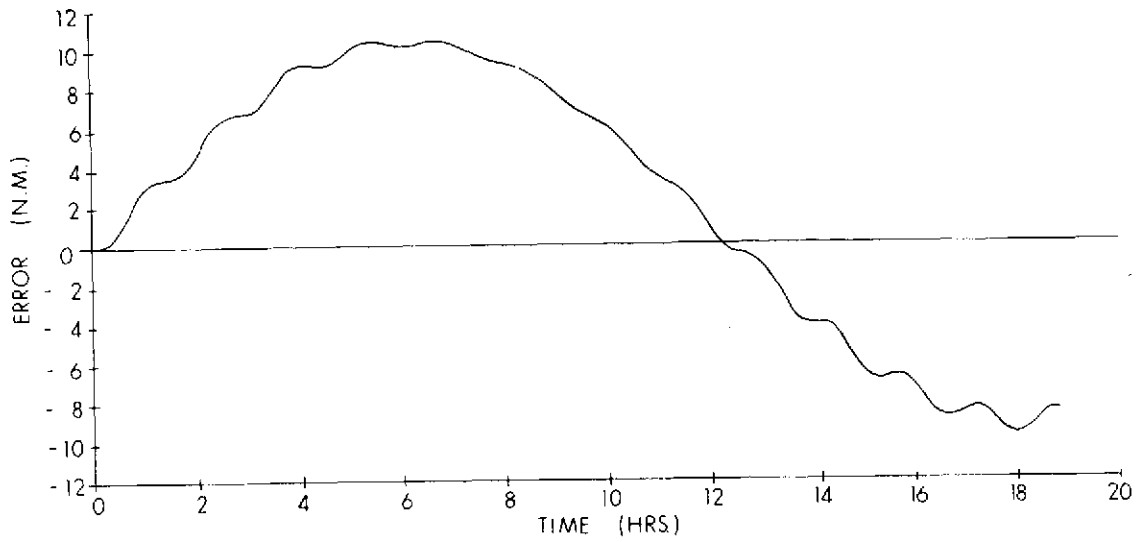


Fig. 6.8 Latitude Error for a 4 milliradians Offset About the Vertical Axis in Cal. Position 2.

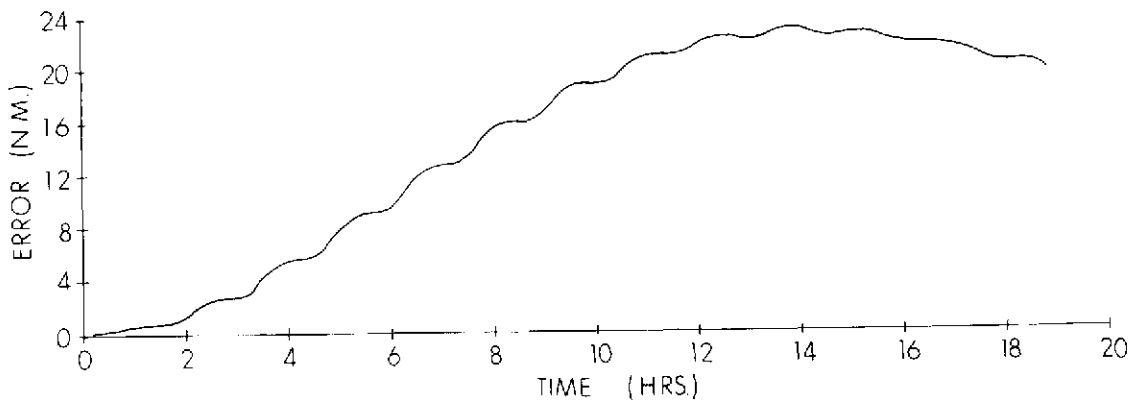


Fig. 6.9 Longitude Error for a 4 milliradians Offset About the Vertical Axis in Cal. Position 2.

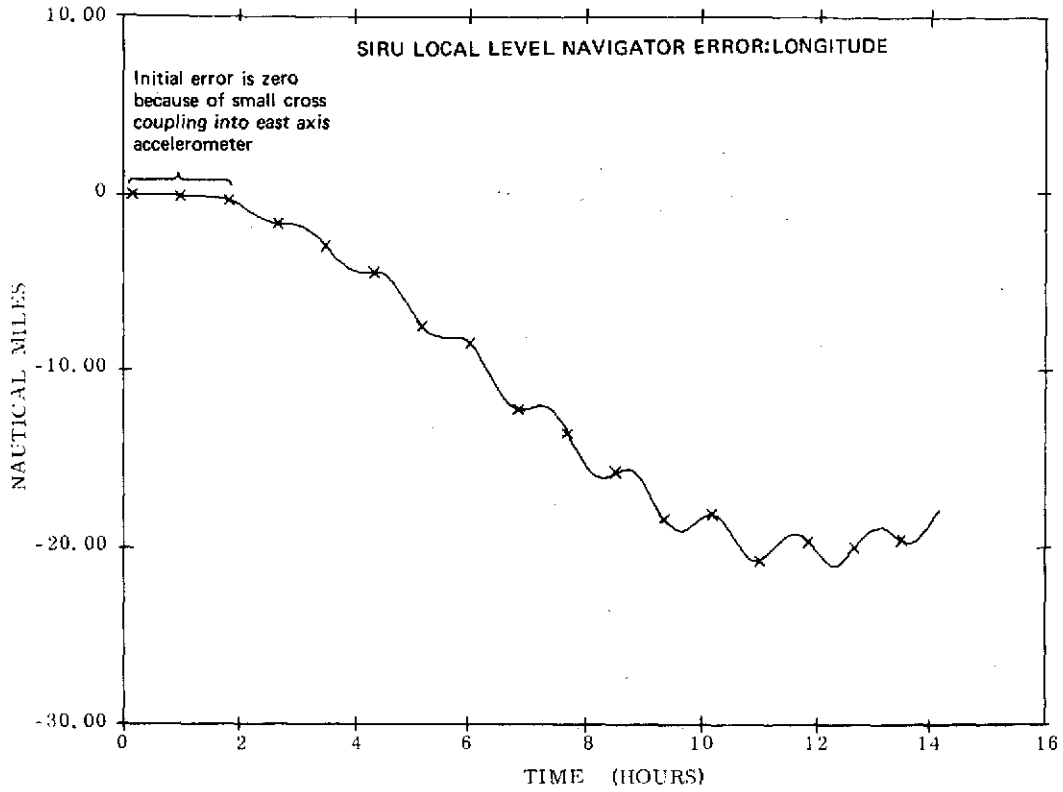


Fig. 6.10 Longitude Error for a .060 Deg/hour Drift Introduced into the East Axis - Cal. Position 2

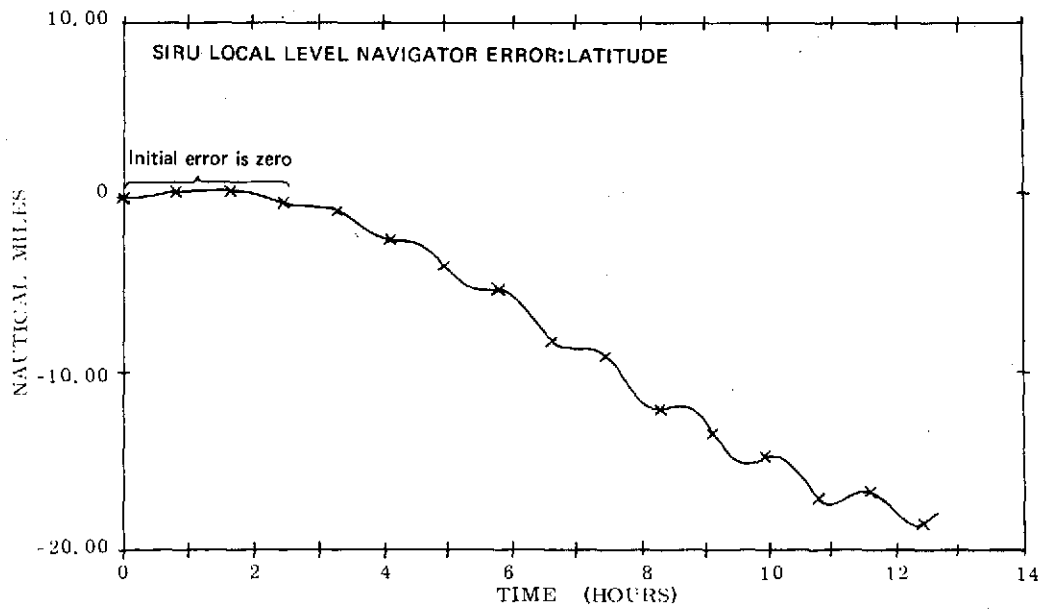


Fig. 6.11 Latitude Error for a .060 Deg/hour Drift Introduced into the North Axis - Cal. Position 2

The following table, Table 6.0, describes the error sensitivities over the first few hours of navigation (with zero initial conditions) computed from SIRU test data.

Error Source	LATITUDE		LONGITUDE	
	Predominant Type of Error	Approx Average Slope or Schuler Peak Value	Predominant Type of Error	Approx Average Slope or Schuler Peak Value
Gyro Drift About North Axis	NA (not applicable)	$\approx 0$	Ramp & 24 hr sinusoid	$-1 \frac{\text{nm}}{\text{hr}}$ per $.015^\circ/\text{hr}$
Gyro Drift About East Axis	24 hr sinusoid	$1 \frac{\text{nm}}{\text{hr}}$ per $.015^\circ/\text{hr}$	NA	$\approx 0^*$
Gyro Drift About Vertical Axis	NA	$\approx 0$	NA	$\approx 0$
North Axis Accelerometer Bias	Foucault Modulated Schuler Sinusoid	Schuler Peak -7 nm per $1 \text{ cm}/\text{sec}^2$	NA	$\approx 0$ (during 1st hr.)
East Axis Accelerometer Bias	NA	$\approx 0$ (during 1st hr.)	Foucault Modulated Schuler Sinusoid	Schuler Peak -7 nm per $1 \text{ cm}/\text{sec}^2$
Azimuth Misalignment	24 hr sinusoid	$1.3 \text{ nm}/\text{hr}$ per 1 mr	NA	$\approx 0$
Misalignment About North Axis	NA	$\approx 0$ (during 1st hour)	Foucault Modulated Schuler Sinusoid	Schuler Peak -7 nm per 1 mr
Misalignment About East Axis	Foucault Modulated Schuler Sinusoid	Schuler Peak -7 nm per 1 mr	NA	$\approx 0$ (during 1st hour)

(\*  $\approx 0$  means  $\leq 1 \text{ nm}$  for the waveform magnitude)

Table 6.0 Error Sensitivities Computed from SIRU Test Data for the First Two Hours and Draper Lab Latitude

#### 6.4 Error Propagation in a Dynamic Environment

In a dynamic environment the principal errors arise from the following causes: OA coupling, anisoinertia, SRA cross coupling due to float offset, and scale factor errors. In SIRU, only OA coupling compensation was implemented. Anisoinertia and SRA cross coupling errors tend to cancel each other for the particular nominal measured parameters of the SIRU gyros in the test range of amplitude for oscillations and slews. This condition is determined as follows.

### 6.4.1 Anisoinertia and Float Offset Drifts

Define:

$$\begin{aligned} W_{ANISO} &= \text{Drift due to anisoinertia} \\ W_{AFA} &= \text{Drift due to float offset} \\ I_{SA}, I_{IA} &= \text{Moment of inertia of the gyro float about} \\ &\quad \text{its spin and input axes, respectively.} \end{aligned}$$

The anisoinertia drift is given by:

$$W_{ANISO} = W_{SRA} W_{IA} \left( \frac{I_{SA} - I_{IA}}{H} \right) \quad (6.18)$$

where:

$$\begin{aligned} W_{SRA} &= \text{Angular velocity about Spin Reference Axis} \\ W_{IA} &= \text{Angular velocity about Input Axis} \\ I_{SA} &= \text{Polar moment of inertia with respect to the} \\ &\quad \text{Spin Axis} \\ I_{IA} &= \text{Polar moment of inertia with respect to the} \\ &\quad \text{Input Axis} \\ H &= \text{Gyro wheel angular momentum} \end{aligned}$$

A typical value for  $\frac{I_{SA} - I_{IA}}{H}$  is given by:

$$\frac{I_{SA} - I_{IA}}{H} = 1.44 \times 10^{-4} \text{ rad/rad/sec} \quad (6.19)$$

For small gyro float angles:

$$W_{AFA} = -W_{SRA} A_{FA} \quad (6.20)$$

where  $A_{FA}$  is the float offset from null that results from closed loop operation.

It has been demonstrated, with the ternary torquing control used in the SIRU configuration, the float offset angle corresponds very closely to:

$$A_{FA} = K_1 + K_2 W_{IA} \quad (6.21)$$

$K_1$  represents the average null offset that occurs with low rate inputs (bias, earth rate, etc) where the torque loop and float dynamics are such that the float average offset is within the ternary threshold.  $K_2$  corresponds to the average offset that reflects the effective "hang off" that occurs with rates about IA in a ternary torque-to-balance control loop.

Typical values for  $K_1$  and  $K_2$  are given by:

$$\begin{aligned} K_1 &= 15 \mu\text{rad} \\ K_2 &= 148 \mu\text{rad/rad/sec} \end{aligned} \quad (6.22)$$

The combined anisoinertia and SRA cross coupling drift is given by:

$$\begin{aligned} W_{DA} \Delta &= W_{AFA} + W_{ANISO} = K_1 W_{SRA} + \left[ \frac{I_{SA} - I_{IA}}{H} - K_2 \right] W_{SRA} W_{IA} \\ &= -15 \times 10^{-6} W_{SRA} - 4 \times 10^{-6} W_{SRA} W_{IA} \end{aligned} \quad (6.23)$$

Note the canceling effect between the anisoinertia error and the "hang-off" cross coupling error:

From Eq. 6.23 it can be seen that the float offset (corresponding to the null region term,  $15 \times 10^{-6} W_{SRA}$ ) contributes an error of 15 ppm which is in the same range as the scale factor stability for the gyro. The combined anisoinertia, "hang-off" ( $K_2$  term) and SRA coupling drift ( $4 \times 10^{-6} W_{SRA} W_{IA}$ ) is also negligible for any rate range of interest.

If one were to consider a typical SIRU test position, calibration position #2, then for an applied table rate,  $W_T$ , four gyros (A, B, C, D) see components of rate about their IA and SRA.

The component of input axis and spin axis rate corresponding for each of these gyros is listed in Eqs. 6.24-6.27.

$$\text{A Gyro} \begin{cases} W_{IA} = W_T \sin \alpha, & W_{SRA} = -W_T \cos \alpha \\ W_{DA} = 12.8 \times 10^{-6} W_T + 1.78 \times 10^{-6} W_T^2 \end{cases} \quad (6.24)$$

$$\text{B Gyro} \begin{cases} W_{IA} = -W_T \sin \alpha, & W_{SRA} = W_T \cos \alpha \\ W_{DA} = -12.8 \times 10^{-6} W_T + 1.78 \times 10^{-6} W_T^2 \end{cases} \quad (6.25)$$

$$\text{C Gyro} \begin{cases} W_{IA} = -W_T \cos \alpha, & W_{SRA} = -W_T \sin \alpha \\ W_{DA} = 7.9 \times 10^{-6} W_T - 1.78 \times 10^{-6} W_T^2 \end{cases} \quad (6.26)$$

$$\text{DGyro} \begin{cases} W_{IA} = -W_T \cos \alpha, & W_{SRA} = -W_T \sin \alpha \\ W_{DA} = 7.9 \times 10^{-6} W_T - 1.78 \times 10^{-6} W_T^2 \end{cases} \quad (6.27)$$

Note that:

$$\begin{aligned} \alpha &= \text{SIRU geometrical angle} \\ \sin \alpha &= 0.5257311122 \\ \cos \alpha &= 0.8506508083 \end{aligned} \quad (6.28)$$

For an oscillatory table input the average magnitude of drift,  $W_{DA}$ , in each of the equations, Eqs. 6.24 through 6.27, reduces to:

$$|\overline{W}_{DA}| \cong (1.8 \times 10^{-6}) \overline{W}_T^2 \quad (6.29)$$

The oscillatory table input magnitude,  $W_T^2$ , is:

$$W_T^2 = \frac{A^2 W^2}{2} \quad (6.30)$$

where:

$$W_T = A W \cos (Wt + \psi) \quad (6.31)$$

Thus, for an oscillatory table input, Eq 6.29 can be written as

$$|\bar{W}_{DA}| = \frac{\left(\frac{A}{57.3}\right)^2 (2\pi f)^2}{2} \times 1.8 \times 10^{-6} \quad (6.32)$$

$$= A^2 f^2 \times 10^{-8}$$

where A is the amplitude (i.e. 1/2 p-p) in degrees, f in Hz, and  $W_{DA}$  in rad/sec. In degrees per hour  $W_{DA}$  is given by:

$$|\bar{W}_{DA}| = .0021 A^2 f^2 \quad (6.33)$$

Table 6.1 lists the theoretical values for  $W_{DA}$  for those values of A and f used in oscillation tests actually run with SIRU.

Table 6.1 Theoretical Average Anisoinertia and SRA Cross Coupling Drift,  $W_{DA}$ , for Oscillatory Input to the Test Table

Motion About Vertical Axis (Cal. 2, pos.)	Average Drift $W_{DA}$ (deg/hr)
0.1 hz, 0.8° P-P	$3.36 \times 10^{-6}$
1.0 hz, 0.8° P-P	$3.36 \times 10^{-4}$
1.0 hz, 10° P-P	$5.25 \times 10^{-2}$
0.5 hz, 15° P-P	$3.0 \times 10^{-2}$

The average drifts shown above are much smaller than pseudo-coning drifts that arise from OA coupling (as will be shown in the next section).

For slew tests, the offset term,  $K_1 W_{SRA}$ , in Eq. 6.23 does not average out to zero and both terms (involving  $K_1$  and  $K_2$ ) must be used. These equations are given by Eqs. 2.26 through 6.29. The equations are transformed as shown below to yield degrees per hour for  $W_T$  in deg/sec.

$$\text{A Gyro } \{W_{DA} = .046 W_T + .0001 W_T^2 \quad (6.34)$$

$$\text{B Gyro } \{W_{DA} = -.046 W_T + .0001 W_T^2 \quad (6.35)$$

$$\text{C Gyro } \{W_{DA} = .028 W_T - .0001 W_T^2 \quad (6.36)$$

$$\text{D Gyro } \{W_{DA} = .028 W_T - .0001 W_T^2 \quad (6.37)$$

The equivalent drifts in degrees per hour about the body reference axes (X, Y, Z) due to  $W_{DA}$  for each gyro are given by:

$$\left[ \begin{array}{l} \text{Drift} \\ \text{About} \\ \text{X-Axis} \end{array} \right] \triangleq W_{DAX} = 8.5 \times 10^{-5} W_T^2 \quad (6.38)$$

$$\left[ \begin{array}{l} \text{Drift} \\ \text{About} \\ \text{Y-Axis} \end{array} \right] \triangleq W_{DAY} = 0 \quad (6.39)$$

$$\left[ \begin{array}{l} \text{Drift} \\ \text{About} \\ \text{Z-Axis} \end{array} \right] \triangleq W_{DAZ} = 8.5 \times 10^{-5} W_T^2 \quad (6.40)$$

The drifts given by Eqs. 6.38 through 6.40 were evaluated by slew testing with different test table rates with the system in calibration position #2. The resulting data is summarized in Table 6.2.

Table 6.2 Theoretical Anisoinertia and SRA Cross Coupling Drift For Slew Inputs to the Test Table

Slew Rate About Test Table Vertical Axis (Cal 2 Position)	Body Axis Drifts		
	$W_{DAX}$ (deg/hr)	$W_{DAY}$ (deg/hr)	$W_{DAZ}$ (deg/hr)
1°/sec	$8.5 \times 10^{-5}$	0	$8.5 \times 10^{-5}$
5°/sec	$2.12 \times 10^{-3}$	0	$2.12 \times 10^{-3}$
10°/sec	$8.5 \times 10^{-3}$	0	$8.5 \times 10^{-3}$
20°/sec	$34 \times 10^{-3}$	0	$34 \times 10^{-3}$

Note that the drifts about the vertical axis (X SIRU reference axis) are least likely to influence navigation errors in a 1/2 hour test (see Table 6.0-Gyro Drift about the Vertical Axis). From the data shown in Table 6.0, one would note that for navigation performance a maximum longitude error of 1.3nm would occur, corresponding to a continuous 20°/sec slew input in the 1/2 hour test. The latitude error should remain close to zero.

#### 6.4.2 Pseudo-Coning Drifts $W_{PC}$

The pseudo-coning drift for SIRU without OA coupling compensation is given by:

$$W_{PC} = .85 \frac{I}{H} W_T^2 \quad (6.41)$$

where  $W_{PC}$  is about the Z axis (for calibration position #2) and

I = Output axis float moment of inertia

H = Gyro angular momentum

Substituting the value 225/151000 for I/H and making appropriate substitutions for  $W_T$  yields the following:

$$W_{PC} = 1.560 A^2 f^2 \text{ } ^\circ/\text{hr} \quad (6.42)$$

where A is in degrees, f is in Hz, and  $W_{PC}$  is in deg/hr. Table 6.2 lists  $W_{PC}$  for the oscillation tests run with the SIRU system.

Table 6.3 Theoretical Pseudo-Coning Drifts for Oscillatory Inputs to the Test Table and No OA Coupling Compensation

Motion About Vertical Axis (Cal Pos 2)	Pseudo-Coning Drift ( $W_{PC}$ ) (deg/hr)
0.1 hz, 0.8° P-P	$2.49 \times 10^{-3}$
1.0 hz, 0.8° P-P	$2.49 \times 10^{-1}$
1.0 hz, 10° P-P	$3.90 \times 10^1$
0.5 hz, 15° P-P	$2.19 \times 10^1$

Comparing Table 6.3 with Tables 6.1 and 6.2 shows that OA coupling compensation is by far the most important.

These test results illustrate that, as derived, there is a large measure of self-canceling of SRA cross coupling, and anisoinertia error propagations for the particular SIRU gyro and control loop configurations used. Because of this self-canceling and the relatively small error that would be induced by dynamics, no software compensation routines were implemented. Test studies were also conducted during the Strapdown Performance Optimizations Testing program (see CSDL Report R-743) and suitable compensation software for anisoinertia and SRA cross coupling was developed. This software will be incorporated for completeness in the SIRU routines in future applications.

An OA coupling compensation routine was implemented in the SIRU configuration. The routine that was used is described and documented in full in CSDL Report R-746, Vol. I and Vol. III. Test data error propagation profiles with and without OA coupling, showing the pseudo-coning error propagation for several oscillatory inputs applied about the X SIRU reference axis, are illustrated in Chapter 7 of R-745, Vol. I. It is interesting to note that the triad rate solution, which is fault tolerant, is used directly to estimate the compensation required for OA coupling because all the gyro OA's lie in orthogonal reference planes in the SIRU geometry.

OA coupling compensation is achieved by estimating the rate that was seen on the OA axes of a specified computational interval based on the computed XYZ triad rates. This rate is scaled corresponding to the gyro I/H and the iteration period. The resulting corrective angle increments are fed to the corresponding registers of the gyros that are experiencing the OA input. Table 6.4 summarizes a series of tests conducted with different oscillatory inputs in which attitude algorithm performance with and without OA coupling compensations was evaluated.

The system was positioned in calibration position #2 (Fig. 7.1, Chapter 7, X-down, Y-east, Z-south) at the start of each quaternion attitude algorithm test. Each of the ten tests was conducted for approximately a 100 second duration. No instruments were failed during these tests.

For each test, scale factor compensation, earth rate compensation, and other static compensations were loaded into the algorithm program (the equivalent end-to-end drift for the case with OA coupling compensation is not necessarily only due to OA coupling compensation errors but is the sum total of other errors, including possible scale factor uncertainties and drift coefficient instabilities).

X-Axis OSC. Inputs	Without OA Coupling Compensation	With OA Coupling Compensation	
	Actual Pseudo- Coning Drift (o/hr)	End-to-End Error Expressed in equiv. o/hr	Attitude Error
15° P. P. at 0.5 Hz	21.75	<0.30	<16 sec
20° P. P. at 0.25 Hz	15.05	<0.30	<16 sec
3/4° P. P. at 3 Hz	1.05	<0.30	<16 sec
2° P. P. at 1 Hz	1.50	<0.30	<16 sec
1/4° P. P. at 5 Hz	None Apparent	<0.06	< 4 sec

Table 6.4 Attitude Drift with and without OA Coupling Compensation

#### 6.4.3 Examination of SIRU Test Data for Dynamic Inputs

Table 6.5 lists the navigation data from a number of 1/2 hour tests with dynamic inputs (oscillations and slews about the test table vertical axis). Tests not shown in Table 6.5 were run with  $RW^2$  and  $R\dot{W}$  normalization for the accelerometers.

Unfortunately, there was an error in the normalization mechanization which resulted in significantly larger errors without the normalization. The mechanization error was due to a computer register overflow. Time did not permit correction of the software and retesting.

Section I (Static Base Line Tests) of Table 6.5 shows the results for SIRU with no dynamic inputs and in calibration position #2. It can be seen that all of the position errors are within 1/2 nm for the first 1/2 hour. From Table 6.0 we conclude that the accelerometer biases were well within  $0.1 \text{ cm/sec}^2$  and that the gyro drift along the computational axis was on the order of  $0.015 \text{ deg/hr}$ .

Section II (Oscillatory Tests—All Compensation Routines Used) shows that for the 1 Hz oscillation the Z computational axis of the system has a drift of about  $0.090^\circ/\text{hr}$  (see Table 6.0) assuming that the accelerometer errors are negligible. This Z axis drift can be attributed to various drifts in any combination of gyros A, B, E, and F. However, gyros E and F have their output axes vertical (i.e. their IA and SRA are perpendicular to the vertical axis). Hence for the calibration position #2 we would suspect that the drift is due to gyros A and B. The drift cannot be due to pseudo-coning (see Table 6.2) and hence must be attributable to the A or B gyro. In Chapter 3 (Single Position Self Calibration) Section 3.10.3 Eq. 3.60, we see that,

Table 6.5 SIRU Navigation Tests for Dynamic Environments

All tests run with SIRU test table in Cal. pos. #2. Errors are those at 1.2 hour after test initiated with zero initial conditions. The C gyro was failed in all tests done before July 15, 1972 .

	Type Test	Test Description	Date (1972)	Lat. Error (NM)	Lon. Error (NM)	Position Error (NM)
I	Static Base-Line Tests	Static-all compensation terms present	6/23	0.065	0.032	0.073
			6/29	0.087	0.08	0.118
			6/30	0.087	0.096	0.130
			7/5	0.259	0.160	0.304
			7/10	0.022	0.176	0.177
			7/21	0.108	0.449	0.462
		Static-all compensation terms present	7/24	0.540	0.096	0.549
Static-all compensation terms present	7/24	0.346	0.160	0.381		
II	Oscillatory tests All compensation terms present	0.1 Hz oscillation 0.8° p-p amplitude	6/30	0.173	0.608	0.632
		1.0 Hz oscillation 0.8° p-p amplitude	6/30	0.886	2.96	3.09
III	Osc. tests No OA compensation	0.1 Hz oscillation 0.8° p-p	6/30	0.324	0.34	0.47
		1 Hz oscillation 0.8° p-p	6/30	3.24	-6.55	6.8
IV	Osc. tests No RW <sup>2</sup> & RW compensation	0.1 Hz oscillation 0.8° p-p	6/30	0.305	0.576	0.652
		1 Hz oscillation 1° p-p	6/29	1.15	4.16	4.3
V	Slew tests No RW <sup>2</sup> & RW compensation	1°/sec slew	4/11/73	0.65	0.064	0.653
		10°/sec slew	4/11/73	0.3	0.112	0.32
		20°/sec slew	4/11/73	0.086	0.384	0.394

for an oscillatory environment, gyros A and B do have dynamically induced drift on the order of  $-0.069^{\circ}/\text{hr}$  for A and  $-0.021^{\circ}/\text{hr}$  for B when the oscillation is  $1/6^{\circ}$  p-p at 1/2 Hz. This data indicates that the A gyro is sensitive to oscillations. We cannot, however, attribute this sensitivity to anisoinertia drift (see Table 6.1). It is now believed that this sensitivity to oscillations is due to a characteristic of the pulse torque-to-balance loop H switch in some of the gyro modules (See the remarks at the end of Chapter 3).

Section III (Oscillatory Tests, No OA Coupling Compensation) shows an increase in the position error over the Section II data for 1 Hz oscillations. Longitude error is  $-6.55$  nm at the end of 1/2 hour. This error corresponds to the pseudo-coning drift of  $0.249^{\circ}/\text{hr}$  presented in Table 6.3. The latitude error increased from less than 1 nm in Section II to 3.24 nm in Section III (for the 1 Hz oscillation). This comparison demonstrates that there may be another source of error arising (other than pseudo-coning) when the OA coupling compensation is removed. The oscillatory tests of Section IV (Oscillatory Tests, No  $RW^2$  and  $R\dot{W}$  Compensation) demonstrate that when OA coupling compensation is restored, there is an improvement in drift along both the Y and Z axes. It also confirms that A and B gyro drifts are induced by the 1 Hz oscillations as was shown in Section II (See the note accompanying the Comments on Section II data).

Section V (Slew Tests, No  $RW^2$  and  $R\dot{W}$  Compensation) demonstrates that the drifts in the A and B gyros induced by the oscillations are not present when the system is slewed about the vertical axis.

Note that whenever OA coupling compensation is implemented (Sections II, IV, and V), it is stable and leads to no oscillations or instability in the navigation and attitude algorithms as had been conjectured as possible.

Figures 6.12 and 6.13 show the error propagation resulting from a  $5^{\circ}/\text{sec}$  slew about the vertical axis. If the curves are examined, it is evident that for the first two hours, the longitude error is dominated by a ramp and most of the error is due to gyro drift about the north axis (the average slope is  $-1.9$  nm/hr and the drift is  $0.030^{\circ}/\text{hr}$  in the north axis). The latitude error hovers about zero during the first 2 hours and is dominated by a Schuler waveform with a magnitude of 1 nm (this drift could be due to a very small accelerometer bias of  $0.14$   $\text{cm}/\text{sec}^2$  about the east axis). Note that after 2 hours there is enough cross coupling to make both latitude and longitude errors appear to ramp. For the calibration position #2 the ramps can be caused by drift about the vertical axis and the north axis. This conclusion implies that the cause of the drift can be either anisoinertia and SRA cross-coupling

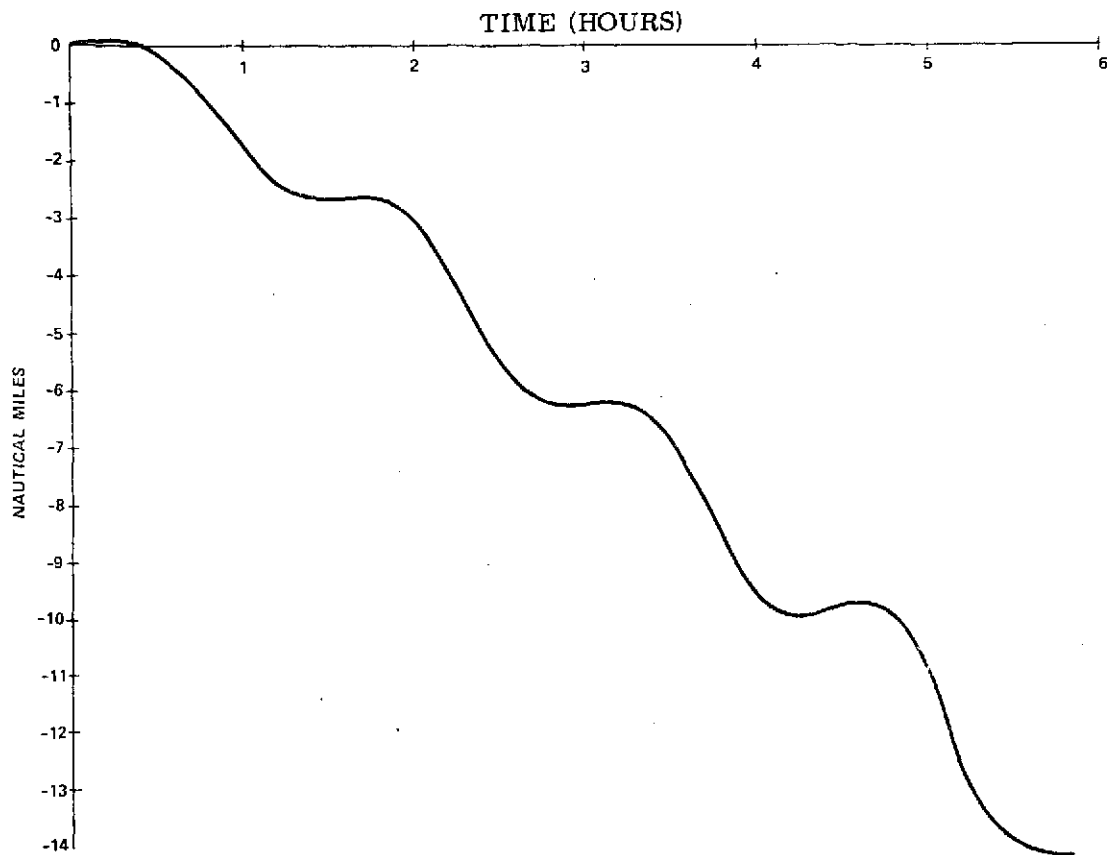


Fig. 6.12 SIRU Navigation Performance Longitude Error  $5^{\circ}$ /second (for 6 hours) About the Vertical Axis

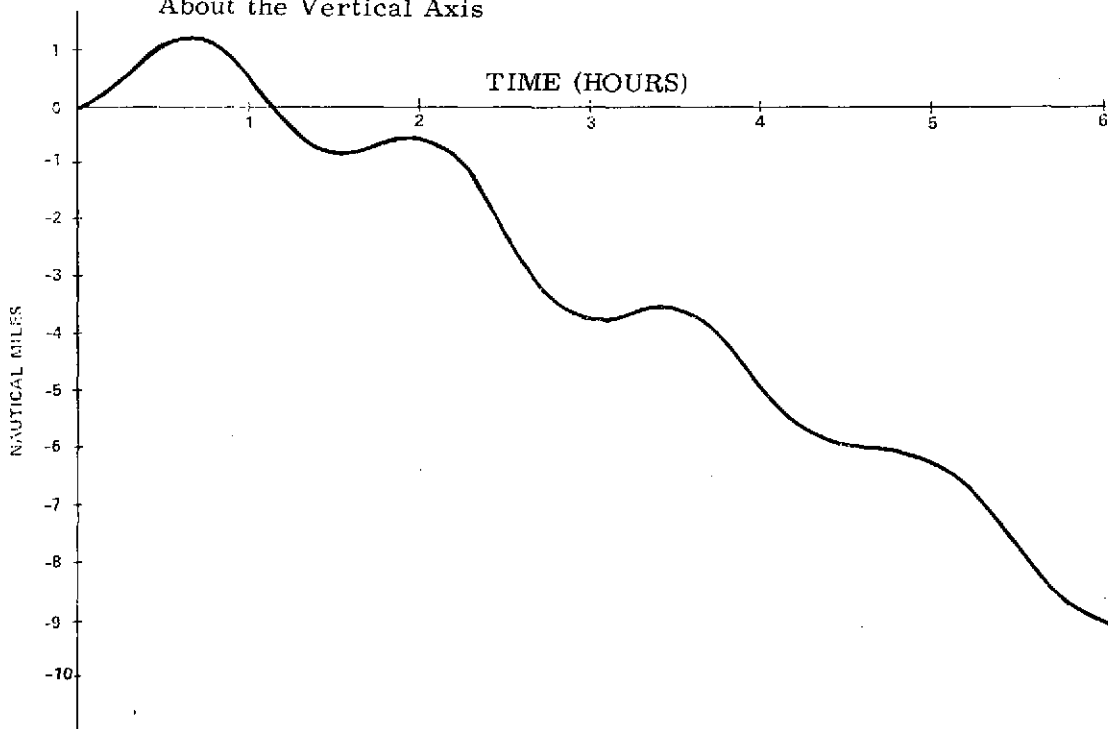


Fig. 6.13 SIRU Navigation Performance Latitude Error  $5^{\circ}$ / second (for 6 hours) About the Vertical Axis

drift (see Table 6.2) about the vertical, X, body axis or scale factor error in gyros A, B, C, or D. The scale factor error can arise because gyros A, B, C, and D have a vertical component in their input axes. At  $5^{\circ}/\text{sec}$ , a drift of  $0.030^{\circ}/\text{hr}$  corresponds to a 1.7 ppm scale factor error.

#### 6.4.4 Examination of SIRU Test Data for Errors Propagated when FDICR is Implemented

The FDICR (Failure Detection, Isolation, Classification and Recompensation) system, implemented for the tests presented below, is fully described in Chapter 2 of this report. Briefly, FDICR for gyros consists of the TSE method of parity equation error detection (described in CSDL Report R-746, SIRU Development Final Report) based on deterministic principles, for detection and isolation of large degradations ( $0.75 \text{ deg/hr}$  and above) and the statistically derived FDICR (see Chapter 2) used for detecting and isolating failures as low in magnitude as the noise standard deviation, and also for classifying the failure as a bias shift, ramp, or increase in variance, and then recompensating for the failure if it is a bias shift or ramp.

The accelerometer FDICR consists solely of the TSE method for degradation detection and isolation. It also includes a procedure for classification (whether the failure is a bias shift or ramp) and recompensation.

Failures (ramps and bias shifts) were simulated in the tests by modifying the system software. This failure simulation was accomplished by appropriately changing the NED compensation value for the particular gyro and the bias compensation for the particular accelerometer as designated by the test procedure.

Tables 6.6, 6.7 and 6.8 list navigation errors propagated as a result of the delay in detecting and isolating gyro and accelerometer constant bias degradations.

Section II of Table 6.6 lists navigation errors propagated due to the delay in detecting and isolating gyro constant bias degradations. Note that all of the position errors are in the order of 1-2 nm (equivalent to  $0.015$  to  $0.030^{\circ}/\text{hr}$  per axis) with the exception of test 3. Here the A and B gyros were "degraded" by the introduction of  $0.15^{\circ}/\text{hr}$  constant biases. This is approximately equivalent to a total tilt about the Z axis of  $1/4 \text{ mr}$ . Table 6.0 shows that such an error will introduce approximately 2 nm peak error in longitude. This factor accounts for most of the 3 nm error in longitude (see test 3 Section I, Table 6.6). The other tests (1 and 2) were run on different days than tests 4 and 5, and it is conjectured that the 1.6 nm and -1.1 nm

### I. Listing of Gyro Failure Tests

Test Number	Date (1972)	No. of Instr. Failed	Gyro	Bias Mag. (°/hr)	Time at Failure (Min)	Time at Failure Detection and Isolation (Min)	Time at Classification (Min)
1	9/22	2	C	0.15	4	12	22
			D	0.15	24	30	34
2	9/22	1	A	0.09	4	30	40
3	9/22	2	B	0.15	4	14	20
			A	0.15	24	32	36
4	9/21	2	E	0.15	0	10	18
			F	0.15	24	34	40
5	10/11	2	D	0.15	4	14	18
			A	0.22	24	30	36

### II. Land Navigation Errors for Each Test in I.

Test Number	Time at Error Measurement (Min)	Latitude Error in Nautical Miles (NM)	Longitude Error (NM)	Position Error (NM)
No Failures 9/22/72	58	0.56	-0.09	0.57
No Failures 9/22/72	34	0.10	0	0.10
1	50	0.8	1.6	1.8
2	50	0.06	-1.1	1.1
3	60	0.5	3.3	3.34
4	62	-0.13	0.4	0.42
5	86	-0.3	-0.7	0.76

Table 6.6 Land Navigation Errors Due to Delay in Detecting and Isolating Gyro Constant Bias Degrations

longitude errors of these two tests are due to uncompensated drift before the failures were introduced. This result is possible even though the longitude error doesn't show in the "NO FAILURES" test of 22 September 1972 because vertical drifts take more than 1 hour to show an effect on latitude and longitude errors.

Table 6.7, Section II lists navigation errors due to the delay in detecting and isolating accelerometer constant bias degradations. Note that the position errors are all on the order of 1 nm or less and represent errors caused by gyro drifts (this system is calibrated to within  $0.015^\circ/\text{hr}$ ). These results indicate that negligible errors are introduced when the detection and isolation of an accelerometer bias degradation of  $0.1$  or  $0.2 \text{ cm}/\text{sec}^2$  are delayed.

### I. Listing of Accelerometer Failure Tests

Test Number	Date 1972	No. of Instr. Failed	Accelerometer	Bias Mag. (cm/sec)	Time at Failure (Min)	Time at Failure Detection and Isolation (Min)	Time at Classification (Min)	Estimated Const. Bias (cm/sec)
1	9/26	2	B	-0.1	4	8	18	-0.092
			A	0.1	24	28	38	0.104
2	9/28	2	F	0.1	4	8	18	0.085
			E	0.2	24	26	36	0.23
3	9/28	2	D	-0.1	4	8	18	-0.11
			C	-0.1	24	26	38	-0.095
4	9/27	2	A	0.1	4	10	20	0.095
			D	-0.2	24	26	36	-0.21

### II. Land Navigation Errors for Each Test in I.

Test Number	Time at Error Measurement (Min)	Latitude Error in Nautical Miles (NM)	Longitude Error (NM)	Position Error (NM)
1	72	-1.5	0.08	1.5
2	74	0.05	0.17	0.18
3	74	0.51	-0.33	0.61
4	56	0.12	-0.04	0.13

Table 6.7 Land Navigation Errors Due to Delay in Detecting and Isolating Accelerometer Constant Bias Degradations-Cal. 2 Pos.

### I. Listing of Instrument Failure Tests

Test Number	Date 1972	No. of Instr. Failed	Instrument	Bias Mag.	Time at Failure (Min)	Time at Failure Detection and Isolation (Min)	Time at Classification (Min)
1	9/21	2	E Acc.	1 cm/sec <sup>2</sup>	4	4	16
			E Gyro	0.15°/hr	24	30	38
2	10/11	2	F Gyro	6 °/hr	4	4	10
			A Acc.	2 cm/sec <sup>2</sup>	24	24	36

### II. Land Navigation Errors for Each Test in I.

Test Number	Time at Error Measurement (Min)	Latitude Error in Nautical Miles (NM)	Longitude Error (NM)	Position Error (NM)
1	50	-0.02	0.03	0.036
2	42	2.09	-0.9	2.28

Table 6.8 Land Navigation Errors Due to Delay in Detecting and Isolating Gyro and Accelerometer Constant Bias Degradations Cal 2 Position

Section II, Table 6.8 lists errors due to the delay in detecting and isolating gyro and accelerometer bias degradations. Note that test 2 lists a latitude error of 2 nm. This discrepancy possibly arises from the delay in detecting the  $6.0^{\circ}/\text{hr}$  degradation in the F-gyro (since the F-gyro contributes to the drift about the Y body axis). Table 6.8, Section I does not show that there is actually a delay on the order of tens of milliseconds between the initiation of the  $6.0^{\circ}/\text{hr}$  gyro failure and its detection and isolation.

As a supplement to the laboratory dynamic tests the results of which have been presented above, Appendix A.6 contains the results of simulations made for typical space shuttle trajectories. In these simulations, those instruments having the best sensing axes for the particular trajectory being considered were failed.

#### 6.5 Software Memory and Timing Requirements

The following are the memory and timing requirements for implementation of the land navigation program in the Honeywell DDP-516 computer:

Memory: 505 words  
Timing: 1.413 msec per update  
Update rate: once per second

Percentage of Computer time for an attitude update rate of 50 hz: 0.14%.

Appendix A6

SIRU Software Simulation Results

The SIRU dodecahedron IMU has been mathematically modeled and subsequently coded in software to provide projected navigation performance information in typical space shuttle trajectories. Recent closed loop simulations have employed a once around, Vandenberg launch, south polar orbit trajectory complete with vehicle dynamics and a thermal protection guidance law. Performance evaluations were made at an altitude of 100,000 feet so as to include the dynamic environments realized in the boost, cruise, transition and entry interface phases. South polar orbit trajectory time profiles of input body rate and body specific force are shown in Figs. A6.1 and A6.2, respectively.

Input performance parameters chosen for the SIRU software model are representative of actual Lockheed Agena inertial sensor performance (GG-334 gyros and GG 177A accelerometers) and are shown in Table A6.1. The resultant projected down range and cross range errors at 100,000 feet altitude are:

Cross Range Error = 1.64 nm  
Down Range Error = 2.18 nm\*

Table A6.1

SIRU Software Simulation Sensor Performance Parameters

GG 334 GYRO

Bias Drift	0.0162 °/hr.
Gyro Mass Drift IA	0.0349 °/hr./g
Gyro Mass Drift SA	0.054 °/hr./g
Positive Scale Factor	30 PPM
Negative Scale Factor	35 PPM
Alignment	13.4 arc-sec.

GG 177 ACCELEROMETER

Bias	21 $\mu$ g
Scale Factor Error	10 PPM
Alignment	6.5 arc-sec.

---

\* These 1 $\sigma$  RSS errors were derived by combining individual measurements of the error sensitivity of each sensor performance parameter using RSS calculations.

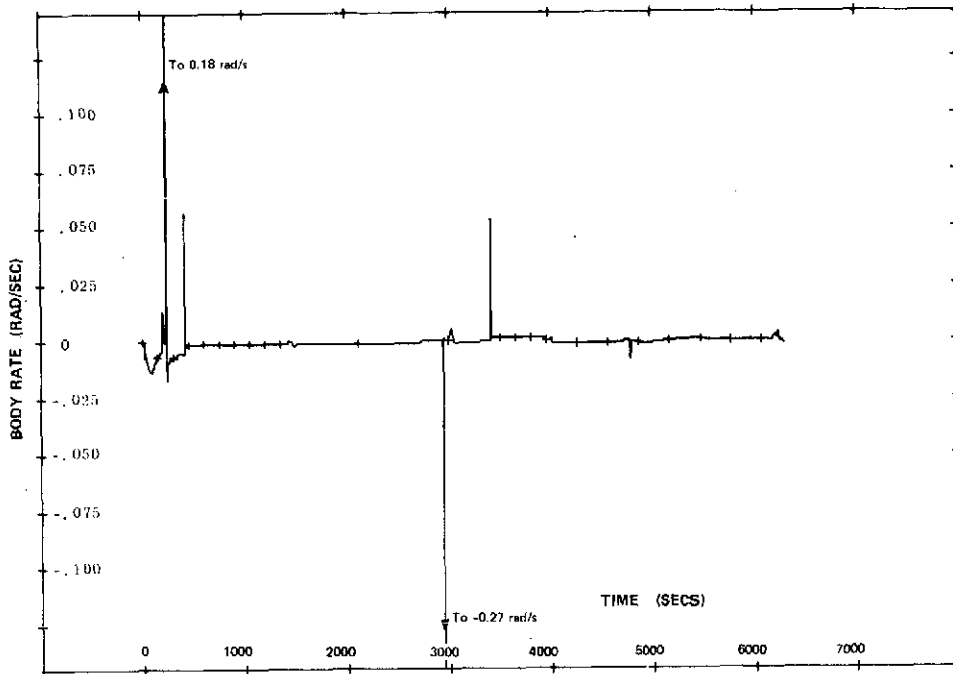


Fig. A6.1(a) Simulated Body Rate vs Time - Pitch

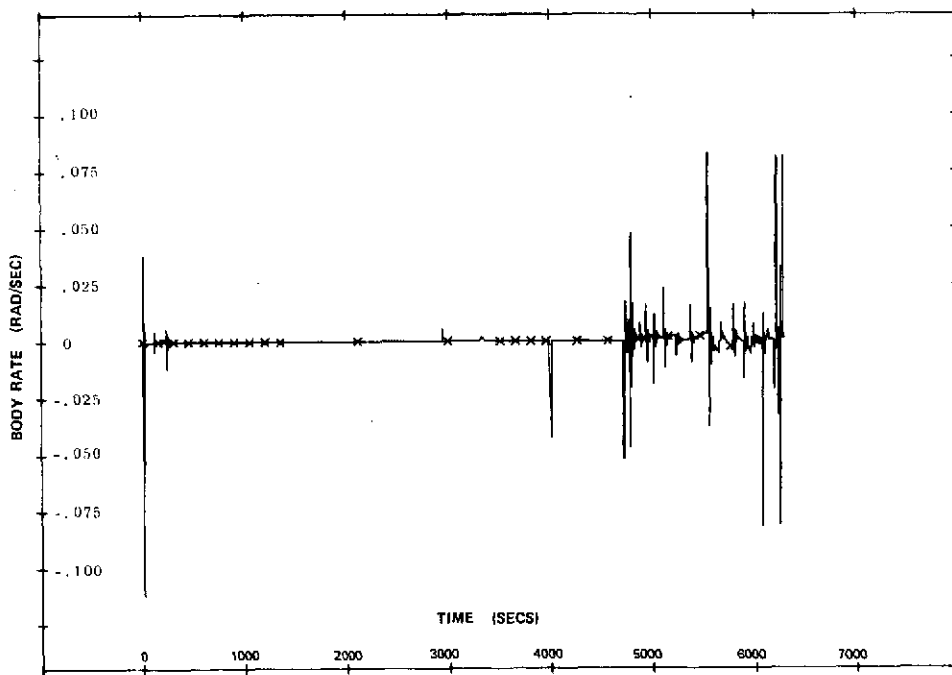


Fig. A6.1(b) Simulated Body Rate vs Time - Roll

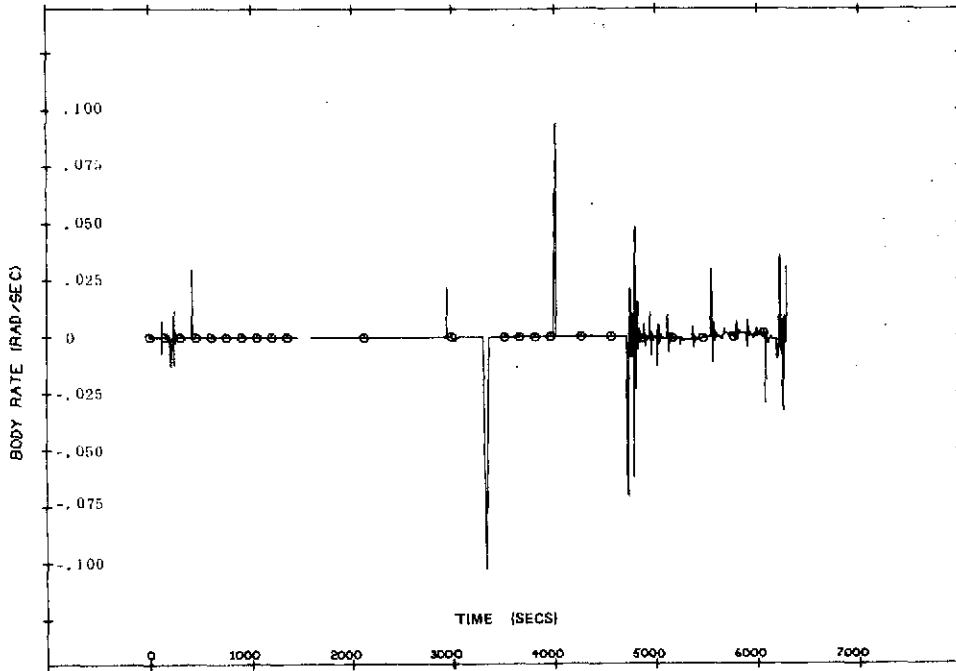


Fig. A6.1(c) Simulated Body Rate vs Time - Yaw

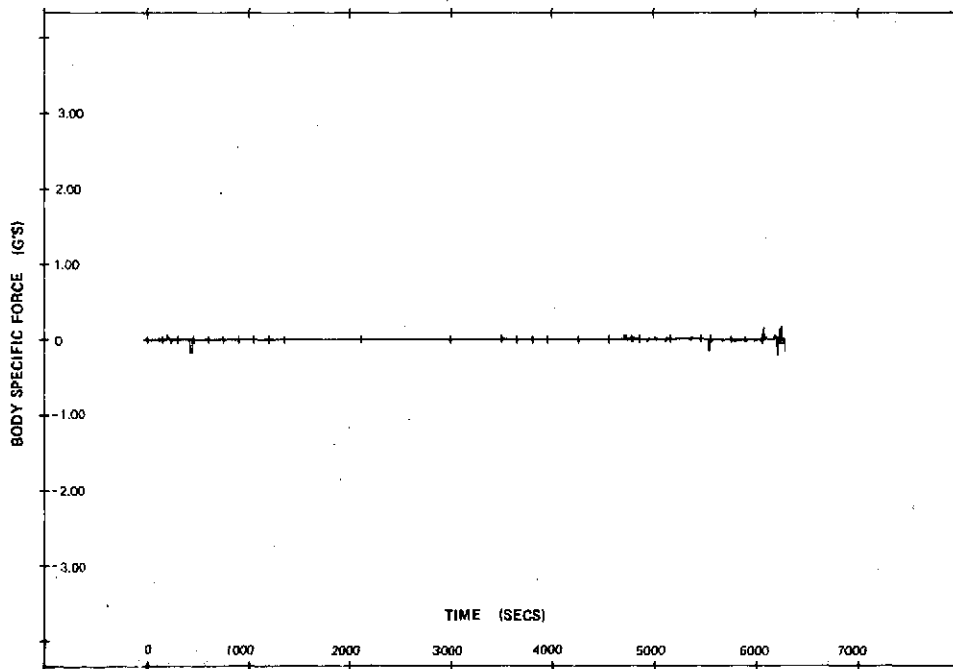


Fig. A6.2(a) Simulated Body Specific Force vs Time - Pitch

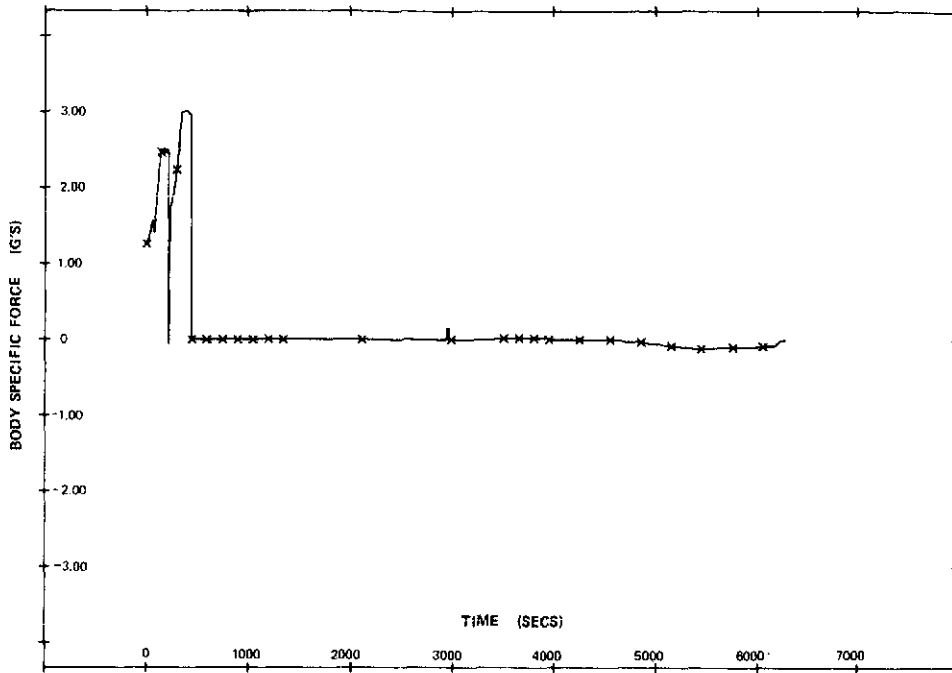


Fig. A6.2(b) Simulated Body Specific Force vs Time - Roll

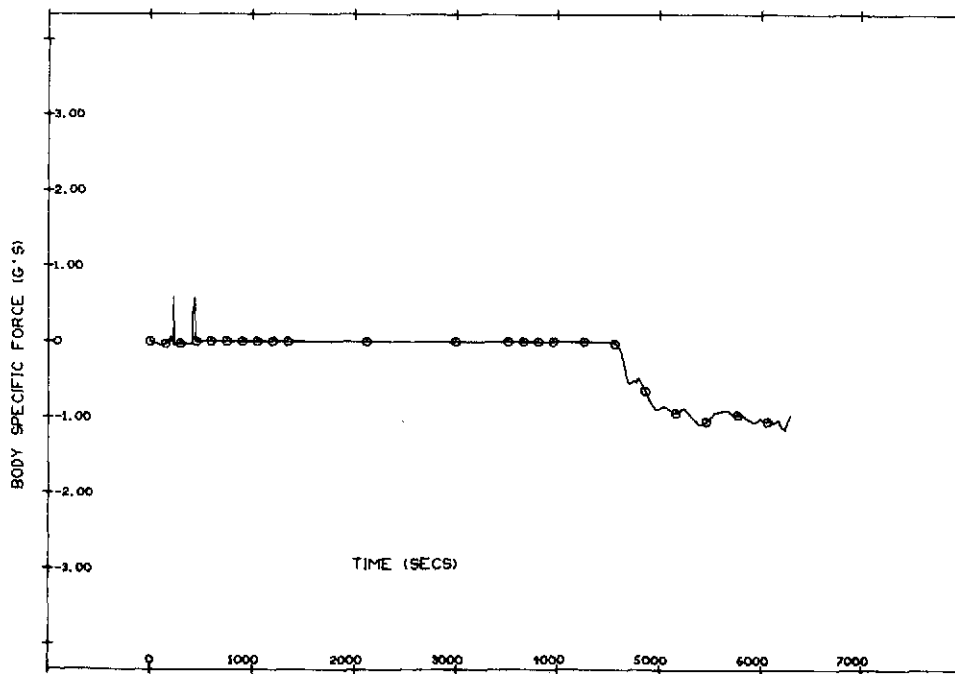


Fig. A6.2(c) Simulated Body Specific Force vs Time - Yaw

Error coefficients were derived for each sensor performance parameter and are presented in Table A6.2.

Table A6.2  
Sensor Performance Parameter Error Coefficients

<u>GG 334 GYRO</u>	<u>CROSS-RANGE ERROR</u>	<u>DOWN-RANGE ERROR</u>
Bias Drift	24.0 NM / <sup>o</sup> /hr.	11.3 NM / <sup>o</sup> /hr.
Gyro Mass Drift IA	7.66 NM / <sup>o</sup> /hr./g	7.54 NM / <sup>o</sup> /hr./g
Gyro Mass Drift SA	9.53 NM / <sup>o</sup> /hr./g	10.80 NM / <sup>o</sup> /hr./g
Gyro Scale Factor	0.0218 NM /PPM	0.0117 NM /PPM
Alignment	0.057 <sup>o</sup> /arc-sec.	0.036 NM /arc-sec.
 <u>GG 177 ACCELEROMETER</u>		
Bias	0.033 NM / $\mu$ g	0.066 NM / $\mu$ g
Scale Factor	0.014 NM /PPM	0.029 NM /PPM
Alignment	0.075 NM /arc-sec.	0.131 NM /arc-sec.
 <u>SYSTEM</u>		
Azimuth Alignment	0.0059 NM /arc-sec.	0.0169 NM /arc-sec.

In order to assess redundant strapdown system performance with a reduced number of inertial instruments, i.e., processing data from only good axes and rejecting data from "failed", detected and isolated axes, additional simulations employing the SIRU software model were exercised using the once around, Vandenberg launch, south polar trajectory.<sup>14</sup> In each simulation, failures were assumed to have occurred at lift-off and processing with the remaining reduced number of instruments was continued throughout the entire flight.

The induced failures, selected to correspond to "worst case" conditions for the once around trajectory that was used, were:

1. C-axis, and in another run C-and D-axis accelerometer processing was deleted (in the orientation used they are the best sensing axes for the measurement of the boost (max. g-sec) and the next best sensing axes in entry).

2. E-axis, and E-and F-axis gyro processing was deleted (these are the best sensing axes for monitoring the pitch-over maneuver in boost and they permit sensing approximately 50% of all the yaw maneuvering).
3. C- and E-axis gyro processing was deleted (deletion of these axes represents a 2 failure, "worst case" processing degradation in a spherical sense for the combined pitchover, yaw and roll entry maneuvers).
4. C- and D-axis accelerometer, and E-and F-axis gyro processing were also deleted (this deletion represents the extreme case of four failures at lift-off).

Several different initial states were used as the load for each of the instrument error sources.

- A. A load corresponding to the  $+1\sigma$  Agena error magnitudes as shown in Table A6.1 and the 1st column of Table A6.3 was introduced on each instrument for each corresponding error source.
- B. One load, selected from typical Monte Carlo runs (most values near  $1\sigma$  with some in the  $2\sigma$  &  $3\sigma$  range and with a random distribution of signs), was introduced similarly. This load is shown in the 2nd column of Table A6.3.
- C. A second load, selected from the Monte Carlo runs that yielded cross range and down range errors that were almost identical to the  $1\sigma$  RSS performance, was introduced. This load is shown in the 3rd column of Table A6.3.

The resultant error for each failure combination with each of the above loads was then compared to the  $1\sigma$  RSS errors of:

Cross Range Error = 1.64 nm  
Down Range Error = 2.18 nm

that were presented earlier in this Appendix.

To provide a basis of comparison, ratios were formulated that correspond to the cross range and down range errors resulting when processing with those

Table A6.3  
Performance Summary

	Lockheed Agena GG 334/G117	CANDIDATE COMPOSITE Mounting & Cooldowns --- 12 mos. (GG 334, 18 IRIG, K7G) -- Gyros (GG 177, 2401, 16 PMP)-- Accel	ASA 120 Day -- 1σ
• <u>GYRO</u>			
BD	0.016°/HR	0.12°/HR	0.15°/HR
ADIA	0.064°/HR/g	0.25°/HR/g	.25°/HR
ADSRA	0.035°/HR/g	0.15°/HR/g	.20°/HR
SF	35 ppm	75 ppm	130 ppm
Alignment	13.4 sec	20 sec	12 sec
• <u>Accel</u>			
BIAS	21μg	50μg	50μg
SF	10 ppm	60 ppm	30 ppm
Alignment	6.5 sec	25 sec	8 sec
• <u>AZ Align</u> (Optical)	60 sec	180 sec	60 sec
RSS-ERRORS			
CROSS RANGE	1.64 NM	5.24 NM	5.71 NM
DOWN RANGE	2.18 NM	6.6 NM	5.21 NM

DYNAMIC ERRORS (Uncompensated)  
GG 334/GG 177

CR  
0.30 NM  
0.40 NM

DR  
0.17 NM  
0.40 NM

TRAJECTORY  
RANDOM (EST.)

instrument combinations that remain after a specific failure combination divided by the above  $1\sigma$  RSS Errors, i.e.,

Ratio/CR = cross range error with selected failure divided by the  $1\sigma$  RSS CR Error (1.64 nm).

Ratio/DR = down range error with selected failure divided by the  $1\sigma$  RSS DR Error (2.18 nm).

Tables A6.4-A6.6 present the results of these simulations.

Table A6.4

Down Range and Cross Range Error Ratio Simulation Results \*

<u>FAILED Instr Axes</u>	<u>Ratio/CR</u>	<u>Ratio/DR</u>
No FAILS	0.09	0.20
C Accel.	0.144	0.087
C & D Accel.	0.492	0.947
E Gyro	0.036	0.416
E & F Gyro	0.208	0.598
C & E Gryo	0.187	0.249
C, D Accel. & E, F Gyro	0.807	1.355

\* Failures introduced per Load A and Agena error magnitudes on each instrument.

It is interesting to note that for each of the different loads, there were no significant variations between error source magnitudes. All individual errors were bounded within the  $3\sigma$  distribution in loads B and C. The variation in the resulting performance appears to be primarily a function of the distribution of error source signs with their corresponding random canceling through the trajectory. This probably explains why the performance with no failures, as well as for most failure combinations in Tables A6.4 and A6.5, is better than the predicted  $1\sigma$  RSS performance, i.e. the derived RSS of all individual error term coefficients taken singularly

(Reference 14 results shows that the RSS of the Monte Carlo runs were approximately 0.7 times our  $1\sigma$  RSS value ).

Table A6.5

Typical Monte Carlo Run\*

<u>Failed Instr Axes</u>	<u>Ratio/CR</u>	<u>Ratio/DR</u>
No FAILS	0.172	-0.125
C Accel.	1.201	-1.564
C & D Accel.	1.590	-2.176
E Gyro	-0.154	0.275
E & F Gyro	-0.741	0.919
C & E Gyro	-0.113	-0.120
C, D Accel. & E, F Gyro	0.824	-1.252

\* Corresponding to load B, random sign distribution typical  $1\sigma$  spread of instrument errors with some  $2$  and  $3\sigma$ .

Table A6.6

Monte Carlo Run with " $1\sigma$  RSS Performance"

<u>Failed Instr Axes</u>	<u>Ratio/CR</u>	<u>Ratio/DR</u>
No FAILS	1.13	-1.00
C Accel.	1.40	-1.09
C & D Accel.	1.62	-1.52
E Gyro	2.22	-2.02
E & F Gyro	2.31	-1.31
C & E Gyro	1.95	-2.60
C, D Accel. & E, F Gyro	2.05	-1.05

\* Corresponding to load C, approximately same DR and CR errors with no fails as in Table A6.1.

The runs made with the instrument error sources (load C) that did yield resulting trajectory errors, with no failures introduced, that closely approximated the  $1\sigma$  RSS performance value did not reflect any significant degradation with various failure combinations. In general, the errors, regardless of the fault combinations, are usually bounded within twice the  $1\sigma$  predicted trajectory error derived earlier in this Appendix.

Chapter 7  
End-to-End Navigation Demonstrations

7.0 Introduction

A number of end-to-end land navigation demonstrations with SIRU were held in order to verify the operation of SIRU Utilization software (described in Chapters 2 to 6), working as a whole. The test demonstration was a continuous sequence of modes starting with a single position calibration, followed by an alignment and then sequenced into local level land navigation operation. The FDICR software was operating during all of the phases of these tests. The demonstration software flow therefore simulated a preflight through inflight operational moding sequence. At various times failures were introduced into both gyros and accelerometers and FDICR was allowed to detect, isolate, classify and recompensate the failures. In all cases the FDICR was successful and the influence of failures with FDICR operation on system navigation performance with different test environment inputs were observed.

Figure 7.1 diagrammatically depicts the SIRU system on the 4-axis test table. Note that all slew and oscillatory inputs were imposed about the RA32 axis. For the offset position, all angular increments of the table axes are with respect to the calibration position #2 shown in the figure.

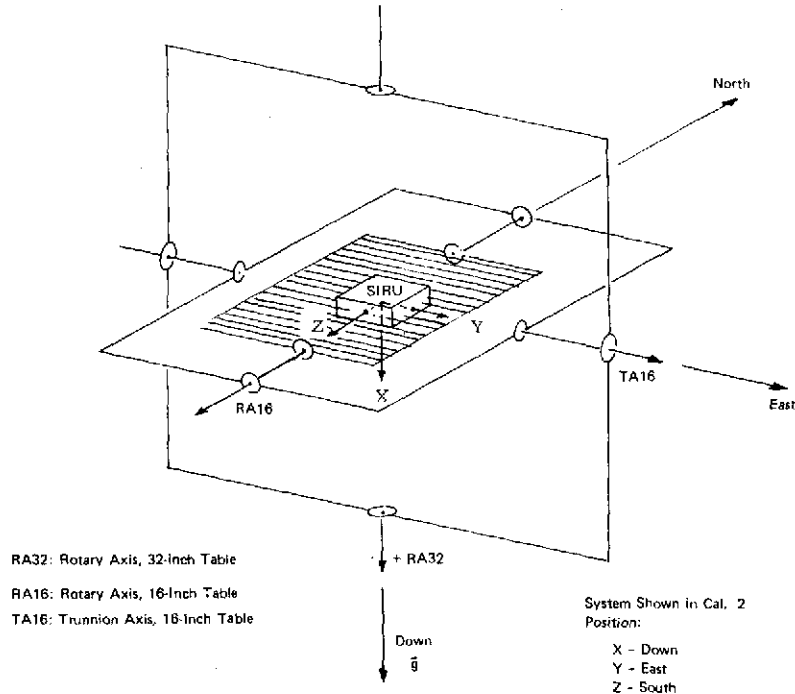


Fig. 7.1 SIRU Mounted on Test-Table System - Showing Orientation of 16 and 32 Inch Table Axes

Except where noted, the self-calibration program (Single Position Calibration) was performed just prior to the navigation program (which contains coarse-align, fine-align and FDICR). In the offset position a coarse-alignment was performed first so that the immediately following self-calibration program could be initialized with the approximate offset quaternion. A determination was made by the test engineer, after each self-calibration sequence, whether or not to update the bias compensation for gyros A, B, C or D.

Figures 7.2 to 7.9 depict the latitude and longitude errors during the respective test runs. Note that these figures have the appearance of broken-line graphs rather than smooth sinusoids for Schuler and 24 hour period error modes. This condition is due to sampling the errors relatively infrequently in order to ease the computation burden (the graphs are hand plotted). The actual errors are sinusoidal.

Table 7.1 lists the gyro and accelerometer failures that were simulated and the time of their insertion for each test demonstration conducted. It also identifies the time at which the FDICR software detected and classified the fault with the corresponding FDICR fault estimate and time of automatic recompensation.

## 7.1 Static Test Results

Three tests were run with a static SIRU environment, no motion (test sequence #1, #2 and #3).

### 7.1.1 Test Sequence #1 (Base line test, no failures were inserted)

SIRU was placed in the calibration position #2 (Fig. 7.1) and run for two hours.

#### 7.1.1.1 Gyro Self-Calibration Estimates

$$\begin{aligned}\epsilon_A &= -0.0084^\circ/\text{hr} \\ \epsilon_B &= -0.0024^\circ/\text{hr} \\ \epsilon_C &= 0.005^\circ/\text{hr} \\ \epsilon_D &= 0.010^\circ/\text{hr}\end{aligned}$$

These estimates were not used to recalibrate.

#### 7.1.1.2 FDICR Results

No failures were inserted and none were detected.

Table 7.1

Gyro and Accelerometer Failure Detection, Classification, and Recomensation Parameters During the Test Sequence

## (a) Gyros

Test Seq. #	Test Duration (h)	Instr. Axis	Simulated Failure Bias(B) (deg/h) or Ramp(R) (deg/h/min)	Time of Failure Insertion (min)	Time at Fail Detection (min)	Time at Classification (min)	Estimate of Bias or Ramp (deg/h)	Time at Recomp. (min)	Notes
2	14	F	(B) 0.15	60	68	80	0.1605	126	
2		A	(R) 0.015	120	134	148	0.0154	200	
3	15	D	(B) 0.15	60	64	72	0.1905	126	See Test Seq. #3
3		A	(B) 1.5	80	82	96	1.4820	150	
5	15	F	(B) 0.375	60	64	78	0.3630	138	See explanation in Test Seq. #5
5		A	(R) 0.0225	190	204	222	0.0222	276	
5		A	—	—	434	450	0.1965	504	
5		A	—	—	692	704	0.1950	764	
5		A	—	—	950	966	0.1980	1022	
6	18	D	(B) 0.375	60	64	70	0.4470	114	
6		A	(B) 2.25	80	82	88	2.2590	134	
7	2	A	(B) 0.225	0	8	18	0.2340	46	
7		D	(B) 0.225	10	18	22	0.2400	68	

## (b) Accelerometers

			(cm/s <sup>2</sup> )							(cm/s <sup>2</sup> )
2	14	C	(B) 0.20	60	64	74	0.18	74		
5		C	(B) 0.40	60	62	72	0.37	74		
7	2	C	(B) 1.00	0	2	18	0.99	20		
7		A	(B) 0.40	5	8	18	0.39	20		

### 7.1.1.3 Navigation Errors

Figure 7.2 shows the latitude error. During the 2 hour test, longitude error was less than 0.02 nm. Using the results of Chapter 6, we see that the latitude error slope is less than 1/2 nm/hr; hence, drift along a computation axis is less than  $0.0075^{\circ}$ /hr. This result indicates that only small initial residual errors existed in the SIRU system at the start of the test sequences.

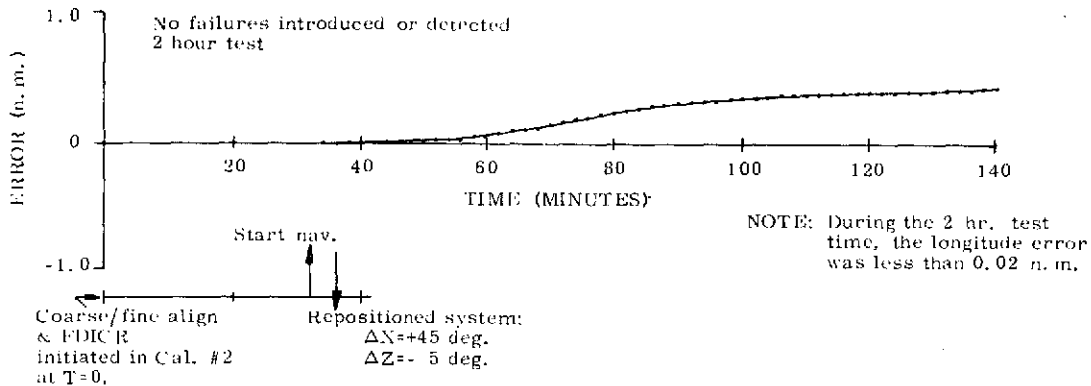


Fig. 7.2 Test #1 - Latitude Error

### 7.1.2 Test Sequence #2

SIRU was placed in an offset position with respect to calibration position #2 ( $\Delta RA32 = +45^{\circ}$ ,  $\Delta RA16 = +5^{\circ}$ , see Fig. 7.1) and run for 14 hours.

#### 7.1.2.1 Self-Calibration Estimates

$$\begin{aligned}
 \epsilon_A &= 0.040^{\circ}/\text{hr} \\
 \epsilon_B &= -0.025^{\circ}/\text{hr} \\
 \epsilon_C &= -0.001^{\circ}/\text{hr} \\
 \epsilon_D &= 0.034^{\circ}/\text{hr}
 \end{aligned}$$

Bias compensation corrections were inserted for the A, B, and D-gyros using the above values. These values are a result of the  $5^{\circ}$  tilt given to SIRU during this test sequence and show there is some uncompensated ADIA and/or ADSRA.

### 7.1.2.2 FDICR Results

The following deviations were inserted:

C-Accelerometer	Bias- $0.2 \text{ cm/s}^2$ at $t=60$ mins.
F-Gyro	Bias- $0.15^\circ/\text{hr}$ at $t=60$ mins.
A-Gyro	Ramp- $0.015^\circ/\text{hr}/\text{min}$ at $t=120$ mins.

All failures were properly detected, isolated, identified and appropriate recompensation applied (Table 7.1).

### 7.1.2.3 Navigation Errors

Figure 7.3 shows the propagation of latitude and longitude errors (note that for long runs (>2 hours) every 10th data point is plotted).

#### EVENTS DURING RUN: 2

1. At T=0, enter coarse/fine align FDICR program.
2. Enter nav. mode at T= 30 mins.
3. Introduced  $0.2 \text{ cm/sec}^2$  bias error C-acc. and  $+ .15 \text{ deg/h}$  bias error F-gyro at T= 60 mins.
4. Detected C-acc. fail and isolated at T=64 mins.
5. Detected F-gyro fail and isolated at T=68 mins.
6. Identified F-gyro fail as a bias at T=86 mins.
7. Identified and recomp'd C-acc. as a bias failure ( $+0.18 \text{ cm/sec}^2$ ) at T=115 mins.
8. Introduced  $.015 \text{ deg/h}/\text{min}$  ramp- A-gyro at T=120 mins.
9. F-gyro recomp'd ( $.1485 \text{ deg/h}$ ) at T=130 mins.
10. A-gyro failure detected at T=137 mins.
11. A-gyro identified as ramp at T=152 mins.
12. A-gyro recomp'd as ramp ( $.0153 \text{ deg/h}/\text{min}$ ) at T=204 mins.

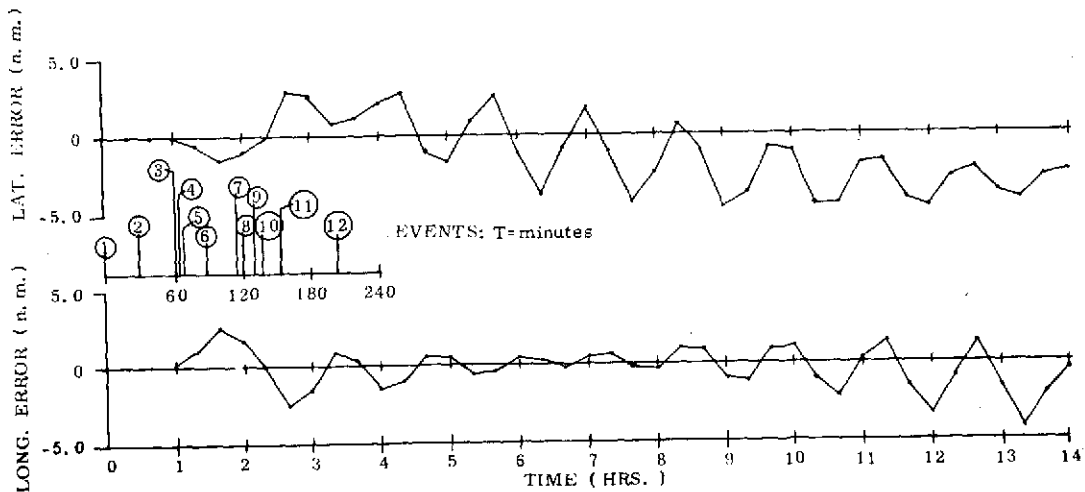


Fig. 7.3 Test #2 - Latitude and Longitude Errors

The navigation errors show predominantly a Foucault modulated, Schuler period waveform with a peak-to-peak magnitude of 5 nm. This mode is caused by attitude errors introduced due to the delay in detecting and isolating the F-gyro. Note in the figure that the Schuler period waveform is initiated at the same time that the F-gyro failure at 60 minutes is introduced. Considering the number and type of faults introduced, navigation performance was well bounded.

### 7.1.3 Test Sequence #3

SIRU was placed in the offset position ( $\Delta RA32 = +45^\circ$ ,  $\Delta RA16 = +5^\circ$ ) and run for 15 hours.

#### 7.1.3.1 Self-Calibration Estimates

$$\begin{aligned}\epsilon_A &= -0.017^\circ/\text{hr} \\ \epsilon_B &= -0.00015^\circ/\text{hr} \\ \epsilon_C &= -0.0046^\circ/\text{hr} \\ \epsilon_D &= 0.0381^\circ/\text{hr}\end{aligned}$$

Because of test scheduling problems, the self-calibration for this sequence was performed after the navigation sequence was completed. As a result none of the gyros were recompensated prior to the navigation run.

#### 7.1.3.2 FDICR Results

The following failures were inserted:

D-Gyro Bias:  $0.15^\circ/\text{hr}$  at  $t=60$  mins.  
A-Gyro Bias:  $1.5^\circ/\text{hr}$  at  $t=80$  mins.

All fails were detected, isolated, classified and the corresponding recompensation applied. It is noted that the D-gyro bias estimate and recompensation was  $0.19^\circ/\text{hr}$  and the A-gyro bias estimate and recompensation was  $1.48^\circ/\text{hr}$ . It is apparent that both the A and D-gyro recompensation biases included the uncorrected drifts shown in the self-calibration results (Section 7.1.3.1).

#### 7.1.3.3 Navigation Errors

Figure 7.4 shows the propagation of latitude and longitude errors.

### EVENTS DURING RUN : 3

1. At T=0, enter coarse/fine align FDICR program.
2. Enter nav. mode at T= 30 mins.
3. Intro. + .15 deg/h bias error - D-gyro at T= 60 mins.
4. Detected D-gyro fail at 64 mins.
5. Identified D-gyro fail as a bias at 72 mins.
6. Intro. 1.5 deg/h bias error - A-gyro at T= 80 mins., and detected it at T= 82 mins.
7. Identified A-gyro fail as a bias at 96 mins.
8. Recomped D-gyro bias ( .1905 deg/h) at T=126 mins.
9. Recomped A-gyro bias ( 1.4835 deg/h) at T=150 mins.

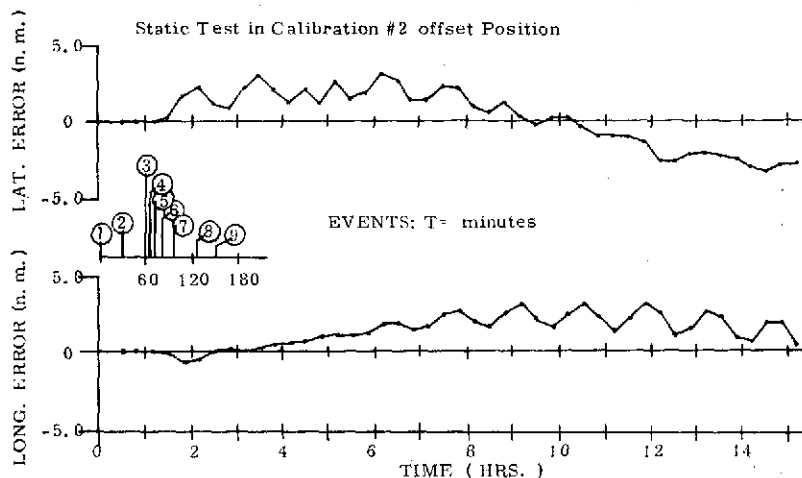


Fig. 7.4 Test #3 - Latitude and Longitude Errors

The error curves consist of a Schuler period mode with an approximate 2 nm peak-to-peak magnitude superimposed on a 24 hour period wave of approximately 2 nm peak.

The attitude error is introduced by the delay in detecting and isolating the 1.5<sup>o</sup>/hr bias change. The A-gyro failure is responsible for the 24 hour period mode and the Schuler mode (see Fig. 7.4, point 6). Most likely, the attitude error introduced by the D-gyro failure also contributed to the modes shown. Contributing also to the 24 hour mode were the drifts in the A and D-gyros which had not been compensated prior to this test.

### 7.2 Dynamic Test Results

Five tests were run with a dynamic SIRU environment (Tests 4, 5, 6, 7 and 8).

Notations have been made on each of the error graphs to show the time and type of dynamic inputs applied to the system during the test sequence.

The zero mean oscillations were applied about the RA32 table axis by a mechanical device which prevented the table from drifting or slewing from the initial position. The frequency of the zero mean oscillation is 0.5 hz with  $\pm 10\%$  variation possible, and the time-variant displacement approximates a triangular wave.

#### 7.2.1 Test Sequence #4 (baseline test-no failures were inserted)

SIRU was initially placed in calibration position #2 and run for 2 hours.

The system was subjected to a zero mean oscillation for the first 35 minutes and then the system was repositioned to the offset position.

##### 7.2.1.1 Self-Calibration Estimates

$$\begin{aligned}\epsilon_A &= -0.069^\circ/\text{hr} \\ \epsilon_B &= -0.018^\circ/\text{hr} \\ \epsilon_C &= -0.005^\circ/\text{hr} \\ \epsilon_D &= 0.031^\circ/\text{hr}\end{aligned}$$

Bias compensation corrections were inserted for the A and D-gyros. Note that the above self-calibration estimates are consistent with the single position calibration data in Chapter 3, Section 3.1.1.1 and corroborate that the A-gyro has a  $-0.069^\circ/\text{hr}$  drift when the system is oscillated. This drift was discovered to be due to a characteristic of the torque loop (as explained in the last paragraph of Chapter 3, Section 3.10.3).

##### 7.2.1.2 FDICR Results

No failures were inserted and none were detected.

##### 7.2.1.3 Navigation Errors

Figure 7.5 shows the propagation of latitude and longitude errors.

The error curves consist primarily of initial ramps of the 24 hour mode. The peak latitude error of 1.3 nm and the peak longitude error of -1.6 nm are both due to uncompensated residual drifts of approximately  $0.0225^\circ/\text{hr}$  on the computation

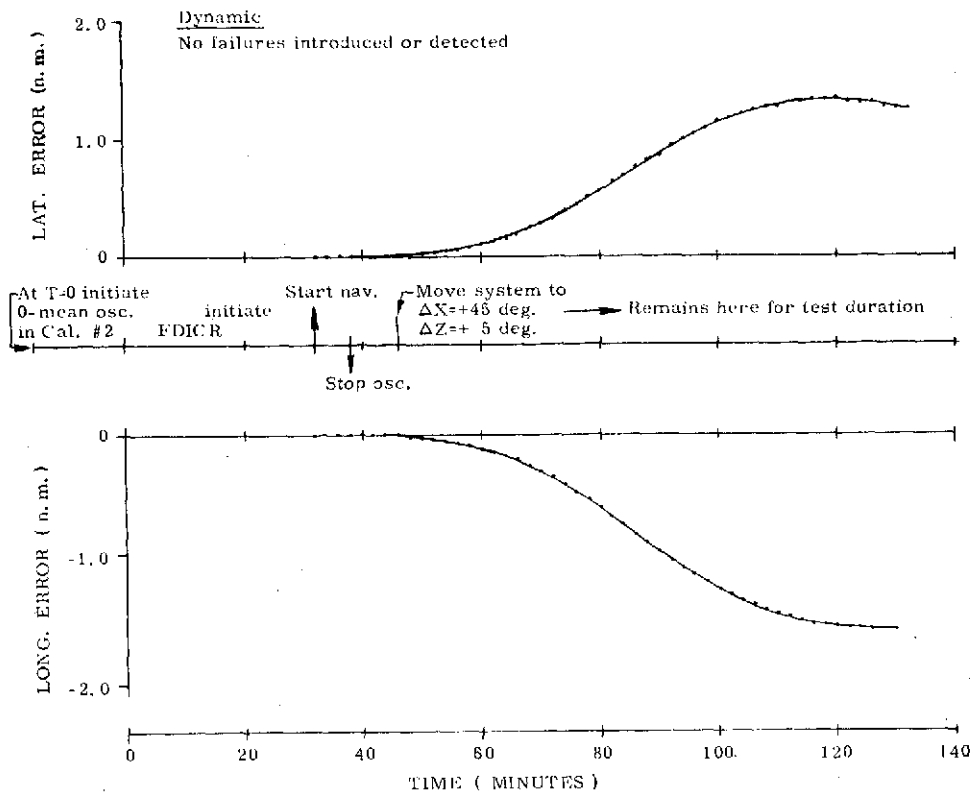


Fig. 7.5 Test #4 - Latitude and Longitude Errors

axes resulting from gyro drift changes which occurred when the oscillation was terminated and SIRU oriented to the offset position.

#### 7.2.2 Test Sequence #5

The SIRU system was placed in the offset position with respect to calibration position #2 ( $\Delta RA32 = +45^\circ$ ,  $\Delta RA16 = +5^\circ$ ) for a 16 hour test run. The dynamic inputs consisted of:

- a. Zero-mean oscillation to T = 35 mins.
- b. Auto-oscillation from T = 50 to T = 110 mins.
- c. Auto-oscillation from T = 180 to T = 300 mins.

(All oscillations were applied about the RA32 axis.)

### 7.2.2.1 Self-Calibration Estimates

$$\begin{aligned}\epsilon_A &= 0.0147^\circ/\text{hr} \\ \epsilon_B &= 0.0074^\circ/\text{hr} \\ \epsilon_C &= -0.0288^\circ/\text{hr} \\ \epsilon_D &= 0.0638^\circ/\text{hr}\end{aligned}$$

Bias compensation corrections were inserted for the C and D-gyros.

### 7.2.2.2 FDICR Results

The following failures were inserted:

C-Accelerometer	Bias- $0.4 \text{ cm/s}^2$ at $t = 60$ mins.
F-gyro	Bias- $0.375^\circ/\text{hr}$ at $t = 60$ mins.
A-gyro	Ramp- $0.0225^\circ/\text{hr}$ at $t = 190$ mins.

All failures were detected, isolated, classified and the corresponding recompensation applied to the respective gyros and accelerometers. The A-gyro was recompensated for a ramp of  $0.0222^\circ/\text{hr}/\text{min}$ . The initial ramp error inserted, however, was  $0.6228^\circ/\text{hr}/\text{min}$ . Even though the error in the ramp recompensation is small ( $0.0006^\circ/\text{hr}/\text{min}$ ) it does, given sufficient time, build up error in the A-gyro sufficient to cause another failure to be detected. Since the ramp recompensation error is small, the program detects and identifies this failure as a bias and recompensates it as such. For the 16 hour test, the A-gyro failed three times at approximately 4.5 hour intervals and the corresponding recompensation each time was approximately  $0.195^\circ/\text{hr}$  (see Fig. 7.6 for exact times and recompensation values).

### 7.2.2.3 Navigation Errors

Figure 7.6 shows the error propagation with respect to time. Note that the longitude error in Fig. 7.6 indicates that the largest rate of change error occurs between events 5 to 8 and 10 to 15, when the system is subjected to the automatic oscillation which consists of a 0.5 Hz; 30 arc minute peak-to-peak oscillation superimposed on a slew rate of approximately 0.2 degree/min. Also the error is that of a 24 hour sinusoid, indicating that there is a Z axis error of about  $0.0428^\circ/\text{hr}$  when the system is oscillated.

EVENTS DURING RUN : 5

1. Start 0 mean osc. ( $\approx 20$  min, P-P at 0.5 Hz)
2. At T=0, enter coarse/fine align FDICR program.
3. Enter nav. mode at T= 30 min.
4. Stop 0-mean osc.
5. Start auto osc.  $\approx 30$  min P-P at 0.5 Hz.
6. Intro. C-acc. bias error +0.4 cm/sec<sup>2</sup> and Fgyro bias error +.375 deg/h.
7. C-acc. fail detected at 62 mins., F-gyro fail detected at 64 mins., and C-acc. recompd (0.37 cm/sec<sup>2</sup>) at 72 mins.
8. Stopped osc. and slewed system back to initial offset position at 110 mins.
9. F-gyro recompd (.363 deg/h) at 136 mins.
10. Restarted auto. osc. at 180 mins.
11. Intro. A-gyro ramp error .0228 deg/h at T= 190 mins.
12. Detected A-gyro fail at T=204 mins.
13. Identified A-gyro fail as ramp, T=222 mins.
14. Recompd A-gyro ramp; .0228 deg/h at T=276 mins.
15. Stopped osc. and slewed system back to initial offset position at T=320 mins.
16. Detected A-gyro fail at T=424 mins.
17. Identified A-gyro fail as a bias, T=460 mins.
18. Recompd A-gyro bias; .1965 deg/h, T=504 mins.
19. Detected A-gyro fail at T=692 mins.
20. Identified A-gyro fail as a bias, T=704 mins.
21. Recompd A-gyro bias; .1950 deg/h, T=764 mins.
22. Detected A-gyro fail at T=950 mins.
23. Identified A-gyro fail as a bias at T=966 mins.
24. Recompd A-gyro bias; .1980 deg/h, T=1022 mins.

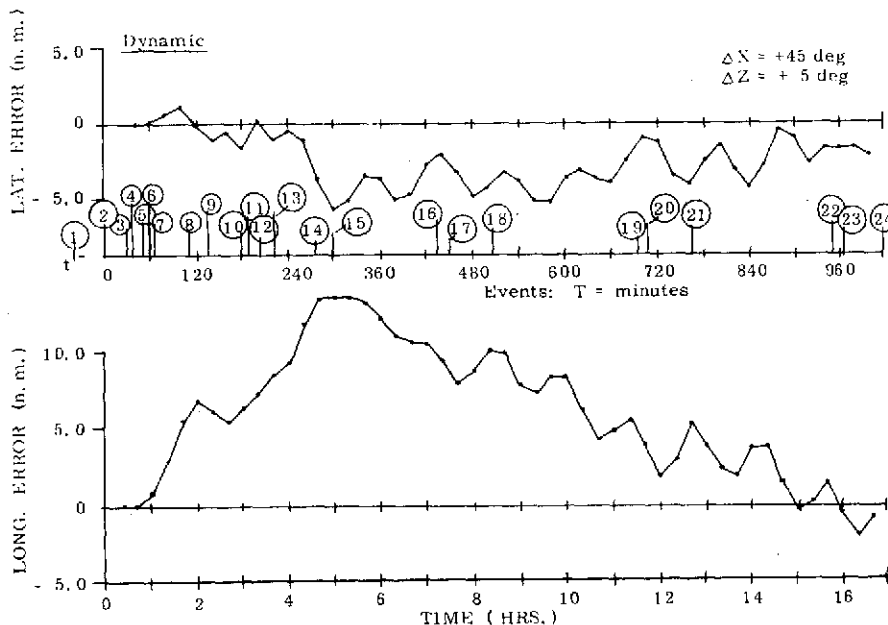


Fig. 7.6 Test #5 - Latitude and Longitude Errors

Calculating the influence of gyro performance on the computational axis drifts for the offset position shows that only E-gyro drift and/or pseudo-coning drift would cause the longitude error to propagate in the 24 hour mode. Note, however, that pseudo-coning at 1/2 Hz, 30 min peak-to-peak would contribute  $0.0225^{\circ}/hr$  to Z axis drift when no OA coupling compensation is present. Because OA coupling compensation is present, we would expect the actual pseudo-coning drift to be

negligible and most of the Z axis drift to be due to the E-gyro. See Appendix 7A for the explanation of why it is the E-gyro drift that leads to a large longitude error propagating in the 24 hour mode.

### 7.2.3 Test Sequence #6

The SIRU system was run in the offset position with respect to calibration position #2 ( $\Delta RA32 = +45^\circ$ ,  $\Delta RA16 = +5^\circ$ ) for 18 hours.

The dynamic inputs were as follows:

- a. Zero-mean oscillation to  $T = 35$  mins.
- b. Auto-oscillation from  $T = 50$  to  $T = 142$  mins.
- c. Two 360 degree ( $1^\circ/\text{sec}$ ) slews about RA32 at times  $T = 142$  and  $T = 240$  mins.

#### 7.2.3.1 Self-Calibration Estimates

$$\begin{aligned}\epsilon_A &= 0.0045^\circ/\text{hr} \\ \epsilon_B &= 0.0495^\circ/\text{hr} \\ \epsilon_C &= -0.0135^\circ/\text{hr} \\ \epsilon_D &= 0.0840^\circ/\text{hr}\end{aligned}$$

Even though the D-gyro and B-gyro self-calibration errors were large enough to warrant correction, it was decided not to change the gyro biases for this test sequence.

#### 7.2.3.2 FDICR Results

The following failures were inserted:

D-gyro      Bias- $0.375^\circ/\text{hr}$  at  $t = 60$  mins.  
A-gyro      Bias- $2.25^\circ/\text{hr}$  at  $t = 80$  mins.

Both of the gyro failures were detected, isolated, classified and each instrument correspondingly recompensated. Note that the D-gyro bias estimate was  $0.447^\circ/\text{hr}$  instead of the  $0.375^\circ/\text{hr}$  which was inserted. It appears that the D-gyro self-calibration error estimate of  $0.0885^\circ/\text{hr}$  was valid (to within  $0.0165^\circ/\text{hr}$ ). Even though the D-gyro was not recompensated prior to the navigation run, the combination of the intentional gyro failure ( $3.75^\circ/\text{hr}$ ) and SPC results ( $0.0885^\circ/\text{hr}$ )

was closely estimated and recompensation applied. The B-gyro error was below the detection threshold.

### 7.2.3.3 Navigation Errors

The latitude and longitude errors propagated are given by Fig. 7.7.

#### EVENTS DURING RUN: 6

1. Start 0-mean osc.  $\approx 20$  min. P-P at 0.5 Hz at T-
2. At T=0, enter coarse/fine align. FDICR program.
3. Enter nav. mode at T=30 mins.
4. Stop 0-mean osc. at T=35 mins.
5. Start auto. osc.  $\approx 30$  min. P-P at 0.5 Hz at T=50 mins.
6. Introduce D-gyro bias error +.375 deg/h at T=60 mins.; detected fail at T=64 mins. and identified at T=70 mins.
7. Introduced A-gyro bias error +2.25 deg/h at T=80 mins.; detected fail at T=82 mins. and identified at T=88 mins.
8. Recomp D-gyro bias; .447 deg/h at T=114 mins.
9. Recomp A-gyro bias; 2.259 deg/h at T=134 mins.
10. Terminated automatic osc. manually, returned system to initial offset position; then slewed system 360 deg. about X-body axis at a rate of  $\approx 1$  deg/sec at T = 142 mins.
11. Slew system 360 deg. about Y-body axis at a rate of  $\approx 1$  deg/sec at T=246 mins.

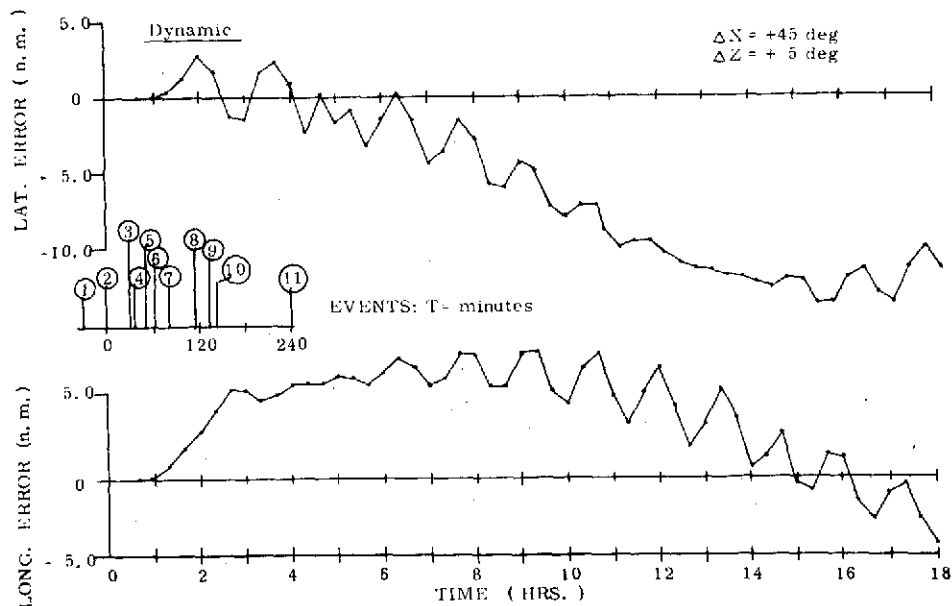


Fig. 7.7 Test #6 - Latitude and Longitude Errors

Note that slewing did not affect the navigation errors. However, at about 7 hours into the run, a 24 hour mode with a slope of  $-0.0188^{\circ}/\text{hr}$  for latitude and longitude appeared. The Schuler mode, also present, comes from the delay in detecting the  $2.25^{\circ}/\text{hr}$  bias (see point 6 on the graph). At point 5 there is also the beginning of a 24 hour mode in longitude that appears to be due to the E-gyro drift as in test sequence #5. This 24 hour mode is eliminated when the oscillation is stopped at point 9. The explanation for this drift is given in the last paragraph of Chapter 3, Section 3.10.3.

#### 7.2.4 Test Sequence #7

SIRU was run in calibration position #2 for two hours.

The dynamic input was a zero-mean oscillation from  $T = 0$  to  $T = 35$  mins.

##### 7.2.4.1 Self-Calibration Estimates

$$\begin{aligned}\epsilon_A &= -0.0628^{\circ}/\text{hr} \\ \epsilon_B &= -0.0313^{\circ}/\text{hr} \\ \epsilon_C &= -0.0172^{\circ}/\text{hr} \\ \epsilon_D &= 0.0249^{\circ}/\text{hr}\end{aligned}$$

Bias compensation was inserted for gyros A, B, and D.

##### 7.2.4.2 FDICR Results

The following failures were inserted:

C-Accelerometer	Bias- $1.0 \text{ cm/s}^2$ at $T = 0$ .
A-Gyro	Bias- $0.225^{\circ}/\text{hr}$ at $T = 0$ .
A-Accelerometer	Bias- $0.4 \text{ cm/s}^2$ at $T = 5$ mins.
D-Gyro	Bias- $0.225^{\circ}/\text{hr}$ at $T = 10$ mins.

All gyro and accelerometer failures were detected, isolated, classified and the corresponding recompensation applied.

##### 7.2.4.3 Navigation Errors

Figure 7.8 depicts the latitude and longitude errors for the sequence #7 test run. The latitude and longitude errors are 24 hour modes. The latitude error

slope is approximately 0.8 nm/hr which is equivalent to a  $0.012^\circ$ /hr drift about the Y axis. The longitude error slope is approximately -2.8 nm/hr which is equivalent to a  $-0.042^\circ$ /hr drift about the Z axis. This error could be due to E-gyro drift. See Appendix 7A for the explanation of why it is the E-gyro drift that leads to propagation of the longitude error.

EVENTS DURING TEST: 7

1. Start 0-mean oscillation  $\approx 30$  min P-P at 0.5 Hz at T=0.
2. At T=0, enter coarse/fine align FDICR prog, and introduced C-acc. bias fail +1.0 cm/sec<sup>2</sup> and A-gyro bias fail +.225 deg/h.
3. Detected C-acc. fail at T= 2 mins.
4. Introduced A-acc. bias fail +0.4 cm/sec<sup>2</sup> at T= 5 mins.
5. At T= 8 mins. detected an A-gyro fail and an A-acc. fail.
6. At T=10 mins. introduced D-gyro bias fail of +.225 deg/h.
7. At T=18 mins. identified C-pip fail as a bias, A pip fail as a bias, A-gyro fail as a bias and detected D-gyro fail.
8. Recompensated C-acc. (0.99 cm/sec<sup>2</sup>) and A-acc. (0.39 cm/sec<sup>2</sup>) at T=20 mins.
9. Entered nav. mode at T=30 mins.
10. Terminated 0-mean oscillation.
11. Recompensated A-gyro (.234 deg/h) at T=46 mins.
12. Recompensated D-gyro (.240 deg/h) at T=68 mins. (Note: the D-gyro fail was identified as a bias at T=22 mins.).

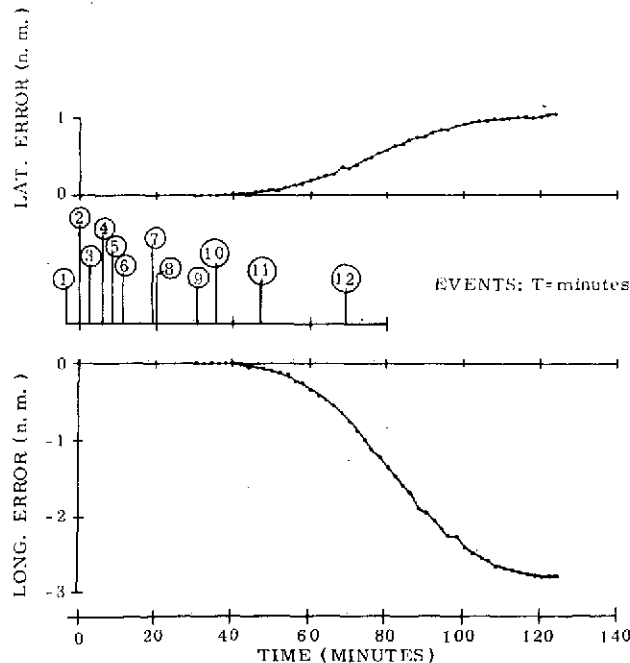


Fig. 7.8 Test #7 - Latitude and Longitude Errors

### 7.2.5 Test Sequence #8

For this test a zero-mean oscillation was impressed about the vertical axis of the system in the calibration position #2. The frequency of oscillation was 0.01 hz with an amplitude of 20 arc minutes peak-to-peak. The waveform of the oscillation approximates a square wave. The maximum latitude rate error was 0.13 nm/hr and the longitude rate error 0.48 nm/hr. Figure 7.9 depicts the error propagation during the test sequence. Note that no failures were introduced and the self-calibration values from Sequence #1 were used.

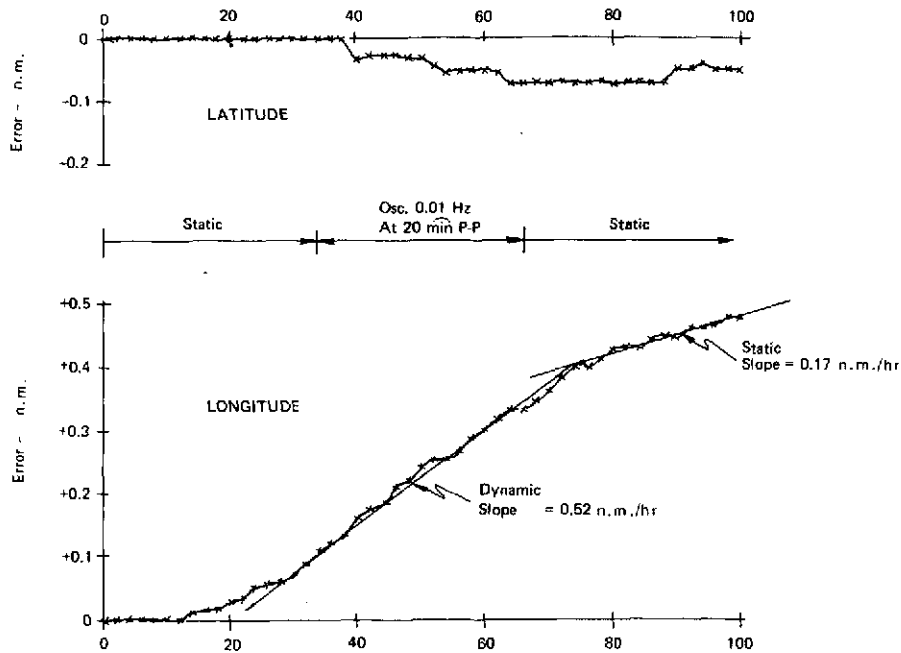


Fig. 7.9 Navigation Errors Incurred During Low Frequency, Zero-Mean Oscillation of SIRU System

### 7.3 Conclusions

In all of the runs, the FDICR algorithm for both gyros and accelerometers worked well without failure.

Self-calibration also worked well (as evidenced by comparing these estimates with FDICR compensation value estimates). Self-calibration also consistently revealed that the A-gyro in the calibration position #2 had a  $-0.069^{\circ}/\text{hr}$  drift when SIRU was oscillated about the vertical axis. Examination of the largest navigation

C-3

errors revealed that the E-gyro (a reference gyro during self-calibration) may have a drift during oscillations when SIRU is tilted from the vertical (These dynamically induced drifts were discovered to be due to a characteristic of the pulse torquing loop that was corrected after the writing of this report. See the last paragraph of Chapter 3, Section 3.10.3 ).

The above single position calibration results also correlate well with the results described in Chapter 3.

Alignment errors were also small as indicated by the latitude and longitude error curves during the first hour of operation of the navigation algorithm.

In general, the error curves show that delay in detecting and isolating a gyro failure leads to a propagation of the Schuler mode, whereas an uncompensated gyro bias generates a 24 hour period mode.

In all cases (see Figs. 7.2 to 7.9) the accelerometers contribute very little error, even when there is a delay in detecting and isolating an accelerometer failure.

Appendix A7  
Computation Axis Drifts as a Function  
of Gyro Drifts in SIRU Offset Position of  
 $\Delta RA32 = +45^\circ$ ,  $\Delta RA16 = +5^\circ$

The approximate orientation of SIRU for  $\Delta RA32 = +45^\circ$  and  $\Delta RA16$  a small angle is shown in Fig. A7.1.

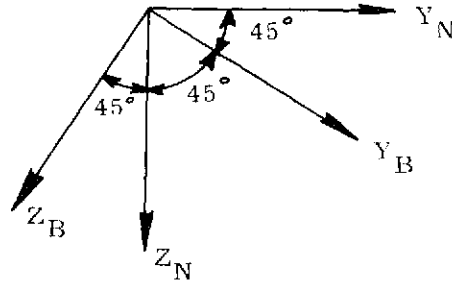


Fig. A7.1 Approximate Orientation of SIRU During Test Sequence

The subscript N refers to the local navigation frame axes and the subscript B refers to the SIRU body axes (or computational frame axes).

From the figure we see that:

$$\begin{aligned} Y_N &= \frac{1}{\sqrt{2}}(Y_B - Z_B) \\ Z_N &= \frac{1}{\sqrt{2}}(Y_B + Z_B) \end{aligned} \tag{A7.1}$$

From Chapter 3, Eqs. 3.5 - 3.7, we obtain the following:

$$\begin{aligned} X_B &= \frac{S}{2}(\epsilon_A - \epsilon_B) - \frac{C}{2}(\epsilon_C + \epsilon_D) \\ Y_B &= \frac{S}{2}(\epsilon_D - \epsilon_C) + \frac{C}{2}(\epsilon_E - \epsilon_F) \\ Z_B &= \frac{C}{2}(\epsilon_A + \epsilon_B) + \frac{S}{2}(\epsilon_E - \epsilon_F) \end{aligned} \tag{A7.2}$$

PRECEDING PAGE BLANK NOT FILMED

Substituting Eq. A7.2 into Eq. A7.1 yields:

$$\begin{aligned}
 Y_N &= -0.3\epsilon_A - 0.3\epsilon_B - 0.2\epsilon_C + 0.2\epsilon_D + 0.12\epsilon_E - 0.5\epsilon_F \\
 Z_N &= 0.3\epsilon_A + 0.3\epsilon_B - 0.2\epsilon_C + 0.2\epsilon_D + 0.5\epsilon_E - 0.12\epsilon_F \\
 X_N &= 0.43\epsilon_A + 0.43\epsilon_B + 0.26\epsilon_E + 0.26\epsilon_F
 \end{aligned}
 \tag{A7.3}$$

Note in Eq. A7.3 that the E-gyro drift is the only one that strongly affects the expressions for south and vertical drift but has little influence on the east drift. It is the south drift that leads to large longitude errors but much smaller latitude error (see Chapter 6.0).

Chapter 8  
SIRU System Reliability Experience and Prediction

8.0 Introduction

SIRU has been operating continually for 35 months. System operation totals 116,000 wheel hours and 140,000 hours of closed loop accelerometer operation. No failures have been experienced in the electronics assembly (EA). No accelerometer has failed, nor has any accelerometer pulse torque electronics (PTE) module failed. Two gyro PTE failures were seen. Of the two gyro failures, one was a wheel start failure. The second gyro failure was attributed to a float freedom (contaminant) problem.

In roughly three years operation four gyro modules and one accelerometer module have failed. Overall, one may then determine that the gyro module has experienced an MTBF of 29,000 hours, while the accelerometer module history indicates an MTBF of 139,000 hours.

In this chapter, the mathematics of reliability prediction are applied to the SIRU system history. Hardware failure rates are tabulated (or predicted) for each component. Equations are developed for the reliability of a triad using comparable hardware, SIRU capable of isolating two failures, and SIRU capable of isolating three failures. Reliability plots are presented (Figs. 8.1-8.4).

In addition, the reliability of the failure detection and isolation algorithms is examined. The theoretical probabilities of false detection and isolation and missed detection and isolation of a constant bias degradation are evaluated. The reader directly concerned about these facets of SIRU reliability should consult sections 8.6-8.8 of this chapter which are independent of all the other sections.

8.1 Assumptions Made in this Analysis

Several assumptions are made in this analysis. Primarily, this is a macroscopic view, and serves solely to predict the probability that the system will be operational at some time after turn on and checkout. To permit making these calculations, a functional form of the failure distribution is postulated for each component. These distributions are combined (added and multiplied) according to the redundancy of the system.

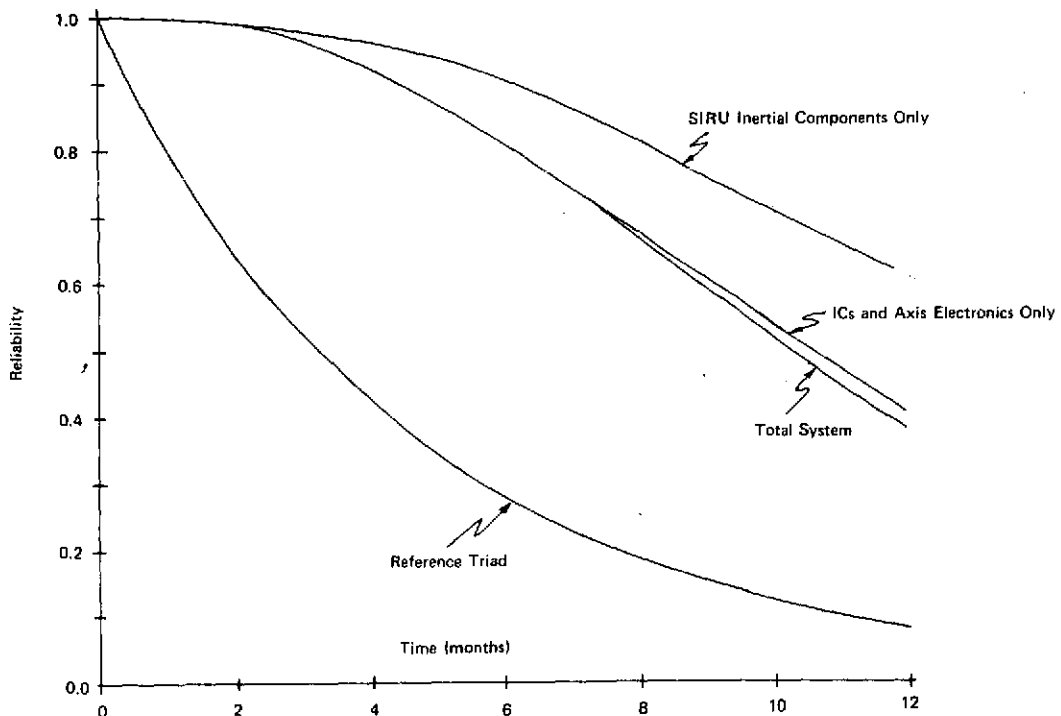


Fig. 8.1 SIRU System Reliability: System Configured to Isolate Two Failures (Experienced Failure Rates)

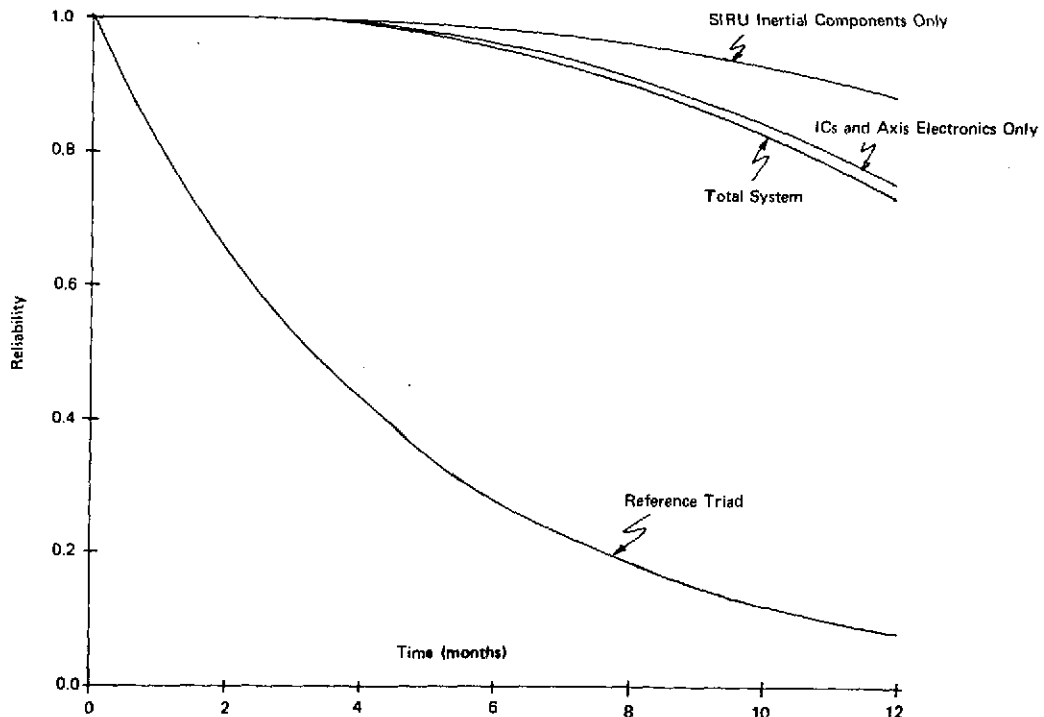


Fig. 8.2 SIRU System Reliability: System Configured to Isolate Three Failures (Experienced Failure Rates)

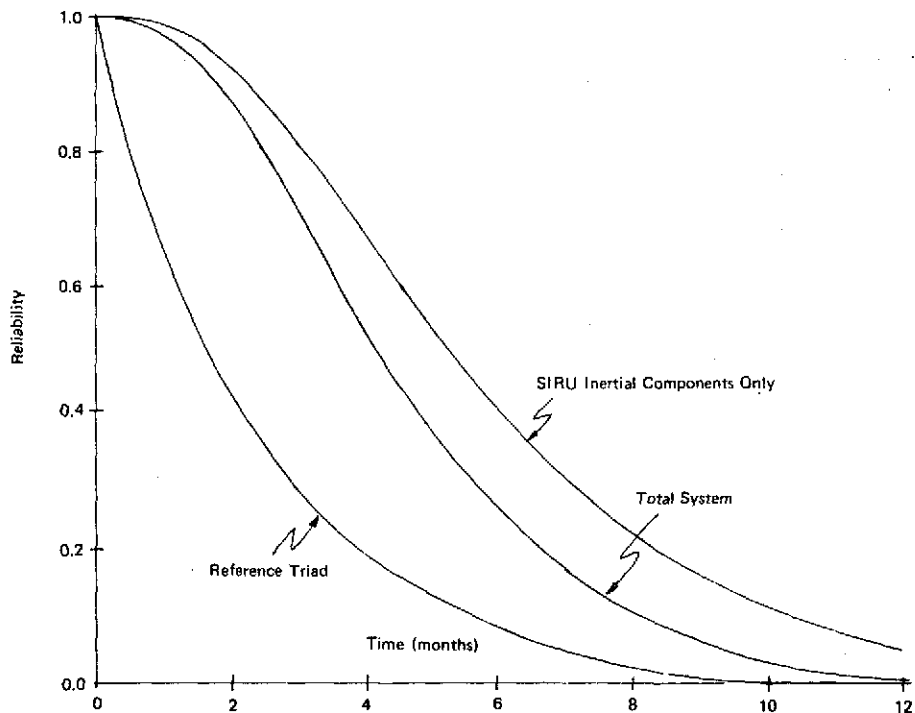


Fig. 8.3 SIRU System Reliability: System Configured to Isolate Two Failures (90% Confidence Failure Rates)

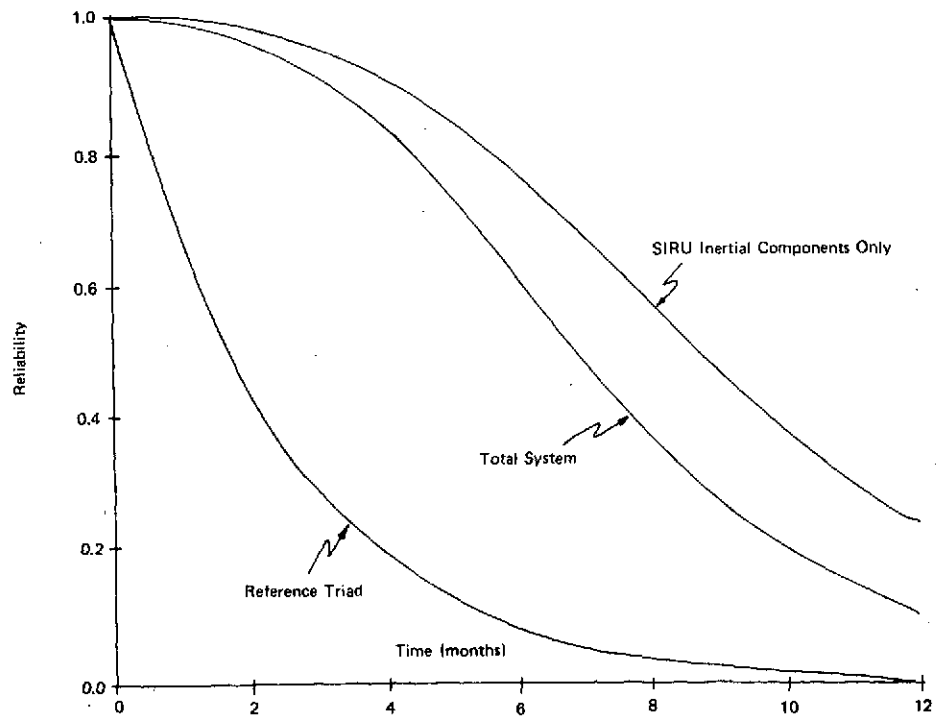


Fig. 8.4 SIRU System Reliability: System Configured to Isolate Three Failures (90% Confidence Failure Rates)

A failure distribution function is defined under two assumptions. The distribution function models only component failures during uninterrupted operation. Wheel restart failures as related to system turn-on/off moding, for instance, are specifically excluded (although the wheel start failure experienced in the system is included in calculation of failure rates). Given that the system is operational, a prediction of its future performance is made. A second assumption is that the failure rate is constant over the time interval of interest. If a classical "bathtub curve" accurately reflects the statistics of these components, then interest lies in an interval after infant mortality failures are eliminated and before wearout failures become important. Then, with  $N$  the number of operational units:

$$\dot{N} = -\lambda N \quad (8.1)$$

$$N = N_0 e^{-\lambda t} \quad (8.2)$$

and so the probability that a unit is operational at time,  $t$ , with a failure rate,  $\lambda$ , is:

$$P(t) = N/N_0 = e^{-\lambda t} \quad (8.3)$$

## 8.2 Assessment of SIRU Hardware Failure Rates

Hardware failures in SIRU are described in the Introduction, Section 8.0. Most component modules have demonstrated faultless operation over the system's lifetime. Table 8.1 lists the failures experienced. A more detailed treatment follows in Table 8.2. This treatment is pessimistic, as it ascribes one failure to each component, even those that have experienced no failures, except that failure rates for the EA are calculated from individual component reliability estimates. In justification, note that the EA has approximately 20,000 hours operation, while its components have expected lifetimes in excess of 80,000 hours.

90% confidence estimates (Table 8.2) are obtained by assuming first that the failures fit an exponential distribution and then by using a chi-squared table. For instance, if one failure has occurred during 256,000 operating hours, an observed MTBF of 256,000 hours results. To derive a 90% confidence estimate, one uses a factor of 3.9 taken from published  $X^2$  tables to deduce an MTBF of 65,600 hours, 90% confidence level (see reference 17 for more details of how confidence estimates were derived for SIRU).

Table 8.1 SIRU System Hardware Failure History

Note: This table summarizes all failures during system operation over the period 27 January 1970 to 28 December 1972.

Component	No. Failures	MTBF		
		System Operating Hours	Observed	90% Confidence
Gyro	2	116400	58200	22000
PTE	2	116400	58200	22000
Temp. Contr.*	0	-	-	-
Gyro Module	4	116400	29100	11000
Accelerometer	0	139800	139800	60800
PTE	0	139800	139800	60800
Temp. Contr.*	1	256200	256200	65800
Acc. Module	1	139800	139800	30400

\*The gyro and accelerometer temperature controllers are identical. One temperature controller failure has occurred among the twelve inertial component modules in the system and, therefore, an experienced MTBF of 256,200 hours is derived.

Table 8.2 SIRU System Hardware Failure Rate Estimation

All rates are given in failures/million hours. MTBF is given in hours.

Gyro Module

Component	MTBF*	Failure Rate	
		Experienced	90% Confidence
Gyro	58200	17.2	45.5
PTE	58200	17.2	45.5
Temp. Contr.	256200	3.9	15.2
Wheel Supply	116000	8.5	19.8
Gyro Module	29100	46.8	126.0
Estimated MTBF		21367	7937

Accelerometer Module

Component	MTBF*	Failure Rate	
		Experienced	90% Confidence
Accelerometer	139800	7.2	16.5
PTE	139800	7.2	16.5
Temp. Contr.	256200	3.9	15.2
Susp. Supply	139800	7.2	16.5
Acc. Module	139800	25.5	64.7
Estimated MTBF		39216	15456

\*MTBF and failure rates experienced or derived by assuming one failure during this period.

Table 8.2 SIRU System Hardware Failure Rate Estimation (cont.)

Axis Electronics

Component	MTBF*	Failure Rate	
		Experienced	90% Confidence
DC Axis Supply	139800	7.2	16.5
9600 hz Supply	139800	7.2	16.5
Fuse/Diode Board	1000000	0.1	1.0
Electronics	139800	15.4	32.6
Estimated MTBF		64935	31250

Electronics Assembly

Component	MTBF*	Failure Rate	
		Predicted**	90% Confidence**
Scaler	100000	10	10
40V/5V Supply	83333	12	12
28V Supply	83333	12	12
Clock	1000000	1	1

The electronics assembly (EA) failure rates cannot be summed directly because the EA consists of both dually and triply redundant components.

\*MTBF and failure rates experienced or derived by assuming one failure during this period.

\*\* For the EA, which has had only 20000 hours of operation, failure rates are predicted using manufacturers' estimates. All other estimates, for components which have shown no failures, reflect the fact that, as observed, SIRU electronics are significantly more reliable than originally predicted.

### 8.3 Triad Reliability Calculations

Reliability estimates are now established for a single gimballed triad system in order to provide a reference for comparing SIRU reliability. As in the SIRU analysis which follows, an exponential distribution is assumed. This triad system is assumed to be built with the same components as SIRU, permitting direct comparison. It is interesting to note that the triad MTBF of 3,438 hours as calculated is a factor of 2 to 10 greater than that reported for many contemporary military systems.

As there is no redundancy in the triad system, one finds simply  $\lambda_{\text{TRIAD}} = \sum \lambda_{\text{Components}}$ . Table 8.3 shows this derivation.

Table 8.3 Derivation of Triad Failure Rate

Component	Failure Rate	Quantity	Total Failures per Million Hours	
			Experienced*	90% Confidence
Gyro	17.2	3	51.6	136.5
Gyro PTE	17.2	1	17.2	45.5
Accelerometer	7.2	3	21.6	49.5
Accelerometer PTE	7.2	3	21.6	49.5
DC Supply	7.2	2	14.4	33.0
Suspension Supply	7.2	1	7.2	16.5
Wheel Supply	8.5	1	8.5	19.8
40/5V Supply	12.0	1	12.0	12.0
Temp. Control	3.9	2	7.8	15.2
Servos	12.0	4	48.0	48.0
R/D Converter	20.0	3	60.0	60.0
Clock/scaler	11.0	1	11.0	11.0
Gimbals, Sliprings, Resolvers, etc.	10.0		10.0	10.0
SUM			290.9	506.5
Estimated MTBF			3438 hours	1927 hours

\*

Where no failures have been experienced, estimates have been drawn from Manufacturers' data.

The experienced  $\lambda_{\text{TRIAD}} = 290.9$  failures/million hours, while the calculated 90% confidence value is  $\lambda_{\text{TRIAD}} = 506.5$  failures/million hours. Reliability is calculated by:

$$R_I(t) = e^{-\lambda_{\text{TRIAD}}t} \quad (8.4)$$

#### 8.4 SIRU Reliability Calculations

Calculations of SIRU reliability are determined by an analysis of the complex redundancy scheme. The system comprises gyro and accelerometer modules, axis electronics and non-axis electronics. The inertial component modules are fully redundant. Axis electronics, as listed in Table 8.2, provide power and a 9600 Hz reference signal to both the gyro and the accelerometer modules on a given axis. The non-axis electronics, also listed in Table 8.2, are identified as the EA in the reliability schematic, Fig. 8.5.

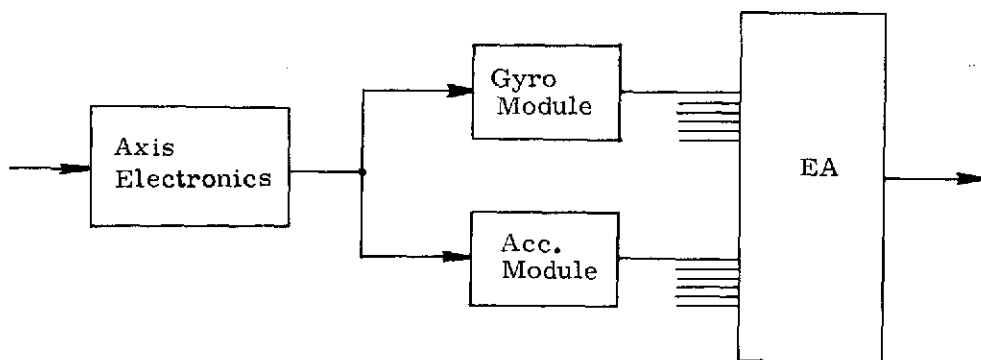


Fig. 8.5 SIRU Reliability Schematic

Reliability calculations hinge on the number of failed redundant components which the system can detect and isolate. SIRU is able to detect failures of three like inertial components, isolating two of them and a third failure much worse than the first two, through the software techniques discussed in Chapter 2. Projections can also be made for the system modified to include hardware failure detection logic which permits isolation of a third (hardware) failure in most cases. In the sections which follow, two failure isolation capability systems are referred to as FO/FS systems, while three failure isolation capability systems are called FO/FO/FS. FO is to be read "Fail Operational" or capable of operating even in the presence of an additional failure. FS, "Fail Safe", implies that the system is functional unless a subsequent failure occurs.

### 8.4.1 EA Reliability

The EA comprises both dually and triply redundant components. In order for the system to survive, at least one of these components must be operational. Some complete path must exist through the diagram, Figure 8.6. For a dually redundant scaler with failure rate  $\lambda_1$ , the probability that at least one scaler is operational at time  $t$  is given by the sum of the probabilities of a favorable event with:

$$R_1 = e^{-\lambda_1 t} \quad (8.5)$$

$$P_1 = R_1^2 + 2R_1(1 - R_1) \quad (8.6)$$

$P_1$  is the sum of the probabilities of both units being operational and of one of the two units being operational. For a 40V/5V supply failure rate,  $\lambda_2$ , one finds similarly that:

$$R_2 = e^{-\lambda_2 t} \quad (8.7)$$

$$P_2 = R_2^2 + 2R_2(1 - R_2) \quad (8.8)$$

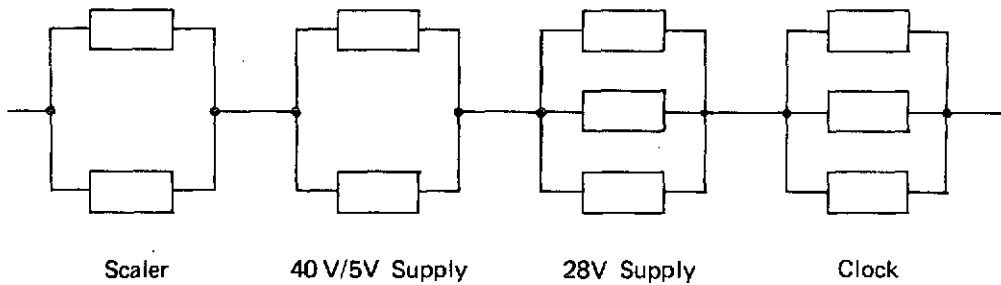


Fig. 8.6 Redundancy Block Diagram

Triply redundant components are the 28V supply, with a failure rate,  $\lambda_3$ , and the clock, with a failure rate,  $\lambda_4$ . In a similar fashion one defines the reliabilities of single supplies and clocks as:

$$\begin{aligned} R_3 &= e^{-\lambda_3 t} \\ R_4 &= e^{-\lambda_4 t} \end{aligned} \quad (8.9)$$

and the probability of at least one unit's being good as:

$$P_3 = R_3^3 + 3R_3^2(1 - R_3) + 3R_3(1 - R_3)^2 \quad (8.10)$$

and:

$$P_4 = R_4^3 + 3R_4^2(1 - R_4) + 3R_4(1 - R_4)^2 \quad (8.11)$$

It follows that the reliability of the EA, where all other EA packaged electronics is considered, for the reliability analysis, as part of an instrument sensing axis or some variations therein, is given by:

$$R_{EA} = P_1 P_2 P_3 P_4 \quad (8.12)$$

#### 8.4.2 Inertial Component Module Axis Reliability

Ignoring axis-dedicated electronics for the moment, one may model the SIRU inertial component reliability as consisting of independent sets of gyroscope and accelerometer modules. The failure rates for these modules,  $\lambda_G$  and  $\lambda_A$  respectively, were derived in Table 8.2. Then:

$$R_G = e^{-\lambda_G t} \quad (8.13)$$

and:

$$R_A = e^{-\lambda_A t} \quad (8.14)$$

Derivation of the accelerometer complement's reliability is identical with that of the gyroscope's, simply substituting  $R_A$  for  $R_G$ . In SIRU, with 6 gyroscope modules, FO/FS operation requires that at least four modules be operational. FO/FO/FS operation implies, in turn, that at least three survive. For these cases:

$$P_G(\text{FO/FS}) = R_G^6 + 6R_G^5(1 - R_G) + 15R_G^4(1 - R_G)^2 \quad (8.15)$$

$$\begin{aligned} P_G(\text{FO/FO/FS}) &= R_G^6 + 6R_G^5(1 - R_G) + 15R_G^4(1 - R_G)^2 + 20R_G^3(1 - R_G)^3 \\ &= P_G(\text{FO/FS}) + 20R_G^3(1 - R_G)^3 \end{aligned} \quad (8.16)$$

The inertial component (IC) complement's overall reliability is:

$$P_{IC} = P_G P_A \quad (8.17)$$

for either case, FO/FS or FO/FO/FS.

### 8.4.3 Consideration of Axis Electronics

Certain functions of the SIRU electronics are dedicated to specific axes, i.e., although modules such as the 9600 hz suspension supply are six fold in the system, each is hard wired into one axis and no cross-strapping between axes for redundancy purposes exists. Therefore, if one such module fails, the corresponding gyroscope and accelerometer modules are lost. Axis electronics of this type and located in the EA are the six DC axis supplies, the six 9600 hz supplies and the fuse and diode modules.

Let us assume SIRU operating as a FO/FS system and consider only gyros (accelerometers are treated identically, and FO/FO/FS operation implies the ability to withstand one additional failure). Loss of a set of axis electronics implies the loss of a gyroscope. Operation is allowable with at most two gyroscopes non-functional. If no axis electronics have failed, 4 of 6 gyros must survive. If one axis fails, 4 of the remaining 5 gyros must survive. If a second axis fails, all of the remaining 4 gyros must be functional.

If the axis electronics have a failure rate,  $\lambda_5$ , the axis reliability is given by  $R_5 = e^{-\lambda_5 t}$ . The FO/FS case described above becomes (adding accelerometers):

$$P_{\text{FO/FS}}^{\text{SIRU}} = P_{\text{EA}} \left\{ R_5^6 (R_G^6 + 6R_G^5 (1-R_G) + 15R_G^4 (1-R_G)^2) (R_A^6 + 6R_A^5 (1-R_A) + 15R_A^4 (1-R_A)^2) + 6R_5^5 (1-R_5) R_G^5 + 5R_G^4 (1-R_G) R_A^5 + 5R_A^4 (1-R_A) + 15R_5^4 (1-R_5)^2 (R_G^4) (R_A^4) \right\} \quad (8.18)$$

The extension of the system to FO/FO/FS extends Eq. 8.18 to allow one additional gyro and/or accelerometer failure. Thus:

$$P_{\text{FO/FO/FS}}^{\text{SIRU}} = P_{\text{EA}} \left\{ R_5^6 (R_G^6 + 6R_G^5 (1-R_G) + 15R_G^4 (1-R_G)^2 + 20R_G^3 (1-R_G)^3) (R_A^6 + 6R_A^5 (1-R_A) + 15R_A^4 (1-R_A)^2 + 20R_A^3 (1-R_A)^3) + R_5^5 (1-R_5) (R_G^5 + 5R_G^4 (1-R_G) + 20R_G^3 (1-R_G)^2) (R_A^5 + 5R_A^4 (1-R_A) + 20R_A^3 (1-R_A)^2) + R_5^4 (1-R_5)^2 (R_G^4 + 4R_G^3 (1-R_G) + 4R_G^2 (1-R_G)^2) (R_A^4 + 4R_A^3 (1-R_A) + 4R_A^2 (1-R_A)^2) + R_5^3 (1-R_5)^3 R_G^3 R_A^3 \right\} \quad (8.19)$$

With  $R_5 = 1$ , Eqs. 8.18 and 8.19 reduce to the form of Eq. 8.17.

#### 8.4.4 Summary

SIRU reliability calculations involve the evaluation of complex formulas. In all cases, however, the redundant properties of the system provide an equivalent system MTBF significantly greater than that of its components. In the curves described in the next section, the reliability, R, after 1 month of continuous operation is shown to be (experienced failure rates, FO/FS implementation) 0.9978.

where:

$$R = e^{-t/MTBF} \quad (8.20)$$

or

$$MTBF = -t/\ln R = -730/-.002202 = 331,500 \text{ hrs.} \quad (8.21)$$

This calculation has been carried out for several configurations, and results are shown in Table 8.4.

		Mission Success Probability		Equivalent MTBF (hours)	
		Two Fail Capability	Three Fail Capability	Two Fail Capability	Three Fail Capability
SIRU	90% Confidence Failure Rates	.9751	.9978	23800	331500
	Experienced Failure Rates	.9978	.9999	331500	730000
TRIAD	90% Confidence Failure Rates	.6642		1974	
	Experienced Failure Rates	.8086		3438	

Table 8.4 Reliability Analysis Summary  
(Mission Time = 730 hours)

#### 8.5 SIRU Reliability Summary

It is concluded that the present SIRU configuration is significantly more reliable than a single triad. Extension of system FDI to permit isolation of a third failure enhances reliability markedly. These relations are shown graphically in Figs. 8.1 through 8.4 where the reliability of two and three failure-tolerating systems are compared with that of a single triad built with identical components.

Examination of Eqs. 8.18 and 8.19 above shows that the dominant elements of SIRU reliability are, first, the gyro module MTBF (21,000 hours estimated) and, second, the fact that certain EA modules are not cross-strapped (axis electronics).

Figures 8.1 to 8.4 show estimates of SIRU system reliability that are conservative for two reasons. One, failure rates are high because failures have been ascribed to components which have experienced no failures. Two, Eqs. 8.18 and 8.19 exclude certain cases in which the system will successfully complete a mission. The figures are derived directly from these equations.

## 8.6 FDI Reliability

### 8.6.1 Introduction

In a discussion of reliability in a redundant implementation, a crucial question that may be posed is; what is the reliability of the fault detection and isolation system? In the prior discussions, the reliability analysis concerns itself with the redundant paths that are available in the event of failures and the statistics of mission success as related to the network of these paths, assuming that the correct path choices are made. In a redundant mechanization, the question regarding the confidence level of the system's fault detection and isolation capability to comprehensively and correctly function and to select the appropriate redundant network path should also be considered. For example, inherent in the detection and isolation techniques used, whether in hardware or in the software computational algorithms, is the possibility that a fault could go undetected (missed alarm) or that an incorrect indication (false alarm) could occur. Similarly, the detection and isolation criteria must be related to a detection threshold or allowable error consistent with the instrumentation and mission objective. The fault detection and isolation (FDI) performance therefore is a crucial element of the redundant system reliability. The following section discusses the two FDI schemes utilized in SIRU and provides analytic and simulation results to confirm their relative performance and reliability.

### 8.6.2 FDI Reliability

The TSE method of failure detection and isolation is presented in detail in the CSDL "SIRU Development" Report R-746. The essential principles of the method are described below. The output of each instrument is accumulated (in a manner to be described shortly). The accumulated outputs are added as indicated by the parity equations presented in sections A2.3.1 and A2.3.2 of Appendix A2, Chapter 2 of this report. The "output" of each parity equation is squared. These squared

terms are then added to form the total squared error, TSE. This value of TSE is compared to a preset threshold at the attitude algorithm update rate. When the threshold is exceeded, the detection of a failure has occurred. The failed instrument is isolated when the ratio of the squared output  $E_i^2$  of the  $i^{\text{th}}$  parity equation (corresponding to failed instrument,  $i$ ) to the TSE exceeds a preset threshold (i.e.  $E_i^2/\text{TSE}$  exceeds a predetermined threshold).

Suppose we are concerned with the probability of a degradation being detected. It then becomes necessary to examine the operation of the accumulators. Each accumulator accepts the output of a gyro (in angular bits) at the attitude algorithm update rate. If we classify the quantization effect as noise, a graph of accumulated angle versus time for a gyro having a bias shift in drift might resemble Fig. 8.7 where noise is not shown. We are assuming that the bias shift has occurred just at an update time for the parity equations at the origin. In practice, the accumulator holds up to four minutes worth of data, but every 2 minutes the oldest 2 minute section of data (out of the previous four minutes) is purged. The accumulation rate (not indicated in the figure) is 50 updates per second (in the SIRU system described in this report). Still discounting the noise, the TSE corresponding to Fig.8.6 might resemble that of Fig. 8.8.

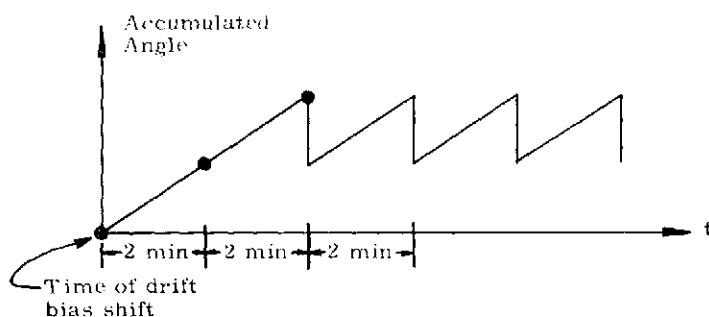


Fig. 8.7 Accumulated Angle (No Quantization) for a Bias Shift in Drift

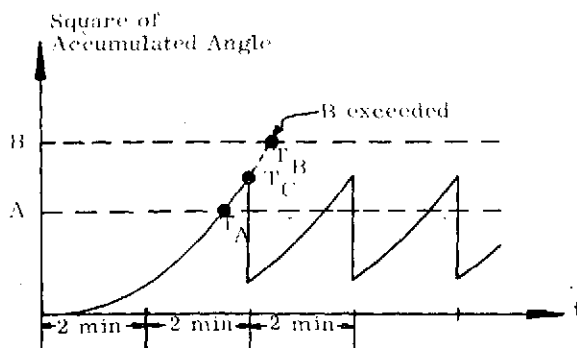


Fig. 8.8 Total Squared Error (No Quantization) for a Bias Shift in Drift

For the conditions shown in Fig. 8.8, there are two significant levels to be considered. One level is the TSE detection threshold. The TSE, including noise, must be above this threshold in order for the degradation to be detected. The other level is the maximum allowable degradation, which is assumed to lie above the detection threshold. If the accumulated angle exceeds this degradation level before detection, we have a missed alarm. Shown in Fig. 8.8 are detection threshold A and degradation threshold B, where the degradation thresholds have been converted to units of angle squared. It is seen in Fig. 8.8 that detection is most likely to take place at update times occurring between points  $T_A$  and  $T_C$  (shown in the figure). If no detection takes place between points  $T_A$  and  $T_B$ , we have a missed alarm because the degradation threshold will be met at point  $T_B$ . The decision to accept or reject gyro data is always made before the data is incorporated by the attitude algorithm. Figure 8.9 shows the situation for a very high drift degradation ( $TSE_1$ ). In the case depicted, the drift degradation is so high that the degradation threshold is reached before the next update (20 msec later). A decision must be made at point  $T_C$  (in the Fig. 8.8) to accept or reject the data. Note that the higher the TSE is at update time, the more likely is the data to be rejected (and the lower the missed alarm probability). This conclusion is valid because the degradation to noise (including quantization) ratio is higher and the noise is less likely to cause the TSE to be below the detection threshold, A, at the time a decision is made. It is seen, therefore, that at infinite drift degradation, the probability of detecting a degradation is 1 and that this probability drops off for lower rates.

The lowest probability of detection is reached when the TSE just crosses the degradation threshold at the update time ( $TSE_2$  in Fig. 8.9). If the degradation drift is lower than the drift corresponding to  $TSE_2$ , a degradation threshold is not reached even if the data is accepted. Furthermore, the data has another chance of being rejected at the next update time. There are two chances of rejecting bad data in the  $TSE_3$  example shown in Fig. 8.9. One chance is at  $T_A$  and the other is at  $T_B$ . Thus, the probability of detection will begin to increase at rates lower than those corresponding to  $TSE_2$  (when the degradation threshold B is reached exactly at the update time immediately following the update time at which the degradation occurred). The lower the degradation rate, the higher is the probability of detecting the degradation, until a maximum is reached. The probability of detection then decreases again because the degradation rate becomes so low that the accumulators do not amass a high enough value before being purged of the oldest two minute segment of data. This situation is depicted in Fig. 8.10. Here is a low probability of detecting the degradation because the noiseless, calculated TSE value is always below the detection threshold (TSE including noise could bring the value above the threshold). If there is no detection before the degradation threshold is reached at

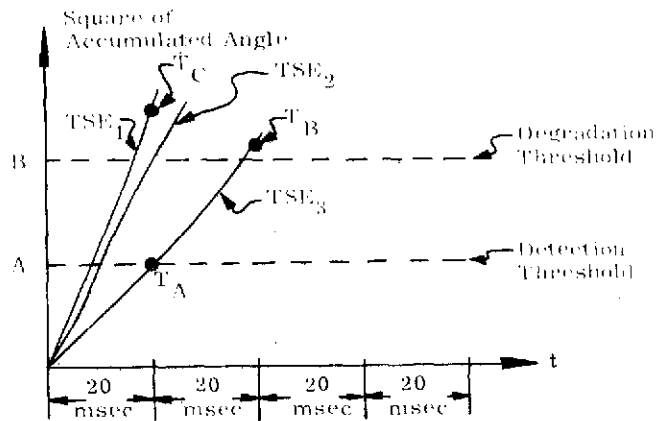


Fig. 8.9 Total Squared Error for High Drift Degradation (No Quantization)

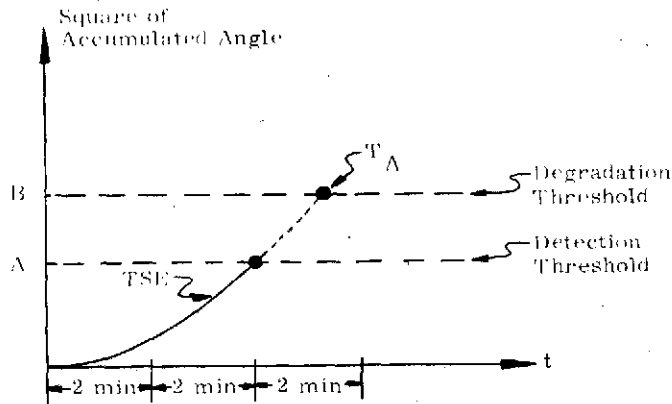


Fig. 8.10 Total Squared Error for Low Drift Degradation (No Quantization)

point  $T_A$  (Fig. 8.10), we have a missed alarm. Figure 8.11 is a sketch (not drawn to scale) representing the probability of detecting a failure as a function of the drift rate degradation. A portion of the curve is dashed because there are local minima during this portion that are not shown although all such minima would necessarily be above the minimum value at point B, which corresponds to the case of  $TSE_2$  depicted in Fig. 8.9 (Here the corresponding rate,  $R_B$ , is given by the degradation threshold divided by the 20 msec update period). All of the preceding arguments were made on the basis of the assumption that the onset of degradation occurred at an update time and at the origin. Some further thought shows that when the degradation occurs between update periods the minimum point B (Fig. 8.11) still occurs but at a different degradation rate.

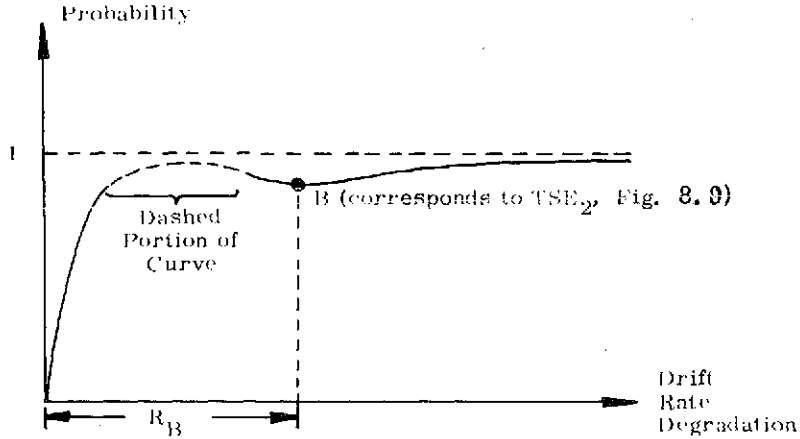


Fig. 8.11 Probability of Detection vs. Drift Rate Degradation

The minimum point B occurs for a degradation rate applicable to the case of the TSE crossing the degradation threshold at the first update time following the onset of the degradation. It is this "worst case" (minimum point B, Fig. 8.11) that is examined in all of the following analyses and simulations. The simulations from which most of the probabilities presented here were derived utilized 10,000 trials for each case. An upper bound on the probability of not detecting a failure was theoretically derived and corresponds well with the simulation-derived data.

### 8.6.3 First Failure

#### 8.6.3.1 Probability of Not Detecting a First Failure

An upper bound on the probability of not detecting a failure is derived using the parity equations for a first failure. The probability of not detecting a failure will be no higher than the upper bound.

The parity equations can be written as follows:

$$\begin{aligned}
 E_1 &= m_1 - \sqrt{0.2} (m_2 - m_3 - m_4 + m_5 + m_6) \\
 E_2 &= m_2 - \sqrt{0.2} (m_1 + m_3 + m_4 + m_5 + m_6) \\
 E_3 &= m_3 - \sqrt{0.2} (-m_1 + m_2 + m_4 - m_5 + m_6) \\
 E_4 &= m_4 - \sqrt{0.2} (-m_1 + m_2 + m_3 + m_5 - m_6) \\
 E_5 &= m_5 - \sqrt{0.2} (m_1 + m_2 - m_3 + m_4 - m_6) \\
 E_6 &= m_6 - \sqrt{0.2} (m_1 + m_2 + m_3 - m_4 - m_5)
 \end{aligned}
 \tag{8.22}$$

Suppose  $m_1$  is degraded with a  $K_1$  bias. Then:

$$\begin{aligned} E_1 &= K_1 + P_1 - \sqrt{0.2} (P_2 + \dots + P_6) \\ E_2 &= P_2 - \sqrt{0.2} K_1 - \sqrt{0.2} (P_1 + P_3 + \dots + P_6), \text{ etc.} \end{aligned} \quad (8.23)$$

The  $P$ 's are gyro noise values.

We define the following noise values:

$$\begin{aligned} n_1 &= -\sqrt{0.2} (P_2 - P_3 - P_4 + P_5 + P_6) \\ n_2 &= -\sqrt{0.2} (P_1 + P_3 + P_4 + P_5 + P_6) \\ n_3 &= -\sqrt{0.2} (-P_1 + P_2 + P_4 - P_5 + P_6) \\ n_4 &= -\sqrt{0.2} (P_1 + P_2 + P_3 + P_5 - P_6) \\ n_5 &= -\sqrt{0.2} (P_1 + P_2 - P_3 + P_4 - P_6) \\ n_6 &= -\sqrt{0.2} (P_1 + P_2 + P_3 - P_4 - P_5) \end{aligned} \quad (8.24)$$

Substituting Eq. 8.24 into Eq. 8.23 yields:

$$\begin{aligned} E_1 &= K_1 + P_1 + n_1 \\ E_2 &= -\sqrt{0.2} K_1 + P_2 + n_2 \\ E_3 &= \sqrt{0.2} K_1 + P_3 + n_3 \\ E_4 &= \sqrt{0.2} K_1 + P_4 + n_4 \\ E_5 &= -\sqrt{0.2} K_1 + P_5 + n_5 \\ E_6 &= -\sqrt{0.2} K_1 + P_6 + n_6 \end{aligned} \quad (8.25)$$

Squaring each equation in Eq. 8.25 yields the following:

$$\begin{aligned}
 E_1^2 &= K_1^2 + 2K_1 (P_1 + n_1) + (P_1 + n_1)^2 \\
 E_2^2 &= 0.2K_1^2 - 2\sqrt{0.2} K_1 (P_2 + n_2) + (P_2 + n_2)^2 \\
 E_3^2 &= 0.2K_1^2 + 2\sqrt{0.2} K_1 (P_3 + n_3) + (P_3 + n_3)^2 \\
 E_4^2 &= 0.2K_1^2 + 2\sqrt{0.2} K_1 (P_4 + n_4) + (P_4 + n_4)^2 \\
 E_5^2 &= 0.2K_1^2 - 2\sqrt{0.2} K_1 (P_5 + n_5) + (P_5 + n_5)^2 \\
 E_6^2 &= 0.2K_1^2 - 2\sqrt{0.2} K_1 (P_6 + n_6) + (P_6 + n_6)^2
 \end{aligned} \tag{8.26}$$

By definition the total squared error (TSE) is given by:

$$\text{TSE} \triangleq E_1^2 + E_2^2 + E_3^2 + E_4^2 + E_5^2 + E_6^2 \tag{8.27}$$

Substituting Eq. 8.26 into Eq. 8.27 results in:

$$\begin{aligned}
 \text{TSE} &= 2K_1^2 + 2K_1 (P_1 + n_1) \\
 &+ 0.9K_1 (-P_2 + P_3 + P_4 - P_5 - P_6 - n_2 + n_3 \\
 &+ n_4 - n_5 - n_6) + N
 \end{aligned} \tag{8.28}$$

where:

$$N \triangleq \sum_1^6 (P_i + n_i)^2 \tag{8.29}$$

Substituting Eq. 8.24 into Eq. 8.28 and simplifying yields the following equation for TSE in terms of the degradation,  $K_1$ , and gyro noises,  $P_1, \dots, P_6$ :

$$\text{TSE} = 2(K_1^2 + K_1 S) + N \tag{8.30}$$

where:

$$S \triangleq 2P_1 - .9P_2 + .9P_3 + .9P_4 - .9P_5 - .9P_6 \tag{8.31}$$

Note that since  $P_1, \dots, P_6$  are independent random variables, the standard deviation,  $\sigma_S$ , of  $S$  is simply given by:

$$\begin{aligned}\sigma_S &= \sqrt{2^2 + 5(.9)^2} \sigma \\ &= 2.84\sigma\end{aligned}\tag{8.32}$$

where  $\sigma$  is the standard deviation of gyro noise. The assumption is that the independent gyro noises all have the same value of standard deviation.

Note in Eq. 8.30 that  $N$  is always a positive number (see Eq. 8.29). If  $N$  is dropped from Eq. 8.30, we obtain a value for the total squared error,  $TSE_{LB}$ , that is always less than the true total squared error. Here:

$$\begin{aligned}TSE_{LB} &= 2(K_1^2 + K_1 S) \\ &\leq 2(K_1^2 + K_1 S) + N \\ &= TSE\end{aligned}\tag{8.33}$$

By setting  $TSE_{LB}$  equal to the threshold value of  $2(132)^2 \text{ sec}^2$  we obtain the proper value of  $S$  that yields an upper bound on the probability of not detecting a degradation. Thus:

$$2(K_1^2 + K_1 S) = 2(132)^2\tag{8.34}$$

and:

$$S = \frac{(132)^2 - K_1^2}{K_1}\tag{8.35}$$

If  $S$  is Gaussian, the upper bound probability value is obtained by dividing  $S$  by  $\sigma_S$  and looking up the result in a table of Gaussian values.

This theoretical upper bound was plotted as a function of the degradation,  $K_1$ , for  $\sigma = 18 \widehat{\text{sec}}$  (see Eq. 8.32). Figure 8.12 contains the resulting curve (dashed line) along with simulations made using Gaussian noise with  $\sigma = 5.4, 12,$  and  $18 \widehat{\text{sec}}$ . Note that the upper bound shows that if the simulation curves were extended, the probability of not detecting a gyro degradation of  $300 \widehat{\text{sec}}$  (which corresponds to less than  $128 \widehat{\text{sec}}$  for the system because data from five other good instruments are used) is less than  $10^{-6}$ . The curves obtained from simulations do not extend

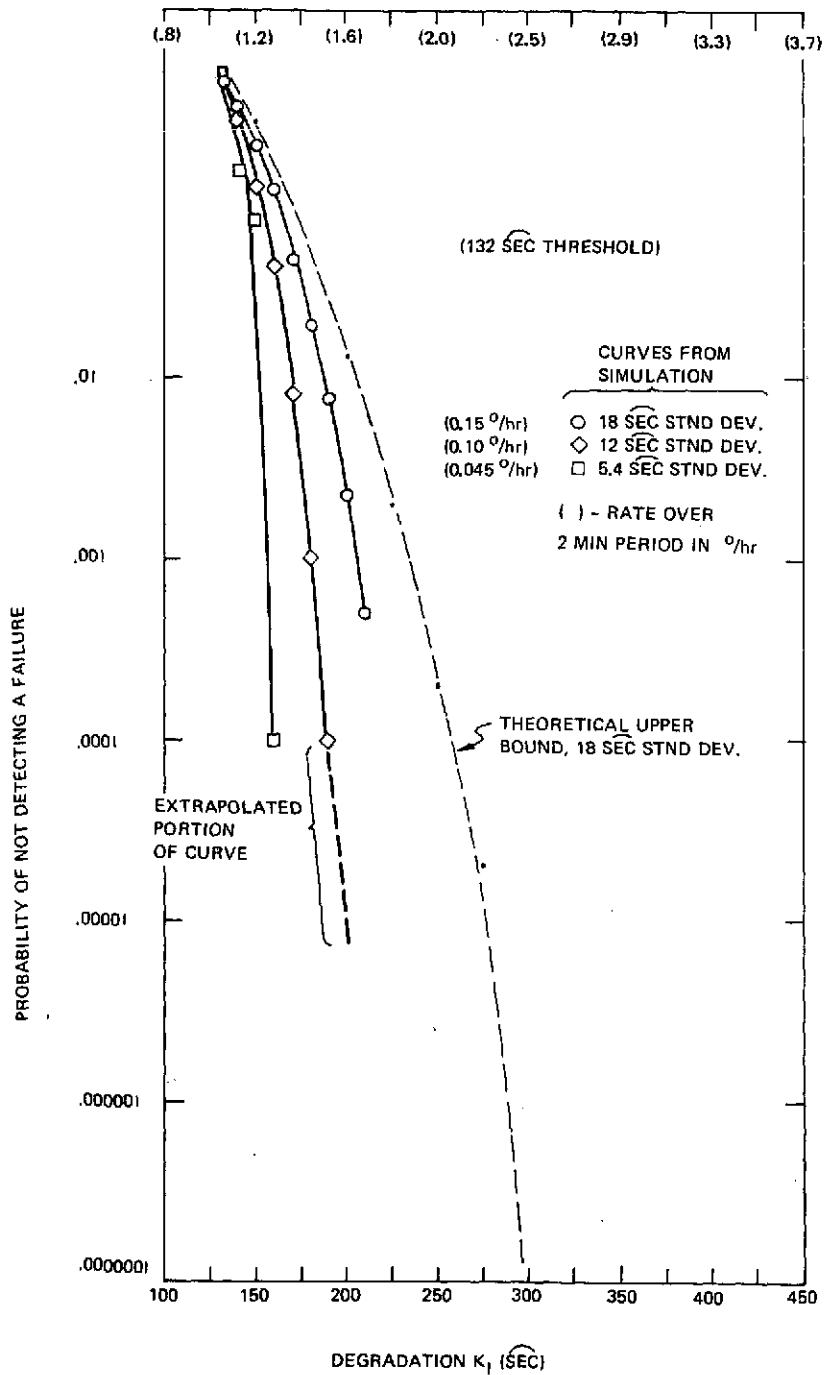


Fig. 8.12 Probability of Not Detecting a Failure - First Failure (A-Gyro)

below  $10^{-4}$  due to the excessive computer time required for the  $10^5$  and  $10^6$  trials needed to determine points below the  $10^{-4}$  ordinate on the graph. The theoretical upper bound demonstrates that we can safely extrapolate these curves below  $10^{-4}$ .

The values in  $\widehat{\text{sec}}$  shown in Fig. 8.12 are converted to rate ( $^\circ/\text{hr}$ ) for a two minute time period and are shown in parentheses on the figure. The standard deviation of  $.045^\circ/\text{hr}$  ( $\sigma = 5.4 \widehat{\text{sec}}$ ) conforms to the measurement of the parity equation residuals (see Chapter 2) made for a static environment, whereas  $0.15^\circ/\text{hr}$  ( $\sigma = 18 \widehat{\text{sec}}$ ) conforms to the parity equation measurements for a dynamic environment. The value of  $0.1^\circ/\text{hr}$  ( $\sigma = 12 \widehat{\text{sec}}$ ) is intermediate between the other two values. The simulation results for each of these noise levels show that the probability of missing a failure (missed alarm) in all cases is well below the theoretical upper bound. For example, the probability of missing a failure with the  $18 \widehat{\text{sec}}$  standard deviation noise simulation was less than 1ppm with a gyro degradation of approximately  $250 \widehat{\text{sec}}$ .

Simulation runs were also made to obtain the probability of false detection (i.e., false alarm) when the degradation,  $K_1$ , is zero. No false alarms were obtained for  $10^4$  trials in any of the runs.

### 8.6.3.2 Probability of Not Isolating a First Failure

Any theoretical solution for the ratio:

$$R_1 = E_1/TSE \quad (8.36)$$

is analytically intractable since we are dealing with the ratio of squared terms that are statistically correlated. Hence we must rely entirely on simulations for the case of failure isolation.

Figure 8.13 is a plot of the results of several simulations in which the isolation threshold is 0.44. The curve, for noise with a standard deviation of  $18 \widehat{\text{sec}}$ , was conservatively extrapolated (as shown) to show a probability of not isolating a first failure as less than  $10^{-4}$ . This extrapolation is allowable because a computer run with  $10^5$  trials was made in which the ratio of 0.44 was exceeded for every trial. Also, the probabilities for all data corresponding to the static case ( $\sigma = 5.4 \widehat{\text{sec}}$ ) were  $<10^{-4}$  and hence are not shown on the graph.

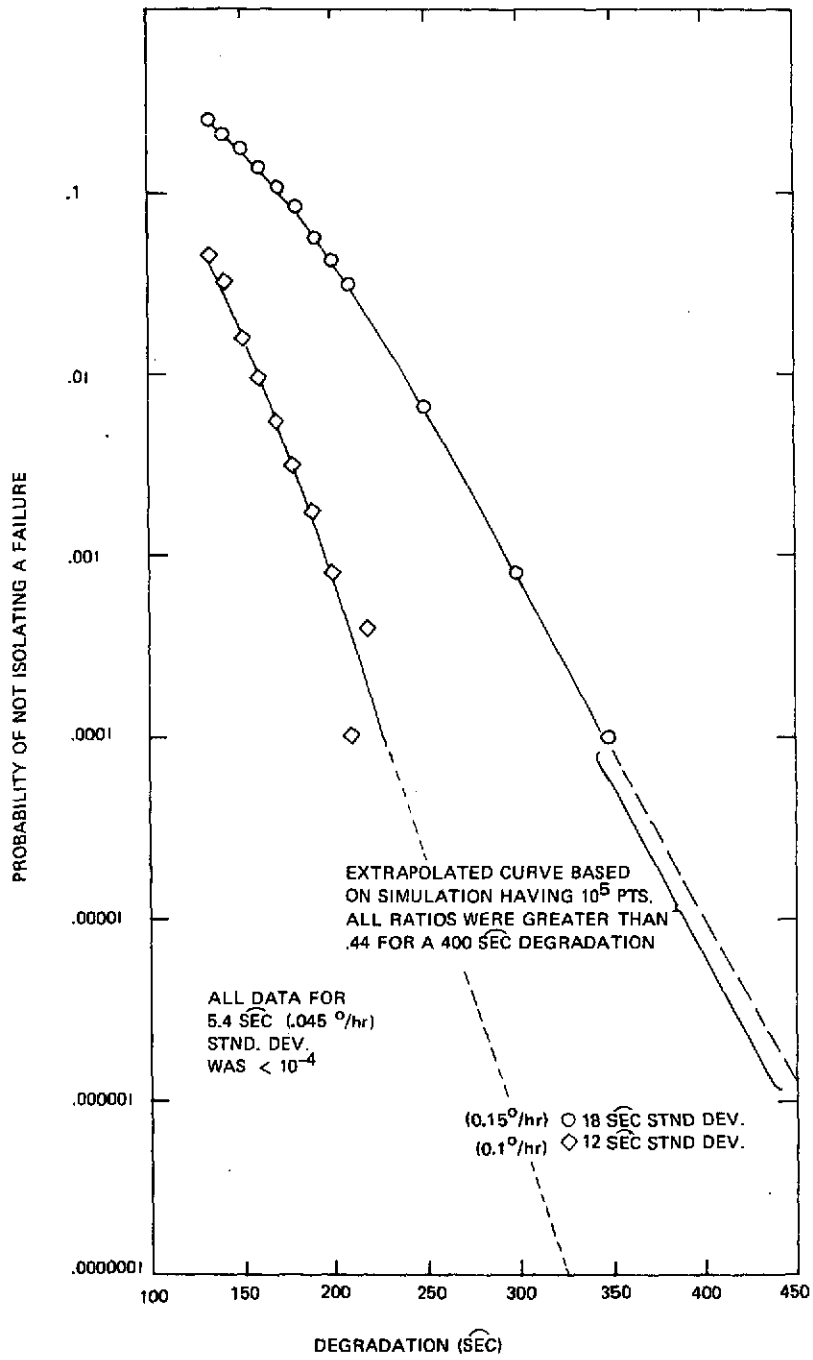


Fig. 8.13 Probability of Not Isolating a Failure - First Failure

Figure 8.14 plots the simulation results for the probability of not isolating a first failure for  $\sigma = 18 \text{ sec}$  and the threshold ratio as a parameter. As expected, the lower the ratio, the lower the probability of not isolating a failure. However, a low threshold increases the probability of isolating the wrong instrument. The simulation results also showed that, for degradations  $>180 \text{ sec}$ , the false isolation probability was less than 0.0001 with all ratios  $\geq 0.4$ .

Figure 8.15 presents similar plots except that standard deviations of  $12 \text{ sec}$ , was used. Comparing Figs. 8.14 and 8.15 reveals, as expected, that lower gyro noise results in lower probabilities of not isolating a failure. The probability of a false isolation for degradations above  $160 \text{ sec}$  is less than  $10^{-4}$  with an isolation ratio  $\geq 0.3$  with this lower  $12 \text{ sec}$  gyro noise.

Trial runs were also made with  $\sigma = 5.4 \text{ sec}$ . In all of these runs the probabilities for not isolating a first failure and for not falsely isolating an instrument were  $<10^{-4}$  with the isolation ratio  $\geq 0.3$ .

The above results indicate that there is a fairly wide range of isolation ratios for which the probability of incorrectly or not isolating a proper failure is low. The exact choice of such a ratio depends on the mission environment. For a relatively severe environment ( $\sigma = 18 \text{ sec}$ ), a choice of R between 0.4 and 0.45 results in low probabilities. The present threshold could therefore be safely lowered from 0.44. However, the exact amount that it could be lowered depends on further experimentation since we would like the false isolation probability to be lower than the probability of not isolating a failure. This preference is reasonable because improperly isolating a good instrument is obviously more deleterious to the redundant management system performance than failure to isolate the degraded instrument (for which a new chance at isolation at the next iteration period is always available).

#### 8.6.4 Second Failure

##### 8.6.4.1 Probability of Not Detecting a Second Failure

An upper bound on the probability of not detecting a second failure is derived using the parity equations for a second failure. The probability of not detecting a second failure will be no higher than the upper bound.

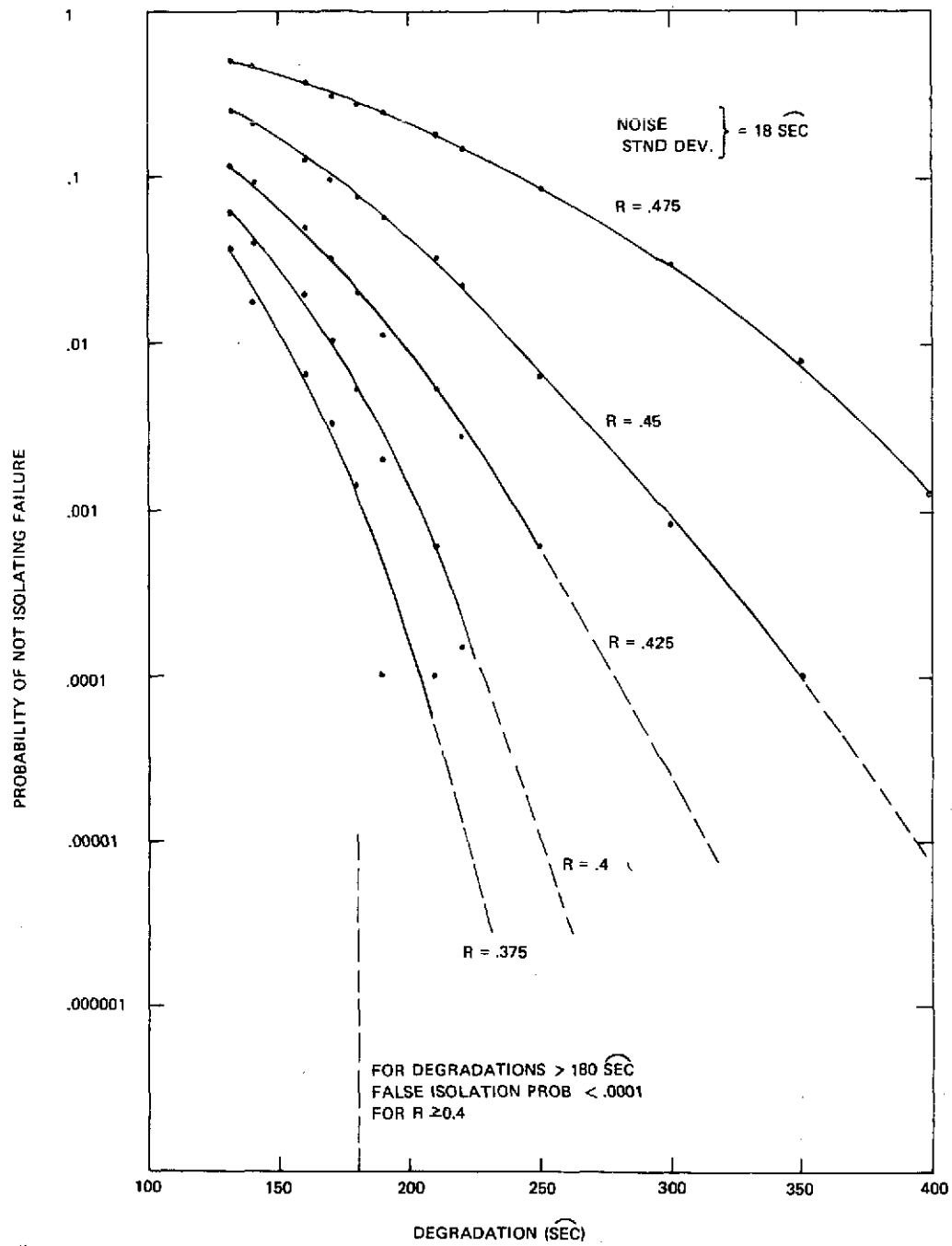


Fig. 8.14 Probability of Not Isolating a Failure - First Failure (A-Gyro)

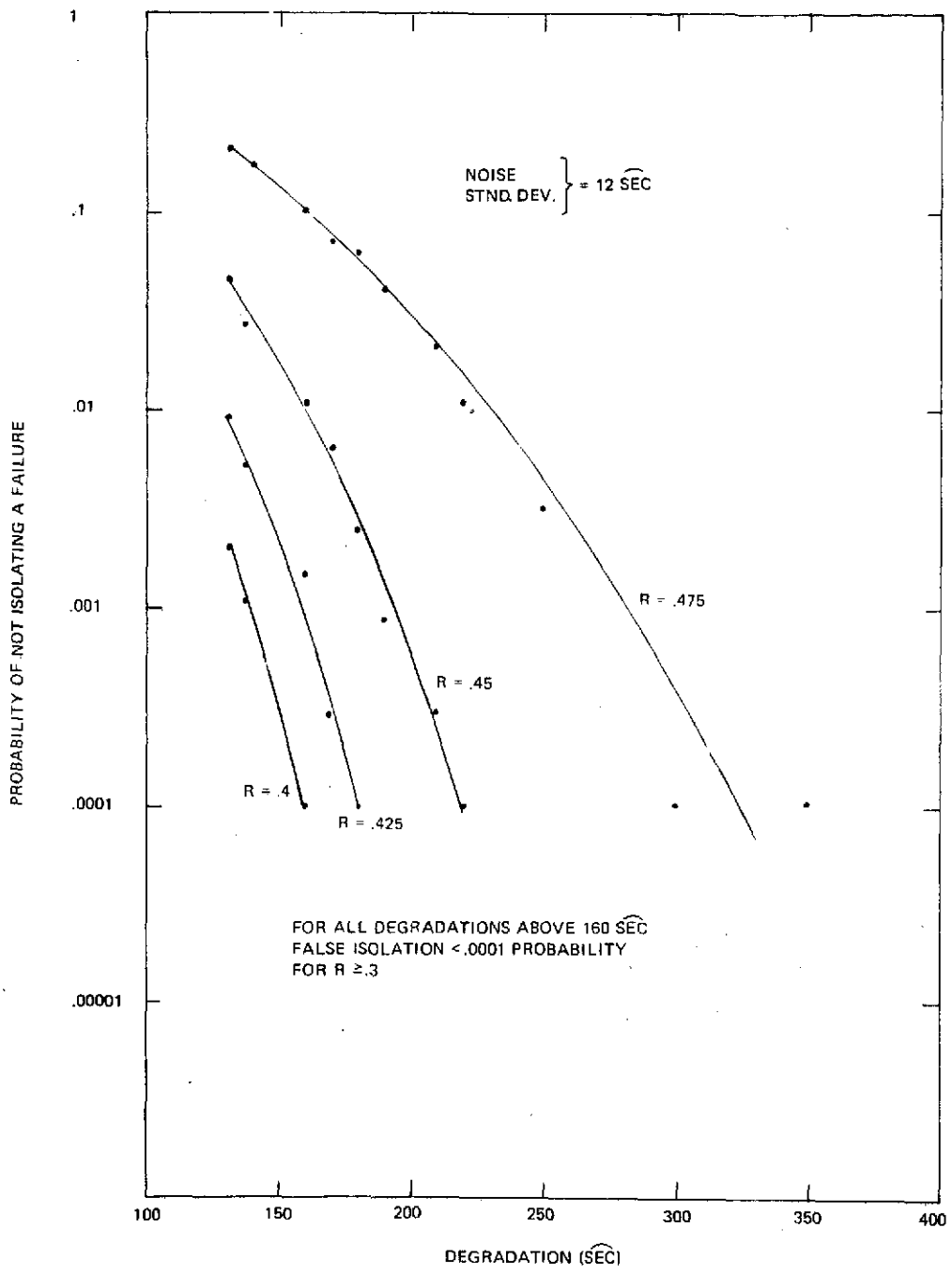


Fig. 8.15 Probability of Not Isolating a Failure - First Failure (A-Gyro)

The parity equations can be written as follows for the gyro #1 (A-gyro) failure:

$$\begin{aligned}
 m_1 &= \sqrt{0.2} (m_2 - m_3 - m_4 + m_5 + m_6) \\
 E_2 &= m_2 - \sqrt{0.2} (m_1 + m_3 + m_4 + m_5 + m_6) \\
 E_3 &= m_3 - \sqrt{0.2} (m_2 - m_1 + m_4 - m_5 + m_6) \\
 E_4 &= m_4 - \sqrt{0.2} (m_2 - m_1 + m_3 + m_5 - m_6) \\
 E_5 &= m_5 - \sqrt{0.2} (m_1 + m_2 - m_3 + m_4 - m_6) \\
 E_6 &= m_6 - \sqrt{0.2} (m_1 + m_2 + m_3 - m_4 - m_6)
 \end{aligned} \tag{8.37}$$

Substituting the first equation of Eq. 8.37 into the remaining 5 equations yields the following:

$$\begin{aligned}
 E_2 &= (1-f^2) m_2 - f (m_3 (1-f) + m_4 (1-f) + m_5 (1+f) + m_6 (1+f)) \\
 E_3 &= m_2 (f^2-f) + m_2 - f (fm_3 + m_4 (1-f) - m_5 (1+f) + m_6 (1-f)) \\
 E_4 &= m_2 (f^2-f) + m_4 - f (m_3 (1+f) + m_4 f + m_5 (1-f) - m_6 (1+f)) \\
 E_5 &= -m_2 (f^2+f) + m_5 - f (m_5 f - m_3 (1+f) + m_4 (1-f) - m_6 (1-f)) \\
 E_6 &= -m_2 (f^2+f) + m_6 - f (m_6 f + m_3 (1-f) - m_4 (1+f) - m_5 (1-f))
 \end{aligned} \tag{8.38}$$

Substituting  $f=\sqrt{0.2}$ , letting the gyro #2 (B-gyro) have a degradation of  $K_2$ , and substituting  $P_2$ - $P_6$  for the gyro noise for instruments 2-6 respectively yields:

$$\begin{aligned}
 E_2 &= .8K_2 + .8P_2 - .247P_3 - .247P_4 - .647P_5 - .647P_6 \\
 E_3 &= -.247K_2 - .247P_2 + .8P_3 - .247P_4 + .647P_5 - .247P_6 \\
 E_4 &= -.247K_2 - .247P_2 - .647P_3 + .8P_4 - .247P_5 + .647P_6 \\
 E_5 &= -.647K_2 - .647P_2 + .647P_3 - .247P_4 + .8P_5 + .247P_6 \\
 E_6 &= -.647K_2 - .647P_2 - .247P_3 - .647P_4 + .247P_5 + .8P_6
 \end{aligned} \tag{8.39}$$

Equation 8.39 is substituted into the following expression for the TSE:

$$\text{TSE} = E_2^2 + E_3^2 + E_4^2 + E_5^2 + E_6^2 \tag{8.40}$$

If we define S as follows:

$$S = 1.6 P_2 - .544 P_3 + .245 P_4 - 1.3 P_5 - 1.3 P_6 \quad (8.41)$$

Then:

$$TSE = 1.6 K_2^2 + 2 K_2 S + Q \quad (8.42)$$

where Q is a positive term  $\geq$  zero.

As was done for the first failure case, we can solve for S by dropping the positive term, Q, in order to find the upper bound on the probability of not detecting a degradation. Thus:

$$TSE_{LB} = 1.6 K_2^2 + 2 K_2 S \quad (8.43)$$

and:

$$S = \frac{1.6 (132)^2 - 1.6 K_2^2}{2 K_2} \quad (8.44)$$

Here  $1.6 (132)^2$  is the detection threshold used in SIRU for the second failure detection TSE.

Also from Eq. 8.41 we see that the standard deviation of S is given by:

$$\sigma_S = 2.51 \sigma \quad (8.45)$$

The value  $\sigma$  is the standard deviation of the noise value,  $P_i$ . If S is Gaussian, then the upper bound probability value is obtained by dividing S by  $\sigma_S$  and looking up the result in a table of Gaussian values as was done for the first failure case.

Figure 8.16 shows the theoretical upper bound (dashed curve) along with simulation results for three different values of the noise standard deviation. Note that the simulation results are all similar in shape to the corresponding curves for the probability of not detecting the first failure (Fig. 8.12). However, all of the curves in Fig. 8.16 do not decrease quite as fast as the Fig. 8.12 curves. This comparison shows that it is slightly more difficult to detect a second failure than a first failure.

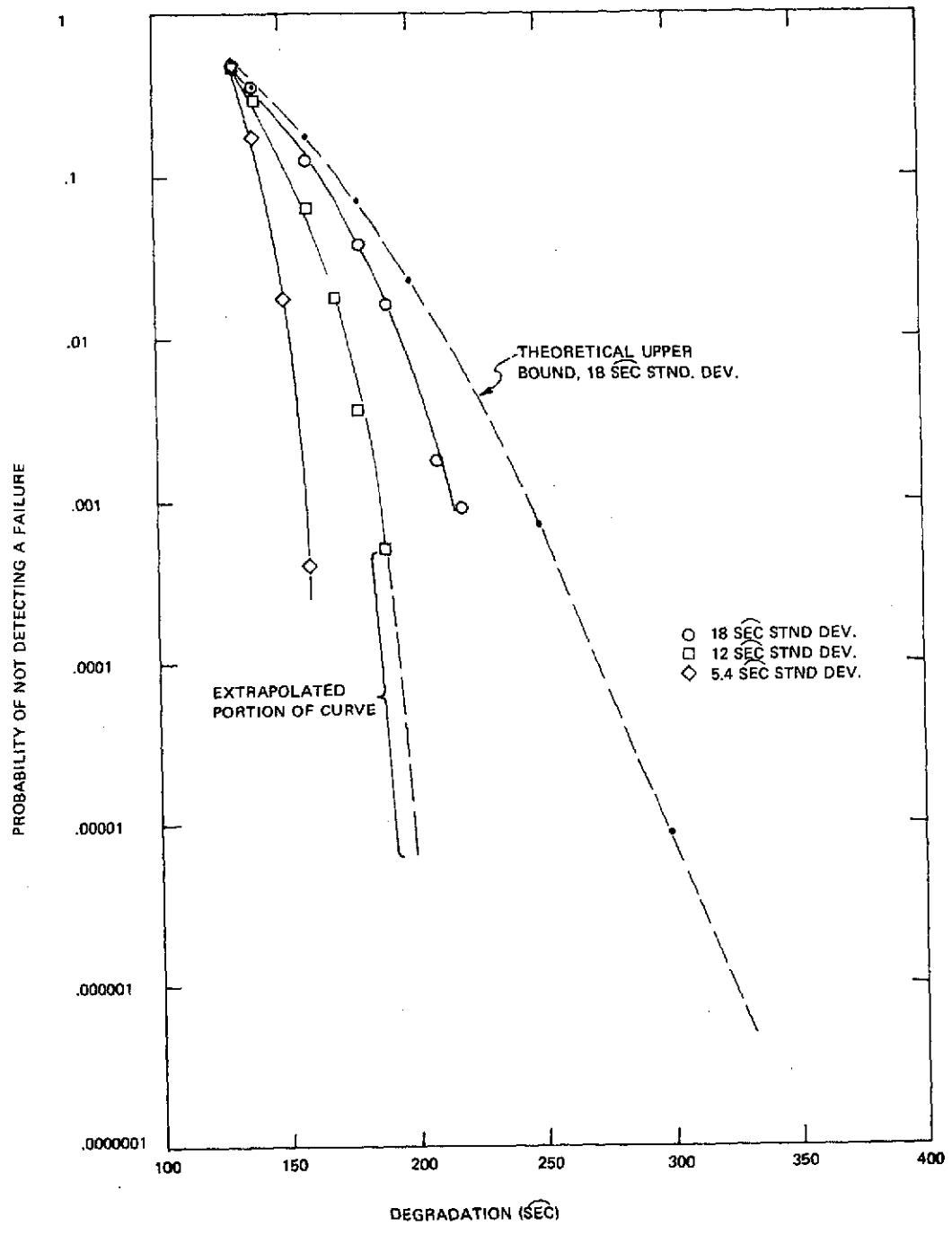


Fig. 8.16 Probability of Not Detecting a Failure - 2nd Failure (A then B Failed)

#### 8.6.4.2 Probability of Not Isolating a Second Failure

Figures 8.17 and 8.18 are plots of the results of simulations made to determine the probability of not isolating a second failure. As expected, the probability decreases with a decrease in the isolation threshold ratio. However, as shown in Figs. 8.19 through 8.20, probability of a false isolation increases as the ratio decreases. A balance must be struck between not isolating a failure and isolating the wrong instrument. The present ratio for a second failure ( $R=.387$ ) admits a low probability of false isolation (see Figs. 8.19 through 8.21) with a moderate probability of not isolating a failure (Figs. 8.17 and 8.18).

The false isolation probabilities for a second failure are considerably higher than those for a first failure. The E and F gyros exhibit the highest false isolation probabilities. Examination of Eq. 8.39 reveals that the E and F gyros do have a higher ratio, i.e.  $E_5/TSE$  and  $E_6/TSE$ , than gyros C and D, i.e.  $E_3/TSE$  and  $E_4/TSE$ , due to the  $K_2$  term in the numerator.

Runs for a noise value of 5.4  $\widehat{\text{sec}}$  were made in addition to the runs for Figs. 8.16 - 8.21. All probabilities (5.4  $\widehat{\text{sec}}$  noise) of not isolating a failure were less than 0.0001 with  $R>.325$ . The probabilities for false isolation were less than 0.0001 with  $R\geq 3$ .

#### 8.6.5 Simulation Accuracies

All but one of the points in Figs. 8.12 - 8.21 were derived from  $10^4$  trials for each point. It can be shown that the standard deviation for each estimate (i.e., each plotted point) is given by:

$$\sigma_P = \frac{1}{\sqrt{n}} \sqrt{(1-P)P} \quad (8.46)$$

Where P is the probability being plotted and n is the number of trials

If  $n = 10^4$ :

$$\sigma_P = \frac{\sqrt{(1-P)P}}{10^2} \quad (8.47)$$

Equation 8.47 is plotted in Fig. 8.22 for the case of  $10^4$  trials and P ranging from 0.1 to  $10^{-4}$ . It is seen from the graph that the standard deviation is reasonable for estimated probabilities of  $10^{-4}$  or higher. For example, at a probability of  $10^{-4}$  we obtain  $\sigma_P = 10^{-4}$ . Hence with 99% confidence we can say that the point is

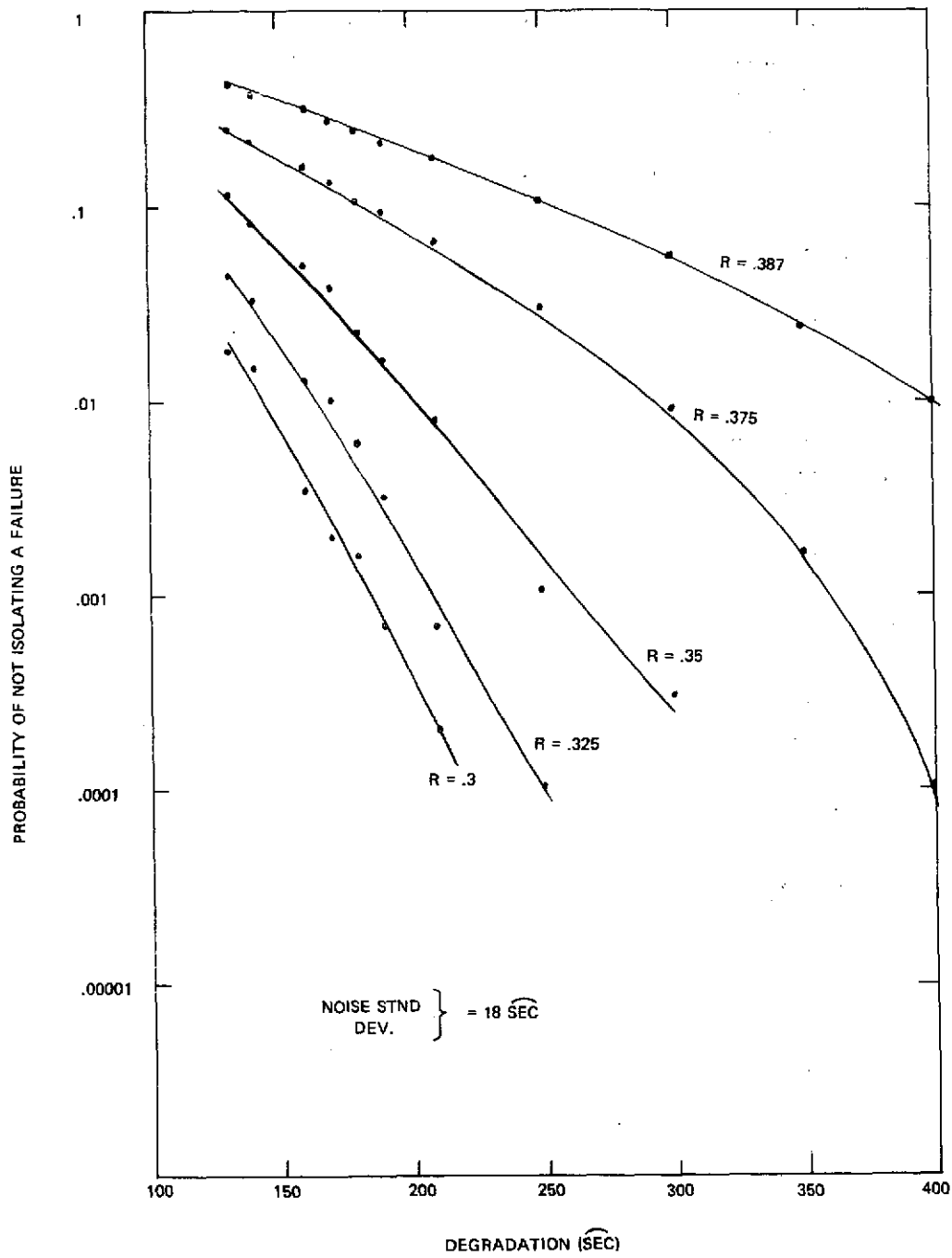


Fig. 8.17 Probability of Not Isolating Second Failure (B-Gyro)

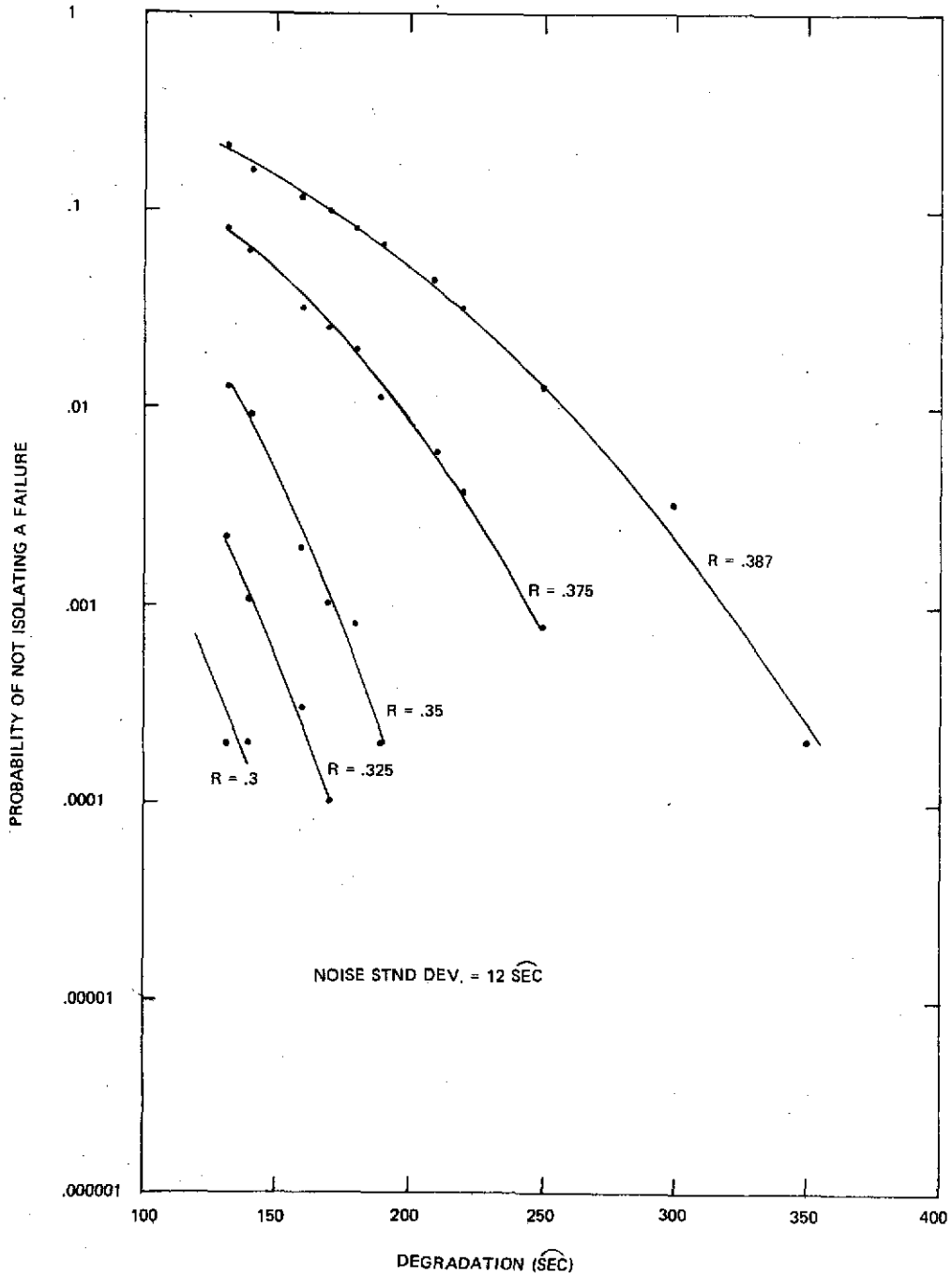


Fig. 8.18 Probability of Not Isolating Second Failure (B-Gyro)

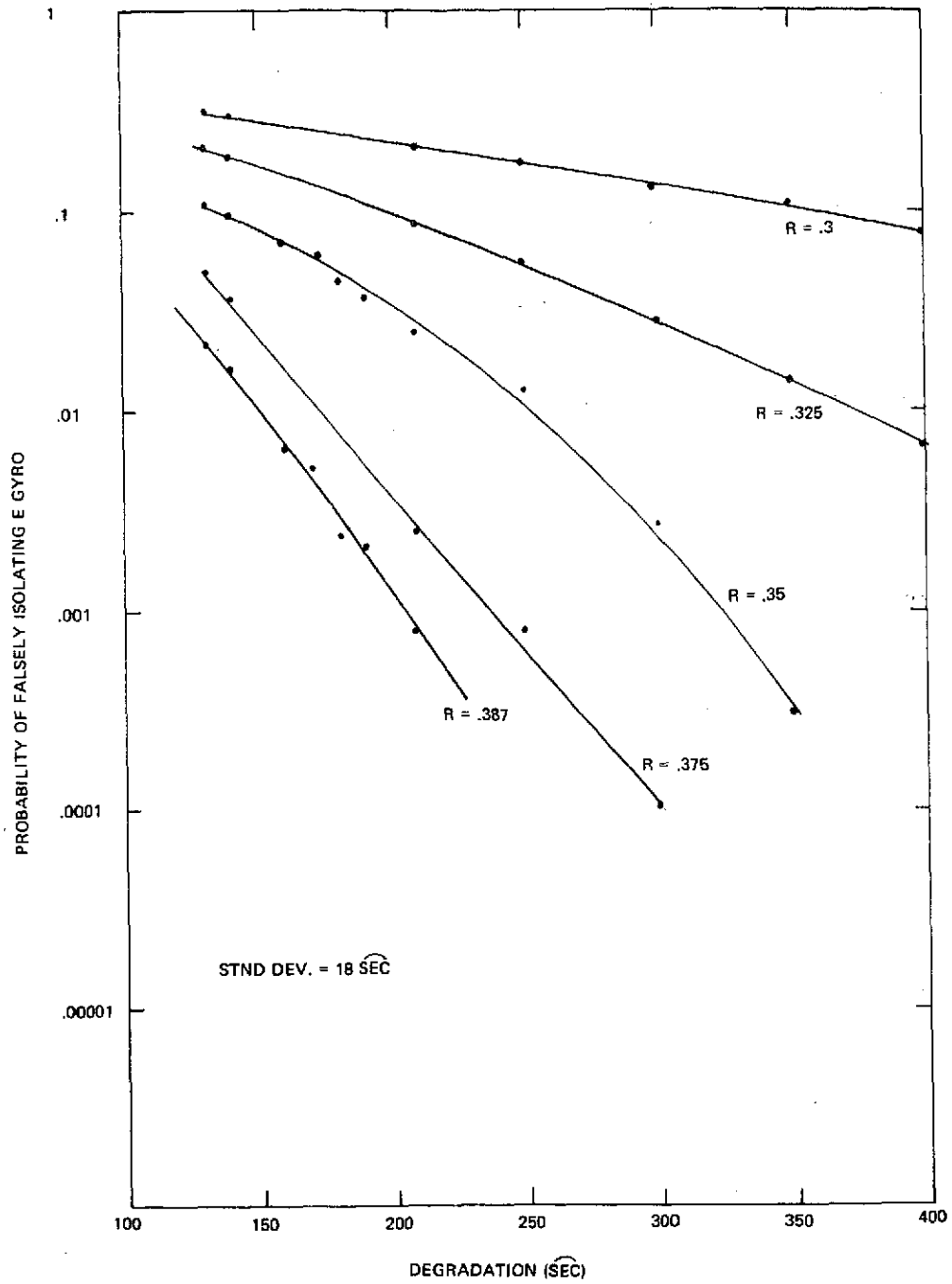


Fig. 8.19 Probability of Falsely Isolating E-Gyro as 2nd Failure (B-Gyro is 2nd Failure)

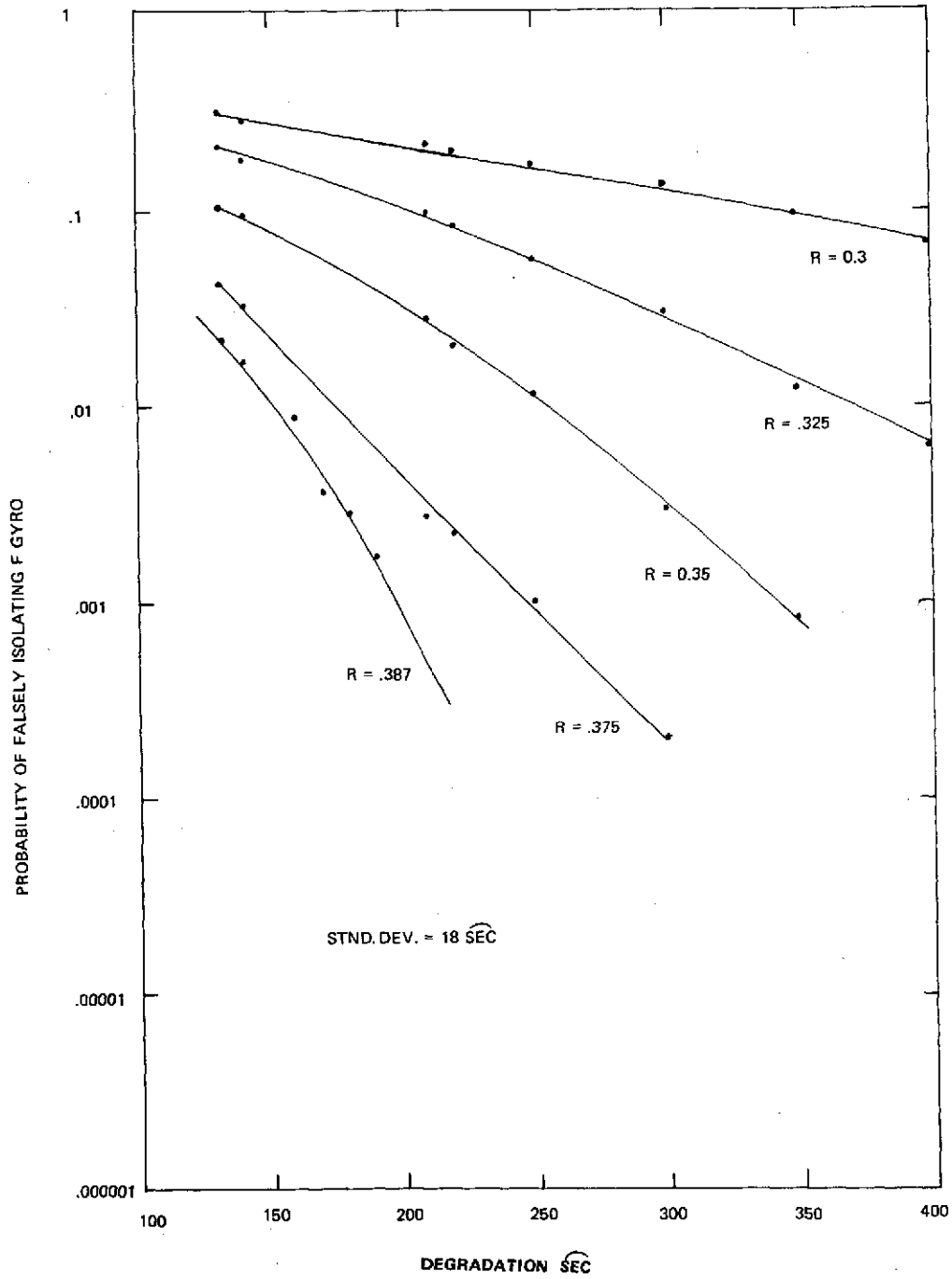


Fig. 8.20 Probability of Falsely Isolating F-Gyro as 2nd Failure (B-Gyro is 2nd Failure)

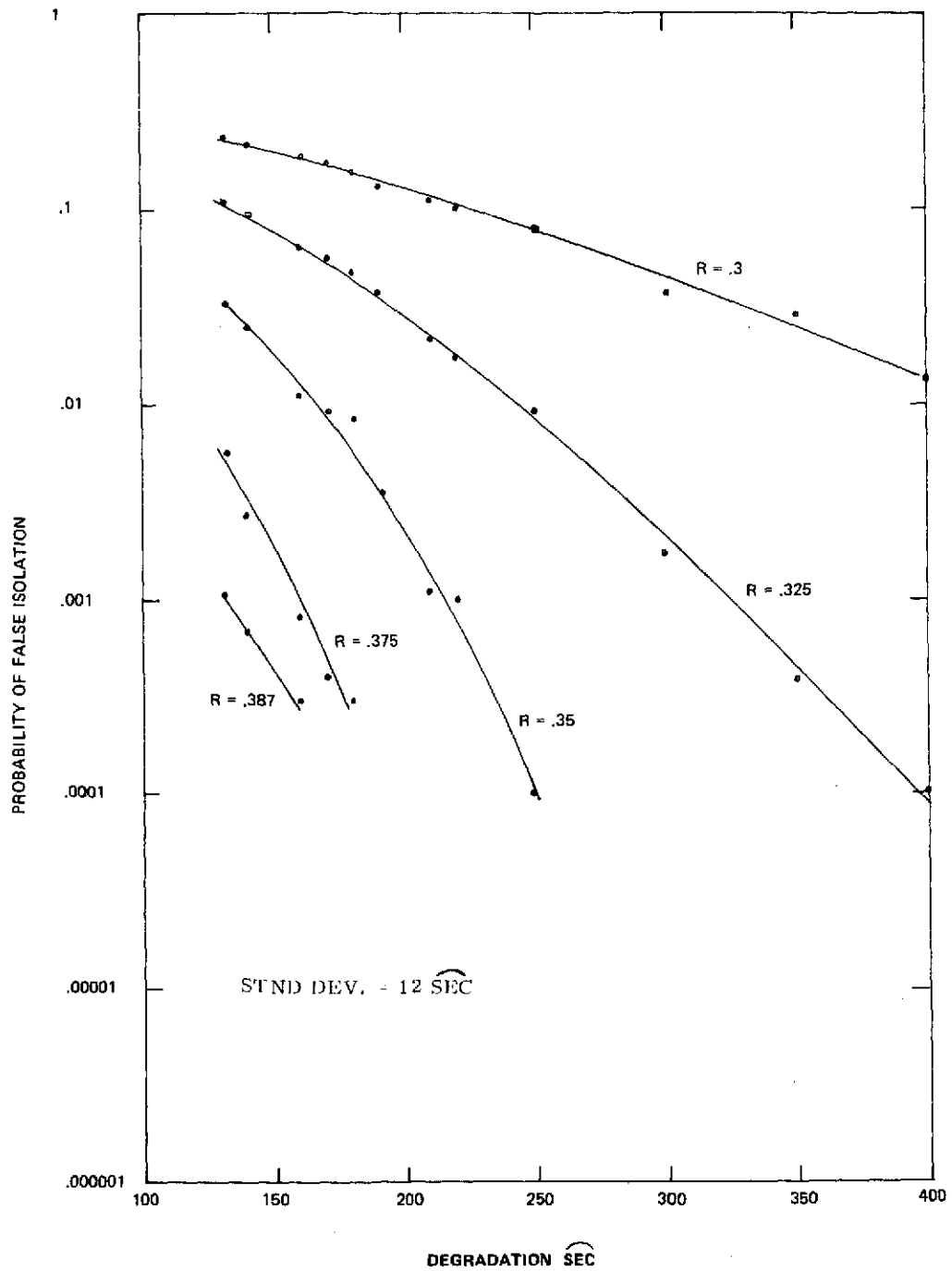


Fig. 8.21 Probability of Falsely Isolating E-Gyro as 2nd Failure (B-Gyro is 2nd Failure)

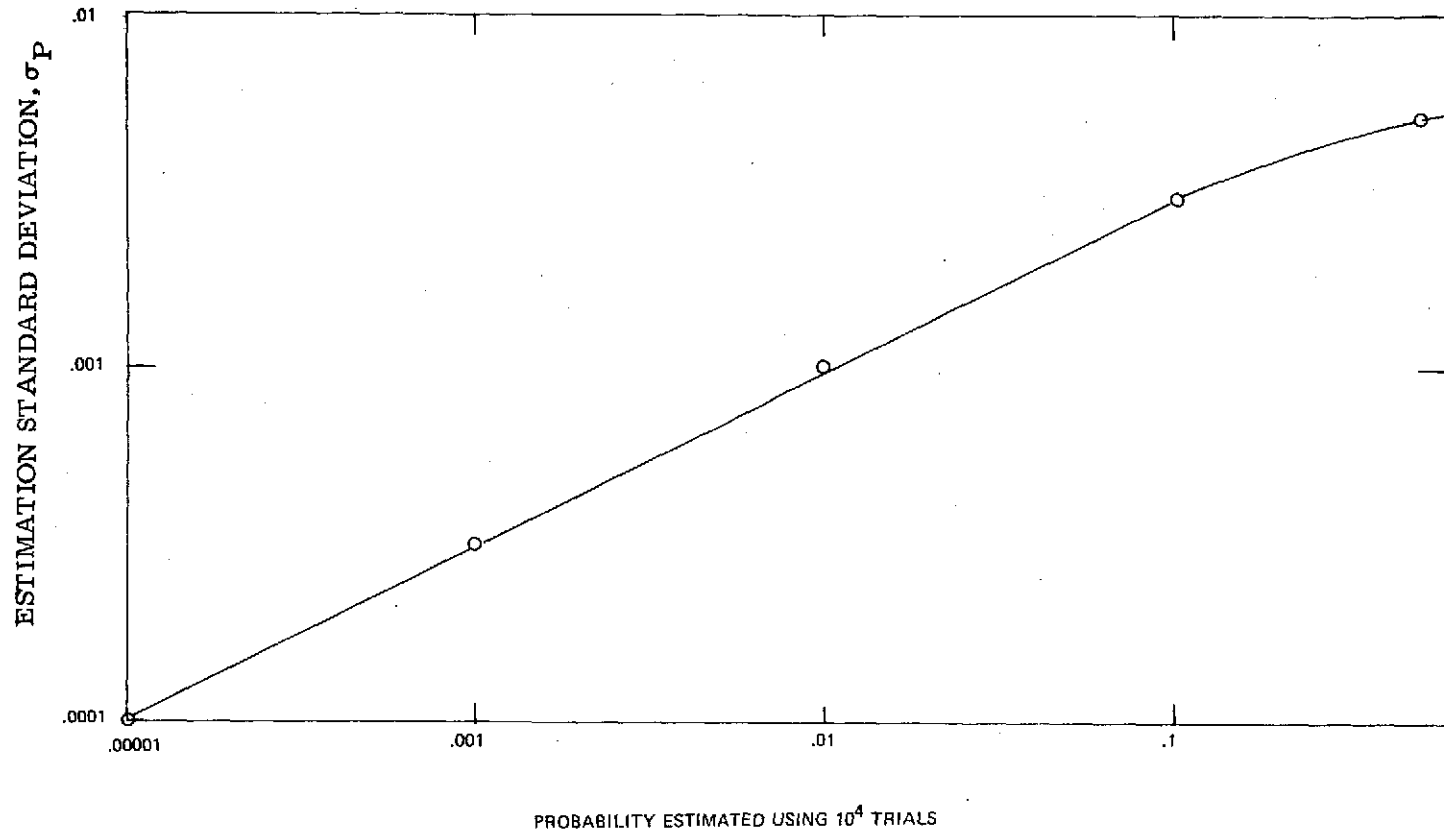


Fig. 8.22 Standard Deviation of Estimated Probability

within  $3 \times 10^{-4}$ . For a probability of  $10^{-3}$ , the standard deviation,  $\sigma_P$ , is 0.0003 which means that this probability point is 0.001 with 99% confidence. Hence, from Figs. 8.12 - 8.21, we can draw the conclusion that  $10^4$  trials is sufficient for the points plotted in those figures.

### 8.6.6 Limitations of Preceding Analysis

The simulations and analysis presented in Section 8.6 were done for the A-gyro degraded for the one failure case and for A-gyro and B-gyro degraded in the two failure case. Due to the symmetry of SIRU we would expect the results to be similar when other gyros are degraded and isolated. This expectation will be confirmed in future simulations and analysis for which gyros other than A and B will be failed.

## 8.7 Statistical FDICR Reliability

The statistical FDICR (Chapter 2) reliability is derived by taking into account the false and missed alarm probabilities.

### 8.7.1 Basic Equations

The performance of the failure detection subsystem is defined by the mean time delay  $\tau(T)$  in detecting a true degradation for a specified mean time T between two false alarms. The appropriate equations are given in Chapter 2 and are repeated below:

1) Equation for computation of T:

$$T = \frac{2\sigma^2}{a_1} \cdot \Delta \cdot (e^{B_1} - B_1 - 1) \quad (8.48)$$

where:

$\sigma$  = standard deviation of the random drift rate for a sample period  $\Delta$

$a_1$  = specified magnitude of parity residual bias drift rate in defining a true degradation

B = decision threshold for the likelihood ratio function in detecting degradation

It is noticed that the miss alarm probability of the implemented detection system is zero for the case of a large specified value of T:

$$B_1 \approx \ln \left( \frac{a_1^2}{2\sigma^2} \cdot \frac{T}{\Delta} \right) \quad (8.49)$$

2) Equation for computation of the detection time  $\tau(T)$  for a specified T is:

$$\begin{aligned} \tau(T) &= \left( \frac{2\sigma^2}{a_1^2} \right) \cdot \Delta \cdot \left[ \ln \left( \frac{T \cdot a_1^2}{\Delta \cdot 2\sigma^2} \right) - \frac{3}{2} \right] \\ &\sim \left( \frac{2\sigma^2}{a_1^2} \right) \cdot \Delta \cdot \left( B_1 - \frac{3}{2} \right) \end{aligned} \quad (8.50)$$

3) Equation for attitude error,  $\psi$ , as a function of detection time  $\tau(T)$  (For 1st failure):

$$\psi = \frac{a_1}{2} \tau(T) \quad (8.51)$$

The attitude error can be easily computed from Eqs. 8.48 - 8.50 if a different mean time between false alarms is specified. Let  $T_1$  be the original mean time between false alarm specification and  $T_2$  be the desired mean time. Then from Eq. 8.19 we have:

$$B(T_2) = B(T_1) + \ln \left( \frac{T_2}{T_1} \right) \quad (8.52)$$

and:

$$\frac{\tau(T_2)}{\tau(T_1)} \approx \frac{B(T_2) - 1.5}{B(T_1) - 1.5} \quad (8.53)$$

Here  $\tau(T_2)$  is the detection time corresponding to  $T_2$  and  $B(T_2)$  is the decision threshold picked to obtain  $T_2$ . Similar comments apply to  $\tau(T_1)$  and  $B(T_1)$ .

### 8.7.2 False and Missed Detection and Isolation

A simplified block diagram of the FDICR subsystem is presented in Fig. 8.23.

The probability of a missed detection and isolation in the detection and isolation portion of the diagram (Fig. 8.23) is assumed to be zero. Using the data from 30

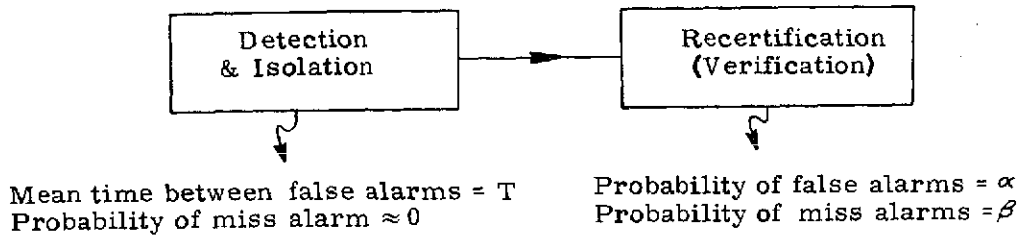


Fig. 8.23 FDICR Simplified Block Diagram

tests presented in chapter 2 for the angular error due to delay in detecting and isolating a failure, it is calculated that the mean error is  $\approx 81 \widehat{\text{sec}}$  with a standard deviation of  $23 \widehat{\text{sec}}$ . For an error of  $200 \widehat{\text{sec}}$  or higher, the probability of missing a failure (i.e. allowing the  $200 \widehat{\text{sec}}$  error) is less than  $3 \times 10^{-7}$ , which is an order of magnitude lower than any of the other probabilities that will be presented later for the statistical FDICR. A missed alarm, however, can occur due to performance of the FDICR system if the recertification portion in Fig. 8.23 wrongly verifies a degradation as being normal.

The following are the pertinent false and missed detection and isolation probabilities for statistical FDICR:

$$P(F_1) \triangleq \left\{ \begin{array}{l} \text{Probability of} \\ \text{First False Alarm} \end{array} \right\} = \frac{T_s}{T} \alpha \quad (8.54)$$

$$P(F_2) \triangleq \left\{ \begin{array}{l} \text{Probability of} \\ \text{False Alarm occurring} \\ \text{after first false alarm} \\ \text{or} \\ \text{a true degradation} \end{array} \right\} = \frac{T_s}{T} (\alpha + (1 - e^{-T_c/T})) \quad (8.55)$$

$$P(E_1) \triangleq \left\{ \begin{array}{l} \text{Probability of a} \\ \text{Miss Alarm in} \\ \text{Recertification} \end{array} \right\} = \beta \left( \frac{\delta}{\psi} \right) \quad (8.56)$$

Here

$T_s \triangleq$  duration of mission

$T \triangleq$  mean time between false alarms (Eq. 8.48)

- $\alpha \triangleq$  specified probability of false alarm in recertification
- $\beta \triangleq$  specified missed alarm probability(See Chapter 2 and Eqs. 2.11 and 2.12)
- $T_c \triangleq$  average time interval for decision in recertification
- $\delta \triangleq$  allowable attitude error
- $\psi \triangleq$  attitude error due to delay in detecting and isolating instrument degradation

The extra exponential term in Eq. 8.55 accounts for the the possibility of the false alarm occurring during the recertification process before a decision has been reached about the first alarm.

Figure 8.24 is a plot of equation 8.56. Probabilities are lower for the statistical FDICR than for the missed detection and isolation probabilities of the TSE algorithm (See Fig. 8.12 through 8.21). The false alarm probability in Eq. 8.54 depends on the specified probability,  $\alpha$ , and the specified mean time between false alarms,  $T$ , as well as on the mission time,  $T_s$ . In addition, Eq. 8.55, for a false alarm occurring after a first false alarm or a first true degradation, contains  $T_c$ , the average recertification time. There is no explicit dependence on noise or degradation values since  $T$ ,  $\alpha$ ,  $T_s$ ,  $T_c$  are all prechosen or predetermined mission design values.

### 8.8 Mission Abort and Loss Probabilities

In order to illustrate use of the probabilities given in Sections 8.6 and 8.7, examples are presented in which we derive the probabilities of a mission abort and vehicle loss.

For both the TSE and statistical FDICR methods, there is an abort whenever any of the following situations arise:

- (1) There is a false isolation followed by a real degradation
- (2) There are 2 false isolations
- (3) There are 2 real degradations
- (4) There is one real degradation followed by a false isolation

The conditions for a vehicle loss are stated separately for the TSE and statistical FDICR methods.

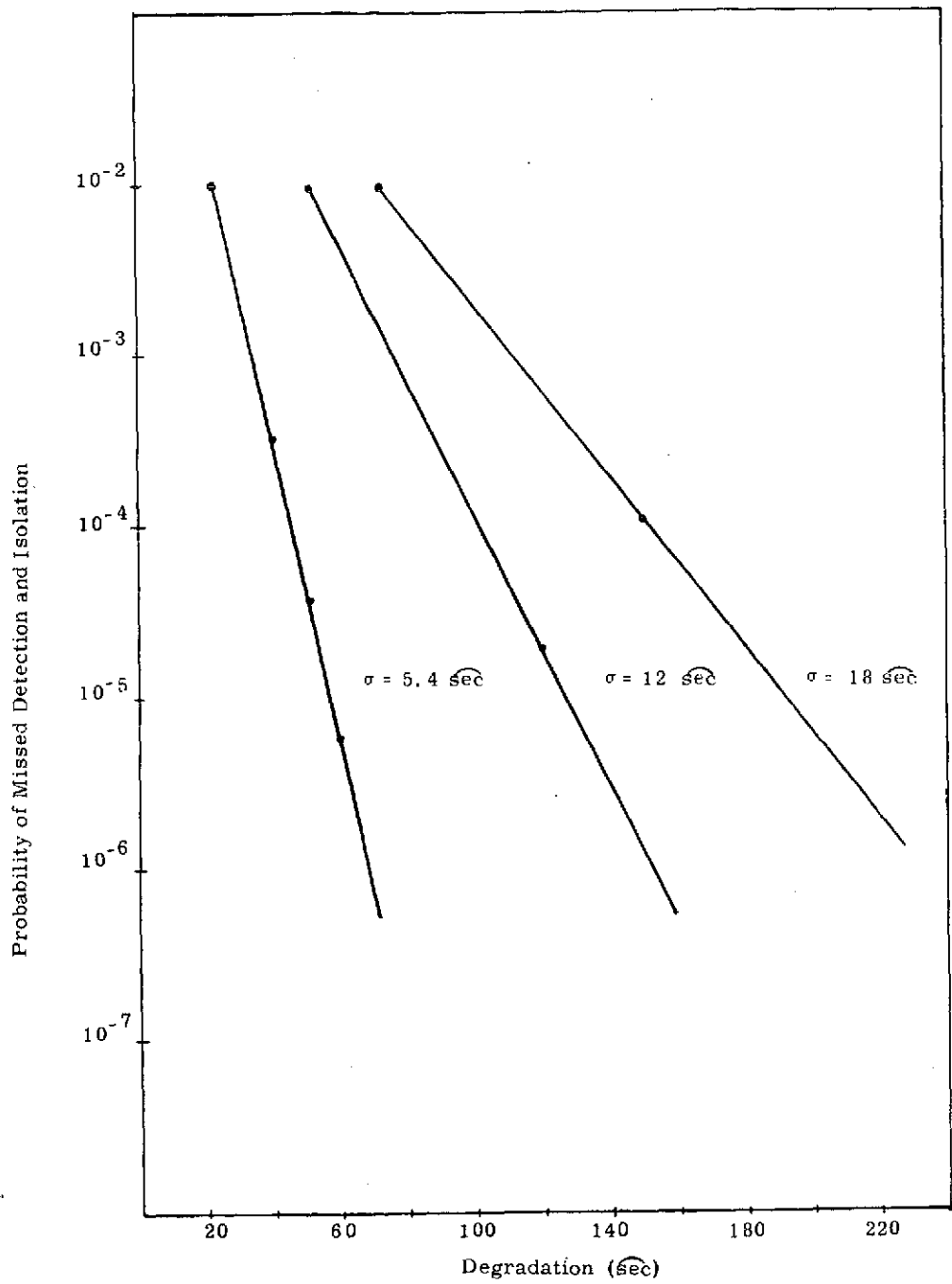


Fig. 8.24 Probability of Not Detecting and Isolating a Degradation-Statistical FDICR

### 8.8.1 TSE Abort and Vehicle Loss Probabilities

Vehicle loss occurs whenever any of the following situations arise:

- (1) A gyro fails but the failure is either not detected or not isolated
- (2) The first gyro failure is detected and isolated but the second failure is either not detected or not isolated
- (3) There is an abort and a third gyro undergoes a real degradation

It is conservatively assumed that a false detection always leads to a false isolation.

It can be shown that, in both first and second failure cases, only one instrument at a time can be isolated (for ratios of 0.44 and 0.387 respectively). Hence, the probability of not isolating a degraded instrument holds for both the case of no instrument being isolated and the case of the wrong instrument being isolated.

#### 8.8.1.1 Appropriate Formulas—TSE Case

(A) Abort

Let:

$P(F_1)$  = probability of a false detection with no instruments failed

$P(F_2)$  = probability of a false detection with one instrument failed

$T_s$  = mission duration

$T_m$  = instrument mean time between failure

Then:

$$P(R_2) \approx 1 - e^{-T_s/T_m} \quad (8.57)$$

is the degradation probability during the entire mission. The probability of abort,  $P(A)$ , is given by:

$$P(A) = P(F_1) P(R_2) + P(F_1) P(F_2) + P(R_2)^2 + P(R_2) P(F_2) \quad (8.58)$$

The probability of a mission abort, P(SA), is given by:

$$P(SA) = \binom{6}{2} P(A) = 15P(A) \quad (8.59)$$

(B) Vehicle Loss

Let:

$P(D_1)$  = Probability of not detecting a failure with no instruments failed

$P(D_2)$  = Probability of not detecting a failure with one instrument failed

$P(I_1)$  = Probability of not isolating a failure with no instruments failed

$P(I_2)$  = Probability of not isolating a failure with one instrument failed

$T_A$  = Average duration of abort

The probability of degradation during abort is given by:

$$P(R_1) = 1 - e^{-T_A/T_m} \quad (8.60)$$

Probability of a gyro failing with failure either not detected or not isolated is given by:

$$P(L_1) = P(R_2) P(D_1) + P(R_2) (1 - P(D_1)) P(I_1) \quad (8.61)$$

Probability of a second gyro failing with second failure either not detected or not isolated is given by:

$$P(L_2) = P(R_2)^2 (P(D_2) + P(I_2)) \quad (8.62)$$

Probability of an instrument degradation occurring during abort is given by:

$$P(L_3) = P(A) P(R_1) \quad (8.63)$$

The probability of a vehicle loss,  $P(SL)$ , is given by:

$$P(SL) = \binom{6}{1} P(L_1) + \binom{6}{2} P(L_2) + \binom{6}{3} P(L_3) = 6P(L_1) + 15P(L_2) + 20P(L_3) \quad (8.64)$$

### 8.8.1.2 Numerical Example-TSE Case

The following are parameters assumed for a hypothetical mission

The gyro noise,  $\sigma_g$ , is  $0.1^\circ/\text{hr}$  ( $12 \overline{\text{sec}}$  over a 2 minute interval)  
 An instrument is considered failed if it is in error by more than  $200 \overline{\text{sec}}$

The mission duration,  $T_g$ , is 166 hours

The average time duration,  $T_A$ , from initiation of an abort condition to a safe landing is 9 hours

The instrument mean time between failure,  $T_m$ , is 20,000 hours

In order to obtain the pertinent probabilities from Figs. 8.12 through 8.21, the curves on these graphs are extrapolated where this appears to be reasonable as in Fig. 8.12. Also, when there is no evidence for reasonable extrapolation and no event has occurred in  $10^4$  trials, the relevant probability is assumed to be  $10^{-4}$ .

The isolation ratios assumed for the TSE method are 0.44 for a first failure and isolation and 0.387 for a second failure and isolation.

From section 8.6.5.2, we have:

$$P(F_1) = P(F_2) = 10^{-4} \quad (8.65)$$

Also:

$$\begin{aligned} P(R_2) &= 1 - e^{-166/20000} \\ &= 8.3 \times 10^{-3} \end{aligned} \quad (8.66)$$

From Fig. 8.12.

$$P(D_1) = 10^{-5} \quad (8.67)$$

From Fig. 8.16.

$$P(D_2) = 10^{-5} \quad (8.68)$$

From Fig. 8.13:

$$P(I_1) = 7 \times 10^{-3} \quad (8.69)$$

From Fig. 8.18:

$$P(I_2) = 5 \times 10^{-2} \quad (8.70)$$

Also:

$$\begin{aligned} P(R_1) &= 1 - e^{-9/20000} \\ &= 4.5 \times 10^{-4} \end{aligned} \quad (8.71)$$

Substituting Eq. 8.65 and Eq. 8.66 into Eq. 8.58 yields:

$$\begin{aligned} P(A) &= 10^{-4} (8.3 \times 10^{-3}) + (10^{-4})^2 + (8.3 \times 10^{-3})^2 + 10^{-4} (8.3 \times 10^{-3}) \\ &\cong 71 \times 10^{-6} \end{aligned} \quad (8.72)$$

Substituting Eq. 8.71 into Eq. 8.59 yields:

$$\begin{aligned} P(SA) &= 15 \times 71 \times 10^{-6} \\ &= 1.07 \times 10^{-3} \end{aligned} \quad (8.73)$$

Substituting Eq. 8.72 and Eqs. 8.65 through 8.71 into Eqs. 8.61 through 8.63 yields the following:

$$\begin{aligned} P(L_1) &= (10^{-5}) (8.3 \times 10^{-3}) + (8.3 \times 10^{-3}) (1 - 10^{-5}) (7 \times 10^{-3}) \\ &= 57 \times 10^{-6} \end{aligned} \quad (8.74)$$

$$\begin{aligned} P(L_2) &= (8.3 \times 10^{-3})^2 \left[ 10^{-5} + (1 - 10^{-5}) (5 \times 10^{-2}) \right] \\ &= 3.6 \times 10^{-6} \end{aligned} \quad (8.75)$$

$$\begin{aligned} P(L_3) &= (71 \times 10^{-6}) (4.5 \times 10^{-4}) \\ &= .032 \times 10^{-6} \end{aligned} \quad (8.76)$$

Substituting Eqs. 8.74 through 8.76 into Eq. 8.64 yields the following probability for vehicle loss:

$$\begin{aligned} P(\text{SL}) &= 6 \times 57 \times 10^{-6} + 15 \times 3.6 \times 10^{-6} + 20 \times .032 \times 10^{-6} \\ &= 4 \times 10^{-4} \end{aligned} \quad (8.77)$$

Examination of Eq. 8.74 shows that most of the contribution to the final probability of  $4 \times 10^{-4}$  comes from the probability of not isolating the first failure,  $P(I_1)$ . The value of  $P(I_1)$  used (Eq. 8.69) corresponds to an instrument error of 200  $\widehat{\text{sec}}$ . However, for a first failure, the instrument error is approximately twice the attitude error. Hence, if we specify the first failure instrument error to be 400  $\widehat{\text{sec}}$  or less, the attitude error on the first failure will still be restricted to 200  $\widehat{\text{sec}}$ . Therefore, for 400  $\widehat{\text{sec}}$  instrument error,  $P(I_1)$  is  $<10^{-7}$  as extrapolated on Fig. 8.13.

This change in  $P(I_1)$  results in:

$$\begin{aligned} P(L_1) &< (10^{-5}) (8.3 \times 10^{-3}) + (8.3 \times 10^{-3}) (1 - 10^{-5}) (10^{-7}) \\ &\approx 8.3 \times 10^{-8} \end{aligned} \quad (8.78)$$

and:

$$\begin{aligned} P(\text{SL}) &\approx 15 \times 3.6 \times 10^{-6} + 20 \times .032 \times 10^{-6} \\ &= 54.64 \times 10^{-6} \\ &= 5.5 \times 10^{-5} \end{aligned} \quad (8.79)$$

Equation 8.79 shows that there is an order of magnitude improvement when we allow the first instrument failure to be 400  $\widehat{\text{sec}}$  or less rather than 200  $\widehat{\text{sec}}$  or less.

### 8.8.2 Statistical FDICR Abort and Vehicle Loss Probabilities

With the statistical FDICR, a vehicle loss occurs when the following events happen:

- (1) There is an abort and an additional real degradation occurs during the abort
- (2) There is a missed detection and isolation.

The conditions for a vehicle loss with the statistical FDICR are stated differently than for the case of TSE detection and isolation because, unlike the TSE method, detection and isolation are part of one process (i.e., picking out the largest parity equation residuals), and one probability value applies to both detection and isolation of a failure.

#### 8.8.2.1 Appropriate Formulas - Statistical FDICR Case

(A) Abort

The formulas are exactly the same as for the TSE case, (Eqs. 8.60-8.62), however, the values for  $P(F_1)$  and  $P(F_2)$  are different and are given respectively by Eqs. 8.54 and 8.55.

(B) Vehicle Loss

Let:

$P(SL)$  = probability of vehicle loss

Then, referring to Eqs. 8.56 and 8.63:

$$\begin{aligned} P(SL) &= \binom{6}{1} P(E_1) + \binom{6}{3} P(L_3) \\ &= 6 P(E_1) + 20 P(L_3) \end{aligned} \tag{8.80}$$

#### 8.8.2.2 Numerical Example-Statistical FDICR Case

In addition to the conditions stated at the beginning of section 8.8.1.2, we have:

$$\begin{aligned} T_c &= 20 \text{ min} \\ \alpha &= 1\% \\ \beta &= 1\% \\ \Delta &= 2 \text{ min} \\ T &= 200 \text{ hrs} \\ \delta &= 200 \text{ sec} \end{aligned} \tag{8.81}$$

We will also assume that in Eqs. 8.49 and 8.50 we have the approximate relationship:

$$a_1 \approx \sigma \quad (\text{signal to noise ratio} \approx 1) \quad (8.82)$$

Then Eqs. 8.49 and 8.50 simplify to:

$$B \approx \ln \frac{T}{2\Delta} \quad (8.83)$$

and:

$$\tau(T) \approx 2\Delta (B - 3/2) \quad (8.84)$$

Then substituting Eq. 8.81 into Eq. 8.83 yields:

$$\begin{aligned} B &\approx \ln \left( \frac{200 \times 60}{(2)(2)} \right) \\ &= \ln(3000) \\ &= 8 \end{aligned} \quad (8.85)$$

Substituting Eq. 8.85 into Eq. 8.84 yields:

$$\tau(T) \approx 4(8 - 1.5) = 26 \text{ min.} \quad (8.86)$$

Hence:

$$\begin{aligned} \psi &= \frac{a_1}{2} \tau(T) \\ &\approx \frac{(.85)(12)}{2 \times 2} \times 26 \\ &= 66 \widehat{\text{sec}} \end{aligned} \quad (8.87)$$

Substituting Eq. 8.87 into Eq. 8.56 along with the appropriate values for  $\delta$  and  $\beta$  yields:

$$\begin{aligned} P(E_1) &= \beta^{\delta/\psi} \\ &= (.01)^{\frac{200}{66}} \\ &= 10^{-6} \end{aligned} \quad (8.88)$$

Also we have for Eqs. 8.54 and 8.55:

$$\begin{aligned} P(F_1) &= (.01) \left(\frac{166}{200}\right) & (8.89) \\ &= .0083 \end{aligned}$$

$$\begin{aligned} P(F_2) &= \frac{166}{200} \left( .01 + (1 - e^{-\frac{1}{(3)(200)}}) \right) & (8.90) \\ &= .83 (.01 + .0015) \\ &= .0096 \end{aligned}$$

Substituting Eqs. 8.89 and 8.90 into Eq. 8.58 along with  $P(R_2)$  (Eq. 8.66) yields:

$$P(A) = 2.98 \times 10^{-4} \quad (8.91)$$

Finally, the probability of a mission abort is given by:

$$P(SA) = 4.5 \times 10^{-3} \quad (8.92)$$

Substituting Eqs. 8.91 and 8.71 into Eq. 8.63 yields:

$$\begin{aligned} P(L_3) &= P(A) P(R_1) & (8.93) \\ &= (4.5) (3 \times 10^{-8}) \\ &= .135 \times 10^{-6} \end{aligned}$$

The probability of a vehicle loss is given by Eq. 8.94.

$$\begin{aligned} P(SL) &= 6 P(E_1) + 20 P(L_3) & (8.94) \\ &= 6 \times 10^{-6} + 2.7 \times 10^{-6} \\ &= 8.7 \times 10^{-6} \end{aligned}$$

As with the TSE case, the above probability,  $P(SL)$ , is lowered if we allow a 400  $\overline{\text{sec}}$  instrument degradation for the first failure.

In this case:

$$\begin{aligned} P(E_1) &= (.01) \frac{400}{66} & (8.95) \\ &= 10^{-12} \end{aligned}$$

Hence (See Eq. 8.94):

$$P(SL) \approx 2.7 \times 10^{-6} \quad (8.96)$$

### 8.9 SIRU Reliability Conclusions

This chapter has examined the reliability of statistics of SIRU with the inertial components (gyros and accelerometers) and the electronics actually used. Comparison of SIRU reliability (probability of mission success) assuming perfect failure detection and isolation (FDI) capability shows a much greater reliability for SIRU than for the three axis reference triad. This comparison is shown in Figs. 8.1 through 8.4 and is summarized in Table 8.4.

In addition to the standard reliability analyses that were conducted, the reliability of both the TSE and statistical FDI methods were studied by means of simulations, statistical FDI data and mathematical analyses.

An example of a hypothetical mission was presented in which the probability of mission loss was calculated using the estimated FDI reliability figures as well as MTBF reliability figures for the inertial instruments.

The hypothetical (space shuttle) mission duration was 166 hours. The average time duration from initiation of an abort condition to a safe landing is 9 hours. Instrument MTBF is 20000 hours. With the use of the TSE FDI the probability of a vehicle loss (assuming a system attitude error on the order of 200  $\widehat{\text{sec}}$  as signifying the loss) is  $5.5 \times 10^{-5}$  for a first failure. An instrument failure of 200  $\widehat{\text{sec}}$  that causes a mission loss has a probability of  $4.5 \times 10^{-4}$ . With the use of the statistical FDI, the probability of a first failure system attitude error of approximately 200  $\widehat{\text{sec}}$  leading to a mission loss is  $8.7 \times 10^{-6}$ . If 200  $\widehat{\text{sec}}$  failure of an instrument leads to vehicle loss the probability of mission loss is  $2.7 \times 10^{-6}$ .

Chapter 9  
Applications Of SIRU Utilization Results

9.0 Introduction

This chapter shows how some of the significant results attained in the SIRU Utilization program may be applied to other redundant systems.

The most pertinent extension of SIRU concepts is to the technology for triple- and quadruple-redundant gimballed inertial measuring units.

It is also shown how some FDICR results may be extended to an aircraft redundant navigation system.

Another example applies the statistical FDICR methodology to a precision attitude pointing system.

Following these examples is a discussion of computation, software and hardware reorganization after a failure, fault detection and isolation, filtering and threshold criteria, and requalification of soft failures.

9.1 Multiple Gimbaled Systems<sup>15</sup>

An alternative to SIRU is to use an array of four or three gimbaled IMUs. These gimbaled systems are aligned so that their respective axes are colinear in order to permit close alignment of the units with each other on an axis by axis basis.

Failure detection and isolation techniques employing redundant gimbal technology present some different problems than apply to SIRU. In the SIRU system, gyro error drifts as well as accelerometer bias and scale factor errors are detected separately by independent gyro and accelerometer FDICR implementations. In contrast, gyroscope error drifts in gimbal systems are reflected as changes in both the attitude and velocity output while accelerometer error sources appear directly in the velocity output only.

Another major difference between SIRU and a redundant gimbaled system exists for pre-launch and in-flight alignment. In the fixed geometry SIRU implementation, FDICR is completely independent of pre-launch or in-flight alignment requirements. In contrast, the redundant gimbaled IMUs must be aligned independently. Because

PRECEDING PAGE BLANK NOT FILMED

of the large sensitivity of the inertial velocity information to the launch alignment accuracy, the gimbaleed FDICR method used is strongly influenced by initial alignment errors.

It is instructive to review the major FDICR techniques used in SIRU before presenting the velocity failure detection and isolation equations useful for redundant gimbaleed systems.

The total squared error method (TSE) proceeds as follows (for the first failure):

- (1) The least square solution for each unit is obtained in terms of the measurements of all of the other units. Thus the solution,  $m_i$ , for instrument,  $i$ , is given by:

$$\hat{m}_i = \sqrt{0.2} (\pm m_j \pm m_k \pm m_l \pm m_n \pm m_o) \quad (9.1)$$

where  $m_j$  through  $m_o$  are the measurements of all the other instruments.

- (2) The estimated error,  $E_i$ , in instrument  $i$  is obtained by subtracting the estimate,  $m_i$ , from the actual measurement,  $m_i$ . Thus:

$$E_i = m_i - \hat{m}_i \quad (9.2)$$

- (3) The sum of the squares of all the instruments,  $E_o^2$ , is calculated.

$$TSE = E_o^2 = \sum_{i=1}^n (E_i)^2 \quad (9.3)$$

- (4) The total squared error,  $E_o^2$ , is compared with a predetermined detection threshold in order to determine whether a failure has occurred.
- (5) The ratio,  $E_i^2/E_o^2$ , is taken and compared with a predetermined isolation threshold in order to isolate the failed instrument.

The procedure for the second failure is similar to the first failure technique.

The statistical FDICR method proceeds as follows for the detection, isolation, and classification of a first failure.

- (1) The residuals of the four instrument parity equations (Appendix A2 of Chapter 2, Eqs. A2.1 - A2.6) are calculated.
- (2) The residuals of each equation are processed to form a likelihood ratio for each equation.
- (3) If the failure detection threshold is exceeded by any of the likelihood ratio variables, the appropriate parity equation is flagged.
- (4) Isolation of the degradation (i.e. failure) is determined by the particular combination of flagged parity equations.
- (5) Identification of the type of failure (constant bias, range or variance increase) and verification of the failure are made by testing both the appropriate parity equation residual and a transformation of this residual (see Section 2.4, Chapter 2) using Wald's sequential probability ratio test.

The procedure for the second failure is similar to the first failure technique.

Next we apply the above SIRU techniques to the multiple gimballed systems.

The TSE method is applied as follows:

- (1) The least square solution for each axis of the IMUs is obtained in terms of the measurements of all of the other co-linear axes. Thus the solution  $V_{ik}$  for the kth axis of the ith IMU for four IMUs is given by:

$$\hat{V}_{ik} = \frac{V_{lk} + V_{mk} + V_{nk}}{3} \quad (9.4)$$

where  $V_{lk}$  through  $V_{nk}$  are the measurements of the kth axis of all the other IMUs.

- (2) The estimated error,  $E_{ik}$ , in axis k of IMU i is obtained as follows:

$$E_{ik} = V_{ik} - \hat{V}_{ik} \quad (9.5)$$

- (3) The sum of the squares of all the IMU s for the kth axis,  $E_{ok}^2$ , is calculated as follows (assuming four IMU s in our example):

$$TSE_k = E_{ok}^2 = \sum_{i=1}^4 E_{ik}^2 \quad (9.6)$$

- (4) The allowable performance (velocity) error will be a function of both mission phase and time into the mission. In order to desensitize the error velocity vector to these two variables, Eq. 9.6 is normalized with respect to the total average velocity as shown in Eq. 9.7.

$$\text{Normalized TSE} = \text{Norm } E_{ok}^2 = \frac{E_{ok}^2}{\left(\sum_{i=1}^4 \frac{V_{ik}}{4}\right)^2} \quad (9.7)$$

In the SIRU TSE method, the TSE is not normalized as shown in Eq. 9.7 but the detection threshold is varied in accordance with the environment.

- (5) The normalized TSE,  $\text{Norm } E_{ok}^2$ , for the kth axis is compared with a predetermined detection threshold in order to determine whether a degradation has occurred.
- (6) The ratio,  $E_{ik}^2 / E_{ok}^2$ , is taken and compared with a predetermined isolation threshold in order to isolate the failed axis and IMU.

The above procedure applies to velocity error detection and isolation for 3 or 4 multiple gimballed systems. If there are only two gimballed systems, then the IMU s should not be colinear. With colinearity, only detection of a failure can be accomplished and isolation of the failure is not possible. The problem is circumvented by skewing one IMU with respect to the other by an optimum Euler angle rotation. In this manner, although only two gimballed systems are employed, enough redundant data is available to properly isolate any detected failure. In the skewed case, the geometrical relationship between axes of two different IMU s is determined using the gimbal attitude resolver readouts. There is some question as to the adequacy of the present off-the-shelf resolvers for FDI, and the reader is referred to reference 15 for further discussion of this point. Once a geometrical relationship is established between the axes of different IMU s, the failure detection and isolation procedure is identical to those outlined for SIRU whether using the TSE method or statistical FDICR.

The SIRU statistical FDICR is applied to the 4 co-linear gimbaled system case as follows for detection, isolation, and classification of a velocity degradation.

- (1) Parity equations are formed as follows for each axis, k:

$$\begin{aligned}
 V_{1k} - V_{2k} &= \epsilon_{1k} \\
 V_{2k} - V_{3k} &= \epsilon_{2k} \\
 V_{3k} - V_{4k} &= \epsilon_{3k} \\
 V_{4k} - V_{1k} &= \epsilon_{4k}
 \end{aligned}
 \tag{9.8}$$

- (2) The residuals  $E_{ik}$  (defined by Eq. 9.8) are processed to form a likelihood ratio for each equation.
- (3) If the failure detection threshold is exceeded by any of the likelihood ratio variables, the appropriate parity equation is flagged and the procedure continues exactly as in steps (4) and (5) previously outlined for SIRU statistical failure detection, isolation, and classification. If desired, re-compensation of the error can also be applied to the accelerometer of the flagged axis. However, this is not recommended because the velocity failure could also be due to gyro drift degradation in the gimbaled IMU. It is therefore sufficient to take the IMU off-line and keep it off-line until we can decide, using the IMU resolver outputs and the accelerometer output, whether the failure is due to a gyro or accelerometer. Once this is done, the appropriate parity equation residual (parity equations can also be formed using resolver outputs as will be shown below) is treated as shown in Chapter 2 to obtain the proper re-compensation value. If the failure is neither a gyro nor an accelerometer degradation, verification of the failed instrument as being "healed" will not occur and the gimbaled IMU is kept off line.

Attitude FDI equations can be developed using only gimbal angles. A four gimbal IMU is used in this example. A quaternion may be developed which represents a rotation from the navigation base to the stable member platform.

$$Q_{B_i}^{SM} = Q_{i0} Q_{i1} Q_{i2} Q_{i3}
 \tag{9.9}$$

Here  $Q_{i0}$ ,  $Q_{i1}$ ,  $Q_{i2}$ ,  $Q_{i3}$  are quaternion representations of the four gimbal angles for the  $i$ th IMU. Since the quaternion in Eq. 9.9 may be represented as:

$$Q_{B_i}^{SM} = \cos\left(\frac{\theta_i}{2}\right) + \underline{i}_1 \sin\left(\frac{\theta_{i1}}{2}\right) + \underline{i}_2 \sin\left(\frac{\theta_{i2}}{2}\right) + \underline{i}_3 \sin\left(\frac{\theta_{i3}}{2}\right) \quad (9.10)$$

A rotation vector may be defined as:

$$\underline{R}_i = \underline{i}_1 \theta_{i1} + \underline{i}_2 \theta_{i2} + \underline{i}_3 \theta_{i3} \quad (9.11)$$

The TSE method is now applied.

- (1) A least square estimation,  $\underline{R}_i$ , of the  $i$ th rotation vector is obtained in terms of all of the other rotation vectors,  $l, m, n$ .

$$\hat{\underline{R}}_i = \frac{\underline{R}_l + \underline{R}_m + \underline{R}_n}{3} \quad (9.12)$$

- (2) The quaternion corresponding to Eq. 9.12 is formed.

$$\hat{Q}_{B_i}^{SM} = \cos\left(\frac{\hat{\theta}_i}{2}\right) + \underline{i}_1 \sin\left(\frac{\hat{\theta}_{i1}}{2}\right) + \underline{i}_2 \sin\left(\frac{\hat{\theta}_{i2}}{2}\right) + \underline{i}_3 \sin\left(\frac{\hat{\theta}_{i3}}{2}\right) \quad (9.13)$$

An error quaternion for the  $i$ th IMU is calculated.

$$Q_{E_i} \triangleq \hat{Q}_{B_i}^{SM*} Q_{B_i}^{SM} \quad (9.14)$$

$$\hat{Q}_{B_i}^{SM*} = \cos\left(\frac{\hat{\theta}_i}{2}\right) - \underline{i}_1 \sin\left(\frac{\hat{\theta}_{i1}}{2}\right) - \underline{i}_2 \sin\left(\frac{\hat{\theta}_{i2}}{2}\right) - \underline{i}_3 \sin\left(\frac{\hat{\theta}_{i3}}{2}\right) \quad (9.15)$$

The rotation vector corresponding to Eq. 9.14 is formed.

$$\underline{R}_{E_i} = \underline{i}_1 \theta_{E_{i1}} + \underline{i}_2 \theta_{E_{i2}} + \underline{i}_3 \theta_{E_{i3}} \quad (9.16)$$

- (3) The error rotation vector information is stored in the computer so that time histories of the rotation vector may be established. In this manner, a drift vector may be defined as:

$$\underline{\text{DRIFT}}_i = (\underline{R}_{E_i} - \underline{R}_{E_{\text{LAST } i}}) / \Delta t \quad (9.17)$$

By defining the attitude error in terms of a drift rate rather than a whole angle, problems involving absolute attitude accuracy are relieved. This is especially important in an IMU with inherently poor gimbal readout chains.

The total squared drift error,  $\text{TSE}_k$ , for each axis  $k$  is calculated.

$$\text{TSE}_k \triangleq \text{DRIFT}_k^2 = \sum_{i=1}^4 \text{DRIFT}_{ik}^2 \quad (9.18)$$

- (4) The total squared error,  $\text{DRIFT}_k^2$ , is compared with a predetermined detection threshold in order to detect a degradation.
- (5) The ratio  $\text{DRIFT}_{ik}^2 / \text{DRIFT}_k^2$  is taken and compared with a predetermined isolation threshold in order to isolate the failed instrument.

The procedure for a second failure detection and isolation is similar.

The statistical FDICR method is applied for detection, isolation, and classification of an attitude degradation.

- (1) Parity equations are formed as follows for each axis,  $k$ :

The following error quaternions are calculated:

$$\left. \begin{aligned} Q_{B1}^{SM*} Q_{B2}^{SM} &\triangleq Q_{\epsilon 1} \\ Q_{B2}^{SM*} Q_{B3}^{SM} &\triangleq Q_{\epsilon 2} \\ Q_{B3}^{SM*} Q_{B4}^{SM} &\triangleq Q_{\epsilon 3} \\ Q_{B4}^{SM*} Q_{B1}^{SM} &\triangleq Q_{\epsilon 4} \end{aligned} \right\} \quad (9.19)$$

Corresponding to each error quaternion is an error rotation vector given by:

$$\underline{R}_{\epsilon_i} = \sum_{k=1}^3 \hat{i}_k \theta_{\epsilon_{ik}} \quad (9.20)$$

A drift vector,  $\underline{DRIFT}_{\epsilon_i}$ , is calculated.

$$\underline{DRIFT}_{\epsilon_i} = (\underline{R}_{\epsilon_i} - \underline{R}_{\epsilon_{LAST_i}}) / \Delta t \quad (9.21)$$

Each component of  $\underline{DRIFT}_{\epsilon_i}$  is a parity equation residual.

$$\begin{array}{l} \text{Parity} \\ \text{Equation} \\ \text{Residual} \end{array} = \underline{DRIFT}_{\epsilon_{ik}} \quad (9.22)$$

The remaining steps of the method applied to gimbale systems proceed exactly as in steps 2 thru 5 as outlined for the SIRU statistical FDICR.

## 9.2 Aircraft Redundant Guidance System

Reference 16 presents a tactical aircraft guidance system (TAGS) with triplex redundancy. Figure 9.1 is a block diagram of part of the active triple redundant force sharing actuators used for each of the control axes.

There are three redundant command signals A, B, C that three D/A converters have converted to analog form before they are fed to the diode median value selector. The median value of the three signals is fed to the actuator servo as a command signal. The output of the actuator goes to a force summing bar. Differential pressure transducers (I, II, III) on the force summing bar provide feedback to close the position loop. The three differential pressure signals are averaged. The average value is compared with the actual value for each channel and the difference is fed back to the input of that channel, thus reducing the load variation between individual actuators on that axis. The difference signal is also fed to a comparison-for-failure block. The output of this block is fed to a bypass valve that removes the actuator output to the force summing bar if the particular actuator is voted as a failure. Here the criterion used is a predetermined threshold on the actuator differential pressure. Failure detection in conjunction with the median value selector consists of comparing the highest signal-to-signal difference of three signals A, B, C with a given constant.

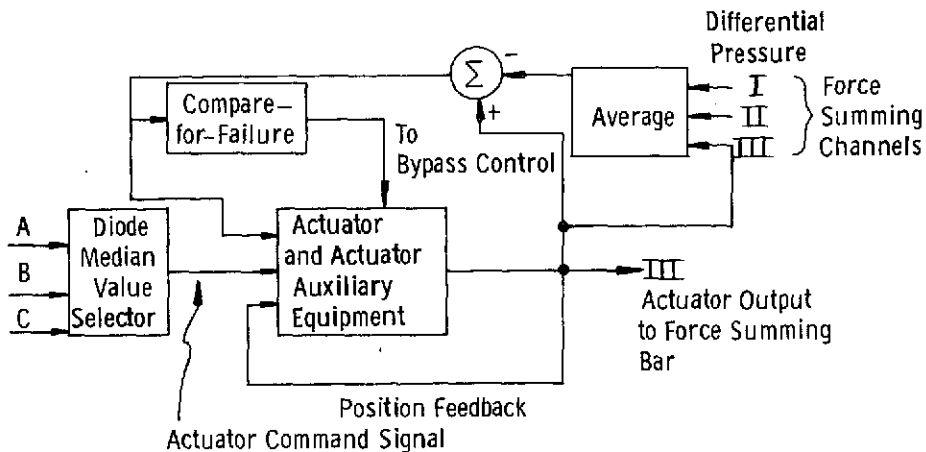


Fig. 9.1 Triple Redundant Force Actuator Block Diagram

A sensor failure is indicated if the difference exceeds a specified level for 3 consecutive computational cycles. Failure selection and signal selection both require ordering the input signals into high, middle, and low values. The median value is selected and the high minus low value is compared to the predetermined tolerance.

If the three signals A, B, C are sufficiently noisy, serious problems may arise in using the deterministic methods presented above. Some of these problems are:

- (1) A step input to the control system (causing an unwanted system transient) arises when the median value rapidly changes, due to noise, through the range between the other two signals.
- (2) Excessive noise in the working channels triggers false failure indications.
- (3) A high worst-case failure tolerance is required in order to overcome noise.

These problems were treated in TAGS by using the three consecutive cycle criterion mentioned above. A more optimum solution is to use the techniques developed for the SIRU statistical FDICR. Use of these techniques will allow operation of the system illustrated (Fig. 9.1) with lower signal-to-noise ratio than a deterministic technique will allow, as demonstrated by the FDI technique for SIRU (See Chapter 2).

Least squares selection (instead of median value selection) and FDI can be performed using signals A, B, C before they are supplied to the D/A converter. This approach allows use of the discrete equations developed in Chapter 2 (See Eqs. 2.14 and 2.15). Application of the statistical FDICR is then straightforward. The parity equations in this case are given by:

$$\begin{aligned} A - B &= \epsilon_1 \\ B - C &= \epsilon_2 \\ C - A &= \epsilon_3 \end{aligned} \tag{9.23}$$

The parity equation residuals  $\epsilon_1, \epsilon_2, \epsilon_3$  are treated in the usual manner. If, for example, the likelihood ratios of  $\epsilon_1$  and  $\epsilon_3$  have exceeded the predetermined threshold, then A is the failed channel and the command signal selected is  $\frac{B+C}{2}$ , superceding the median value selected before there was any indication of a failure.

This least squares selection should only be done after the failure is discovered. Note that, if the noises for B and C have the same standard deviation and are independent, the least squares selection results in a less noisy command signal than median selection. This conclusion is demonstrated as follows:

$$\left\{ \begin{array}{l} \text{Standard Deviation of} \\ \text{Noise for Least} \\ \text{Squares Selection} \end{array} \right\} \Delta = \frac{\sigma_{B+C}}{2} = \frac{\sqrt{2\sigma^2}}{2} = \frac{\sigma}{\sqrt{2}} \tag{9.24}$$

where  $\sigma$  is the standard deviation of the noise for the A, B, and C signals. The reduction in noise (Eq. 9.24) is therefore 29% as measured by the standard deviation.

The compare-for-failure block in Fig. 9.1 cannot easily be mechanized using the statistical FDICR approach of Chapter 2 because the signals are all in analog form. It would be necessary therefore to augment this box with A/D and D/A converters before using the digital forms of the Chapter 2 equations. However, a more acceptable approach might be to mechanize the likelihood ratio calculation in analog form. This approach warrants further investigation and could be useful in other systems that have analog signals.

The continuous form of the likelihood ratio,  $\lambda(t)$ , is given by Eq. 4-211 in reference 2.

$$d\lambda(t) = \frac{a_1}{\sigma^2} \left[ dy(t) - \frac{a_1}{2} dt \right] \tag{9.25}$$

where (according to Eq. 4-212, reference 2.):

$$dy(t) = a dt + \sigma dw(t) \quad (9.26)$$

where:

- $a_1$  = degradation design value
- $\sigma$  = noise standard deviation
- $y(t)$  = observation
- $a$  = actual degradation
- $w(t)$  = Wiener process with unit variance rate

If  $n(t)$  represents white noise of unit variance, Eq. 9.26 can be written as:

$$dy(t) = a dt + \sigma \dot{n} dt \quad (9.27)$$

Integrating Eq. 9.27 yields:

$$y(t) = \int (a + \sigma \dot{n}) dt \quad (9.28)$$

But the parity equation residual,  $z(t)$ , is given by:

$$z(t) = a + \sigma \dot{n} \quad (9.29)$$

Substituting Eq. 9.29 into Eq. 9.27 yields:

$$dy(t) = z(t) dt \quad (9.30)$$

Substituting Eq. 9.30 into Eq. 9.25 and integrating yields:

$$\lambda(t) = \frac{a_1}{\sigma^2} \left[ \int_0^t (z(t) - \frac{a_1}{2}) dt \right] \quad (9.31)$$

Equation 9.31 is the continuous version of the likelihood ratio. An analog likelihood ratio detection filter that implements Eq. 9.31 is shown in Fig. 9.2. This filter can now be used with analog signals in order to implement statistical failure detection. Classification and recompensation analog circuits can also be designed in a similar manner.

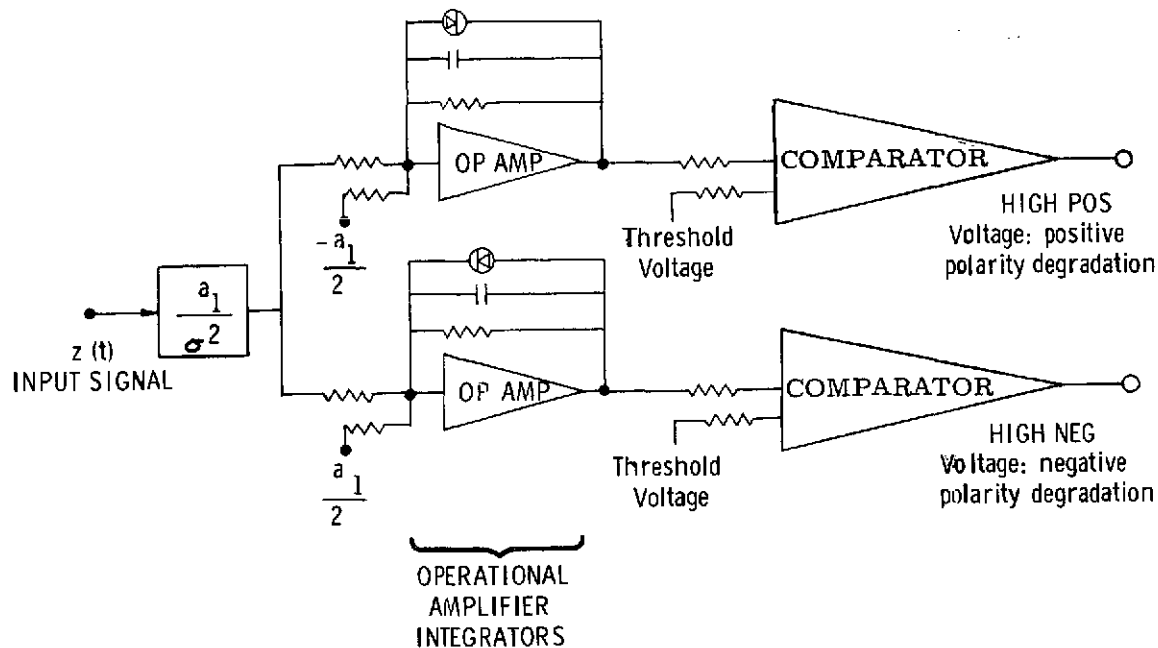


Fig. 9.2 Analog Likelihood Ratio Detection Filter

### 9.3 Precision Attitude Pointing System

Figure 9.3 is a block diagram of a proposed precision attitude pointing system.

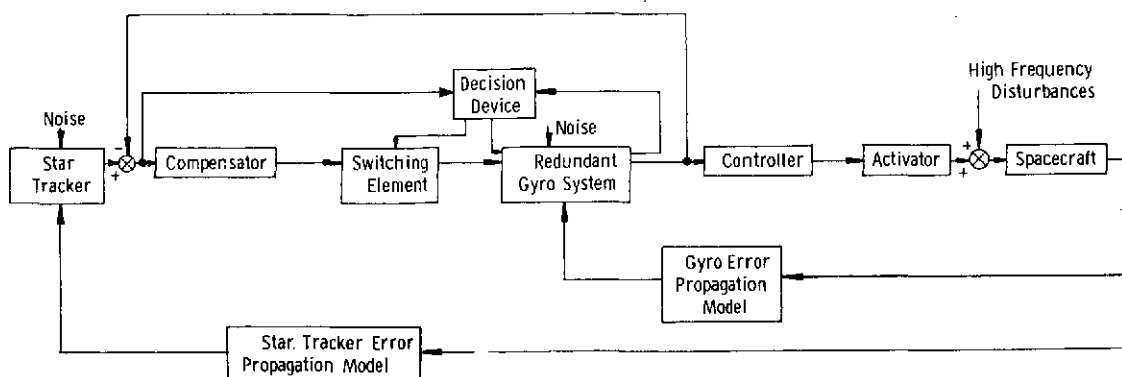


Fig. 9.3 Precision Attitude Pointing System

The attitude sensors in the proposed system are a star tracker and a redundant gyro system. The star tracker noise resembles white noise in the frequency range of interest (see Fig. 9.4a), whereas the gyro noise is high at low frequencies (since we include gyro long term drift as part of the gyro noise) but is lower than the star tracker noise at higher frequencies (See Fig. 9.4b).

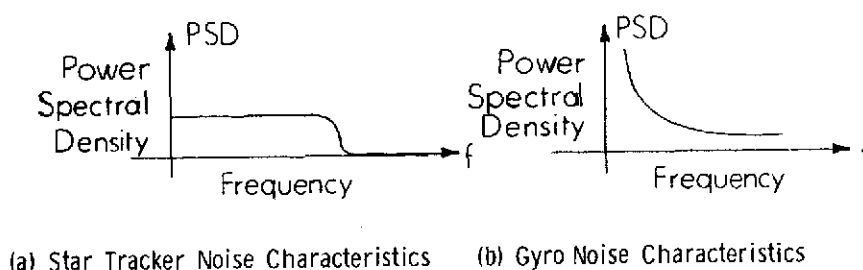


Fig. 9.4 Attitude Sensor Noise Characteristics

Hence the star tracker output will be used as a low frequency reference and the gyro package will be used to control and smooth out the high frequency disturbances to the spacecraft. The decision device shown in the block diagram uses the principles of optimal decision making employed for SIRU statistical FDICR. The decision device has two functions. One function is the usual FDICR of the instruments in the redundant gyro system. The other function is to make an optimal decision of how much output from the star tracker should be used as long term compensation for the gyro package drift. In one extreme case, the star tracker output is completely switched off and the gyro package output completely controls the spacecraft actuator in order to attenuate the spacecraft's high frequency disturbances. However, the signal difference between the star tracker and gyro package output is monitored by the decision device and an optimal decision is made on when to switch the star tracker back into the loop to compensate for the low frequency gyro drift. Depending on the signal difference magnitude, either all or a fraction of the star tracker output is switched into the loop. This decision is also made in an optimal fashion. The above example, briefly presented, indicates how SIRU FDICR results might also be applied to systems with components that are not completely redundant (star tracker and gyros) but overlap in function.

#### 9.4 Computation, Software, and Hardware Reorganization after a Failure

The preceding Sections (9.1-9.3) dealt with mechanization of SIRU FDI procedures as applied to various systems. In addition to these mechanizations, it is also necessary to have a scheme for computation, software, and possibly hardware reorganization after the failure is detected and isolated.

Computational and software reorganization in SIRU is thoroughly described in the SIRU Development Final Report, R746. The computational procedure is based on taking the least squares estimate for a set of the operating nonorthogonal instruments. Weighting of the instruments when making the estimate is a function of the instrument configuration geometry only and does not depend on the statistics of the instruments. In order to include accurate statistical weighting (such as, for example, weighting each instrument output according to the variance of its lumped drift) one would need an extremely detailed array of instrument statistics which is difficult to obtain during vehicle operations. Furthermore, better system performance is obtained when it is possible to take the bad instruments off-line rather than to continue to weight the output of an instrument that has failed, so long as there are enough remaining instruments to complete the mission. If there are too many instrument failures, it is necessary to keep the best of the failed instruments on line.

In the example dealing with multiple gimbal systems that have co-linear axes, the least squares averaging technique results in simply arithmetically averaging the outputs for each axis of the non-failed IMUs. Other schemes could be used for operating the non-failed instruments, such as median selection (described in section 9.2). However, under the conditions of independent Gaussian noises, the least squares procedure yields lower noise as measured by the standard deviation. Also, the least squares method is easy to implement (See SIRU Development Final Report).

Software re-organization after a failure in SIRU consists of using the appropriate least squares geometrical weighting matrix and reorganizing the parity equation structure. These actions must also be taken in each of the examples presented above. The particular geometrical weighting matrix and parity equation structure used depends on the particular system and failure detection scheme being considered. Note that, when the instrument axes are co-linear, the minimum number of instruments' outputs per parity equation is 2 (Eq. 9.20) and three such equations and instruments are required to uniquely isolate a failure. If only two instruments are available, the one parity equation remaining allows only detection but not isolation. If the instrument axes are skewed as with SIRU, a minimum of 4 instruments is needed per parity equation. It is not necessary to use four instruments, and a larger number

of instruments could be used as is done in the TSE method where the total number of operating instruments is required per parity equation (i.e. 6 if no instruments out of 6 have failed, 5 if 1 instrument out of 6 has failed). It is advisable however that as few instruments per parity equation be used whenever possible in order to cut down on the parity equation residual noise. This can be seen by comparing the parity equation residual noise of the TSE method (which requires 6 instruments per parity equation, Equations A2.16-A2.24) with the parity equation residual noise of the statistical FDICR method (which requires 4 instruments per parity equation; Eqs. A2.1-A2.15). For independent Gaussian noise per instrument, it can be shown that the 4 instrument equation noise standard deviation is  $1/\sqrt{2}$  times the TSE parity equation noise.

An example of hardware re-organization after failure is the skewing of the two gimbal IMU axes when only two systems are operating. This reorientation is necessary in order to be able to isolate an additional failure.

Obvious hardware reorganization procedures for any redundant system consist of voting among redundant hardware components and the switching out of the failed component. Note that the switching out of failed inertial components is done in the computer and is therefore classified as a software reorganization rather than a hardware reorganization.

#### 9.5 Threshold and Filtering Criteria for Reliable Fault Detection and Non-ambiguous Isolation

Implicit in any redundant FDI scheme is the proper choice of parameters for reliable FDI. The choice of TSE parameters is discussed in the SIRU Development Final Report. Note that, because this method is highly non-linear, extensive simulations are required to choose the proper parameters. When the TSE method is applied to any other redundant system (such as multiple gimbal IMU's), simulations pertinent to the particular system must be performed. Chapter 8 contains many SIRU TSE simulation results that imply that the choice of 0.44 and 0.387 for respective first failure and second failure isolation threshold ratios made for SIRU are reasonable but that a readjustment of these ratios for different detection and isolation probabilities is possible. The particular criteria applicable to any simulation are the false alarm and missed alarm probabilities and the signal (i.e. degradation)-to-noise ratios. The Chapter 8 simulations can easily be interpreted in terms of these criteria. In general, higher signal-to-noise ratios lead to smaller false alarm and missed alarm probabilities.

The statistical FDICR method can be applied to redundant systems other than SIRU without the need for extensive simulations because the algorithms are linear (unlike the TSE method). For detection and isolation the pertinent criteria, which are the algorithm parameters, are: mean time between false alarms  $T$ , degradation  $a_1$ , and parity equation residual noise standard deviation,  $\sigma_p$  (see Chapter 2 for the details on how these criteria are used in the detection and isolation algorithms). The missed alarm probability is zero for this portion of the statistical FDICR algorithm. Verification of a failure is accomplished by use of the Wald sequential probability ratio test. Here the pertinent parameters are again the noise standard deviation,  $\sigma_p$ , and degradation,  $a_1$ , and, in addition, the false and missed alarm probabilities (See Chapter 2).

The statistical FDICR algorithms as applied to SIRU are based on the fact that the parity equation residual noise is white. If this is not the case in another application, the parity equation residual noise must be "whitened". This is easily accomplished by use of a steady-state Kalman filter and is described in detail in reference 2.

#### 9.6 Requalification of Soft Failures

Before a soft failure can be requalified, the degradation must be classified as to type (i.e. constant bias, ramp, variance increase). The method, in general, is to perform a transformation of the isolated parity equation residual such that the two alternate hypothesis can be tested using Wald's sequential probability ratio test. The details of these transformations are given in Chapter 2. Compensation (i.e. requalification of failures) is made after the constant bias or ramp has been estimated. Chapter 2 (Figs. 2.8 and 2.9) gives the details of these estimations and how the estimates are fed back to the instruments. Estimation is based on the fact that the parity equation residual noise is white. If this is not the case in another application, the decoupled bias estimator (Chapter 6 of reference 2) must be used. The reader is referred to the reference for details.

Note that if the failure is a variance increase, recompensation of the failed instrument cannot be performed even if an estimate were made of the increased variance.

## Chapter 10

### Conclusions and Recommendations

#### 10.0 Conclusion

A complete software package for use with SIRU has been developed and tested successfully. This package includes failure detection, isolation, classification and automatic recompensation, single position self-calibration, coarse and fine alignment and local level land navigation. The failure detection and isolation resolution is approximately equal to the parity equation residual noise. In a static environment, with a parity equation residual noise of  $0.057^{\circ}/\text{hr}$ , a system axis error of  $0.068^{\circ}/\text{hr}$ , which is equivalent to a triad axis error of  $0.057^{\circ}/\text{hr}$ , was successfully detected in repeated trials. The parity equation residual noise does increase in a dynamic environment, but the ratio of detectable error to residual noise remains constant.

Degradations have been successfully classified into the following categories: constant bias, ramp, and variance increase. Automatic recompensation for both the ramp and constant bias was demonstrated. Recompensation accuracies of  $0.0008^{\circ}/\text{hr}$  for bias and  $0.0008^{\circ}/\text{hr}/\text{min}$  for ramp errors were achieved consistently.

The fail detection software, in its present form, can identify the third instrument failure under certain conditions (i.e., when the third failure is of greater magnitude than either of the first two failures). This potential was realized and software has been developed to identify the third failure and reorganize the processing matrix (Appendix A Vol 1, R746) to work with only the remaining three good instruments. This arrangement was verified during SIRU Shuttle test demonstrations. A third failure whose degradation was on the order of 5 to 10 times that of the second soft failure was successfully detected and isolated. It provided another improvement in the performance capability of the system under extreme failure conditions.

A single position self-calibration method was devised for calibrating the lumped gyro drifts of four gyros while assuming zero drift for the two reference gyros whose OA axes are approximately vertical (within  $10^{\circ}$ ). The procedure ties the system calibration accuracy to the more stable NBD terms of the reference gyros and eliminates the errors due to the more unstable ADIA and ADSRA terms of the non-reference gyros. Calibration accuracy is on the order of  $0.015^{\circ}/\text{hr}$ .

Coarse and fine alignment algorithms were designed and verified. Fine alignment to within 1 milliradian in 15 minutes was accomplished. Coarse alignment

accuracy is on the order of  $1^\circ$  in a fixed 260 second time period. The alignment algorithms are easily implemented in software and modification to accommodate the environment dynamics, once established for a given mission, are trivial.

A land navigation algorithm was used as an evaluation aid for characterizing performance degradation due to error propagation arising from a dynamic environment or from the time delay in detecting and isolating an instrument failure. The navigation algorithm was tested for basic sensitivities to instrument errors.

The Schuler mode is excited by system level misalignments and accelerometer bias. Peak error during the first 1/2 hour was  $7 \text{ nm/cm/sec}^2$  where 1 milliradian of misalignment is approximately equal to  $1 \text{ cm/sec}^2$ . The 24 hour period mode is excited by gyro bias error with an initial slope of  $1 \text{ nm/hr}/0.015^\circ/\text{hr}$ .

The principle cause of dynamic error propagation is pseudo-coning drift due to gyro output axis coupling. Output axis coupling compensation proved stable under various combinations of instrument failures.

System performance with FDICR operating is on the order of  $0.015^\circ/\text{hr}$ .

End-to-end system performance demonstrations proved out the compatibility and operational readiness of all the software algorithms.

#### 10.1 Capabilities and Limitations of the Redundant Strapdown Approach

Major SIRU capabilities are as follows:

1. High Reliability - (See Chapter 8 SIRU Reliability). The system has been in continuous operation for three years and has a predicted MTBF of 28,800 hours (90% confidence) for a mission duration of one month.
2. Ease of Maintenance - Failed instrument modules are extremely easy to replace during system operation in contrast with a gimbal system. Failed modules were replaced during SIRU Utilization testing without catastrophic delays.
3. Failure Detection, Isolation, Classification and Recompensation (FDICR) - A system was demonstrated for FDICR of failed instruments for various dynamic environments (where FDICR parameters were adjusted manually for the environment). The parity equations and least squares matrices are reorganized after a failure is detected and isolated without the concern for IMU alignment accuracies required of redundant gimbal IMU s.

Two successive failures of gyros and of accelerometers can be detected, isolated, and compensated.

A third gyro failure that is significantly worse than the first two failures can also be detected and isolated (The same logic can easily be implemented for accelerometers).

Failed instruments can be recompensated easily and accurately without the problems accompanying redundant gimbal IMU's (where the gyro errors affect the accelerometer outputs and necessary alignment for recompensation of the failed IMU is changed due to the failure).

4. Single Position Calibration - Single position calibration results in attitude alignment being dependent on the smaller reference gyro constant bias terms and independent of larger ADIA and ADSRA terms.
5. Output Axis Coupling Compensation - This major source of instrument dynamic errors is stably compensated.

Additional capabilities are summarized in Section 10.0 of this Chapter.

Major limitations to the redundant strapdown approach are as follows:

1. Pre-launch Calibration - The present single position calibration procedure cannot separate ADIA and ADSRA gyro errors from the measured gyro lumped drifts.
2. Instrument Dynamic Errors - There are small residual dynamic errors on the order of  $0.06^{\circ}/\text{hr}$  in some of the instruments. (This is further discussed in Section 10.2 "Recommendations").

Other limitations are given in Section 10.2 "Recommendations" of this Chapter.

## 10.2 Recommendations

Presently, the FDICR degradation detection thresholds are set manually in accord with the parity equation residual noise standard deviation. This standard deviation varies with the environment and becomes larger for more severe dynamic

environments. A dynamic compensation should be developed to automatically adjust the threshold to be compatible with the environment.

The single position self-calibration algorithm yields only the lumped drifts of the four non-reference gyros. Techniques should be developed to apportion the lumped drift among the bias and "g" sensitive terms. This could be accomplished through the use of past performance history for the instruments and a test sequence, similar to that used in single instrument testing, to isolate the bias drifts. An additional check on the validity of the assumed bias stability of the reference gyros should be implemented through the use of the system north axis drift. An alternate method for estimating vertical axis drift has been proposed that is insensitive to low frequency environmental inputs. A comparison study should be made between this method and the presently implemented method to determine the better implementation.

Single position calibration tests, land navigation algorithm tests and end-to-end system demonstrations reveal that a marginal condition exists in some of the SIRU gyro modules. This sensitivity was excited in the oscillatory testing and is visible as a drift of approximately  $0.06^{\circ}/\text{hr}$ . It is believed that a sensitivity of the dc amplifier, in the pulse-torque electronics module, to the 40 volt excitation is responsible for this drift error. The hardware in the sensitive modules should be revised, testing done, and results analyzed to verify the design solution.

Presently, the SIRU dynamic compensation software is operating for only gyro output axis coupling and accelerometer  $RW^2$  and  $R\dot{W}$  normalization. Software routines matured on the SPOT (System Performance Optimization Tests) program for compensation of anisoinertia, SRA cross coupling and the four parameter scale factor compensation algorithm should be coded and test confirmed for the SIRU system.

The multiplexer, originally planned for development during the SIRU build effort, and BITE (electronic fail detection) hardware should be fabricated and integrated into the SIRU system to fill out and complete the system redundancy envisioned at the outset of the program.

It is desirable that after the previous recommendations have been accomplished, the system be flight tested to confirm the indicated performance in an environment representative of a possible application.

Preliminary estimates have been made on a revised mechanization of the SIRU system, based on the hardware and software developed under this contract, that

would take advantage of state-of-the-art electronics technology. The system would utilize medium scale integration with hybrid circuitry and incorporate modular construction concepts. The instrument modules, for instance, would be nearly self-sufficient requiring only 28 volts dc and an input/output digital word representing data or data requests. Basic to this concept is the premise that different sensors could be incorporated in the instrument module assembly and these modules would be completely interchangeable in system usage. A program to implement this mechanization should be initiated.

## LIST OF REFERENCES

1. Gilmore, J.P., Cooper, R.J., SIRU Development - Final Report, Volume I, System Development, CSDL Report R-746, July 1973.
2. Chien, T.T., An Adaptive Technique for a Redundant-Sensor Navigation System, MIT/CSDL Report T-560, February 1972.
3. McKern, R.A., A Study of Transformation Algorithms for Use in Digital Computers, MIT/CSDL Report T-493, January 1968.
4. Britting, K.R., Palsson, T., Self Alignment Techniques for Strapdown Inertial Navigation Systems with Aircraft Application, MIT/EAL Report RE-33, November 1968.
5. Fay, S., Leveling of Analytic Platforms, IEEE, Volume AES-5, #1, January 1969.
6. Optimum Digital Filter Study for Strapdown Inertial Alignment N69-10879 General Electric, Pittsfield, Ma., July 1969.
7. Howard, P.B., Gyrocompassing Strapdown System for the Sonaray Vehicle, MIT/IL, Report E-2406, April 1969.
8. Muller, P.E., Special Problems of Gyrodynamics, Technical University of Munchen, Course held at Dept. of General Mechanics, International Center for Mechanical Sciences, October 1970.
9. Tvirbutas, A.A., Platform Alignment to an Inertial Orientation Using an On-Line Statistical Filter, MIT/CSDL, Report T-529, January 1970.
10. Ryan, T.J., Alignment and Calibration of a Strapdown Inertial Measurement Unit, MIT Measurements Systems Lab, Report RE-67, December 1970.
11. Schmidt, G.T., Brock, L.D., General Questions on Kalman Filtering in Navigation Systems, MIT/IL, Report E-2406, April 1969.
12. Broxmeyer, C., Inertial Navigation Systems, McGraw-Hill, 1964.
13. Britting, K.R., Unified Error Analysis of Terrestrial Inertial Navigation Systems, Doctor of Science Thesis, MIT Dept. of Aeronautics and Astronautics, October 1970.
14. Kriegsman, B.A., Marcus, F.J., Space Shuttle GN&C Equation Document, No. 17 (Rev. 1) Entry Guidance, MIT/CSDL, April 1972.

REFERENCES (cont)

15. Space Shuttle Avionics, A Redundant IMU On-Board Checkout and Redundancy Management System (INTERIM Report) R-733, MIT/CSDL, September 1972.
16. TAGS Redundancy Management - Final Report. IBM Electronics Systems Center, Owego, N.Y., 29 December 1972, IBM File #72-L56-68.
17. Freund, John E., Mathematical Statistics, Prentice Hall, Inc., Englewood, NJ, 1962.